Single Ion Polymer Electrolytes for Safe and Sustainable Batteries

Yunfan Shao

THÈSE

Pour obtenir le grade de

DOCTEUR DE L'UNIVERSITÉ GRENOBLE ALPES

École doctorale : I-MEP2 - Ingénierie - Matériaux, Mécanique, Environnement, Energétique, Procédés, Production
Spécialité : 2MGE - Matériaux, Mécanique, Génie civil, Electrochimie
Unité de recherche : Laboratoire d'Electrochimie et de Physico-Chimie des Matériaux et des Interfaces.

Electrolytes polymères à conduction unipolaire pour des batteries sûres et durables

Single Ion Polymer Electrolytes for Safe and Sustainable Batteries

Présentée par :

Yunfan SHAO

Direction de thèse :

Cristina IOJOIU DIRECTRICE DE RECHERCHE, CNRS délégation Alpes	Directrice de thèse
Fannie ALLOIN DIRECTRICE DE RECHERCHE, CNRS délégation Alpes	Co-encadrante de thèse
Dominic Bresser DIRECTEUR DE RECHERCHE, Helmholtz Institute Ulm/ Karlsruhe Institute of Technology	Co-encadrant de thèse

Rapporteurs :

Philippe POIZOT
PROFESSEUR DES UNIVERSITES, Université de Nantes
Daniel BRANDELL
FULL PROFESSOR, Uppsala University

Thèse soutenue publiquement le **15 décembre 2023**, devant le jury composé de :

Cristina IOJOIU DIRECTRICE DE RECHERCHE, CNRS délégation Alpes	Directrice de thèse
Philippe POIZOT PROFESSEUR DES UNIVERSITES, Université de Nantes	Rapporteur
Daniel BRANDELL FULL PROFESSOR, Uppsala University	Rapporteur
Niki HALTTUNEN INGENIEUR DE RECHERCHE, IFP - Energies nouvelles	Examinateur
Jean Claude LEPRETRE PROFESSEUR DES UNIVERSITES, Université Grenoble Alpes	Président

Invités :

Fannie ALLOIN
DIRECTRICE DE RECHERCHE, CNRS Alpes
Dominic BRESSER
DIRECTEUR DE RECHERCHE, Helmholtz Institute Ulm/ Karlsruhe Institute of Technology

Preface

This thesis is based on my studies from September 2020 to November 2023 in the Laboratory of Electrochemistry and Physical Chemistry of Materials and Interfaces (LEPMI, UMR5279) in Grenoble, France. The work is a part of the French-German project *Metal- and Liquid-free Organic Lithium-Ion BatteriEs for Sustainable and Safe Energy Storage (MOLIBE)*, jointly funded by the ANR and BMBF.

The aim of this research was to develop novel polymer electrolytes to improve the safety of organic lithium batteries. Single-ion polymer electrolytes (SIPEs) with a high lithium transference number are a promising solution to enhance the safety of batteries. This thesis focuses on the following three aspects: 1) the development of new SIPEs, 2) the adaptation of SIPEs in combination with organic active materials, and 3) the examination of the interface and interphase between the SIPEs and lithium metal. Accordingly, this thesis covers the three important components in such lithium batteries, i.e., the electrolyte as well as the positive and negative electrode.

After these three years of research, I could glimpse on some clues for better energy storage, and I am excited to share these findings in this thesis. However, with more new phenomena observed and studied, I must admit that there are more and more questions to be answered. I hope this thesis will not put an end to my studies on electrolyte and energy storage but become the foundation for further studies in this direction.

I must emphasize that it would not have been possible to finish this thesis without the guidance of my supervisors: Dr. Cristina Iojoiu, Dr. Fannie Alloin, and Dr. Dominic Bresser, to whom I would like to express my deep appreciation. Not only the knowledge, but also the rigorous attitude to science that I learned from them supported me during the studies at LEPMI and will still guide me in the future.

I would like to thank all the colleagues in the project for the seamless collaboration: Kai Shi, Dr. Jakob Asenbauer, Dr. Valentin Gouget, Dr. Lionel Picard, Anja Lenzer, Merve Erakca, Sebastian Pinto Bautista, Dr. Sandrine Lyonnard, Dr. Simon Jestin and Dr. Yassine Bouhoute. Thanks to Dr. Maider Zarrabeitia Ipina and Dr. Clarie Villevieille for the help with the XPS measurements and helpful discussion. Thanks to Dr. Francine Roussel-Dherbey for the help with the SEM analysis. Thanks also to Dr. Laure Cointeaux and Tony Bertaux for their help with the electrolyte synthesis. Thanks to Dr. Yiwei Dai for the helpful discussion on organic synthesis. Thanks to Prof. Renaud Bouchet, Dr. Didier Devaux, Régis, Sajad, Ernest, Mohamed, Justine, Tanguy, Misgina, Adriana, Thomas BB., Thomas B., Kaique, Alexandru, Nieves, Phil, Gregoire, Natalia, Guillaume, Nicolas, James, Faiz, Hippolyte, Lysandre, Anne, Benjamin, Timothee, Baptiste, Lihua, Lucas, Adrien, Célia and all the colleagues in LEPMI during these 3 years. I would also like to express my gratitude to my friends and family. Without your support, I could not face the difficulties alone in this journey.

Specially I would thank all the people who make efforts in advancing science open, free and rigor.

Yunfan Shao

Grenoble, October 2023

Abstract

Lithium batteries are considered as the most successful energy storage systems due to their high energy and power density. However, there are concerns over the current lithium batteries, including safety, sustainability, etc. On the one hand, the safety issue involves thermal runaway phenomena which is mainly ascribed to the currently used flammable organic liquid electrolytes. To improve the safety of batteries, polymer electrolytes with better thermal stability and mechanical strength have been developed to substitute the organic electrolytes. Among them, single-ion polymer electrolytes (SIPEs) with an immobilized anionic group at the polymer chain exhibit extra advantages owing to their high lithium transference number. This special design reduced the polarization inside the electrolyte to avoid salt precipitation, concentration gradient and more importantly lithium dendrite growth. On the other hand, the sustainability issue of current batteries comes from the use of critical minerals such as Cu, Co, and Ni which are widely used in positive electrode materials and current collector. Organic active materials are composed of earth abundant elements (C, H, N, O and S) with a lower environmental footprint and toxicity. And the production of organic active materials could be independent from the price and geopolitical limits of such elements, rendering them potentially greener and more sustainable candidates for battery applications.

In this thesis, organic active materials were applied with SIPEs to answer these concerns. SIPEs with different structures were designed, synthesized, and characterized to reach high ionic conductivity, lithium transference number close to 1 and good electrochemical stability. The SIPEs were then applied in lithium-metal batteries (LMBs) with an organic positive electrode with long-term cycling stability and high Coulombic efficiency. Additionally, the interaction between the lithium-metal electrode and the SIPEs were also studied by lithium plating/stripping tests. With lithium nitrite doping in the SIPE, I observed improved cycling stability and reversibility with lithium-metal electrodes by modifying the solid electrolyte interphase (SEI) to reduce the interfacial resistance and improve surface morphologies of the lithium metal. The rational designed SIPEs could deliver high performance facing both organic and metallic lithium electrodes to promote safe and sustainable organic batteries, rendering them a powerful candidate for future energy storage devices.

Table of Contents

Chapter 1 Research Background

1 Trend in energy storage technologies and lithium-ion batteries

Energy storage systems such as batteries, capacitors, flywheel, pumped hydro, etc. are crucial to the functioning of modern society. From grid scale, the energy storage systems are needed to improve grid reliability, avoiding powers blackouts such as India blackout in 2012 which affected more than 600 million people. Moreover, the energy storage systems are the bridges to link renewable energy including wind, solar, tidal and soon that cannot be used before converting to electricity.[1] Different technologies are chosen by their properties to facing different tasks. For example, supercapacitors with ultra-high power density are suitable for improving power quality and flow batteries could provide low-cost solutions for load shifting applications. Among these technologies, secondary lithium-ion batteries (LIBs) play a dominant role due to their high energy and power density. Commercial Li ion battery delivers high energy density of more than 2.5 times than Ni-metal hydride batteries and outperform on the power output. The high performance of Li batteries are related to the Li characteristics and electrochemistry, i.e., low molar mass, small ionic radius, fast kinetic and low redox potential[2]. The LIBs meet most of the application scenarios, from tiny portable electronic devices such as earphones (level of mWh) to electric vehicles (kWh) and to grid-scale energy storage (MWh) systems.

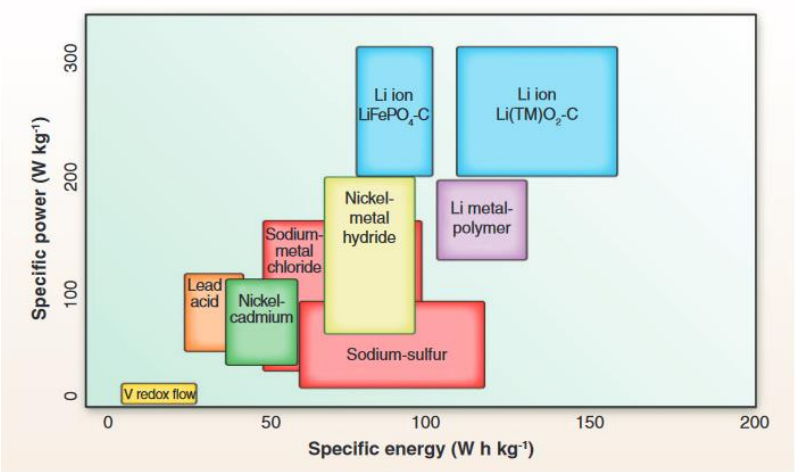

Figure 1. Specific power and energy of different energy storage technologies.[2] Reuse with permission of AAAS.

For energy storage devices, the Li battery has already gained most of the market and increased continuously during the last decades. For example, in 2013, about 60% of energy storage deployments were based on lithium-ion batteries, reaching 93% in 2020, whereas the total energy storage increased from ~0.2 GW in 2013 to more than 3 GW in 2020. At the same time, Li batteries have also been chosen to reform the modern transportations with electric vehicles (EVs) and replace fossil fuels.[3] According to international energy agency (IEA), the electric car sales exceeded 10 million in 2022 and are anticipated to further increase in 2023 by around 35%.

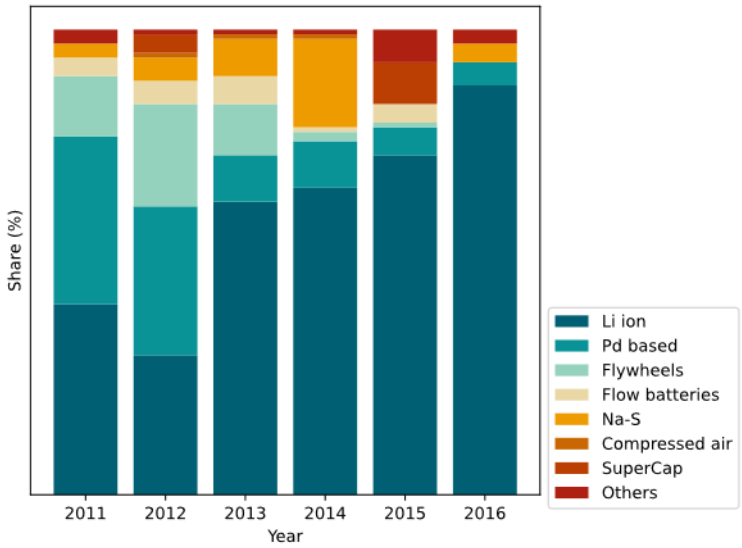

Figure 2. Technology mix in energy storage deployments from 2011 to 2016, according to data from IEA.

Due to the dramatic increase of lithium powered energy storage and rising trend of EVs, the cost of LIBs decreased from more than 900 in 2011 to ~132 USD per kWh in 2021. The price of LIBs was reduced mainly due to the rapid increase in scale of production, which saved costs from bulk production, better supply chain, automatic factories, and technological improvements. Taking a closer look to the shares in the battery price, in 10 years from 2011 to 2021, the packing cost significantly decreased from 290 to 31 USD per kWh and the costs other than positive electrode materials (including other materials, labor, energy, etc.) also decreased dramatically from 600 to 72 USD per kWh. However, the cost from cathode materials did not decrease at a proportional rate as the other costs but remained almost constant during these 10 years. The cost of positive electrode materials in 2011 was 32.6 and 28.7 USD per kWh after a decade. Although it is only a small share of the total price, this stable cost of the positive electrode materials is getting more and more important for the battery price, and the contribution increased from 5% to 21%. Thus, the positive electrode material is becoming a bottleneck for lowering the price of LIBs in the future. On the contrary, it could be the reason leading to a rise in the price due to the shortage of the critical raw materials. Lithium, cobalt, nickel, and aluminum are widely present in electrode active materials including lithium cobalt oxide ($LiCoO_2$, LCO), lithium nickel manganese cobalt oxides ($LiNi_xMn_yCo_{1-x-y}O_2$, NMC), lithium

nickel cobalt aluminum oxides ($LiNi_xCo_yAl_{1-x-y}O_2$, NCA), etc. Aluminum is also used as positive current collector. Copper is used as conducting wires and negative current collector. During the last decade for all these metals the price has risen rapidly (Figure 4) due to the largely increased demand.

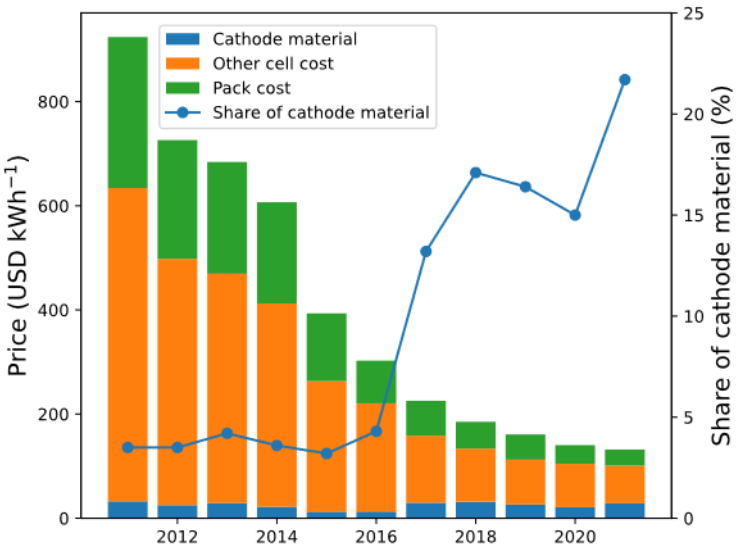

Figure 3. Price of lithium-ion battery from 2011 to 2021 with the share of cathode material cost, according to data from IEA.

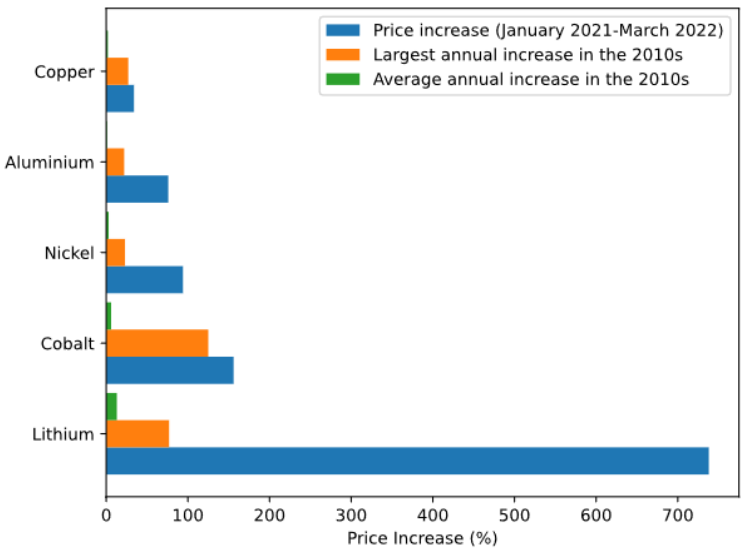

Figure 4. Price increase of critical minerals in lithium ion battery. Data from IEA, according to data from IEA.

It has been predicted that the demand of LIB will be significantly increased in near future (6x times by 2030 and 100x times in 2040 comparing to 2020) to meet the transition to EVs (in the sustainable development scenario of IEA).[4] With such a large demanding market, the cost and sustainability of the batteries will become even more important in the near future.

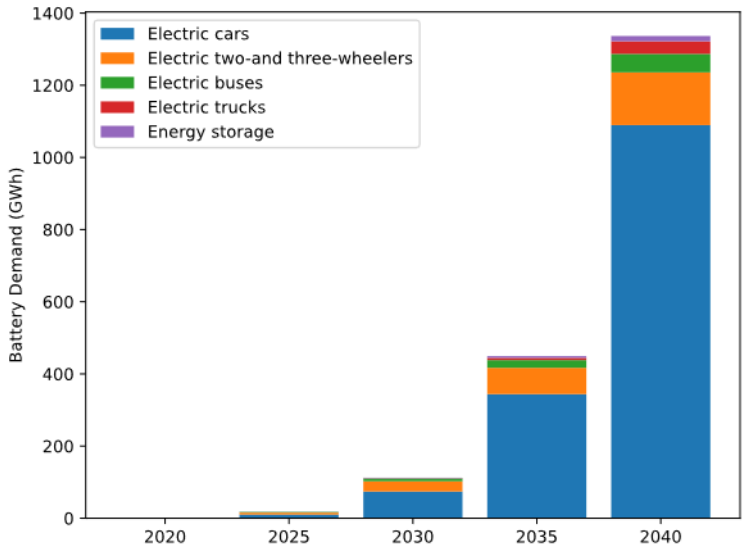

Figure 5. Annual battery demand for electric vehicles and storage in the sustainable development scenario, according to data from IEA.

In summary, the rapidly increasing demand for energy storage is pushing for the developing devices with better efficiency and higher energy/power density. Lithium batteries have gained a vast market share due to their outstanding performance. However, to get prepared for the accelerating demand increase for batteries in the near future, sustainable and low-cost Li batteries with higher performance are needed.

2 Lithium batteries

Lithium batteries were invented in 1912 and primary batteries using lithium metal as anode and MnO_2 or fluorinated graphite as cathode were commercialized in the 1970s. The primary lithium battery was designed to be used only once and not be recharged (the electrochemical reaction is not reversible) and soon be substituted by more economical secondary LIBs, which were developed and commercialized in 1991 by Sony. These batteries are based on graphite as

negative electrode and lithium cobalt oxide as positive electrode materials, which are still one of the mainstream choices in LIB industry.

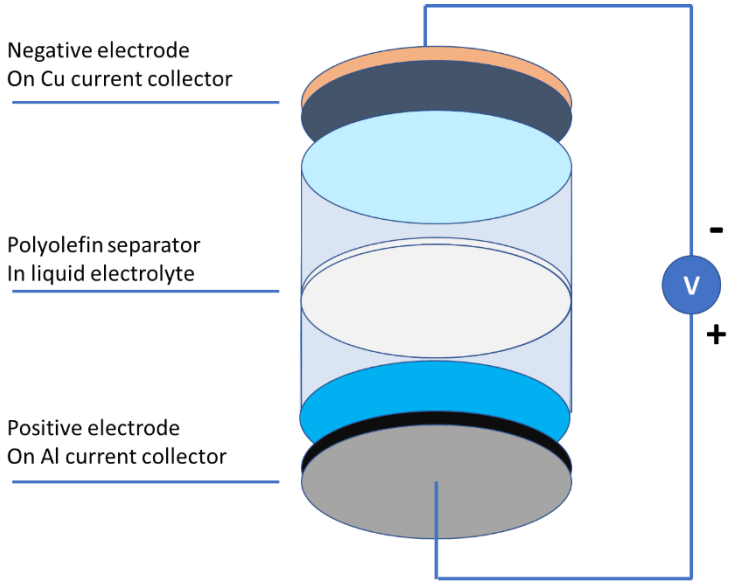

Figure 6. Structure of a typical LIB.

A typical LIB consists of a negative electrode, a positive electrode, current collector, electrolyte, and separator. The negative and positive electrodes are the site of redox reaction and the key to lithium storage. Upon discharge, the lithium ions are released from the anode (negative electrode) material and travels though the electrolyte to the cathode (positive electrode). The battery voltage decreases during discharge and the cell can power a device. Upon charge, the lithium ions are forced to be released from the positive electrode and received by the negative electrode, which leads to an increasing cell voltage and the storage of energy. In the whole process, the electrolyte comprised in the separator assures the transport of lithium ions from one electrode to the other. In current LIBs, the separator is commonly a porous, non-conductive polymer film (filled with the liquid electrolyte), sandwiched between the two electrodes to avoid direct contact and direct electron transfer, i.e., a short-circuit.

2.1 Electrodes

2.1.1 Inorganic electrode materials

The commonly used electrode active materials are listed in Figure 7. Materials at low potential

are usually used for the negative electrode and high voltage materials are used for the positive electrode. As comparison, the electrochemical stability window of common organic liquid electrolytes was marked as the pale blue region in Figure 7 (approximately 1 - 4.7 V *vs*. Li^+/Li).[5]

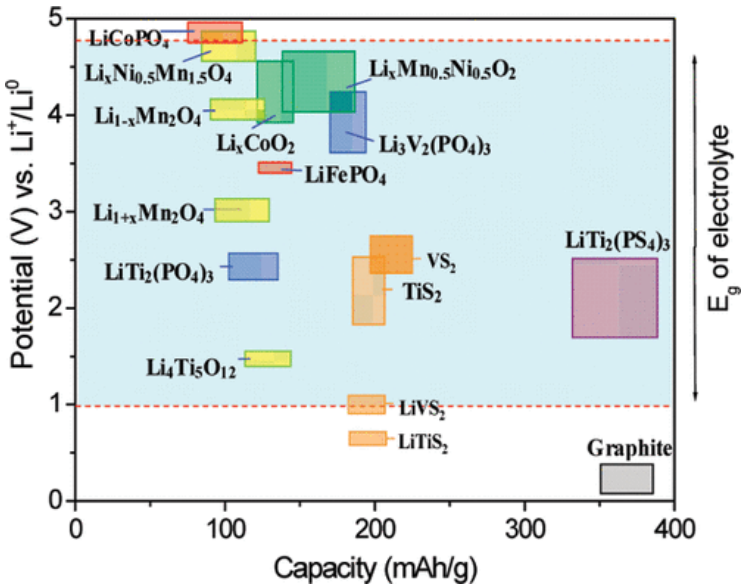

Figure 7. Capacity and potential of electrode materials and the electrochemical window of electrolyte. Reprinted with permission from Ref.[5] Copyright 2010 American Chemical Society.

Negative electrode

Graphite is the most used active material nowadays,[6] which provides a theoretical specific capacity of 372 mAh g^{-1}, with a very low de-/lithiation potential of 0.2 V *vs*. Li^+/Li. The graphite's layered crystal structure allows lithium-ion intercalation to form LiC_6 complex.

Other than graphite, hard carbon and lithium titanium oxide ($Li_4Ti_5O_{12}$, LTO) have also been applied for high-power batteries. Hard carbon is a class of material yielded by carbonizing resin, pitch or biomass at temperatures lower than 1500 °C, which results in a less crystalline structure than graphite.[7] The hard carbon could be an ideal anode of LIBs in low temperature or fast-charging scenarios, because of its specific lithium storage mechanism.[8] In addition to LIBs, hard carbon is also suitable negative electrode for sodium batteries, as these cations are not able to be reversibly intercalated into graphite. LTO is a spinel-structured material that holds the second largest market share in negative electrode materials.[9] LTO has a relatively low

theoretical specific capacity of 175 mAh g^{-1} and high redox potential of 1.55 V *vs.* Li^+/Li, leading to a lower energy density compare to graphite. However, due to its ultra-low volume change of less than 1% (12% for graphite) during de-/lithiation, a very stable cycling of more than 10,000 cycles can be achieved. More importantly, the fast lithium ion diffusion in LTO allows it to be used in high-power batteries with high charge/discharge rates, which is favored in EV applications.[10] However, the relatively low energy density, which is due to both the high redox potential and lower specific capacity, limits the application of LTO only to high-power batteries.

Meanwhile, silicon and lithium metal were also considered as the most promising candidates for next-generation negative electrodes due to their extremely high specific capacity. Silicon could electrochemically alloy with lithium to deliver the highest specific capacity of 4200 mAh g^{-1} (3578 mAh g^{-1} at room temperature). However, the huge volume expansion (320%) during the lithiation process will lead to a failure of the Si electrode. The Si particles get pulverized upon cycling, leading to the collapse of the entire electrode, which strongly hinders the reversibility and cycle life.[11]

Lithium metal has been considered as the ultimate negative electrode with an ultra-high specific capacity of 3860 mAh·g^{-1} or 2760 mAh cm^{-3}, low redox potential of -3.04 V *vs.* SHE. However, the utilization of lithium metal was hindered by multiple concerns including lithium dendrite growth[12,13], inhomogeneous SEI formation[14], dead lithium[15], low Coulombic efficiency[16], etc. Aurbach et al.[17] reviewed the failure of Li metal in rechargeable Li batteries with liquid electrolytes. The passivation of lithium metal in any polar aprotic electrolyte solution is unavoidable. Together with small Li grains formed upon fast charging, i.e., high surface area, the cycle life of the Li metal is very limited.

Positive electrode

For the positive electrode material, LCO, NMC and lithium iron phosphate ($LiFePO_4$, LFP) are most well-known and used in commercial batteries. LFP has an olivine-type crystal structure with orthorhombic lattice structure, which is stable during the lithiation/delithiation cycles. The volume change is only 6.8%, from discharged to charged state, which going through the phase

transition from $FePO_4$ to $LiFePO_4$ with a theoretical specific capacity of 170 mAh g^{-1}.[18]

4V-class positive electrode material such as NMC, NCA have also been commercialized during recent years and provide better energy density than LFP. These layered materials have occupied the EV markets quickly.

High energy densities can also be obtained with positive electrodes with higher voltage such as lithium nickel manganese oxide ($LiNi_{0.5}Mn_{1.5}O_4$, LNMO)[19], lithium manganese oxide ($LiMn_2O_4$, LMO)[20], lithium vanadium phosphate ($Li_3V_2(PO_4)_3$, LVP),[21] which have been intensively investigated in recent years. However, especially for LNMO, the high voltage exceeds the electrochemical window of most of the electrolytes.[22]

As conclusion of this part, the gigantic demand of energy storage will push the battery to use advanced electrode materials, to feed the never satisfied battery performance. For negative electrode, Si and Li metal are the most promising candidates. For the positive side, Ni-rich layered materials, high-voltage spinel and olivine materials are in the list. Additionally, sulfur could also be a great choice for high capacity, low-cost positive electrodes.

However, these high energy electrodes are facing challenges not only in the stability of the active materials, but also the electrolytes. Thus, the development of next-generation electrolytes is crucial, not only for safety but also for the energy density.

2.1.2 Organic active materials

In the context of the high demand for LIBs, the sustainability and price of the positive electrode materials, which represent, currently, more than 20% of the price of the whole battery, will be very sensitive to the mineral resources such cobalt and nickel, which led to uprising price, geopolitical issues, and environmental concerns. By substituting metal elements with organic compounds which contain earth abundant elements such as C, H, N, O, and S, the organic active materials are more sustainable, less toxic, and flexible on the properties. The organic active materials could be synthesized from renewable sources of biomass and go through a close loop of CO_2 to create fully green and sustainable batteries, as shown in Figure 8.[23,24]

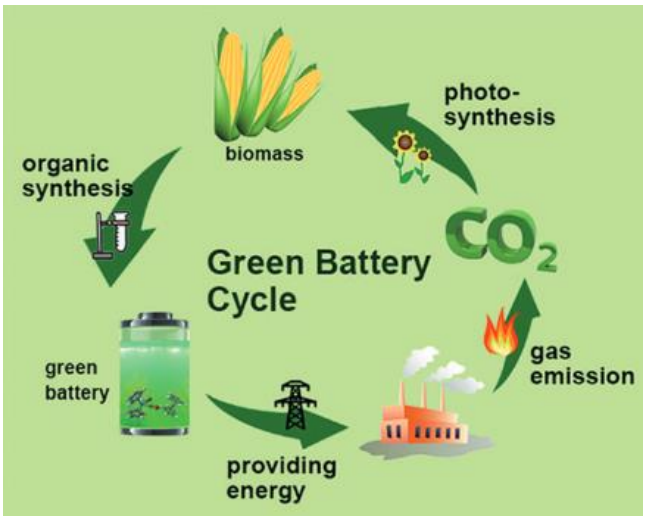

Figure 8. Close loop of ideal biomass-based battery. Reused with permission of Wiley and Sons.

Thus, organic active materials can be a potential candidate, to reduce the reliance of these mineral resource, not only for sustainable and low cost but also for the stability and the safety of the energy. Other than these advantages, due to the design, flexibility, the redox-active organic materials can be easily modified with the molecular structure to achieve tunable redox potentials and can be used as both electrodes by the introduction of functional groups. E.g., a series of nitroxylbenzene derivatives with different substitutions (Figure 9.)[25] showed altered redox potentials. With electron donating methoxy, t-butyl group and hydrogen on the *para*-site, the redox potential was shifted from 0.56 to 0.75 and 0.83 V *vs*. AgCl/Ag, respectively, which corresponded to the oxidation of the nitroxide radical to the oxoammonium cation (p-type doping). In the case of the electron withdrawing trifluoromethyl group, the redox potential shifted to -0.92 V *vs*. AgCl/Ag, and the mechanism was altered to the reduction of nitroxide radical to anioxy anion (n-type doping). This remarkable study can fully address the designability of organic active materials to tune their electrochemical properties.

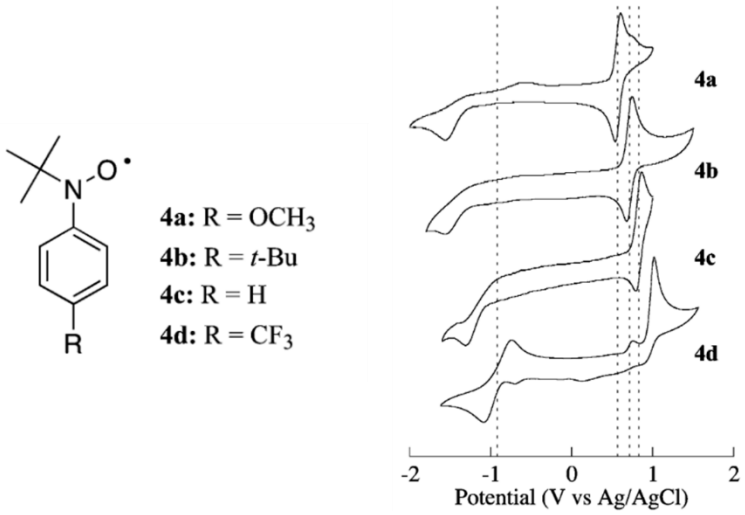

Figure 9. Nitroxylbenzene derivatives with different substituent groups and their cyclic voltammograms. Reprinted with permission from Ref[25]. Copyright 2007 American Chemical Society.

However, the organic active materials generally suffer from shortcomings, including solubility in organic solvent, limited thermal stability, low density, insufficient electric conductivity and need for prelithiation. Some of these shortcomings are intrinsic to the organic structure, especially those related to the thermal stability and density issue, but some issues such as the solubility in organic solvents and low electronic conductivity can be overcome by the molecular design. For example, to limit the solubility, polymerization and introduction of ionic functions[26] are efficient methods.

Conjugated polymers have been commercially used as organic active materials since 1980s, which is based on poly(aniline)[27,28]. The redox reaction of poly(aniline) was shown in Figure 10. Although the batteries suffered from low energy density which is due to the limited achievable degree of doping (usually 30-50% as compared to the number of repeating units). More conjugated polymers are investigated and utilized in energy storage such as poly(thiophene)[29] poly(paraphenylene)[30], etc. These conducting polymers could be applied as both positive and negative electrodes with a high rate of redox reaction, due to their conducting properties, which allow them to be used in high power applications. However, the low capacities strongly hindered these materials to complete with the conventional active materials.

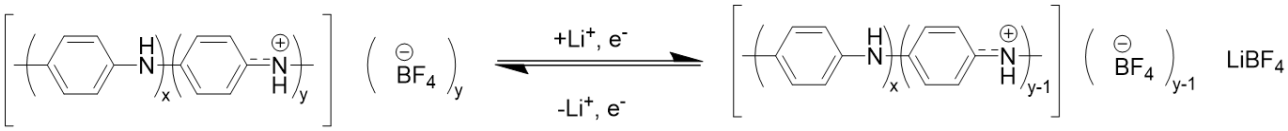

Figure 10. Electrochemistry of poly(aniline) organic active material.

The low capacity of these conjugated polymers can be ascribed to their rigid, planar structure which leads to incomplete doping. The effect of conjugated backbone was clearly demonstrated with a family of ferrocene based polymers by Tamura and coworkers.[31] Ferrocene is a classic organic active material that is used as reference electrode in redox potential measurement. Non-conjugated (poly(vinylferrocene)), conjugated poly(ethynylferrocene) and poly(ferrocene) were examined (Figure 11). By galvanostatic cycling the polymers *vs*. lithium metal electrodes, the three polymers showed different reversible capacities and redox behaviors. The poly(vinylferrocene) showed complete reversibility and reached 83% of theoretical capacity. While the poly(ethynlferrocene) and poly(ferrocene) showed less reversible behaviors and reached only around 50% and 30% of the theoretical capacity initially, if only considering the plateau part. Notably, in the conjugated poly(ethynlferrocene) and poly(ferrocene), the discharge profiles showed a tail at lower voltage which suggest the doping (lithiation) was hindered by the conjugated backbone.

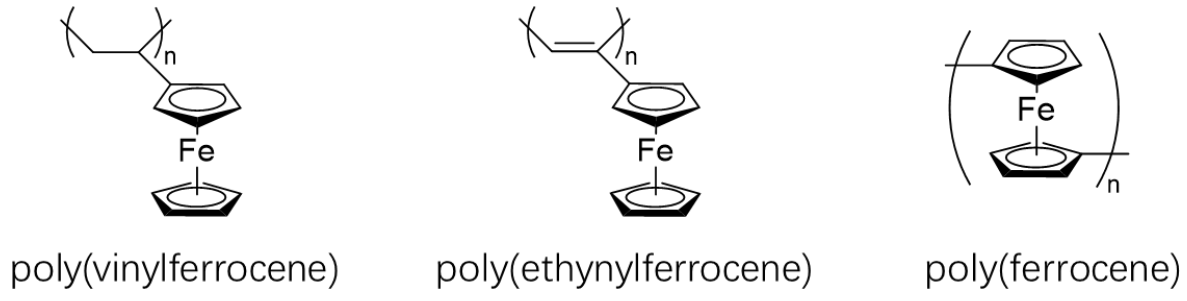

Figure 11. Ferrocene based polymers with non-conjugated and conjugated backbones.

Despite the conjugated polymers with obvious drawbacks, three families of non-conjugated organic active materials were developed, which are carbonyl, organosulfur, free radical type of organic molecules. Figure 12 shows the typical capacity and redox potential of the three classes

of materials.[32]

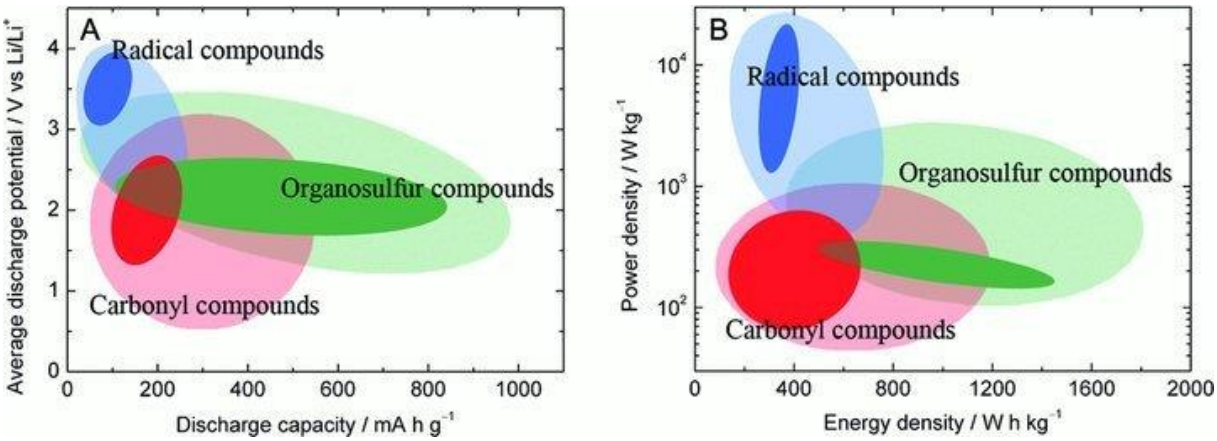

Figure 12. Capacity and energy density of the non-conjugated organic active materials. Reused with permission of John Wiley and Sons.

With a one electron redox reaction, the carbonyl could reversibly receive and give a lithium ion to complete the electrochemistry in secondary lithium battery. Quinone based compounds are the most studied due to their simplicity. Tetrahydroxybenzoquinone ($Li_4C_6O_6$)[33] showed a reversible specific capacity of 200 mAh g^{-1} with an average potential of 1.8 V *vs*. Li^+/Li. The compound was proved as a sustainable redox-active material with more efficient life cycle assessment than inorganic electrolytes. Wang et al.[34] reported another quinone based active material, organic tetralithium salts of 2,5-dihydroxyterephthalic acid ($Li_4C_8H_2O_6$), which involved 2-step of 2-electron reaction, which is shown in Figure 13A. The material could be further reduced to $Li_6C_8H_2O_6$ or oxidized to $Li_2C_8H_2O_6$. Due to the different position of the carbonyl groups in the molecule, the redox voltages of the 2-step reaction from $Li_2C_8H_2O_6$ to $Li_6C_8H_2O_6$ were different, i.e., 0.8 V and 2.6 V, respectively. A full organic symmetrical cell was assembled with $Li_4C_8H_2O_6$ electrodes and cycled between 2.7 and 1.0 V with initial charge and discharge capacities of 225 and 208 mAh g^{-1}, respectively, which are close to the theoretical capacity (241 mAh g^{-1}). More interestingly, the same organic compound, but with sodium ($Na_4C_8H_2O_6$), was able to adapt in all organic sodium ion battery systems.[35] With a similar redox reaction (Figure 13B), the symmetrical cell could deliver a stable reversible capacity of more than 180 mAh g^{-1}. This example has fully demonstrated the capability of organic active

material, which allows them easily to shift from different batteries with different charge carriers.

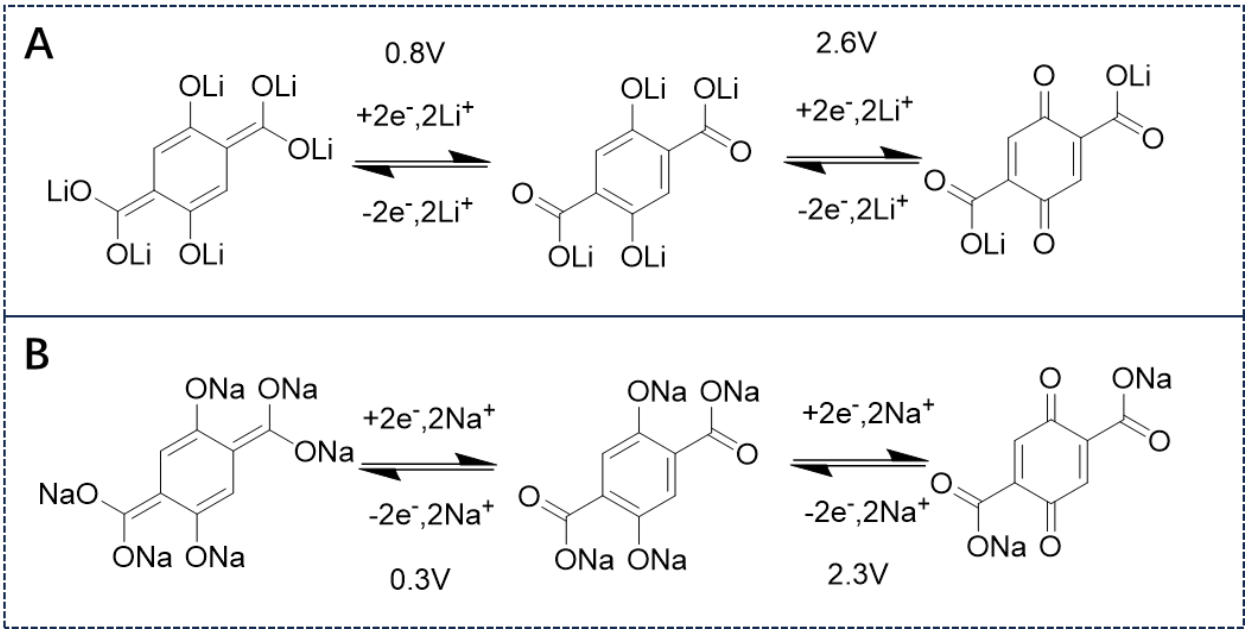

Figure 13. electrochemical redox reactions of (A) tetralithium salt of 2,5-dihydroxyterephthalic acid and (B) tetrasodium salt of 2,5-dihydroxyterephthalic acid.

Small organic molecules are usually soluble in the organic solvents that are used in electrolytes. This dissolution could lead to a capacity loss during the battery cycling by a mechanism similar to the shuttle effect in Li-S batteries.[36] To improve the stability of the organic electrodes, the immobilization of the organic active materials is necessary.[37] Polymerization or oligomerization is one of the methods that is widely applied for organic active materials. Geng et al.[38] studied a series of tetrakeopoperazine based molecules. These molecules (Figure 14, a-d) shared the same N-cyclic polyketone moieties, but with different modifications on the N atoms. The molecules with phenyl, allyl and alkyl substitute showed a reversible redox reaction at 2.5 V, but with very poor cyclability of less than 20 cycles. The quick fading of specific capacity was attributed to the dissolution of the small molecules in electrolyte. Only the oligomeric product (Figure 14, d) showed better cycling stability due to its reduced solubility compared to its monomer.

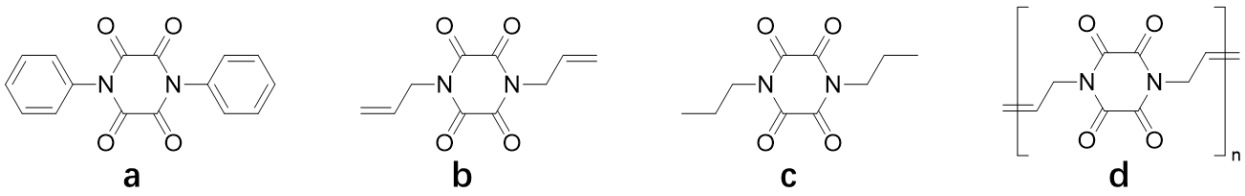

Figure 14. Tetrakeopoperazine-based active materials.

Other than polymerization, salt formation is the other way to decrease the solubility by enhancing the polarities. Various compounds including quinone derivatives[33,39], anthraquinone derivative[40] and pyromellitic diimide[41] exhibited improved cycling stability by salt formation. By introducing strong polar sulfonate group on the indigo dye, indigo carmine positive electrode also showed stable cycling for 100 cycles without obvious capacity decay.[42]

Organic active materials opened another way of pursuing high-performance, safe, sustainable, and low-cost battery applications as both positive and negative electrodes. More importantly, with rational design, the electrochemical proprieties including capacity, voltage, conductivity of organic active materials can be adjusted to adapt different battery systems and showed competitive electrochemical performance compared to the inorganic materials.

2.2 Electrolyte and separator

Conventional electrolytes of LIBs are based on a lithium salt dissolved in organic solvents. The basic function of the electrolyte is to transport ions but block electron conduction between the two electrodes. Due to the nature of a liquid, a porous separator is needed to prevent direct contact of the electrodes. Thus, ionic conductivity is one of the most important properties to characterize the electrolyte. Other than conductivity, lithium-ion transference number, thermal and electrochemical stabilities are also important parameters to evaluate the electrolytes.

Lithium salts used in LIB usually contain a large superacid anion substituted by electron withdrawing functions, generally fluorinated ones, and allow a broad delocalization of the negative charge. In the state of art, the most investigated salts are $LiPF_6$, $LiBF_4$, LiTFSI ($LiN(CF_3SO_2)_2$), LiFSI, $LiClO_4$, LiTf ($LiCF_3SO_3$), etc. The most used salt in liquid electrolyte is $LiPF_6$ due to its good solubility in organic solvents, high ionic conductivity (as high as 10^{-2}

S cm^{-1} at room temperature), high electrochemical stability (up to 4.2 V). The PF_6^- anion was also proved to be able to form a passivation layer on the positive current collector which is Al and prevent the further corrosion.[43] However, LiPF6 is not stable at temperature higher than 50 °C and sensitive to traces of moisture with formation of HF.

The salts are usually dissolved in organic carbonate-based solvents such as ethylene carbonate (EC), propylene carbonate (PC), dimethyl carbonate (DMC) and diethyl carbonate (DEC). The cyclic carbonates (EC, PC) have the advantages of high dielectric constant and ability to form high concentrated lithium salt solutions, but their drawbacks are related to their high viscosity and melting point (especially for EC). Therefore, they are usually mixed with linear carbonates such as DMC, DEC, or EMC (ethylmethyl carbonate), which exhibit low viscosity and dielectric constant, to optimize the properties. In addition to carbonates, ether-based electrolytes are also widely used, especially in alternative battery systems, e.g., dioxolane and dimethoxyethane (DOL/DME) were widely used in Li-S batteries. The drawbacks of these low viscosity solvents are their low flash point and boiling temperature and limited stability in oxidation).

Although liquid electrolytes are the standard in the current battery industry, the conventional liquid electrolytes are facing severe challenges on battery safety. During battery failure, thermal runaway could be triggered by electrical, mechanical, thermal abuse or latent defect inside the cell[44]. Liquid electrolyte without mechanical strength naturally cannot protect the battery from all the 3 types of battery abuse. Mechanical abuse such as impact and penetration could lead to leak of the electrolyte and then followed by overcharge/overdischarge or internal short circuit. Regardless of the origin, the abuse finally led to an increase of temperature and local overheating (can also initiate directly by thermal abuse) and form a loop of chain reactions to irreversibly end in a fire and thermal runaway.

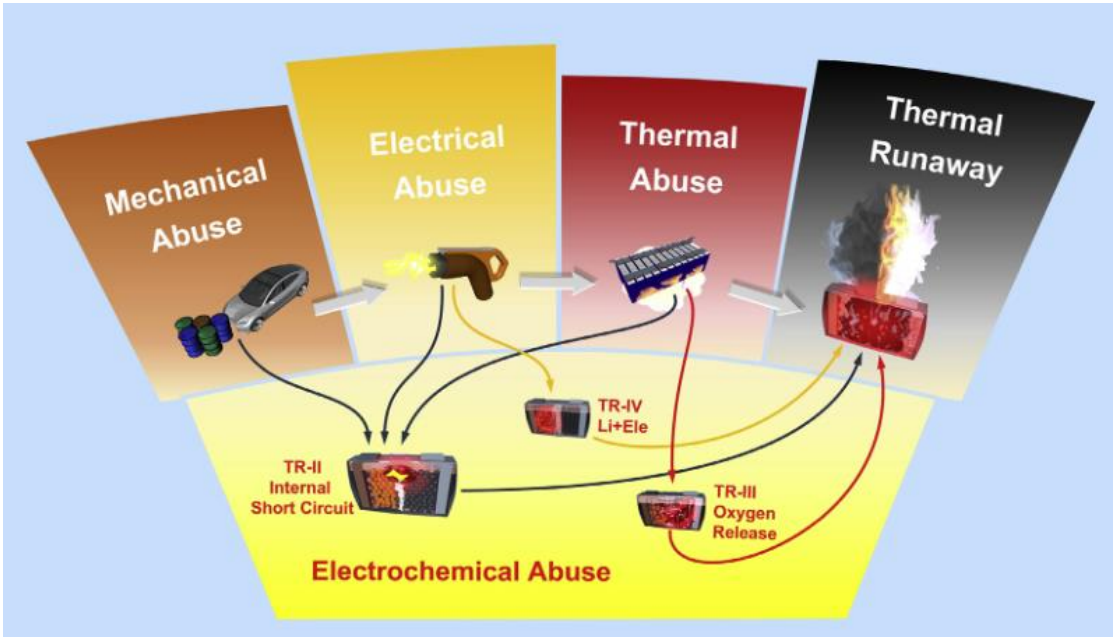

Figure 15. The relationship between abuse conditions and battery thermal runaway. Reused with permission of Elsevier.

The degradation of liquid electrolyte generates gases including H_2, C_2H_4, CO and CO_2 and their accumulation could lead to cell failure.[45] The liquid electrolyte could evaporate and accelerate the thermal runaway during the cell failure. Therefore, substituting the hazardous organic liquid with electrolyte which is safer and more stable is necessary.

3 Polymer electrolytes

Polymer electrolytes are generally considered as a good alternative to organic liquid electrolytes to improve the safety of batteries. Polymer electrolytes can be considered as simply a polymer mixed with some salt, where the polymer acts as a solvent with mechanical strength and the salt is the source of charge carriers, i.e., ions. With the polymer matrix, the electrolyte could gain a better mechanical strength and improvement on safety compared to liquid electrolytes. Additionally, some polymer with properties such as good elasticity,[46,47] self-healing[48] could also allow the battery to withstand mechanical deformation such as blending and stretching.[49,50]

As a matter of fact, polymer electrolytes have been one of the hotspots in the field of energy storage materials. By searching on Google Scholar with the key word “polymer electrolyte”, around 2.4 million items can be found in total. Among them, 16,900 items were published in

2023. Admittedly, a lot of innovations and new materials on the topic have been developed in recent years which need to be taken a close look at.

To classify the polymer electrolytes, different standards can be used. One way is to differentiate by i) dual ion conducting, which means the electrolyte is a blend of polymer and salt or ii) single-ion conducting, in which the anionic functions are fixed, e.g., by bonding it to the polymer chain. The other way is more related to the role of the polymer. It can play the role of the solvent and thus transport the ions by itself, or an organic solvent is added. The system with comprise of polymer matrix, lithium salt and solvent (or plasticizer) can be classified as gel polymer electrolyte. And the solvent-free polymer electrolytes are generally considered as solid polymer electrolyte or "dry" polymer electrolyte. In this chapter, the first classification will be more meaningful in determining the ion transporting condition. But the use of solvent/ plasticizer should also be aware, especially when comparing the ionic conductivity – even tiny amounts of small molecules could greatly improve the ionic conductivity, which make it meaning less the compare between "dry" electrolytes and gel polymer electrolyte.

3.1 Mechanism of lithium transport in polymers

In the "dry" polymer electrolyte, the ionic transportation has been widely accepted as in the amorphous state via the polymer segmental motion, especially in the PEO-based semi-crystalline polymers. In the amorphous phase, at temperatures above T_g, the polymer chain is in the state of local segmental motion, creating free volume for the intra- and inter-molecular coordination of lithium ions. The lithium ion, either as a "free" ion or as ion clusters, driven by strong interactions with the polar group on the polymer chain, could move together with the polymer segment motion along polymer chain or transport from one polymer chain to another. The molecular scheme of the transportation mechanism was shown in Figure 16.

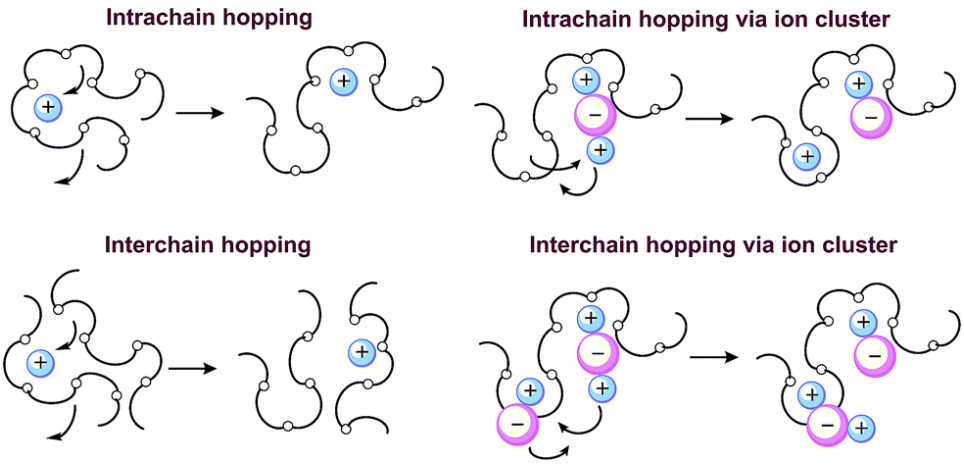

Figure 16. Li transport in amorphous polymer.[51] Reused with permission of Royal Society of Chemistry.

In amorphous phase, the ionic conductivity could be described with the well-known non-linear Vogel-Tammann-Fulcher (VTF) equation,[52,53] which was originally made for glasses:

$$\sigma(T) = \sigma_0 \cdot T^{\frac{1}{2}} \cdot e^{-\frac{E_a}{K_b \cdot (T - T_0)}}$$

Where σ_0 is pre-exponential factor which reflects the charge carrier concentration, E_a is the pseudo-activation energy and T_0 is referred as Vogel temperature. K_b is the Boltzmann constant. The model reflects the relationship between polymer chain motion and ionic transportation.

On the contrary, the crystalline phase of the polymer could be considered as only blocking to the ion motion in most of cases. Thus, below the melting temperature, the polymer mobility was greatly reduced by crystallization, leading to a much lower ionic conductivity.

Due to the crystalline issue, a transition on conductivity could always observed around the melting point which splits the ionic conductivity-temperature trend into two different regions, as shown in Figure 17.

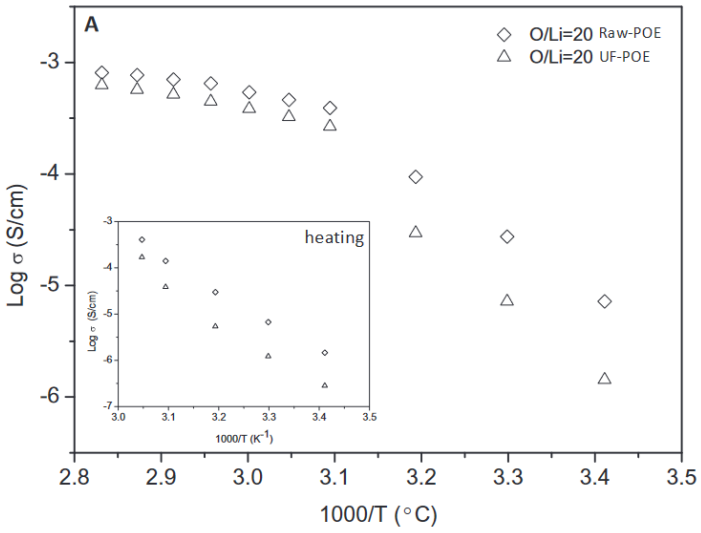

Figure 17. Ionic conductivity of PEO/LiTFSI blend with O/Li ratio of 20.[54] Reused with permission of Elsevier.

3.2 Dual ion conducting polymer electrolytes (DIPEs)

Different from liquid electrolytes which use small molecular organic solvents, polymer electrolytes use macromolecules to dissolve the lithium salts. It is also called dual ion polymer electrolyte, due to the salts being directly blended with polymer matrix. The polymers with polar groups such as oxygen, nitrile, ester, carbonate can have strong interactions with lithium ions to act as the solvent. At the same time the polymer chain provides mechanical strength to the system to maintain a solid, quasi solid or gel state. The polymers and salts used in these simple blend electrolytes are listed in Figure 18 and 19.

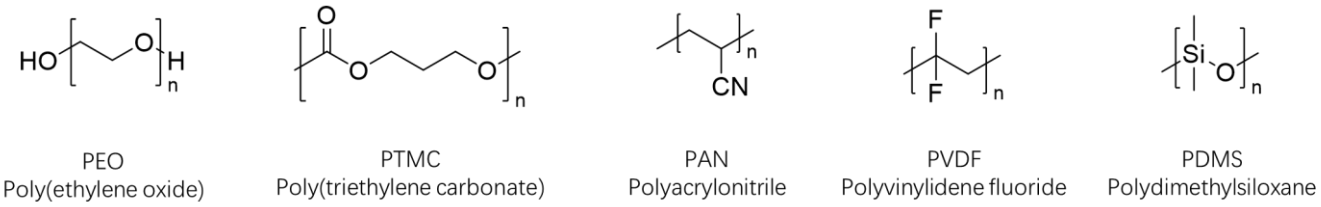

Figure 18. Polymers are used in conventional polymer electrolytes.

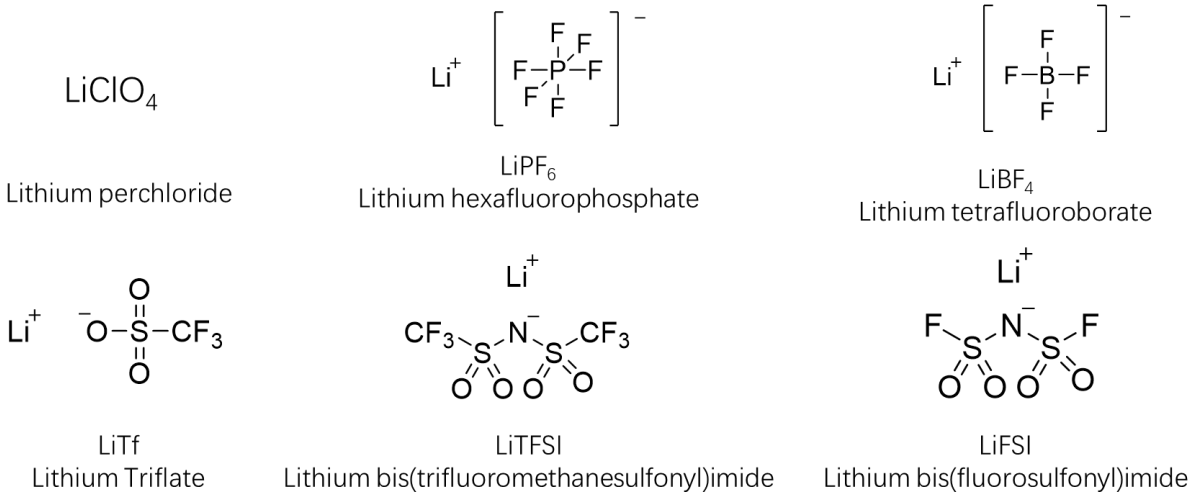

Figure 19. Lithium salts are used in conventional polymer electrolytes.

3.2.1 PEO-based DIPEs

Poly(ethylene oxide) (PEO), or poly(ethylene glycol) (PEG), is the most researched polymer matrix for electrolytes since 1970s.[55] PEO is a semicrystalline polymer with -CH_2-CH_2-O- repeat unit. For high molecular weight PEO, the melting point (T_m) is around 65 °C and glass transition temperature (T_g) is around -60 °C. The T_m and T_g are following a decreasing trend with decreasing PEO molecular weight when the molecular weight is lower than the chain entanglement molecular weight (~1.6 kg/mol[56]). The oxygen atom on the backbone provides a good flexibility to the polymer chain and high donor number.[57] The PEO chain has a strong solvation effect to the lithium cation, due to high donor number of ether function, which allows it to be applied with various salts. PEO was blended with different lithium salts including lithium halide, $LiClO_4$, $LiCF_3SO_3$, $LiPF_6$, LiTFSI, and $LiBF_4$.

Due to its good solubility, dissociation, and stability, LiTFSI has been first introduced with PEO in 1973 and become the most used salt combined with PEO. The classic PEO/LiTFSI electrolyte contains PEO with high molecular weight, EO:Li (Li concentration expressed by the ratio between number of structural of PEO units) varies between 15 to 30. The ionic conductivity of PEO/LiTFSI electrolyte could reach 10^{-3} S cm^{-1} at elevated temperatures (after the PEO melting). The ionic conductivity strongly depends on the temperature, which is shown in Figure 17.[54] The electrolyte shows different conductivity and activation energy before and after melting temperature of PEO (~ 60 °C). At low temperatures, the PEO electrolytes have a high

crystallinity (can be higher >60% as a function of salt)[58] even in presence of a salt, which hindered the ion transportation, leading to an insufficient ionic conductivity of 10^{-8} ~ 10^{-6} S cm^{-1}.[51]

Although PEO/salt blends could provide adequate ionic conductivity at higher temperature above PEO's melting point, by elimination of crystalline phase, the mechanical strength is other end of the scale which is reduced by elevated temperature. To avoid crystallization, improving the mechanism strength and ionic conductivity, various methods including copolymerization, crosslinking, blending, adding plasticizer, adding inorganic filler were applied to creating PEO-based DIPEs (Figure 20). In the latest studies, multiple strategies can be applied to improve various aspects of the polymer electrolyte and usually showed synergistic effect.

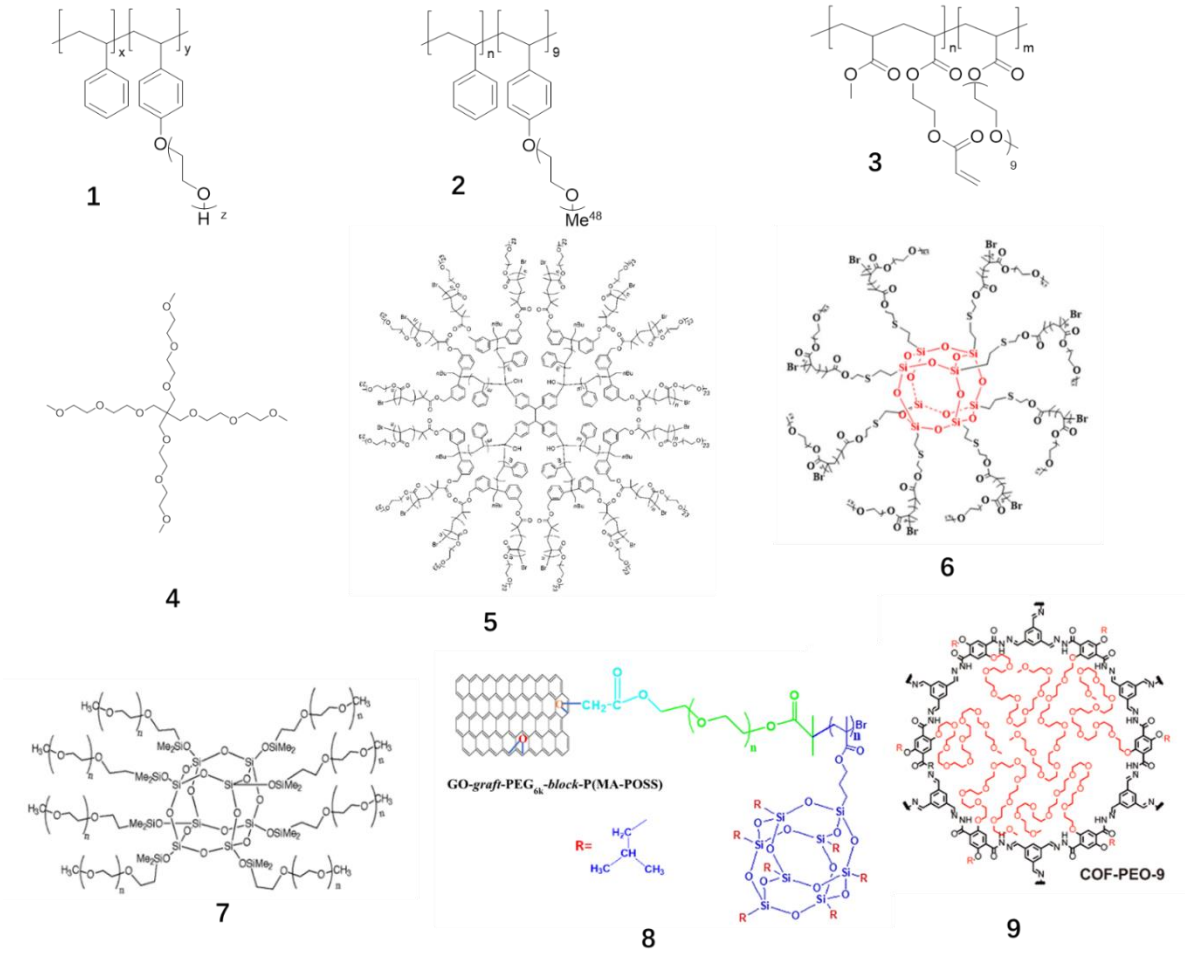

Figure 20. Polymers are used in PEO based DIPEs. 8: Adapted with permission from Ref.[59] Copyright 2023 American Chemical Society. 9: Adapted with permission from Ref.[60] Copyright 2019 American Chemical Society.

Zardalidis et al.[61] studied the effect of grafting PEO brushes on a random and a block copolymer (1) with a polystyrene backbone. Significantly lower crystallinity was observed for both grafted brushes and block copolymers, leading to increased ionic conductivity by 1-2 order of magnitude. The PS block improved mechanical properties to allow a high elasticity without creeping with an EO:Li ratio of 8.

A crosslinked block copolymer (3) was synthesized by He et al.[62]. By introducing double bond, the linear copolymer could be crosslinked by UV irradiation. The short pending PEG chains showed a low crystallinity and stable up to 4 V *vs*. Li^+/Li. The ionic conductivity was 4.4×10^{-6} S cm^{-1} at ambient temperature. By adding PEG250 oligomer as plasticizer the conductivity can be improved to 6×10^{-4} S cm^{-1}. The crosslinked network showed good stability against lithium metal with a plating/stripping test of >700 h (0.2 mAh cm^{-2}). Battery with LFP cathodes could cycle at a dis-/charge rate of 2C for 1,000 cycles.

Star-shaped electrolytes has been prepared by grafting PEG on an organic core (4),[63] hydrophobic polymer block (5)[64] or inorganic nanoparticles (6,7).[59,65,66] Khan et al.[59] reported a graphene oxide graft PEG with poly(POSS) block nanocomposite (8), which avoids filler aggregation to reach a high ionic conductivity of 3×10^{-4} S cm^{-1} at 50 °C. Ma et al.[66] obtained star-shaped polyethylene glycol methyl ether methacrylate-co-polyhedral oligomeric silsesquioxane nanoparticles by ATRP polymerization. By blending with PEO/$LiClO_4$, less crystallization was achieved, which leads to a good ionic conductivity of 1.4×10^{-4} S cm^{-1} at 50 °C. Lithium batteries with an LFP cathode showed stable cycling for 100 cycles.

Covalent organic frameworks (COFs) are novel organic polymers which have unique periodic crystalline structure. By combining imine-bonded 2D COF and short chain PEO, Zhang and coworkers[60] achieved solid-state Li conductors (9) with amorphous PEO by a self-assembly approach. The COF-based polymer with LiTFSI doping could convey an ionic conductivity over 10^{-3} S cm^{-1} at 200 °C with maintain the solid-state properties and electrochemical stability. However, the COF based electrolyte showed very low conductivity of around 10^{-9} S cm^{-1} at 30 °C, due to the rigid COF structure strongly confining the PEO chain motion.

Other than molecular engineering to alter the polymer structure, composite with other polymers or adding additives could be another way to enhance the desired properties. Wan et al.[67] reported

a thin polymer composite of PEO/LiTFSI with nanoporous polyimide (PI). The nonflammable and strong PI film could act as a host and the PEO/LiTFSI act as ionically conducting filler in the vertical channels. The composite electrolyte showed an enhanced ionic conductivity (2.3×10^{-4} S cm^{-1} at 30 °C) and five orders of magnitude higher modulus compared to the conventional PEO/LiTFSI electrolyte. The authors assume that the improvement of the composite was due to the porous PI forcing PEO chains aligned to form an ionic diffusion path. The high mechanical stability could help the cell resist thermal and mechanical abuse including cutting and nail penetration.

Butzelaar et al.[68] synthesized a block copolymer (2), which could be considered as modification of (1). The diblock structure leads to a microphase separation with a PS phase maintaining the mechanical strength and PEO phase ionic conducting. To further improve the ionic conductivity, ionic liquids (IL) N-butyl-N-methyl pyrrolidinium bis(trifluoromethylsulfonyl)imide (Pyr_{14}TFSI) and N-oligo(ethylene oxide)-N-methyl pyrrolidinium bis(trifluoromethylsulfonyl)imide ($PyrO_7$TFSI) were introduced as plasticizers. With 10% of IL, on one hand the ionic conductivity of the electrolyte could reach 4×10^{-4} S cm^{-1} at 40 °C. On the other hand, the Li transference number was decreased from 0.13 to 0.06 with the addition of IL using the Evans method.[69]

Noticeably, different from the polymer (1) those grafting PEO chain ended with hydroxyl group (-OH), polymer (2) has a terminal group of methoxy ($-OCH_3$). Although the authors did not discuss on the electrochemical stability of the electrolyte, as pointed out by Yang et al.,[70] the terminal -OH group of PEO could be oxidized at 4.05 V which could be a major limitation of the electrochemical stable window. Additionally, the -OH group could also react with Li electrode to hinder its stability, and form H_2 gas. Thus, $-OCH_3$ terminal group could bring extra benefit on the battery performance.

Li et al.[71] and Liang et al.[72] investigated electrolyte with crosslinked PEGDA with LiTFSI/LiBOB (lithium bis(oxalato)borate) dual salt and nitrile solvents (glutaronitrile and succinonitrile). The electrolyte showed a high ionic conductivity of 1 mS cm^{-1} at RT with no crystallization. By adding LiBOB, the cycling stability of LFP cell could be enhanced, with an average CE of 99.99% after 370 cycles. The electrolyte could also adapt to 4V cathode

$LiNi_{0.8}Co_{0.15}Al_{0.05}O_2$, and it was reported a stable cycling of 1,000 cycles. By XPS studies, the LiBOB additive could prevent the degradation of the PEO matrix from ether bond cleavage (oxidation) and finally improved the stability of the battery.

Although PEO provides strong solubilization and dissociation of lithium salts, leading to good ionic conductivity, the strong interaction between EO (due to high donor number of ether function) and Li^+ limited the mobility of the last but permits the dissociation in a low dielectric constant medium.[73] Additionally, the interaction of the PEO and the anion is very poor, thus, the PEO based electrolyte usually exhibited a low lithium transference number. The values reported for a LiTFSI based PEO electrolytes are usually lower than 0.2.[54,74,75]

To sum up, as the majority in polymer electrolyte, PEO and its derivatives provides a strong host for lithium salts. The strong interaction between EO group and lithium cation assures the dissociation of lithium salt which is ideal for lithium battery application. However, there is still issues remaining: (i) due to the semi-crystalline nature of PEO, high ionic conductivity can only be achieved at high temperature or in presence of plasticizer (ii) the mechanism strength of PEO is insufficient, especially after melting of crystalline phase, therefore reinforcement is required (iii) the strong interaction between polymer matrix and lithium ion hinders the cation movement which leads to a low lithium transference number, (iv) the EO groups are facing oxidation reaction below 4 V *vs.* Li^+/Li, which limits the application of high voltage positive electrode materials. With the current studies, the PEO based DIPE could overcome the first two issues by different methods. However, it must be clarified that using organic solvents as plasticizer to gain extra ionic conductivity is also a trade-off of safety, depending on the volatility and flammability of the organic solvents. The latter two issues can be improved by using less dissociated salt and introducing additives. But this low transference number issue finally seems not able to be fully solved with PEO based DIPE.

3.2.2 Other DIPEs

DIPEs using polymers other than PEO could be further classified by the type of polymer matrix into serval major types including other polyethers (generally, with longer alkyl chain than in PEO), polycarbonates, etc. These materials are considered as potential alternative to the PEO

base DIPE to overcome the drawbacks including low Li transference number and limited electrochemical stable window.[76]

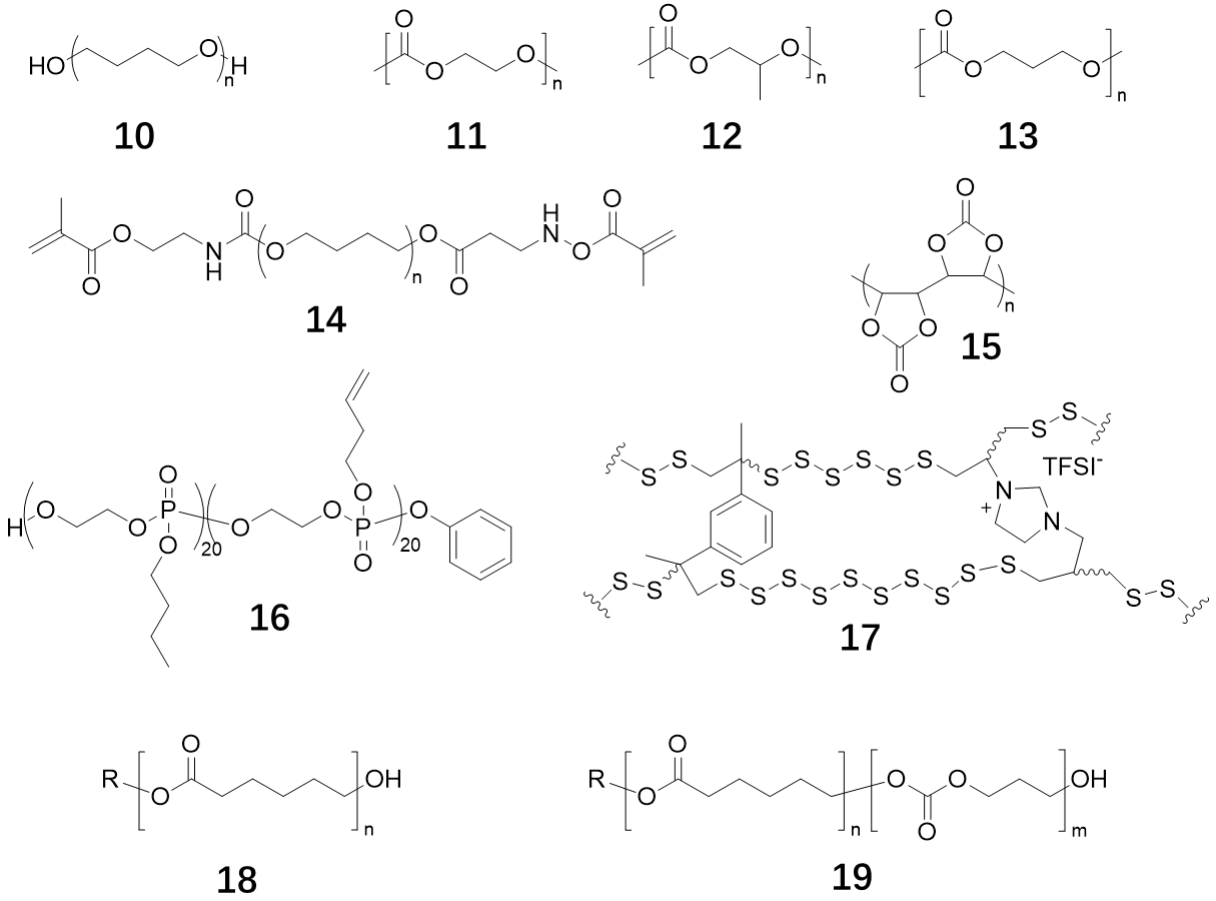

Figure 20. Non-PEO based polymer matrix used in DIPEs.

Polytetrahydrofuran

Polytetrahydrofuran (PTHF,10) has a similar structure to PEO but with 4 methylene groups (CH_2) between two oxygen atoms which lead to a more loosely interaction with lithium ion. PTHF has a lower glass transition temperature (-86 °C) and melting temperature (42 °C) than PEO, which indicates a more flexible polymer chain. PTHF/$LiClO_4$ blend was characterized by Alamgir et al.[77], showing ion conductivity of 10^{-5} S cm^{-1} at 50 °C with an O:Li ratio of 8. More importantly, the lithium transference number of this blend was reported to be between 0.55-0.60, which is much higher than the PEO based DIEPs. Huang et al.[78] reported an in-situ polymerized PTHF polymer electrolyte, by polymerization of THF monomer (with $LiClO_4$)

using BF_3 as initiator. The electrolyte exhibited conductivity of 2.3×10^{-4} S cm^{-1} with transference number of 0.36. Mackanic et al.[79] reported a crosslinked PTHF electrolyte by modifying the PTHF with crosslinkable isocyanate functions (14). The electrolyte showed a high transference number of 0.53. The high transference number is due to a weaker interaction between the O and Li^+, which was supported by ^{7}Li NMR spectroscopy, molecular dynamics and DFT simulations.

Polycarbonates

Other than polyethers, aliphatic polycarbonates are also popular to act as the polymer matrix in the electrolytes due to its amorphous structure, high dielectric constant, and good thermal stability. Cyclic carbonates such as EC and PC are widely used as solvents in liquid electrolytes. These carbonates molecules could be polymerized by ring-opening reactions[80] to form linear aliphatic polycarbonates, which is ideal for blending type DIPE. Kimura et al.[81] reported a membrane of poly(ethylene carbonate) (PEC, 11)/polyimide blend matrix with LiFSI salt. The membrane showed a glass transition temperature of -47 °C and an ionic conductivity of 1.6×10^{-5} S cm^{-1} at 30 °C. More importantly, the reported Li transference number was over 0.5 and electrochemical stable window is larger than 5 V determined by linear sweep voltammetry (LSV). Zhang et al.[82] obtained polypropylene carbonate (PPC, 12) based DIPE with LiTFSI and cellulose nonwoven to improve the mechanical property. The electrolyte is amorphous. By mixing lithium salt (30 wt.% to PPC), the T_g of PPC was decreased from 24.4 to 4.7 °C, suggesting that the TFSI anions may act as plasticizer in polycarbonate. Ionic conductivity of 3×10^{-4} S cm^{-1} at 20 °C with an electrochemical window up to 4.6 V was observed. The plasticizing effect of TFSI anion has also been observed in PEC/LiTFSI system by Tominaga et al.[83] Different salts were blended with PEC and their T_g behaved different trend with salt concentration. With LiTf and $LiClO_4$, a typical T_g increasing with salt concentration (like in polyethers) trend was observed. But in the case of LiTFSI, $LiBF_4$ and $LiN(SO_2C_2F_5)_2$, the T_g was decreasing by increasing salt concentration.

Poly(triethylene carbonate) (PTMC, 13) has been widely investigated due to its biodegradability and good mechanical properties. Thus, PTMC has also become one of the most

popular polymer matrixes to dissolve lithium salts. With a cationic ring-opening polymerization, high molecular weight PTMC can be synthesized. Sun et al.[84] investigated PTMC/LiTFSI blend with different salt concentrations (carbonate:Li ratio from 2 to 21). The highest ionic conductivity of 10^{-7} S cm^{-1} at 60 °C was observed at a carbonate: Li ratio of 8 or 13. However, the T_g of PTMC/LiTFSI increased with an increasing LiTFSI concentration, which is in contrast to the phenomena observed in PPC and PEC. The author assumed the decrease of the T_g for the PPC and PEC electrolytes was due to the strong hydrophilicity of TFSI absorbing humidity. Thus, the interaction between polycarbonate and anions remains unclear due to the varied phenomena, which need further investigation and theoretical analysis.

Poly(vinylene carbonate) (PVCA, 15) is a kind of aliphatic polycarbonate that is synthesized by radical polymerization of vinyl carbonate that keeps the ring carbonate structure which has higher dielectric constant than the linear carbonates. PVCA/lithium difluoro(oxalate) borate (LiDFOB)[85] polymer electrolyte was obtained via in-situ polymerization initiated by azobisisobutyronitrile (AIBN) at 60 °C. The polymer electrolyte (1M LiDFOB in PVAC) exhibited ionic conductivity of 2.2×10^{-5} cm^{-1} at 25 °C with lithium transference number of 0.57. The PVCA polymer electrolyte showed a good ionic conductivity with its cyclic carbonate structure with high dielectric constant, even with a high glass transition temperature (18.9 °C for PVCA, 26.6 °C for PVCA/LiDFOB electrolyte). Additionally, the electrolyte achieved a higher Li transference number than PEO (<0.2 in most of cases, for PEO) due to the weak interaction of carbonate functions with Li ion.

Polyphosphoester and Polymeric sulfur

A very specific DIPE was composed with polyphosphoester and LiTFSI showed flame retardant behavior.[86] Polyphosphoester and block copolymer of polyphosphoester and PEG were synthesized and tested as linear and crosslinked polymers (16). Although the DIPE showed less conductivity than PEO/LiTFSI, the study unveiled that lithium salt can be coordinated and transported with -P=O groups, which provides different possibility on non-flammable DIPEs.

Polymeric sulfur (17) could also use as DIPE host, which is first reported by Sun et al.[87] The flexible -S-S- bond could create solvating environment for Li ion. By blending with LiTFSI,

the polymeric sulfur exhibited ionic conductivity of 1.7×10^{-3} S cm^{-1} at 80 °C and stable lithium plating/stripping. The polymeric sulfur opens a new way for low-cost and simple electrolyte for Li ion and Li-S batteries.

As described previously, with different polymer matrix, the interaction between Li cation could be tuned and reflected as the ionic conductivity and lithium transference number. To understand the difference between polymers with different coordination effects, Rosenwinkel et al.[74] compared ether (PEO), ester (polycaprolactone, PCL, 18), carbonate (PTMC) and PTMC-PCL (19) copolymer based DIPEs with electrophoretic NMR (eNMR). Linear carbonyl polymers (PCL, PTMC) characterized by weaker interaction with Li ion leading to more ion pairs and lower overall ionic conductivity than PEO base electrolyte which has strong EO-Li interaction. On the contrary, less coordinated Li ion could gain more freedom to transport faster with a higher lithium transference number. This study unraveled the relationship between the electrolyte performance and the Li-polymer interaction, which could be very inspiring in designing polymer electrolyte.

3.3 Single ion polymer electrolytes

Different from the blend type of polymer electrolyte, single-ion polymer electrolytes (SIPEs) are commonly characterized by a high lithium-ion transference number by anchoring anionic groups on the macromolecule to limit the lithium mobility. The difference between SIPEs and DIPEs is shown in Figure 21.

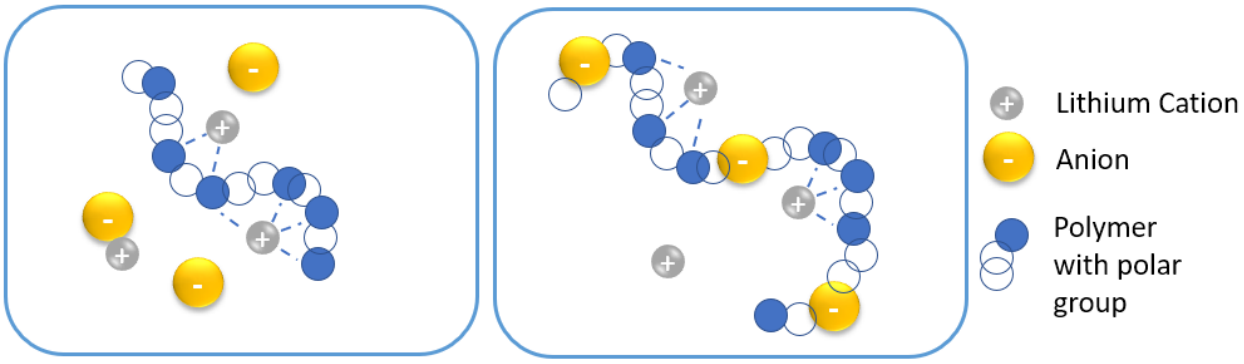

Figure 21. Structure scheme of SIPE and DIPE.

In an electrolyte, both cation and anion act as charge carriers and conduct the current. The total current i can be considered as the sum of the current conducted by the cations i^+ and the current conducted by the anions i^-.[88] Therefore, the cation transference number T^+ is defined as:

$$T^+ = \frac{i^+}{i^+ + i^-}$$

In LIBs, the energy was stored/released by migrating lithium ion between the two electrodes. Thus, the lithium transference number refers to the efficiency of lithium transportation, which is crucial to battery performance.

The SIPE can be a polyelectrolyte or so-called ionomer. The anion is bonded to the polymer chain and the free counter ion is Li^+, the lithium transference number is greatly improved due to the immobilization of the anionic groups on the polymer chain. Thus, SIPEs could intrinsically achieve a higher transference number than DIPEs, usually larger than 0.7, and in a lot of cases could reach unity.

The high transference number of SIPEs could improve the performance of the battery in several aspects, especially stability and safety (avoiding lithium dendrite). With the analysis of Diederichsen et al.,[89] even the modest improvement in the transference number could be beneficial on the fast charge of battery. A lower Li transference number below 0.5 indicates that the majority of the ionic motion is attributable to the anion motion, which tends to migrate in the opposite direction of the lithium ion and accumulate on the electrode surface to buildup concentration gradient. The concentration gradient can be further demonstrated as an extra polarization on the charge/discharge voltages (Figure 22) that limits the operating voltage of the cell and the thickness of the electrodes.

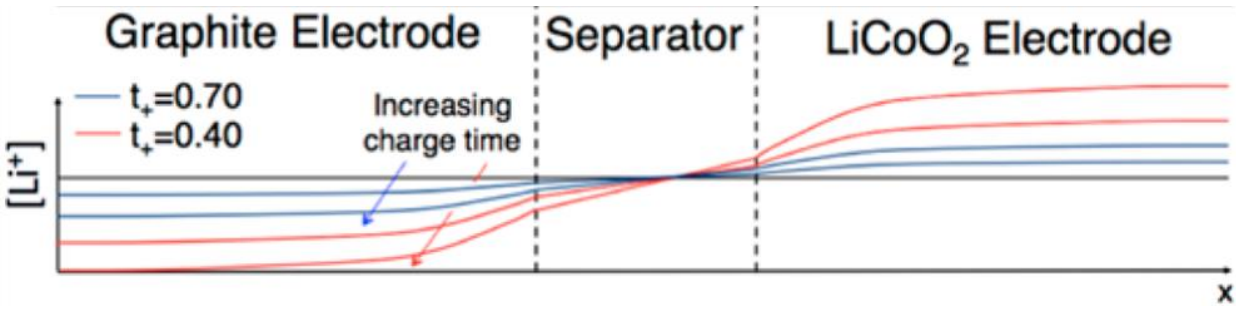

Figure 22. Li concentration gradient in Newman's 1D battery model. Adapted with permission from Ref.[89]. Copyright 2017 American Chemical Society.

Due to the immobilization of the anion, SIPEs can get rid of the gradient in the ideal case, which avoids the reversed polarization and improves the battery performance at higher current density. Stolz et al.[90] investigated the concentration polarization in both single ion and dual ion electrolytes with Li||Li cells. The electrolyte with mobile anions suffered from concentration polarization due to the Li ion depletion toward the electrolyte|electrode interface, which follows the Sand and diffusion equations. While as in the SIPE, the Sand and diffusion coherences are invalid and Li^+ transport proceeds via migration mechanisms which leads to no concentration polarization. The ion transportation behaviors of both electrolytes are schematically depicted in Figure 23.

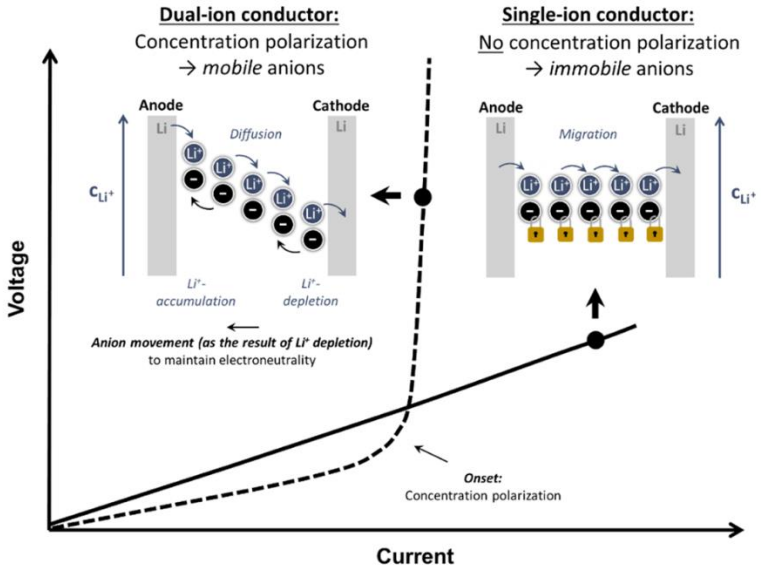

Figure 23. Dual-ion and single-ion conduction in symmetric Li‖Li cells.[90] Reused under CC-BY-NC-ND 4.0.

Kim and Srinivasan[91] mathematically simulated cells with a transference number varying from 0.2 to 1 using Newman's model. The transport parameters for the cell were set as the same value as polystyrene-b-PEO block copolymer based DIPE (Li^+ transference number = 0.2, conductivity= 0.05 S m^{-1} and diffusion coefficient= 4.7×10^{-12} m^2 s^{-1}). The simulation revealed that the required ionic conductivity, enabling similar energy density as liquid electrolytes, decreased with the increasing transference number (Figure 24). Especially, when the Li^+ transference number exceeds 0.9 or more, a sudden drop of the required ionic conductivity was observed.

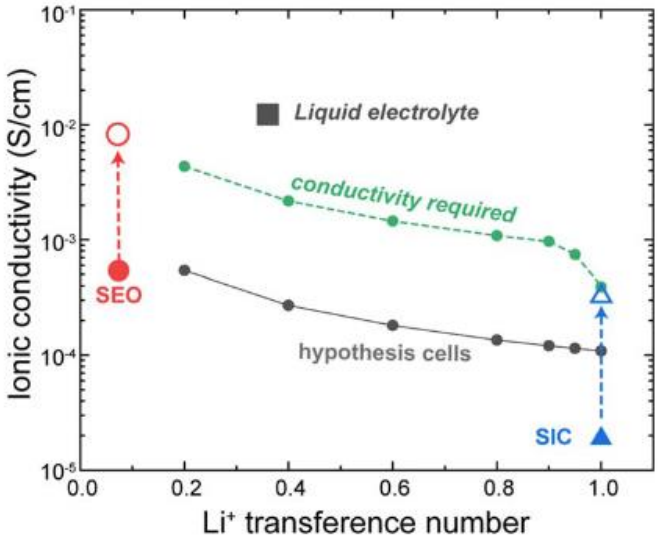

Figure 24. The trend of the required ionic conductivity for varying Li^+ transference numbers. SEO and SIC refers to the polystyrene-b-PEO block copolymer and single ion conductors, respectively. Reproduced with permission of IOP publishing, Ltd.

More importantly, when using lithium metal electrodes, the concentration gradient could lead to lithium dendrite growth and threaten the safety of the battery. The model of Chazalviel[92] showed that the ramified metallic electrodeposits in dilute salt solution is essentially driven by the space charge that tends to develop upon anion depletion near the cathode. Another theoretic analysis was developed by Tikekar et al.,[93] which predicts that tethering anions is effectively curbing dendrite growth and improving the electrolyte conductivity at large overpotentials, especially at high current density. Thus, SIPEs with high lithium transference number

electrolyte could lead to homogenous plating of dendrite-free lithium, which is promising for lithium metal batteries with higher current densities.

However, the ionic conductivity of SIPEs is generally insufficient at room temperature, even after consideration of the effect of such elevated Li^+ transference number. Thus, the SIPEs are usually tested at elevated temperatures. New chemistry and molecular design are therefore strongly needed to explore new SIPE to alleviate the challenges and finally allow SIPE-based batteries to reach competitive energy and power densities at ambient temperatures.

3.2.1 Classification of SIPEs

Similar to the DIPEs, SIPEs can also be simply classified as two conditions by additionally mixing with solvent or not. The first class is to directly integrate the solvating group into the polyelectrolyte. With this method, the polymer is both salt and solvent at the same time, which avoids the small molecular solvent or plasticizer and thus keeps a non-volatile and a solid-state nature. In general, “dry” SIPEs suffer from low ionic conductivities, especially at ambient temperatures. The electrolytes are utilized at elevated temperatures of 60-80 °C. Additionally, the SIPEs which are additionally blended with high molecular weight PEO and other solvating polymers can also be considered as “dry” SIPEs, even though the solvating chains are not chemically bonded with ionic moieties.

The second class of SIPEs consists of ionic polymers only with poor solvating groups which require to be used with solvents or plasticizers, either small molecules or oligomers such as PEG. On the one hand, the conductivity of these SIPEs benefits from the high mobility of the additional solvent to reach conductivies as high as 10^{-4} S cm^{-1} at room temperature. From the review of Diederichsen et al.,[89] the polyelectrolyte solutions could be the promising choice for them to apply in already implemented cell design due to its high transference number and conductivity. But on the other hand, which is always noteworthy, the addition of organic solvents or plasticizers also bears the drawbacks of presence of such potentially evaporating and flammable solvents.

3.2.2 Designs of SIPEs

SIPEs can be obtained by polymerization of an ionic monomer or by post modification of a polymer. As a lithium salt, the ionic function must be able to dissociate and provide lithium ion. Therefore, organic anions with low acidity must be used and attached to the polymers. Different families such as sulfonyl imides, sulfonates, borates, etc. were studied. To minimize diffusion coefficient of the anions the polymer backbone must be long enough, at least larger than the polymer entanglement threshold.

As classified in the previous paragraph, the solvent can be the polymer with solvating groups ("dry" SIPE) or added as small molecules (quasi-solid SIPEs). This part mainly reviews the design of the SIPE from three aspects: solvating groups, ionic functions, and molecular structures. These designs on molecular structure affect the ionic conductivity, stability, mechanical properties of SIPE in a synergetic way. So, it is difficult to compare the values in the literature directly, especially if they are reported with different testing conditions (temperature, concentration, etc.). In this part, representative works are selected to address the general way to design a SIPE and the attempts on improving the performance with structure optimization.

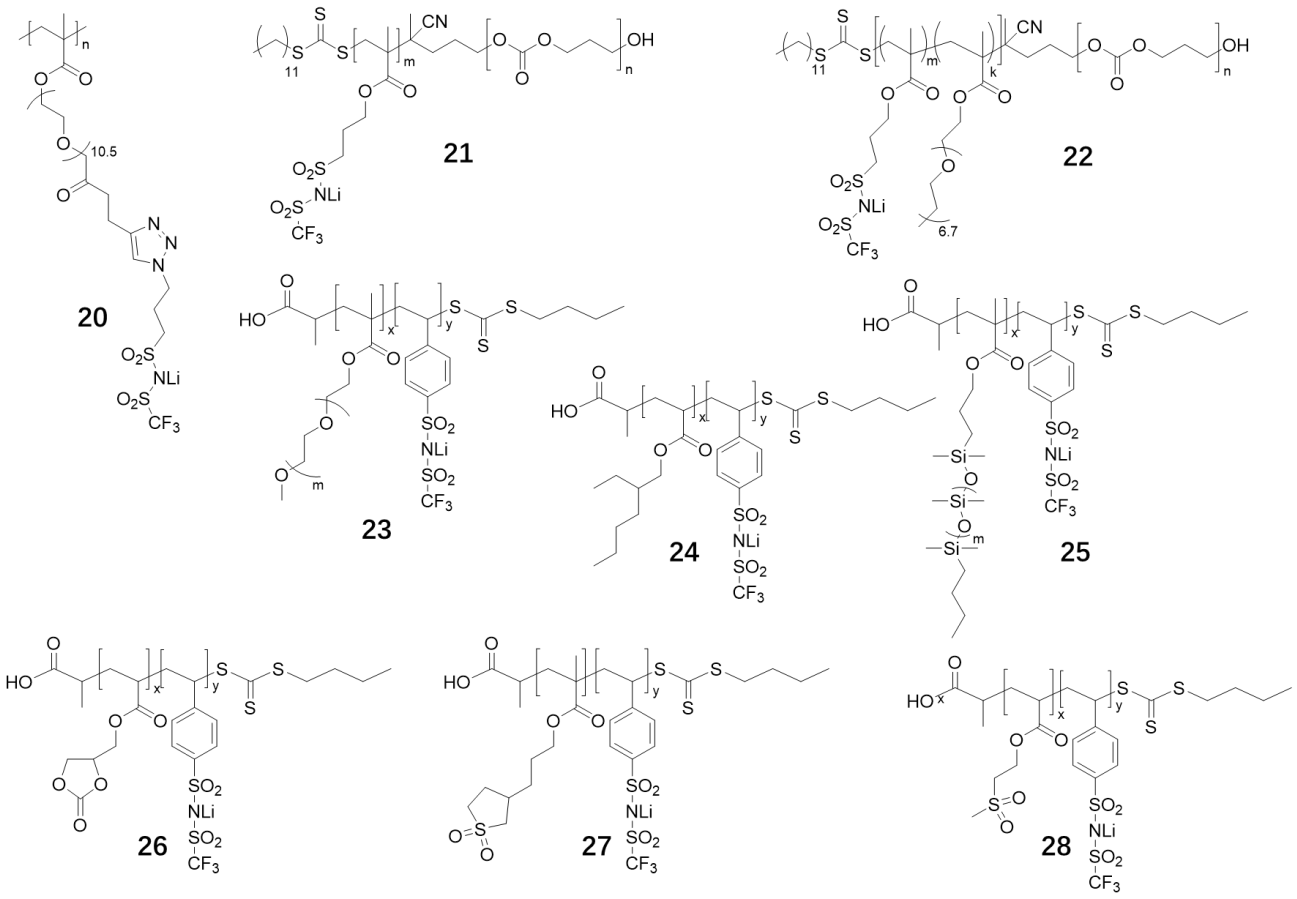

Figure 25. Overview of SIPEs with different solvating groups.

Solvating groups

Solvating groups are essential parts in the first class of SIPEs which do not require additional solvent to dissolve the ionic functions. Generally, the polar chains with high dielectric constant or high donor number (Lewis basicity) were preferred, due to their good miscibility with ionic function. At the same time, flexibility and low crystallinity are also required since the ion conduction is driven by chain segmental motion.

PEO based solvating groups are still the majority in "dry" SIPEs. Li et al.[94] obtained a methacrylate monomer with PEG solvating chain and $-SO_2-N^{(-)}-SO_2CF_3$ TFSI based ionic function *via* azide-alkyne "click" reaction. The monomer was further polymerized by controlled ATRP polymerization yielding a homopolymer SIPE (20). The SIPE showed an ionic conductivity of 2.4×10^{-5} cm^{-1} at 90 °C with a Li^+ transference number of 0.97. This work successfully demonstrated the power of "click" reactions and ATRP for the design of SIPE, especially for producing unique pending ionic function at the end of a PEO side chain.

Unlike DIPEs, solvating groups other than PEO are rarely used in dry SIPEs due to conductivity limitation and difficulty in synthesis. Lingua and coworkers[95] prepared SIPE with carbonate based solvating groups (21). PTMC based macro-RAFT agent was first generated by ring-opening polymerization of TMC. Then RAFT polymerization was conducted with TFSI based methacrylate and TFSI/PEG based methacrylate mixture to form block copolymers. The block copolymer with only PTMC showed conductivity of 1.3×10^{-7} S cm^{-1} at 70 °C, while the copolymer with both PTMC and PEG could achieve better conductivity of 4×10^{-6} S cm^{-1} at 70 °C. Phase separation between PTMC and PEG was observed with a quasi-hexagonally packed cylinder structure by atomic force microscopy, which suggests the poor miscibility between PTMC and ionic function.

Zhao et al.[96] systematically studied the neutral units in SIPE, which included PEG (23), alkane (24), siloxane(25), carbonate (26), and sulfone (27,28). Acrylate and methacrylate-based monomers with different neutral units were copolymerized with TFSI based ionic styrene *via* a RAFT polymerization to synthesize the SIPEs containing different moieties. The SIPEs with alkane and siloxane side chains showed low T_g and low ionic conductivity due to the low dielectric constant of these polymer chains, leading to poor miscibility and dissociation of the ionic functions. However, in the case of high dielectric constant side chains such as sulfone (both linear and ring) and carbonate, low ionic conductivities were observed due to the high T_g and slow segmental dynamics. The work is very inspiring since less research has been done on the effect on different solvating groups, especially sulfone. In this work, the superiority of PEO was fully demonstrated. The author drawn the conclusion that high dielectric constant will not necessarily improve ionic conductivity at ambient temperatures. Similar effect has also been observed by Schauser and coworkers.[97] However, considering the ratio between the solvating units and ionic function could be too low (i.e., the lithium salt concentration is too high) in the report, the conductivities of copolymers 26-28 could be improved after optimization. Except for the PEO based SIPE, carbonate or ether-based solvents could be added to the other SIPEs (26-28), to boost the conductivity.

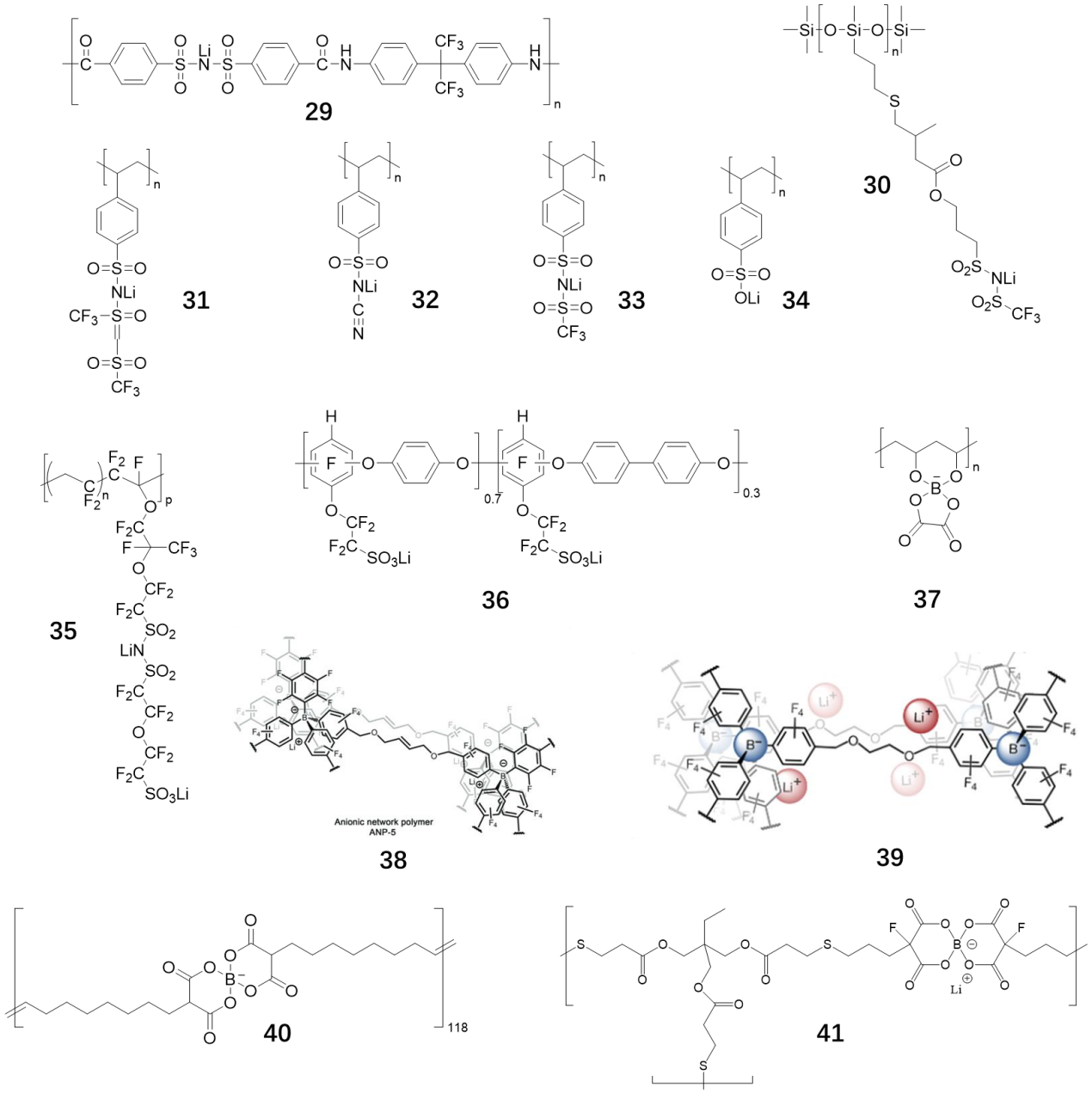

Figure 26. Overview of SIPEs with different ionic functions 38: reused with permission of John Wiley and Sons. 39: Adapted with permission from Ref.[98] Copyright 2021 American Chemical Society.

Ionic functions

Sulfonyl imides-based anions

Among the ionic functions, those with sulfonyl imide based anions are the most investigated. Similar to TFSI and FSI groups in the DIPE, the sulfonyl imides possess a highly delocalized negative charge which entitled its good solubility and dissociation in different solvents. TFSI

based SIPEs can be synthesized directly by (co)polymerization of ionic monomers by both step growth (polycondensation and polyaddition) and chain growth polymerizations (mostly free-radical mechanism).

The sulfonimide functions were grafted on different polymer chains and used as quasi-solid SIPE or dry SIPE. Polysulfonimide based SIPE (29) was synthesized by Borzutzki et al.[99] By blending with PVDF-HFP (PVDF-HFP: SIPE=1:3) and EC:PC solvent (solvent uptake of 130 wt.%), the quasi-solid SIPE could achieve an ionic conductivity of 5×10^{-4} S cm^{-1} and a Li^+ transference number of 0.9. The electrolyte was also tested by lithium plating/stripping and Li||NMC_{111} cells. Another highly flexible backbone, polydimethylsiloxane functionalized with TFSI based ionic functions *via* thiol-ene reaction quasi-solid SIPE (30) was developed by Liang et al.[100]. The single ion conductor based on PDMS blended with PVDF-HFP and organic carbonates (EC: DEC: FEC=48.8:48.8:2.4, 57 wt.%) exhibited an ionic conductivity of 4×10^{-4} S cm^{-1} at 20 °C with a Li transference number of 0.96, as determined by the Bruce-Vincent method. The quasi-solid SIPE showed good stability in lithium plating/stripping tests and Li||NMC_{622} cells.

Modification of sulfonyl imide anion was an innovative way to improve the SIPE performance. Ma et al.[101] designed a super-delocalized polyanion (31) with $-SO_2N^{(-)}-SO(=NSO_2CF_3)-CF_3$ group (sTFSI). Blending with PEO with an EO:Li ratio of 20, an ionic conductivity of 7.6×10^{-5} S cm^{-1} was obtained at 70 °C with a Li transference number of 0.91. Compared to the SIPEs with similar structure but different anion (sulfonate (34), TFSI (33)), the conductivity of Li cations ($\sigma_{Li^+}=\sigma\times t_{Li^+}$) follows the order of sulfonate<TFSI<sTFSI. sTFSI showed around one order of magnitude higher σ_{Li^+} than TFSI based SIPE and 3 orders of magnitude higher than sulfonated based SIPE at 70 °C. Although it is still less conductive than PEO/LiTFSI, the work proved that the modification on ionic functions towards highly delocalization could improve the transport properties of SIPE. Yuan et al.[102] reported a SIPE with a modified sulfonyl imide (32). By cyanidation, the anion contained an ionic function of $-SO_2-N^{(-)}-CN$ structure. By blending with PEO with an EO:Li ratio of 8, the SIPE reached ionic conductivity of 7.3×10^{-5} S cm^{-1} at 60 °C with a Li transference number of 0.84. With the electron withdrawing -CN group, it is believed that the highest occupied molecular orbital level could be lower and then improve

the stability of the ionic function. Additionally, with -CN substitution, the ionic function is fluorine-free, which could be more environmentally friendly compared to more popular fluorinated anions.

Sulfonates-based anions

Sulfonates are another category of strong dissociated ionic functions, which are commonly used in proton exchange membranes for PEMFCs, such as Nafion. Lithium sulfonates can be used also as SIPE and provide similar performance as sulfonyl imide type ionic functions. Oh et al.[103] reported a poly(arylene ether)-based SIPE (36), which contains -$OCF_2CF_2SO_3Li$ perfluorosulfonate group grafting on the aromatic backbone. The dry SIPE exhibited low conductivity of less than 10^{-7} S cm^{-1} due to lack of solvating groups. By adding DEC/EC/PC mixture (1:1:1 by volume, 92 wt.%) as solvent, the ionic conductivity at room temperature reached 3×10^{-3} S cm^{-1}. A Li^+ transference number of 0.98 was determined by the Bruce-Vincent method. Nguyen et al.[104] reported a novel design of SIPE with combined sulfonyl imide and perfluorosulfonate on the same side chain (35). The ionic function was grafted on the PVDF based backbone which contains 94% vinylidene fluoride (VDF) moiety. The polymer was swelled in an EC/PC mixture to form quasi-solid SIPE. An ionic conductivity of 5×10^{-4} S cm^{-1} was obtained at 25 °C with a high transference number close to 1. This quasi-solid SIPE exhibited the possibility of combining different ionic functions in the same SIPE molecule, which is inspiring in the molecule designing aspect. However, the synergistic effect of the two different anions was not fully understood.

Borate-based anions

Borate based salts are widely used in liquid electrolytes and DIPEs including LiBOB and LiDFOB, which are believed to have a wide electrochemical window and a positive effect on the stabilization of the interface with the negative electrodes. In SIPEs, borate-based ionic functions are also designed with different structures. The sp^3 hybridization of the boron core could be a Lewis acid and host a negative charge. At the same time, the boron could also act as a crosslinking center. Shin and coworkers[105] reported a quasi-solid SIPE based on a borate

network (38). The boron was bonded with 4 tetrafluoro phenyl groups which are electron withdrawing to yield weakly coordinating anions and spaced by another crosslinkable butenediol linkers. An ionic conductivity of 1.5×10^{-4} S cm^{-1} at 26 °C was obtained with 30% of plasticizer (PC and triglyme) with a transference number of 0.95. The same borate ionic function (39) was examined with six different linkers by Aubrey et al.[98] The SIPEs with PEG 400 and PEG1000 spacers were found as pliable flakes and show a decent conductivity (10^{-6} S cm^{-1} at 100 °C) without the presence of any plasticizer. While the others with shorter spacers could also form quasi-solid SIPE with plasticizer(65 wt.% of PC) and showed good ionic conductivity of 10^{-4} S cm^{-1} at room temperature.

Other than the tetrahedral boron, borate with spiro structure also showed enormous potential for the design of SIPEs. Zhu et al.[106] reported a very inspiring SIPE based on spiro borate ionic function (37). The SIPE was synthesized with a 2-step reaction. Poly(vinyl alcohol) and boric acid first reacted to form borate ring on the polymer chain and then the spiro sp^3 boric center was formed by cyclization with oxalic acid and lithium carbonate. With adding PC, the optimized SIPE exhibited ionic conductivity of 6×10^{-6} S cm^{-1} at room temperature. Dewing et al.[107] designed a spiro borate salt with two malonate-based rings (40), and further polymerized with acyclic diene using metathesis reaction catalyzed by ruthenium catalyst. The single ion polymer was then dissolved in PC and a Li^+ transference number of 0.98 was determined electrochemically, 0.91 obtained by DOSY-NMR spectroscopy. The ionic conductivity was calculated with the Nernst-Einstein equation with NMR determined diffusion coefficients, showing a value of 3.6×10^{-4} S cm^{-1} at 295 K with a concentration of 0.1 mol L^{-1}. Continuing with similar borate, Liu et al.[108] designed spiro borate with fluorine substituted malonate ring (41). With molecular orbital calculation, with a F substitution, the dissociation energy of the lithium borate was decreased by 20 kJ mol^{-1}. The SIPE was then synthesized via thiol-ene crosslinking and blending with PC/EC/FEC (6:3:1 by volume). The quasi-solid SIPE exhibited an ionic conductivity of 2×10^{-4} S cm^{-1} at 35 °C with a Li transference number of 0.93.

The various studies on borate-based SIPEs clearly showed competitive ionic conductivity compared to more common sulfonyl imide or sulfonate based materials. But it is a pity that the interfacial behavior and other interesting properties have not yet been well-studied with these

SIPEs, even though a lot of interesting results on boron-based salts were already reported with liquid electrolytes and DIPEs.

Morphology and structure

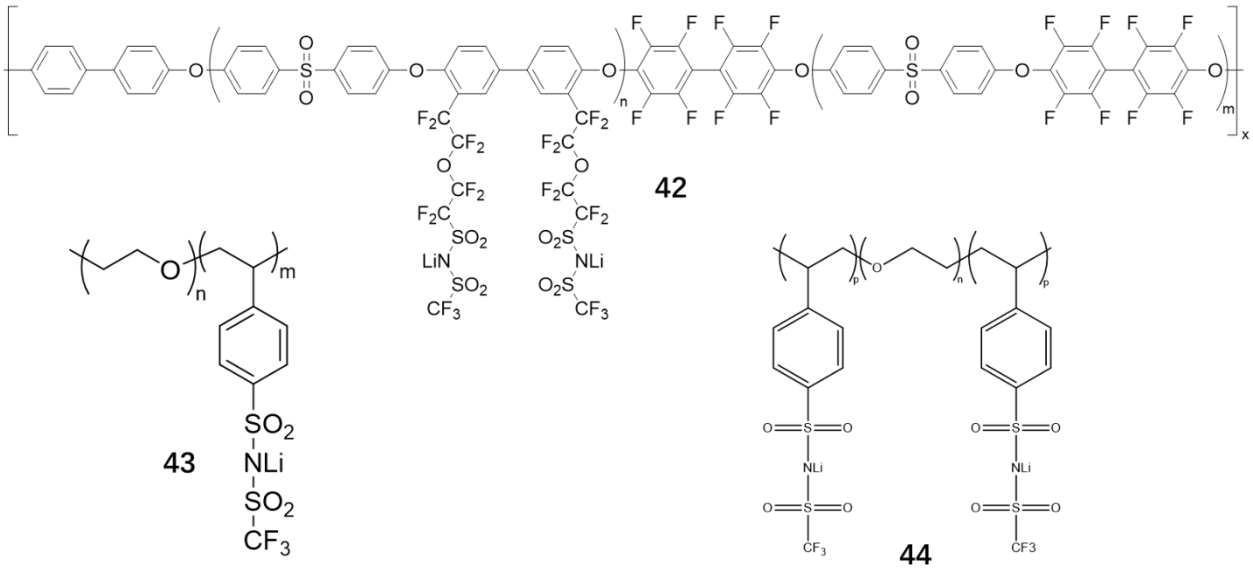

Figure 27. Morphology design of SIPEs. 45: Adapted with permission from Ref.[109]. Copyright 2017 American Chemical Society.46: Adapted with permission from Ref.[110]. Copyright 2020 American Chemical Society.

One of the largest advantages of SIPEs is the tunable polymer morphology and structure by molecular designing. With methods such as block copolymer, grafting polymer, nano composite, and so on, the SIPE properties including ion transport, phase segregation, mechanical strength can be rational designed to fit the application scenario.

The most common strategy to achieve phase segregation is building block copolymers. The

SIPE contains ionic and neutral components that could arrange as a block copolymer and go through micro separation. Inceoglu et al.[111] reported a simple block copolymer of TFSI based polystyrene (PSLiTFSI) and PEO with a molecular weight ratio of 5:3.2 (43). Micro phase separation was confirmed by small-angle X ray scattering (SAXS) and scanning transmission electron microscopy (STEM). An ordered structure with crystalline PEO-rich phase and glassy PSLiTFSI-rich phase (T_g=160°C) was observed at temperature lower than 50 °C and a disordered morphology with amorphous PEO mixed with PSLiTFSI blocks was obtained at higher temperatures. Electrochemical testing proved that the lithium ions were able to transport from glassy PSLiTFSI-rich phase to PEO-rich domains with an ionic conductivity of 3.8×10^{-4} S cm^{-1} at 90 °C. Similarly, BAB triblock copolymer of PSLiTFSI-PEO-PSLiTFSI (44) was also reported[112]. Triblock SIPE showed conductivity of 1.3×10^{-5} S cm^{-1} at 60 °C with transference number more than 0.85 and improved mechanical strength (compared to PS-PEO-PS triblock copolymer) was applied with lithium metal battery and showed high power density.

More importantly, by introducing "rigid" building blocks together with an ion conducting building block, SIPEs with great mechanical strength could be built. Nguyen et al.[113] developed a multi-block copolymer with ionic and "rigid" poly(arylene ether sulfone) blocks (42). Swelled in EC, the quasi-solid SIPE was examined by small-angle neutron scattering (SANS) and field emission scanning electron microscopy (FE-SEM) to confirm the phase segregation. The quasi-solid SIPE exhibited a great ionic conductivity of more than 10^{-3} S cm^{-1} at 30 °C due to the efficient charge transport pathways. With high ionic conductivity, transference number, electrochemical and mechanical stability, this SIPE could be one of the best quasi-solid SIPEs in all the state-of-art works so far.

Grafting ionic functions on the nanoparticles also allows immobilization of anion movement. Irune et al.[109] grafted PSLiTFSI polymer chains on the POSS nanoparticles (45). On each POSS core, 8 chains of PSLiTFSI were grafted from a giant hybrid particle of lithium salt. The nanoparticle/mixture with varied ratio was examined with ionic conductivity and phase separation behaviors. Lamellar phase was obtained at low nanoparticle ratio and the PSLiTFSI-rich phase turns to cylinders at higher nanoparticle loading. The best mixture with Li:EO ratio of 0.085 exhibited ionic conductivity of 1.1×10^{-5} S cm^{-1} at 90 °C. Notably even at elevated

temperature, the mixture remains the shape as rigid solid.

Yang et al.[110] reported a novel SIPE (46) based on a UiO-66 metal-organic framework (MOF). The sulfonate group was introduced during synthesizing of the MOF. Due to the highly connected crystalline of MOF, the SIPE could be incorporated with organic carbonates without turning into a gel. The MOF based SIPE with 50 wt.% of EC/PC exhibited an ionic conductivity of 7.8×10^{-4} S cm^{-1} at room temperature, with a Li^+ transference number of 0.9.

3.3 Challenges and perspectives for polymer electrolytes

3.3.1 Electrochemical stability

Insufficient electrochemical stability, or so called electrochemical stability window (ESW), is one of the bottle necks for using contemporary polymer electrolytes with advanced positive electrodes. The most used PEO or PEG based electrolyte only has stable window up to about 4 V *vs*. Li^+/Li, which blocked the application of high voltage positive electrode materials. In the state-of-art studies, the ESW is usually determined with CV or LSV techniques. The upper limit of the ESW is often about 4.5 V or even about 5.0 V *vs*. Li^+/Li. However, few of them were able to provide battery data with NMC or LCO positive electrodes which requires 4.3 V and none of the electrolyte was tested with 5 V LNMO electrodes. These facts suggest that the LSV or CV test with an inert working electrode (such as stainless steel, and Ni foils) is insufficient to reflect the electrochemical stability at high voltages. The reported ESW ranges are usually overestimated.

The uncertainty of electrochemical stability does not only concern the high voltage range with the risk of oxidation, but also exists on the negative side when Li metal is used. Similar to all the electrolytes, the SIPE degrades on the surface of the negative electrode and forms the famous solid electrolyte interphase (SEI) layer, which is crucial in stabilization of the electrochemical process in battery, especially with very reactive lithium metal. The current research was mostly focused on developing dendrite-free lithium electrode, which is extremely important for LMB safety. The lithium dendrite formation can be ruled out with long-term lithium plating/stripping test and lithium metal batteries test. However, the reactivity between the polymer and lithium was seldom studied. With only CV data that usually reported in the

publications, the details of the SEI formation and lithium reversibility with polymer electrolytes, especially in the solid-state are far from being well understood.

A recent study[114] revealed that the SEI layer between SIPE and Li could strongly influence the polarization of lithium plating/stripping. Following Chazalviel's model, no polarization is expected for an ideal single-ion conductor. However, with the experimental plating/stripping, a constant increase in overvoltage with an increasing cycle number was overserved (Figure 28), which may be associated with the depletion of Li ions in the SEI layer. Thus, in the case of high current density, the Li ions diffusion coefficient in the SEI layer is the limiting factor which threatens the theoretic polarization-free behavior of the SIPE.

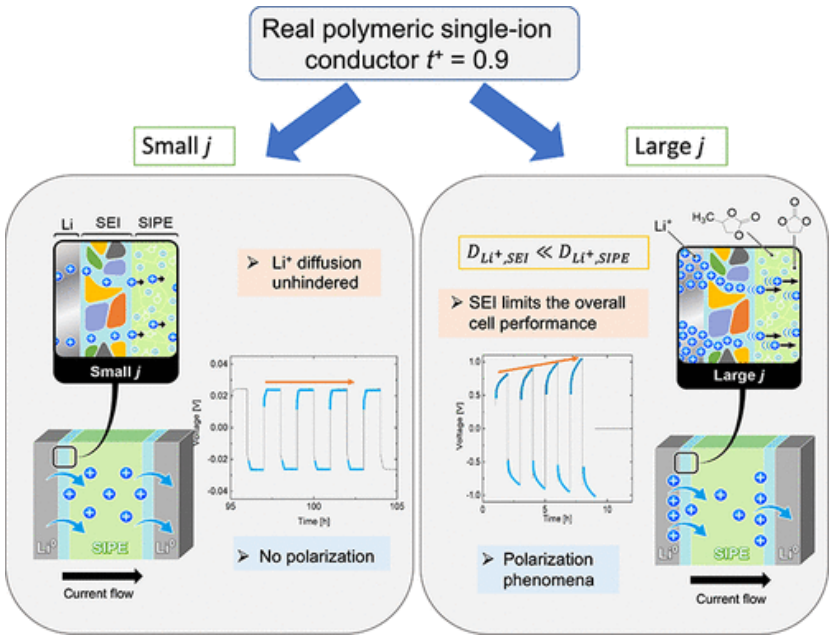

Figure 28. The polarization in Li|SIPE|Li cells due to the depletion of Li ions in the SEI. Adapted with permission from Ref.[114] Copyright 2022 American Chemical Society.

Therefore, to evaluate the electrochemical stability of polymer electrolytes with a reliable result that could be used to guide the electrode selection, electrochemical chemical techniques (LSV and CV) is not sufficient. Chemical and morphology information are also extremely important, which can be proved by techniques such as X-ray/ultraviolet photoelectron spectroscopy (XPS/UPS), quartz crystal microbalance (QCM), electron microscopies, atom force microscopies, X-ray tomography etc. More research on both oxidation and reduction stabilities

to understand the reaction details is needed. For the current studies, the best way to evaluate electrochemical stability of polymer electrolytes is to judge by long-term battery cycling and lithium plating/stripping test.

3.3.2. Accurate determination of the transference number

In the previous paragraphs, I have already fully demonstrated the importance of high Li transference number and different approach to improve the transference number. Most of the literature published with new electrolyte design report Li transference number, both in DIPE and SIPE. Nevertheless, even similar electrolytes could yield hugely different Li transference numbers in different articles. For example, the most studied PEO/LiTFSI system has been reported various times but with much different values. It seems that the only conclusion that can be drawn is that transference number is very low (between 0.1 and 0.2), but without a consistent value.

The SIPEs are also facing similar problems of inaccuracy in Li^+ transference number determination, even though they intrinsically have a higher Li^+ transference number. As explained previously, a high Li^+ transference number is crucial for battery applications. A sudden drop in the required conductivity was predicted for a transference number of 0.9, which underlined its importance to reach high transference numbers close to unity. Although most of the literature reports a value of Li transference number, both in DIPE and SIPE, the data was not accurate or reliable in a lot of cases, especially when using electrochemical methods. To understand the reasoning behind the inaccuracy, a closer look at the electrochemical polarization method is needed.

The easiest estimation of T^+ is conducted by polarizing a symmetric Li||Li cell with a small constant voltage. At the beginning of the polarization, both Li^+ and the counter ion migrate in the electric field. And then the anion is depleted at the negative side and accumulated at the positive electrode whereas the Li^+ flow remains. The current will be dropping due to the blocked anions, and finally established a steady state. The motion of the ions is shown in Figure 29.

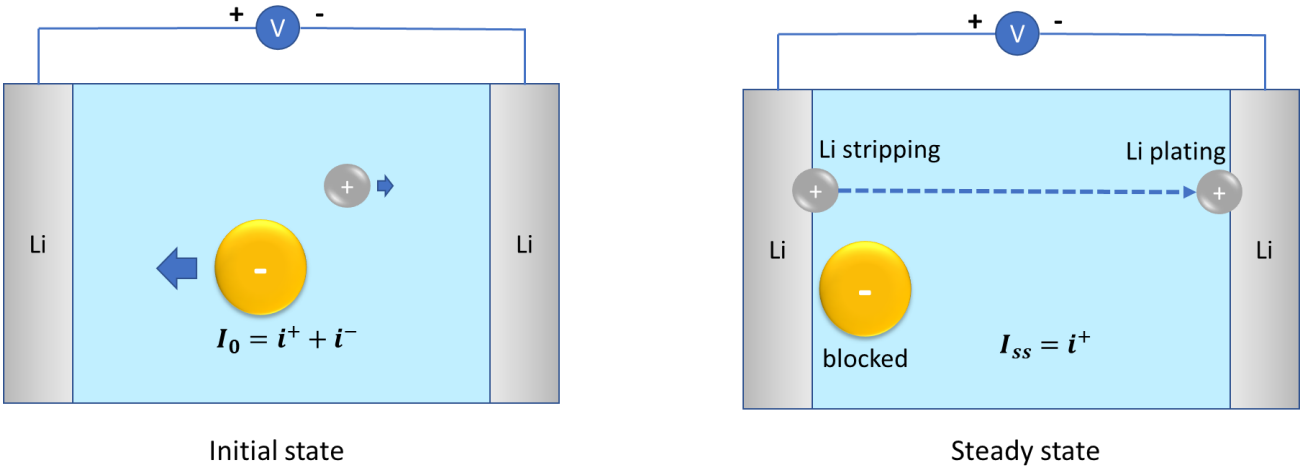

Figure 29. Schematic presentation of the DC polarization of a Li||Li symmetric cell. Left: initial state. Right: Steady state.

Therefore, the T^+ can be considered as the ratio between the steady-state and the initial current:[115]

$$T^+ = \frac{I_{ss}}{I_0}$$

where, I_{ss} is the steady-state current and I_0 is initial state current. However, during the establishment of the steady-state, which may take more than 6 h, passivation layer formed on the surface of lithium electrode due to the reaction between lithium metal and electrolyte can change and influence the value of I_{ss}. To evaluate the influence of passivation, interfacial resistance is measured before and after the polarization by electrochemical impedance spectrum (EIS). T^+ can be calculated by:

$$T_{Li}^+ = \frac{I_{ss}(\Delta V - I_0 R_0)}{I_0(\Delta V - I_{ss} R_{ss})}$$

where R_0, R_{ss} was the interfacial resistance of the initial and steady-state[69]. In addition to SEI response, the error can also arise from the measurement of initial current. The current decreases mainly in the very beginning of the polarization and the response time of measurement can

introduce huge error to the result. Thus, a third method (Watanabe method) which does not require the initial state, is described as follows:

$$T_{Li}^{+} = \frac{R_b}{\frac{\Delta V}{I_{ss}} - R_e}$$

where R_b is the bulk resistance after polarization and R_e is the charge transfer resistance before polarization[116].

Other than the mainstream methods of Bruce-Vincent and Watanabe, there is also the Sørensen and Jacobsen method[117] based on MacDonald model[118] of a battery. The transference number could be express as follows:

$$T_{Li}^{+} = \frac{1}{1 + \frac{Z_d(0)}{R_b}}$$

where $Z_d(0)$ is the impedance at low frequencies (Warburg region). It has been pointed out ,though, that Sørensen and Jacobsen did not consider diffusion behaviors in the SEI layer. [119] This method also could be only used at high temperatures, because the $Z_d(0)$ is not easy to obtain at low temperature due to the extremely low frequency needed.

The Wiemhöfer method[120] is based on the relaxation behavior after the DC polarization. The voltage during relaxation reflects the diffusion of the charge carries. By linear extrapolation of the voltage profile, the potential difference $\Delta\varphi(0)$ within the electrolyte to the time zero after stopping the DC polarization can be obtained. The transference number is then determined by the following equation:

$$T_{Li}^{+} = \frac{R_b I_{ss}}{\Delta\varphi(0)}$$

where R_b is the bulk resistance of electrolyte, I_{ss} is the steady-state current.

Bublil et al.[121] examined the four methods (Bruce-Vincent, Watanabe, Sørensen- Jacobsen and

Wiemhöfer) with PEO/$NaPF_6$ electrolyte with and without TiO_2 ceramic filler. The experiment indicates that the Wiemhöfer method was the most inaccurate among the four methods, which yielded comparable results in electrolytes with/without the TiO_2 filler with large standard deviation. The other three could show an improved transference number for the electrolyte with ceramic filler. The Bruce-Vincent method showed the largest error and standard deviation due to the most variables (4 parameters) needed. The Watanabe method exhibited a lower error, but the resulting value decreased after the aging of the samples. The Sørensen-Jacobsen method yielded the most reliable results with lowest errors and standard deviation in case of PEO-based DIPE.

Although the measurement seems easy to perform, to get an accurate value could be very tricky. All the three methods should be equivalent in the ideal situation, which requires that: (1) the device responds immediately at the beginning of polarization, (2) the polarization reaches steady-state in long time scale , and that (3) the impedance of the cell does not change during the polarization. However, in reality, the 3 methods usually give a trend of $T^+_{(DC\ polarization)} > T^+_{(Bruce\text{-}Vincent)} > T^+_{(Watanabe)}$. Except for inaccuracies introduced from the measurement, wrongly performed experiments are not rare in the literature. In all the 3 methods, a polarization to reach steady-state is needed in a long-time scale, as explained by the original article, for polymer electrolytes, 6-20 h are needed. A shorter polarization time will lead to a higher I_{ss}, which directly leads to a T^+ larger than it should be. The other problem is related to EIS measurements, as need for the Bruce-Vincent methods, EIS measurements are needed to obtain the interfacial or charge transfer resistance at low frequencies. The fitting of the EIS spectra could be very tricky especially when the semicircle of the electrolyte and interface responses are overlapping. If the impedance of the initial and final state showed similar results, the simple DC polarization could also provide correct result without the disruptions from EIS fitting. Additionally, it is always worthwhile to verify the current-voltage relationship simply with Ohm's law to check if the EIS spectra are performed in the relevant frequency range (low frequency measurement).

Thus, non-electrochemical methods, such as pulsed-field gradients nuclear magnetic resonance (PFG-NMR) or electrophoretic NMR (eNMR) spectroscopy are meaningful, and the result can

be an effective way to compare and verify the electrochemical results. The NMR measurement can be used to determine the auto diffusion coefficient the of Li cation and its counter ion. The lithium transference number can be derived from the equation:

$$T_{Li}^{+} = \frac{D^{+}}{D^{+} + D^{-}}$$

where D^+ and D^- are the diffusion coefficient of the Li^+ ion and the anion, respectively.

The NMR methods provide additional information on the ion transport apart from the electrochemical processes. The self-diffusion coefficient could be measured separately for anion and cation. However, the NMR based measurements still have their limitations. First, the electrolyte component must contain elements that could be detected by NMR. Luckily the two isotopes of Li, ^{6}Li (with specific probe) and ^{7}Li, both can be used in NMR measurements, but the anion is not always the case. For the anions (or SIPE) containing ^{19}F or ^{1}H could be easily followed with NMR, but salts such as $LiClO_4$ or $LiNO_3$ could not be determined with NMR. However, the conductivity determined with the Nernst-Einstein equation considering the anion and cation diffusion coefficients, is generally overestimated, because by NMR all the species (dissociated ion, ion pairs and ion aggregates) were taking into account. The second issue is due to the NMR determination of the transference number is in an electrode-free system, thus the possible influence of SEI layer between the Li and electrolyte, which can be extremely important in ion transport, was ignored. Therefore, the NMR methods could provide an accurate transference number as an intrinsic property of bulk electrolyte but not in a real electrochemical system which may face electrolyte degradation and induces polarization.

In summary, multiple methods can be used to evaluate Li transference number, including electrochemical methods and NMR methods. All the measurements could yield an estimation of Li transference number with different accuracy. However, all the measurements could lead to meaningful when the experiment reaches the requirements of its original model. In addition, comparing different methods could be very meaningful to evaluate an electrolyte.

4 Conclusions and Thesis Objectives

In summary, this chapter has discussed the general background of batteries as an electrochemical energy storage system. In facing the fast-increasing demand for energy storage, better lithium batteries are strongly needed. As summarized by Goodenough,[5] the principal challenges for the battery are cost, safety, energy density, rate of charge/discharge and service life. Additionally, considering the climate change, environmental pollution (including the mining of raw material, battery production and end-of-life impacts) and geopolitical factors (considering most of critical minerals are localized in certain regions), the sustainability of the battery should also draw intense concern.

The safety issues are mainly linked to the flammability of organic liquid electrolytes. Organic solvents such as carbonate and ethers with high volatility and low flash point could catch fire when the battery get abused either mechanically, electronically, or thermally, and leading to thermal runaway. To avoid or mitigate the risk of thermal runaway, from the material side, substitute the flammability organic liquid electrolytes with polymer or ceramic electrolytes which is safer and more stable could be practical solutions.

On the other topic, to improve energy density, advanced electrodes have been developed, such as high voltage spinel LNMO material as positive electrode, Li metal and silicon as negative electrode. Together with post-Li-ion batteries techniques such as Li-S, Li-O_2 batteries. However, these advanced materials are either limited by the voltage window of electrolyte or facing instability such as dendrite growth, SEI formation, volume expansion, active material shuttling, etc. These instabilities are not only undermining the cycle life of battery but also risking its safety e.g., the lithium dendrite growth could lead to short circuit.

Developing advanced electrolyte which could adapt to and stabilize these advanced electrodes again will be necessary. Therefore, developing safe, stable electrolyte with high performance is one of the core topics in battery research. The polymer electrolytes were one of the candidates to substitute the liquid electrolytes. Two categories of polymer electrolytes including DIPE and SIPEs were introduced in detail. With rational design, the SIPE could reach high ionic conductivity, Li^+ transference numbers close to unity and good electrochemical stability, which is ideal for lithium metal anodes.

For sustainability, two possible paths should be taken to answer the concern: (1) the reduction of the amount of critical minerals used in batteries and (2) recycling the materials from end-of-life batteries. Both ways are very important for developing sustainable, eco-friendly battery systems. In this chapter, the reduction or substitution of critical minerals was discussed, which includes, for instance, the development of organic active materials. Organic active materials, which are composed of earth abundant elements including C, H, O, N, and S, are considered as a class of sustainable, low-cost, and designable active materials for both positive and negative electrodes.

5 Organization of the Thesis and Challenges

In this thesis, to fulfill the goal of sustainable and safe batteries, single ion polymer electrolyte was designed, synthesized, and modified to overcome different challenges in combination with both organic active materials and lithium metal electrodes. In the following chapters, the design and optimization of the electrolytes, electrodes and battery elaboration will be discussed in detail.

In organic batteries, the focus in the state-of-art research is on exploring new chemistry and materials. The studies on the level of batteries are still insufficient, particularly with polymer electrolytes. The polymer electrolyte generally exhibits lower ionic conductivity and wettability compared to liquid electrolytes. At the same time, organic active materials are facing drawbacks such as low electronic conductivity, low density, and dissolution in organic solvents. Applying polymer electrolytes could be helpful in reducing electrode material dissolution, but electrode fabrication to ensure both ionic and electronic conductivity remains challenging. Thus, engineering to adapt polymer electrolytes with organic electrodes is necessary. Moreover, among the polymer electrolytes, the SIPE is considered very promising, especially considering the compatibility with lithium metal electrode. Therefore, in this manuscript, for the first time, SIPEs were coupled with an organic electrode to develop organic LMBs.

In the Chapter 2 and 3, poly(*N*-n-hexyl-3,4,9,10-perylene tetracarboxylic)imide (PTCI) (provided by CEA in the frame of the MOLIBE project) was studied as organic positive electrode material with two types of SIPEs, the first (mPEGME-PTFSIVE) was originally

developed in this work (Chapter 2) with the aim to obtain highly conducting SIPE at lower temperature. The molecular design, synthesis, and characterization of the mPEGME-PTFSIVE was discussed in Chapter 2 and finally LMBs with LFP and PTCI positive electrode were prepared and cycled.

Second, a SIPE (I_{1000}p-SO_3-cr) developed previously was applied to PTCI positive electrode. The electrode elaboration was improved from using the normal Al foil to 3D carbon nonwoven matrices as current collector to increase the mass loading of the organic electrode.

In addition to the organic positive electrode, I realized that the interphase between the SIPEs and the lithium metal electrode was still important for the battery performance. Thus, in the last Chapter 4, the lithium-SIPE interphase improved by doping $LiNO_3$ salt in the I_{1000}p-SO_3-cr SIPE. Electrochemical (CV, EIS, Li plating/stripping) methods were combined with chemical information from XPS and SEM studies to understand the Li reversibility, SEI formation and the effect of the $LiNO_3$ doping.

To sum up, this thesis focused on the organic LMB with SIPEs, which has advantages in sustainability and safety. All the important components in the battery including electrolyte, positive/negative electrodes, and interphase between them was studied in this thesis.

References

1. Dell, R. M. & Rand, D. A. J. Energy storage — a key technology for global energy sustainability. *Journal of Power Sources* 16 (2001) doi:10.1016/S0378-7753(01)00894-1.
2. Dunn, B., Kamath, H. & Tarascon, J.-M. Electrical Energy Storage for the Grid: A Battery of Choices. *Science* **334**, 928–935 (2011).
3. Tollefson, J. Car industry: Charging up the future. *Nature* **456**, 436–440 (2008).
4. *The Role of Critical Minerals in Clean Energy Transitions*. https://www.iea.org/reports/the-role-of-critical-minerals-in-clean-energy-transitions (2021).
5. Goodenough, J. B. & Kim, Y. Challenges for Rechargeable Li Batteries †. *Chem. Mater.* **22**, 587–603 (2010).
6. Asenbauer, J. *et al.* The success story of graphite as a lithium-ion anode material – fundamentals, remaining challenges, and recent developments including silicon (oxide) composites. *Sustainable Energy Fuels* **4**, 5387–5416 (2020).
7. Xie, L. *et al.* Hard Carbon Anodes for Next-Generation Li-Ion Batteries: Review and Perspective. *Advanced Energy Materials* **11**, 2101650 (2021).
8. Winter, M., Besenhard, J. O., Spahr, M. E. & Novák, P. Insertion Electrode Materials for Rechargeable Lithium Batteries. *Adv. Mater.* **10**, 725–763 (1998).
9. Zhang, H. *et al.* $Li_4Ti_5O_{12}$ spinel anode: Fundamentals and advances in rechargeable batteries. *InfoMat* **4**, e12228 (2022).
10. Zhao, B., Ran, R., Liu, M. & Shao, Z. A comprehensive review of Li4Ti5O12-based electrodes for lithium-ion batteries: The latest advancements and future perspectives. *Materials Science and Engineering: R: Reports* **98**, 1–71 (2015).

11. Zuo, X., Zhu, J., Müller-Buschbaum, P. & Cheng, Y.-J. Silicon based lithium-ion battery anodes: A chronicle perspective review. *Nano Energy* **31**, 113–143 (2017).
12. Harry, K. J., Hallinan, D. T., Parkinson, D. Y., MacDowell, A. A. & Balsara, N. P. Detection of subsurface structures underneath dendrites formed on cycled lithium metal electrodes. *Nature Mater* **13**, 69–73 (2014).
13. Chandrashekar, S. *et al.* 7Li MRI of Li batteries reveals location of microstructural lithium. *Nature Mater* **11**, 311–315 (2012).
14. Xu, K. Nonaqueous Liquid Electrolytes for Lithium-Based Rechargeable Batteries. *Chem. Rev.* **104**, 4303–4418 (2004).
15. Liu, Q. *et al.* Insight on lithium metal anode interphasial chemistry: Reduction mechanism of cyclic ether solvent and SEI film formation. *Energy Storage Materials* **17**, 366–373 (2019).
16. Ota, H., Sakata, Y., Wang, X., Sasahara, J. & Yasukawa, E. Characterization of Lithium Electrode in Lithium Imides/Ethylene Carbonate and Cyclic Ether Electrolytes. *Journal of The Electrochemical Society*.
17. Aurbach, D. A short review of failure mechanisms of lithium metal and lithiated graphite anodes in liquid electrolyte solutions. *Solid State Ionics* **148**, 405–416 (2002).
18. Shen, Y. *et al.* Structure and Performance of LiFePO4 Cathode Material: from Bulk to Surface. *Nanoscale* **10**, 1622–1630 (2018).
19. Yi, T.-F., Mei, J. & Zhu, Y.-R. Key strategies for enhancing the cycling stability and rate capacity of LiNi0.5Mn1.5O4 as high-voltage cathode materials for high power lithium-ion batteries. *Journal of Power Sources* **316**, 85–105 (2016).

20. Bhandari, A. & Bhattacharya, J. Review—Manganese Dissolution from Spinel Cathode: Few Unanswered Questions. *J. Electrochem. Soc.* **164**, A106–A127 (2017).
21. Rui, X., Yan, Q., Skyllas-Kazacos, M. & Lim, T. M. Li3V2(PO4)3 cathode materials for lithium-ion batteries: A review. *Journal of Power Sources* **258**, 19–38 (2014).
22. Jung, R., Metzger, M., Maglia, F., Stinner, C. & Gasteiger, H. A. Chemical versus Electrochemical Electrolyte Oxidation on NMC111, NMC622, NMC811, LNMO, and Conductive Carbon. *J. Phys. Chem. Lett.* **8**, 4820–4825 (2017).
23. Liedel, C. Sustainable Battery Materials from Biomass. *ChemSusChem* **13**, 2110–2141 (2020).
24. Ding, Y. & Yu, G. The Promise of Environmentally Benign Redox Flow Batteries by Molecular Engineering. *Angew. Chem. Int. Ed.* **56**, 8614–8616 (2017).
25. Suga, T., Pu, Y.-J., Kasatori, S. & Nishide, H. Cathode- and Anode-Active Poly(nitroxylstyrene)s for Rechargeable Batteries: p- and n-Type Redox Switching via Substituent Effects. *Macromolecules* **40**, 3167–3173 (2007).
26. Lakraychi, A. E. *et al.* Carboxylic and sulfonic N-substituted naphthalene diimide salts as highly stable non-polymeric organic electrodes for lithium batteries. *Electrochemistry Communications* **76**, 47–50 (2017).
27. Goto, F., Abe, K., Ikabayashi, K., Yoshida, T. & Morimoto, H. The polyaniline/lithium battery. *Journal of Power Sources* **20**, 243–248 (1987).
28. Matsunaga, T., Daifuku, H., Nakajima, T. & Kawagoe, T. Development of polyaniline–lithium secondary battery. *Polym. Adv. Technol.* **1**, 33–39 (1990).
29. Wang, C. Y. *et al.* Functionalised polyterthiophenes as anode materials in polymer/polymer batteries. *Synthetic Metals* **160**, 76–82 (2010).

30. Zhu, L. M., Lei, A. W., Cao, Y. L., Ai, X. P. & Yang, H. X. An all-organic rechargeable battery using bipolar polyparaphenylene as a redox-active cathode and anode. *Chem. Commun.* **49**, 567–569 (2013).
31. Tamura, K., Akutagawa, N., Satoh, M., Wada, J. & Masuda, T. Charge/Discharge Properties of Organometallic Batteries Fabricated with Ferrocene-Containing Polymers. *Macromol. Rapid Commun.* **29**, 1944–1949 (2008).
32. Muench, S. *et al.* Polymer-Based Organic Batteries. *Chem. Rev.* **116**, 9438–9484 (2016).
33. Chen, H. *et al.* Lithium Salt of Tetrahydroxybenzoquinone: Toward the Development of a Sustainable Li-Ion Battery. *J. Am. Chem. Soc.* **131**, 8984–8988 (2009).
34. Wang, S. *et al.* Organic $Li_4C_8H_2O_6$ Nanosheets for Lithium-Ion Batteries. *Nano Lett.* **13**, 4404–4409 (2013).
35. Wang, S. *et al.* All Organic Sodium-Ion Batteries with $Na_4C_8H_2O_6$. *Angew. Chem. Int. Ed.* **53**, 5892–5896 (2014).
36. Ren, W., Ma, W., Zhang, S. & Tang, B. Recent advances in shuttle effect inhibition for lithium sulfur batteries. *Energy Storage Materials* **23**, 707–732 (2019).
37. Liang, Y., Tao, Z. & Chen, J. Organic Electrode Materials for Rechargeable Lithium Batteries. *Adv. Energy Mater.* **2**, 742–769 (2012).
38. Geng, J., Bonnet, J.-P., Renault, S., Dolhem, F. & Poizot, P. Evaluation of polyketones with N-cyclic structure as electrode material for electrochemical energy storage: case of tetraketopiperazine unit. *Energy Environ. Sci.* **3**, 1929 (2010).
39. Lee, M. *et al.* High-performance sodium–organic battery by realizing four-sodium storage in disodium rhodizonate. *Nat Energy* **2**, 861–868 (2017).

40. Zeng, R. *et al.* Synthesis and properties of a lithium-organic coordination compound as lithium-inserted material for lithium ion batteries. *Electrochemistry Communications* **12**, 1253–1256 (2010).
41. Renault, S., Geng, J., Dolhem, F. & Poizot, P. Evaluation of polyketones with N-cyclic structure as electrode material for electrochemical energy storage: case of pyromellitic diimide dilithium salt. *Chem. Commun.* **47**, 2414–2416 (2011).
42. Yao, M. *et al.* Indigo Dye as a Positive-electrode Material for Rechargeable Lithium Batteries. *Chem. Lett.* **39**, 950–952 (2010).
43. Quartarone, E. & Mustarelli, P. Electrolytes for solid-state lithium rechargeable batteries: recent advances and perspectives. *Chem. Soc. Rev.* **40**, 2525 (2011).
44. Feng, X., Ren, D., He, X. & Ouyang, M. Mitigating Thermal Runaway of Lithium-Ion Batteries. *Joule* **4**, 743–770 (2020).
45. Galushkin, N. E., Yazvinskaya, N. N. & Galushkin, D. N. Mechanism of Gases Generation during Lithium-Ion Batteries Cycling. *J. Electrochem. Soc.* **166**, A897–A908 (2019).
46. Cao, P.-F. *et al.* Elastic Single-Ion Conducting Polymer Electrolytes: Toward a Versatile Approach for Intrinsically Stretchable Functional Polymers. *Macromolecules* **53**, 3591–3601 (2020).
47. Yiming, B. *et al.* A Mechanically Robust and Versatile Liquid-Free Ionic Conductive Elastomer. *Adv. Mater.* 2006111 (2021) doi:10/gh3bnm.
48. Deng, K., Zhou, S., Xu, Z., Xiao, M. & Meng, Y. A high ion-conducting, self-healing and nonflammable polymer electrolyte with dynamic imine bonds for dendrite-free lithium metal batteries. *Chemical Engineering Journal* **428**, 131224 (2022).
49. Mackanic, D. G., Kao, M. & Bao, Z. Enabling Deformable and Stretchable Batteries. *Adv. Energy Mater.* **10**, 2001424 (2020).

50. Mackanic, D. G., Chang, T.-H., Huang, Z., Cui, Y. & Bao, Z. Stretchable electrochemical energy storage devices. *Chem. Soc. Rev.* **49**, 4466–4495 (2020).

51. Xue, Z., He, D. & Xie, X. Poly(ethylene oxide)-based electrolytes for lithium-ion batteries. *J. Mater. Chem. A* **3**, 19218–19253 (2015).

52. Tammann, G. & Hesse, W. Die Abhängigkeit der Viscosität von der Temperatur bie unterkühlten Flüssigkeiten. *Z. Anorg. Allg. Chem.* **156**, 245–257 (1926).

53. Fulcher, G. S. ANALYSIS OF RECENT MEASUREMENTS OF THE VISCOSITY OF GLASSES. *J American Ceramic Society* **8**, 339–355 (1925).

54. Thiam, A., Martinez-Cisneros, C., Molméret, Y., Iojoiu, C. & Sanchez, J.-Y. PEO: An immobile solvent? *Electrochimica Acta* **302**, 338–343 (2019).

55. Fenton, D. E., Parker, J. M. & Wright, P. V. Complexes of alkali metal ions with poly(ethylene oxide). *Polymer* **14**, 589 (1973).

56. Eckert, A., Abbasi, M., Mang, T., Saalwächter, K. & Walther, A. Structure, Mechanical Properties, and Dynamics of Polyethylenoxide/Nanoclay Nacre-Mimetic Nanocomposites. *Macromolecules* **53**, 1716–1725 (2020).

57. Gutmann, V. Empirical parameters for donor and acceptor properties of solvents. *Electrochimica Acta* **21**, 661–670 (1976).

58. Takahashi, Y. & Tadokoro, H. Structural Studies of Polyethers, (-(CH2)TO-0-)re. X. Crystal Structure of Poly(ethylene oxide). *Macromolecules* **6**, 672–675 (1973).

59. Khan, K. H., Golitsyn, Y., Reichert, D., Kressler, J. & Hussain, H. Graphene Oxide-Grafted Hybrid Diblock Copolymer Brush (GO- *graft* -PEG $_{6k}$ - *block* -P(MA-POSS)) as Nanofillers for Enhanced

Lithium Ion Conductivity of PEO-Based Nanocomposite Solid Polymer Electrolytes. *J. Phys. Chem. B* **127**, 2066–2082 (2023).

60. Zhang, G. *et al.* Accumulation of Glassy Poly(ethylene oxide) Anchored in a Covalent Organic Framework as a Solid-State Li^+ Electrolyte. *J. Am. Chem. Soc.* **141**, 1227–1234 (2019).
61. Zardalidis, G. *et al.* Effect of Polymer Architecture on the Ionic Conductivity. Densely Grafted Poly(ethylene oxide) Brushes Doped with LiTf. *Macromolecules* **49**, 2679–2687 (2016).
62. He, Y., Liu, N. & Kohl, P. A. Difunctional block copolymer with ion solvating and crosslinking sites as solid polymer electrolyte for lithium batteries. *Journal of Power Sources* **481**, 228832 (2021).
63. Stowe, M. K., Liu, P. & Baker, G. L. Star Poly(ethylene oxide) as a Low Temperature Electrolyte and Crystallization Inhibitor. *Chem. Mater.* **17**, 6555–6559 (2005).
64. Niitani, T., Amaike, M., Nakano, H., Dokko, K. & Kanamura, K. Star-Shaped Polymer Electrolyte with Microphase Separation Structure for All-Solid-State Lithium Batteries. *J. Electrochem. Soc.* **156**, A577 (2009).
65. Chinnam, P. R. & Wunder, S. L. Polyoctahedral Silsesquioxane-Nanoparticle Electrolytes for Lithium Batteries: POSS-Lithium Salts and POSS-PEGs. *Chem. Mater.* **23**, 5111–5121 (2011).
66. Ma, J. *et al.* Star-shaped polyethylene glycol methyl ether methacrylate-co-polyhedral oligomeric silsesquioxane modified poly(ethylene oxide)-based solid polymer electrolyte for lithium secondary battery. *Solid State Ionics* **380**, 115923 (2022).
67. Wan, J. *et al.* Ultrathin, flexible, solid polymer composite electrolyte enabled with aligned nanoporous host for lithium batteries. *Nat. Nanotechnol.* **14**, 705–711 (2019).

68. Butzelaar, A. J. *et al.* Advanced Block Copolymer Design for Polymer Electrolytes: Prospects of Microphase Separation. *Macromolecules* **54**, 11101–11112 (2021).

69. Evans, J., Vincent, C. A. & Bruce, P. G. Electrochemical measurement of transference numbers in polymer electrolytes. *Polymer* **28**, 2324–2328 (1987).

70. Yang, X. *et al.* Determining the limiting factor of the electrochemical stability window for PEO-based solid polymer electrolytes: main chain or terminal –OH group? *Energy Environ. Sci.* **13**, 1318–1325 (2020).

71. Li, S. *et al.* A Superionic Conductive, Electrochemically Stable Dual-Salt Polymer Electrolyte. *Joule* **2**, 1838–1856 (2018).

72. Liang, W., Shao, Y., Chen, Y.-M. & Zhu, Y. A 4 V Cathode Compatible, Superionic Conductive Solid Polymer Electrolyte for Solid Lithium Metal Batteries with Long Cycle Life. *ACS Appl. Energy Mater.* **1**, 6064–6071 (2018).

73. Bruce, P. G. & Vincent, C. A. Polymer electrolytes. *Faraday Trans.* **89**, 3187 (1993).

74. Rosenwinkel, M. P., Andersson, R., Mindemark, J. & Schönhoff, M. Coordination Effects in Polymer Electrolytes: Fast Li $^{+}$ Transport by Weak Ion Binding. *J. Phys. Chem. C* **124**, 23588–23596 (2020).

75. Rosenwinkel, M. P. & Schönhoff, M. Lithium Transference Numbers in PEO/LiTFSA Electrolytes Determined by Electrophoretic NMR. *J. Electrochem. Soc.* **166**, A1977–A1983 (2019).

76. Mindemark, J., Lacey, M. J., Bowden, T. & Brandell, D. Beyond PEO—Alternative host materials for Li + -conducting solid polymer electrolytes. *Progress in Polymer Science* **81**, 114–143 (2018).

77. Alamgir, M., Moulton, R. D. & Abraham, K. M. Li+-conductive polymer electrolytes derived from poly(1,3-dioxolane) and polytetrahydrofuran. *Electrochimica Acta* **36**, 773–782 (1991).

78. Huang, S. *et al.* An in-situ polymerized solid polymer electrolyte enables excellent interfacial compatibility in lithium batteries. *Electrochimica Acta* **299**, 820–827 (2019).

79. Mackanic, D. G. *et al.* Crosslinked Poly(tetrahydrofuran) as a Loosely Coordinating Polymer Electrolyte. *Adv. Energy Mater.* **8**, 1800703 (2018).

80. Rokicki, G. & Parzuchowski, P. G. ROP of Cyclic Carbonates and ROP of Macrocycles. in *Polymer Science: A Comprehensive Reference* 247–308 (Elsevier, 2012). doi:10.1016/B978-0-444-53349-4.00107-2.

81. Kimura, K., Yajima, M. & Tominaga, Y. A highly-concentrated poly(ethylene carbonate)-based electrolyte for all-solid-state Li battery working at room temperature. *Electrochemistry Communications* **66**, 46–48 (2016).

82. Zhang, J. *et al.* Safety-Reinforced Poly(Propylene Carbonate)-Based All-Solid-State Polymer Electrolyte for Ambient-Temperature Solid Polymer Lithium Batteries. *Adv. Energy Mater.* **5**, 1501082 (2015).

83. Tominaga, Y., Nanthana, V. & Tohyama, D. Ionic conduction in poly(ethylene carbonate)-based rubbery electrolytes including lithium salts. *Polym J* **44**, 1155–1158 (2012).

84. Sun, B., Mindemark, J., Edström, K. & Brandell, D. Polycarbonate-based solid polymer electrolytes for Li-ion batteries. *Solid State Ionics* **262**, 738–742 (2014).

85. Chai, J. *et al.* In Situ Generation of Poly (Vinylene Carbonate) Based Solid Electrolyte with Interfacial Stability for $LiCoO_2$ Lithium Batteries. *Adv. Sci.* **4**, 1600377 (2017).

86. Olmedo-Martínez, J. L. *et al.* Flame retardant polyphosphoester copolymers as solid polymer electrolyte for lithium batteries. *Polym. Chem.* **12**, 3441–3450 (2021).

87. Sun, Y. *et al.* Polymeric Sulfur as a Li Ion Conductor. *Nano Lett.* **20**, 2191–2196 (2020).

88. Hamann, C. H., Hamnett, A. & Vielstich, W. *Electrochemistry*. (Wiley-VCH, 2007).

89. Diederichsen, K. M., McShane, E. J. & McCloskey, B. D. Promising Routes to a High Li^+ Transference Number Electrolyte for Lithium Ion Batteries. *ACS Energy Lett.* **2**, 2563–2575 (2017).

90. Stolz, L. *et al.* Single-Ion *versus* Dual-Ion Conducting Electrolytes: The Relevance of Concentration Polarization in Solid-State Batteries. *ACS Appl. Mater. Interfaces* **14**, 11559–11566 (2022).

91. Kim, H.-K. & Srinivasan, V. Status and Targets for Polymer-Based Solid-State Batteries for Electric Vehicle Applications. *J. Electrochem. Soc.* **167**, 130520 (2020).

92. Chazalviel, J.-N. Electrochemical aspects of the generation of ramified metallic electrodeposits. *Phys. Rev. A* **42**, 7355–7367 (1990).

93. Tikekar, M. D., Archer, L. A. & Koch, D. L. Stability Analysis of Electrodeposition across a Structured Electrolyte with Immobilized Anions. *J. Electrochem. Soc.* **161**, A847–A855 (2014).

94. Li, S. *et al.* Single-Ion Homopolymer Electrolytes with High Transference Number Prepared by Click Chemistry and Photoinduced Metal-Free Atom-Transfer Radical Polymerization. *ACS Energy Lett.* **3**, 20–27 (2018).

95. Lingua, G. *et al.* Unique Carbonate-Based Single Ion Conducting Block Copolymers Enabling High-Voltage, All-Solid-State Lithium Metal Batteries. *Macromolecules* **54**, 6911–6924 (2021).

96. Zhao, S. *et al.* Unraveling the Role of Neutral Units for Single-Ion Conducting Polymer Electrolytes. *ACS Appl. Mater. Interfaces* **13**, 51525–51534 (2021).

97. Schauser, N. S. *et al.* The Role of Backbone Polarity on Aggregation and Conduction of Ions in Polymer Electrolytes. *J. Am. Chem. Soc.* **142**, 7055–7065 (2020).

98. Aubrey, M. L., Axelson, J. C., Engler, K. E. & Long, J. R. Dependence of Linker Length and Composition on Ionic Conductivity and Lithium Deposition in Single-Ion Conducting Network Polymers. *Macromolecules* acs.macromol.1c00911 (2021) doi:10/gmhxrk.

99. Borzutzki, K., Thienenkamp, J., Diehl, M., Winter, M. & Brunklaus, G. Fluorinated polysulfonamide based single ion conducting room temperature applicable gel-type polymer electrolytes for lithium ion batteries. *J. Mater. Chem. A* **7**, 188–201 (2019).

100. Liang, H. *et al.* Polysiloxane-Based Single-Ion Conducting Polymer Blend Electrolyte Comprising Small-Molecule Organic Carbonates for High-Energy and High-Power Lithium-Metal Batteries. *Advanced Energy Materials* **12**, 2200013 (2022).

101. Ma, Q. *et al.* Single Lithium-Ion Conducting Polymer Electrolytes Based on a Super-Delocalized Polyanion. *Angew. Chem. Int. Ed.* **55**, 2521–2525 (2016).

102. Yuan, H. *et al.* Single Lithium-Ion Conducting Solid Polymer Electrolyte with Superior Electrochemical Stability and Interfacial Compatibility for Solid-State Lithium Metal Batteries. *ACS Appl. Mater. Interfaces* **12**, 7249–7256 (2020).

103. Oh, H. *et al.* Poly(arylene ether)-Based Single-Ion Conductors for Lithium-Ion Batteries. *Chem. Mater.* **28**, 188–196 (2016).

104. Nguyen, T. K. L., Lopez, G., Iojoiu, C., Bouchet, R. & Ameduri, B. Novel single-ion conducting electrolytes based on vinylidene fluoride copolymer for lithium metal batteries. *Journal of Power Sources* **498**, 229920 (2021).

105. Shin, D. *et al.* A Single-Ion Conducting Borate Network Polymer as a Viable Quasi-Solid Electrolyte for Lithium Metal Batteries. *Adv. Mater.* **32**, 1905771 (2020).

106. Zhu, Y. S. *et al.* A new single-ion polymer electrolyte based on polyvinyl alcohol for lithium ion batteries. *Electrochimica Acta* **87**, 113–118 (2013).

107. Dewing, B. L., Bible, N. G., Ellison, C. J. & Mahanthappa, M. K. Electrochemically Stable, High Transference Number Lithium Bis(malonato)borate Polymer Solution Electrolytes. *Chem. Mater.* **32**, 3794–3804 (2020).

108. Liu, K. *et al.* Molecular Design of a Highly Stable Single-Ion Conducting Polymer Gel Electrolyte. *ACS Appl. Mater. Interfaces* acsami.0c03363 (2020) doi:10/gg88tx.

109. Villaluenga, I. *et al.* Nanostructured Single-Ion-Conducting Hybrid Electrolytes Based on Salty Nanoparticles and Block Copolymers. *Macromolecules* **50**, 1998–2005 (2017).

110. Yang, H. *et al.* A Single-Ion Conducting UiO-66 Metal–Organic Framework Electrolyte for All-Solid-State Lithium Batteries. *ACS Appl. Energy Mater.* **3**, 4007–4013 (2020).

111. Inceoglu, S. *et al.* Morphology–Conductivity Relationship of Single-Ion-Conducting Block Copolymer Electrolytes for Lithium Batteries. *ACS Macro Lett.* **3**, 510–514 (2014).

112. Bouchet, R. *et al.* Single-ion BAB triblock copolymers as highly efficient electrolytes for lithium-metal batteries. *Nature Mater* **12**, 452–457 (2013).

113. Nguyen, H.-D. *et al.* Nanostructured multi-block copolymer single-ion conductors for safer high-performance lithium batteries. *Energy Environ. Sci.* **11**, 3298–3309 (2018).

114. Borzutzki, K., Nair, J. R., Winter, M. & Brunklaus, G. Does Cell Polarization Matter in Single-Ion Conducting Electrolytes? *ACS Appl. Mater. Interfaces* **14**, 5211–5222 (2022).

115. Bruce, P. Conductivity and transference number measurements on polymer electrolytes. *Solid State Ionics* **28–30**, 918–922 (1988).

116. Watanabe, M., Nagano, S., Sanui, K. & Ogata, N. Estimation of Li+ transport number in polymer electrolytes by the combination of complex impedance and potentiostatic polarization measurements. *Solid State Ionics* **28–30**, 911–917 (1988).

117. Ravn Sørensen, P. & Jacobsen, T. Conductivity, charge transfer and transport number—an ac-investigation of the polymer electrolyte LiSCN-poly(ethyleneoxide). *Electrochimica Acta* **27**, 1671–1675 (1982).

118. Macdonald, J. R. Theory of space-charge polarization and electrode-discharge effects. *The Journal of Chemical Physics* **58**, 4982–5001 (1973).

119. Fauteux, D. Formation of a passivating film at the lithium-PEO-LiCF3SO3 interface. *Solid State Ionics* **17**, 133–138 (1985).

120. Hiller, M. M., Joost, M., Gores, H. J., Passerini, S. & Wiemhöfer, H.-D. The influence of interface polarization on the determination of lithium transference numbers of salt in polyethylene oxide electrolytes. *Electrochimica Acta* **114**, 21–29 (2013).

121. Bublil, S. *et al.* Electrochemical Methods of Transference Number Determination for Polymer Electrolyte Systems: A Comparative Study. *J. Electrochem. Soc.* **169**, 110523 (2022).

Chapter 2 Linear SIPE for Lithium Battery via Unique Donor-acceptor Polymerization

This chapter is focused on a novel single ion polymer electrolyte (SIPE) which has a linear structure with short PEG branches. The SIPE was synthesized via a donor-acceptor (D-A) reaction, a specific structure (2A-1D) was obtained which has never been reported before. The SIPE has been characterized by thermal and electrochemical methods both as membrane and electrode. It was tested in LMBs with both lithium iron phosphate ($LiFePO_4$, LFP) and an organic positive electrode (poly(N-n-hexyl-3,4,9,10-perylene tetracarboxylic)imide (PTCI)).
This chapter is divided into three parts:

1) Synthesis and characterization of monomers and branched polymer electrolyte.
2) Fabrication of the electrolyte membrane - thermal and electrochemical properties.
3) Batteries tests with LFP and organic PTCI electrodes at different temperatures.

1 Molecular design of the linear SIPEs

As discussed in Chapter 1 the important properties of SIPEs, including ionic conductivity, mechanical strength, electrochemical and thermal stabilities, are linked directly to the polymer structure. However, there are remaining drawbacks which can be improved. First, the conductivity is not high enough to use the battery at ambient temperature. Although this is a general hindrance of all the SIPEs, there is still space to improve the ionic conductivity. The conductivity of the polymer electrolyte is linked to two main factors: polymer chain flexibility and salt dissociation, which could be improved by the molecular design.
Second, the crosslinked polymer is a thermoset, which can neither dissolve nor melt. This will require a specific step to add the polymer electrolyte to ensure ionic conductivity inside the electrodes e.g., via infiltration and polymerization of the monomers in the electrode. In such experimental conditions, the polymerization is not controlled, and the monomer conversion is generally never 100%. Thus, the non-polymerized ionic monomer could undermine the single-ion conducting properties. Additionally, crosslinked polymers are facing difficulties for

determining the reaction mechanism because characterizations methods such as NMR and SEC require the polymer to be soluble.

A linear polymer electrolyte, particularly, with a branched structure, could overcome the issues mentioned before, due to its better chain flexibility which could provide better ionic conductivity and its solubility that lead to easier processing methods.

An alternative copolymer is a class of copolymer that is distinctly different to others including random, and block copolymers, which could evenly distribute different moieties along the polymer chain.[1] Alternative copolymer could be an ideal choice for SIPEs because of its evenly distributed ionic functions and solvating chains, which could maximize the lithium ion dissociation. Donor-acceptor polymerization is a specific reaction to form alternative sequence by copolymerizing electron-rich and electron-poor monomers. The combination between vinyl ether and maleic monomers was studied and proved as a strict alternative sequence[2,3]. The vinyl ether carries electron-rich double bonds, due to the donating effect of the oxygen atom. Whereas maleic monomers (anhydride, esters, and imide) own the electron-poor double bond, due to the strongly electron-withdrawing of two carboxyl groups. The two monomers cannot homopolymerize under free radical conditions.[4]

As discussed before, TFSI-based ionic functions and PEO based solvating chains are the classic choice in polymer electrolyte. Therefore, functionalizing these two moieties with vinyl ether and maleic groups will be the key to get desired alternating structure. To reach the linear structure, monofunctional monomers are required, which means each monomer molecule could have sorely one polymerizable double bond in the case of chain growth polymerization. Monofunctional TFSI-based vinyl ether can be achieved by nucleophilic aromatic substitution reaction. Maleate can be synthesized simply by ring-opening of maleic anhydride with PEG monomethyl ether.

The copolymerization of the two monomers can be done by a free-radical photoinitiation with ultraviolet irradiation. Ideally the product will be strictly alternative with a D:A ratio of 1:1. The short branch of the mPEG chain could form a brush-like polymer which improved its mobility. Additionally, the methoxy end of PEG is reported to be more stable than the hydroxyl group facing higher voltage[5] and metallic lithium, which is an extra advantage of this design.

The scheme of the polymer electrolyte and its synthesis is shown in Figure 30.

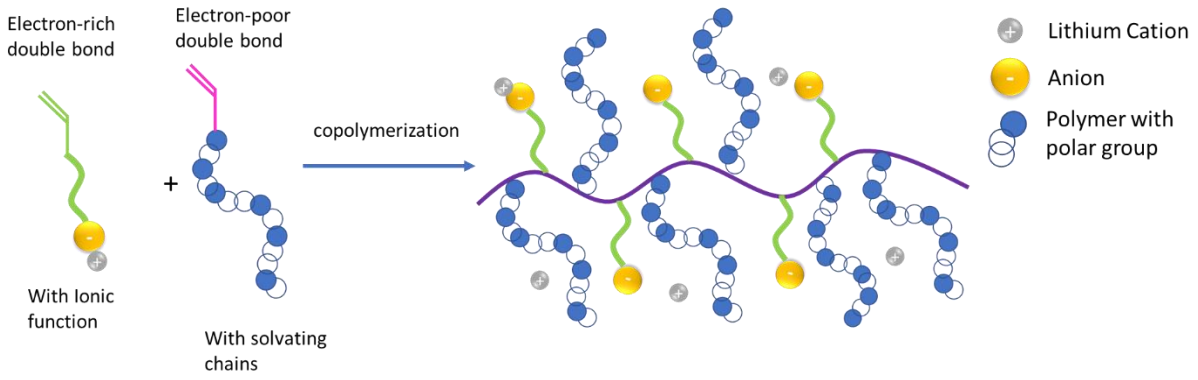

Figure 30. Illustrative scheme of designing brush-like linear SIPE.

2 Synthesis of the SIPE

The first steps were focused on the synthesis of the monomers, which were maleate and vinyl ether. The maleate was synthesized by a one-step reaction of opening the maleic anhydride ring by poly(ethylene glycol) methyl ether (mPEG, M_w=1000 g mol^{-1}), scheme 1. The mPEG was first dried under vacuum to remove water and deprotonated by adding lithium hydride (equal molar amount to the -OH group). The reaction took place in anhydrous tetrahydrofuran with an argon flow at 40°C. Then maleic anhydride was added and reacted overnight. Then THF was removed by rotary evaporation and yielded a product of white wax. The product was used without additional purification.

The ionic vinyl ether monomer with trifluoromethane sulfonimide (TFSI) function, lithium ((trifluoromethyl)sulfonyl)((4-(4-(vinyloxy)butoxy)phenyl)sulfonyl)amide (PTFSIVE) was synthesized via two steps. The first step was the synthesis of the TFSI function by a substitution reaction between trifluoromethansulfonamide and 4-fluorobenzenesulfonyl chloride with the aid of triethylamine in THF. At the end of the reaction NaOH was added to the reaction mixture and then the triethylamine and the THF were removed by evaporation. The solid product was dissolved in acetonitrile (AcN) and the solution filtered to remove the NaCl and the excess of NaOH. After AcN evaporation the intermediate product sodium ((4-fluorophenyl) sulfonyl) ((trifluoromethyl) sulfonyl) amide was yielded. The second step consisted of nucleophilic substitution on the aromatic ring by hydroxybutyl vinyl ether. The reaction took place in

diglyme solution, once the hydroxybutyl vinyl ether was deprotonated by NaH at 60°C, the sodium ((4-fluorophenyl)sulfonyl)((trifluoromethyl)sulfonyl)amide was added and the reaction temperature was raised to 120 °C. The product was purified by filtration to remove solid impurity and then the Na^+ ion was exchanged by Li^+ by passing a column of anion exchange resin (Amberlite IR 120 Li form) for 3 times in a water/acetonitrile (1:1) mixture.

The copolymerization of mPEGME and PTFSIVE monomers was conducted by UV irradiation, i.e., photopolymerization. The two monomers were placed in a Schlenk tube with 1 wt.% of diphenyl(2,4,6-trimethylbenzoyl)phosphine Oxide (Lucirin lr 8893) photoinitiator and diluted with THF (50 wt.% of monomers). The mixture was then degassed via three loops of freeze-pump-thaw to remove all the dissolved oxygen, which is an inhibitor of the free radical polymerization. The Schlenk tube was filled with Ar gas and sealed. Then it was placed under UV irradiation (6.8W, 365 nm) with magnetic stirring for 3 h at room temperature.

After 3 hours, the viscosity of the reaction solution was obviously increased associated with the molecular weight increase during the reaction. The reaction solution was diluted with DI water and purified with dialysis to remove all the small molecular impurities. After dialysis for two days, the aqueous solution was freeze dried to yield a yellowish wax-like product, which is shown in Figure 31.

Figure 31. Photo of mPEGME-PTFSIVE copolymer.

The complete synthesis route of the mPEGME-PTFSIVE copolymer was shown in Figure 32.

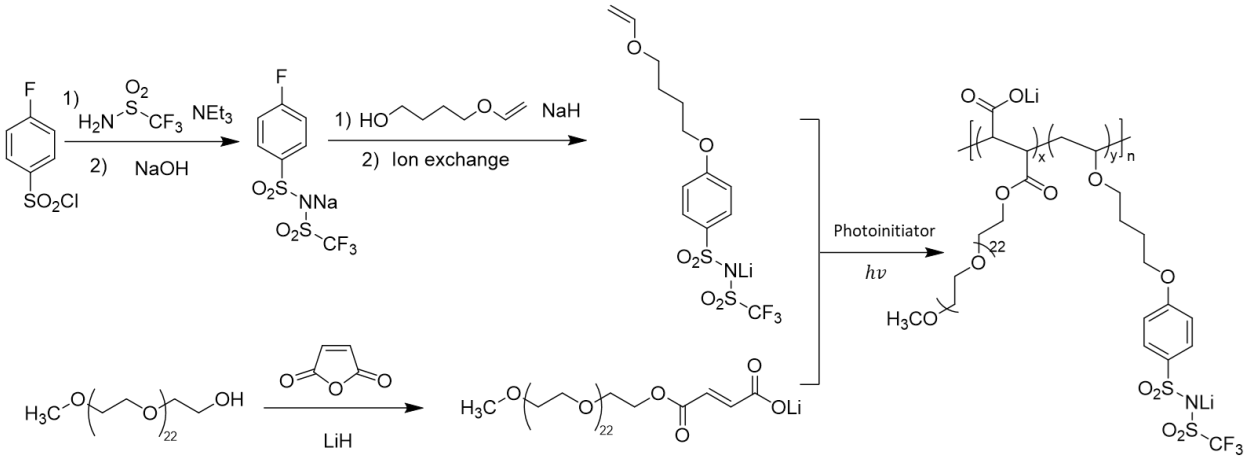

Figure 32. Complete synthesis route of the mPEGME-PTFSIVE copolymer.

2.1 Determination of the polymer structure

To confirm the structure of the copolymer,^{1}H, ^{19}F and ^{7}Li NMR spectra were taken (Figure 33). Deuterium oxide (D_2O) was used as solvent to avoid an overlap of the solvent signal with the product. In the ^{1}H spectrum, broad peaks were observed, as characteristic for a polymer. The representative peaks from the vinyl ether monomer are the aromatic H on the disubstituted benzene ring, which are presented at a chemical shift of 7.86 and 7.15 ppm. The peaks from the maleate can be found at 3.5-3.9 ppm corresponding to the poly(ethylene glycol) side chain and at 3.39 ppm with a singlet peak corresponding to the methoxy group. By calibrating the methoxy group with 3 (3H), integration of the polyether side chain gives ~95 (90 H on the side chain with 3.5 H from backbone) which is aligned with the molecular weight of the starting material (mPEG, M_w=1000 g mol^{-1}). However, the aromatic hydrogens integrated as two peaks of 0.99 (~2 in total), which means the ratio between electron acceptor (A, maleate) and electron donor (D, vinyl ether) is specifically 2:1. In the ^{19}F NMR spectrum the representative peak of the trifluoromethanesulfonic imide (TFSI) was observed at -78.3 ppm, and in the ^{7}Li NMR spectrum, the lithium signal was observed with only one peak despite the presence of two lithiated function, i.e. TFSI and carboxylate This could be ascribed to the fast exchange of the lithium ion between the two groups in water.

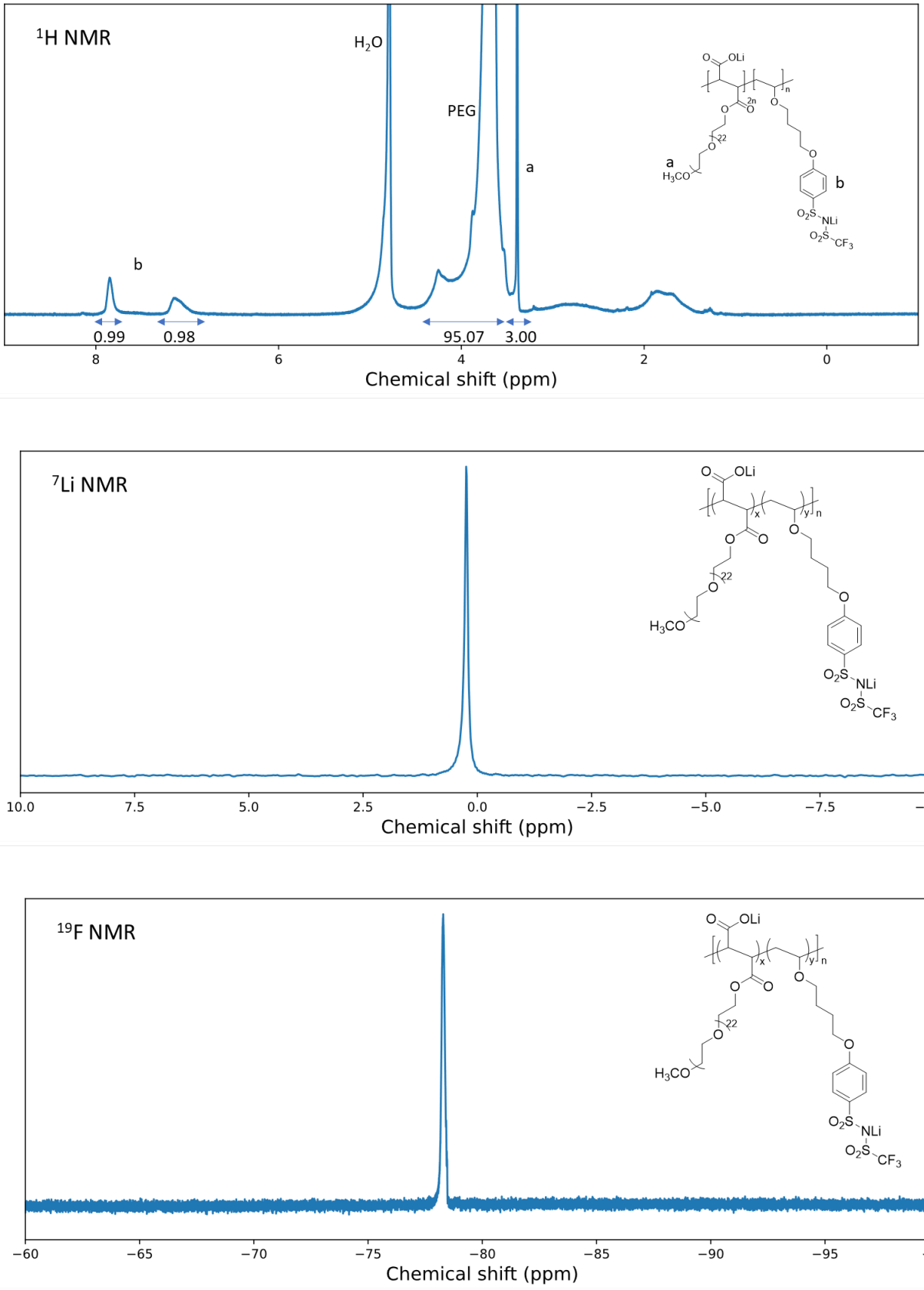

Figure 33. ^{1}H, ^{19}F and ^{7}Li NMR spectra of mPEGME-PTFSIVE copolymer in D_2O.

Since the vinyl ether and maleic monomer copolymerization has been well studied, AB alternating copolymer is expected. Additionally, as described previously the two monomers cannot homopolymerize though free radical mechanism. Thus, the ratio of electron acceptor (A) and electron donor (D) should be 1:1. However, I observed the 2:1 ratio for A:D, which suggests a different reaction mechanism. This 2A:1D polymerization has never been reported so far to the best of our knowledge. The unexpected A:D ratio also led to a lower concentration of ionic functions (in PTFSIVE) in the final product and high EO:Li ratio.

The chemical structure of the polymer was also analyzed by Fourier-transform infrared (FTIR) spectroscopy with attenuated total reflectance (ATR). The absorption spectrum from 3500 to 450 cm^{-1} is shown in Figure 34. It is obvious that the vibration of the PEG side chain plays the leading role in the absorption, such as stretching of the C-H and C-O bonds at 2865 and 1091 cm^{-1}, respectively. Other than the PEG signals, the stretching of ester function, C=O, appears at 1735 cm^{-1}; aromatic C=C bond stretching and bending can be found at 1597 and 843 cm^{-1}. For the TFSI group, the vibrations modes are more weak and complicated, by referring the spectra from literature[6], the stretching of the S-N-S and bending of C-F, S-N-S, S=O can be recognized in the magnified spectrum between 800-450 cm^{-1} (Figure 35). All the expected functional groups were observed in the IR spectrum, which correspond to the proposed polymer structure.

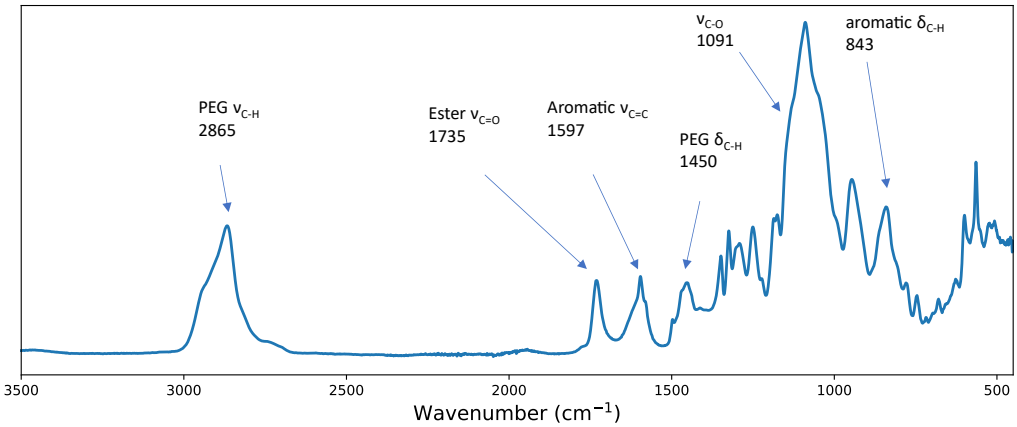

Figure 34. ATR-FTIR absorption spectrum of mPEGME-PTFSIVE copolymer.

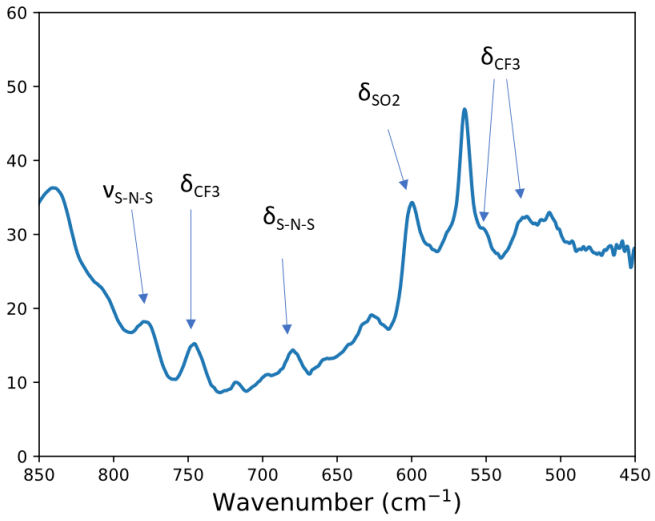

Figure 35. ATR-FTIR absorption spectrum of mPEGME-PTFSIVE copolymer, magnified from 850-450 cm^{-1}.

Molecular weight determination of the copolymer is crucial to eliminate the possibility that the product is an A-D-A trimer rather than a polymer. The product was characterized by size exclusion chromatography (SEC) to evaluate the molecular weight and polydispersity index. For SEC, the sample was prepared in a THF solution of 4 mg mL^{-1} and passed through a SEC column which was filled with porous particles to sort the size of the passing molecules. The retention time of varied species was recorded by reflective index detector and compared to a calibration curve made by standard polystyrene to convert into molecular weights. The molecular weight of the mPEGME-PTFSIVE copolymer can be characterized by different numbers as averaged molecular weight (M_n), weight averaged molecular weight (M_w), and peak molecular weight (M_P). The dispersity of the molecular weight contribution can be reflected in polydispersity index (PDI) which is the ratio between M_w and M_n.

The product exhibited a Mn of 13600 g mol^{-1} with a narrow PDI of 1.14. This result eliminated the possibility that the product is just ME-VE-ME trimer which has only a molecular weight of ~2500 g mol^{-1}. However, the SEC data was referred to hydrophobic polystyrene standards which have different sizes than hydrophilic products in same solvent. Thus, to confirm the result, SEC with light scattering detector (SEC-LS) was used. The mobile phase is dimethylacetamide with 0.5% of LiCl to avoid aggregation of the product due to the ionic functions. This method

should provide a better resolution of molecular weight distribution. By SEC-LS, the Mn was 10500 g mol^{-1} with a PDI of 2.5 which suggests a much broader distribution of molecule size.

Table 1. Molecular weights and PDI of mPEGME-PTFSIVE copolymer.

Method	Mobile phase	M_n (g mol^{-1})	M_w (g mol^{-1})	M_P (g mol^{-1})	PDI
GPC	THF	13600	15560	17350	1.14
GPC-LS	DMAc/LiCl (0.5%)	10470	26470	34870	2.53

The molecular weight of the product was less than our expectation. The Mn of 13600 g mol^{-1} suggests that by average the degree of polymerization is only around 5.5 (A-D-A repeat unites, ~17 molecules of monomers). The relatively low molecular weight (or degree of polymerization) could be ascribed to the kinetic of polymerization[7]. With a radical mechanism, the molecular weight of a propagating specie is called kinetic chain length ν. ν can be derived by:

$$\nu = \frac{k_p[M]^2}{2\sqrt{f k_d k_t[I]}}$$

where k_d, k_p and k_t are the rate constants of initiator decomposition, chain propagation and chain termination, respectively; [*M*] and [*I*] are the concentrations of monomers and initiator; *f* is the efficiency of the initiation. In our case, due to the size of the monomer, especially mPEGME (M_w ~1100g mol^{-1}), the concentration of monomers [*M*] is always low, even in the bulk. And due to the high viscosity of the reaction mixture, the k_p should be low. Thus, the kinetics of the polymerization are not favorable to yield a product with extremely high molecular weight. Lower initiator concentration, better string and de-oxygen could improve the molecular weight of the copolymer.

Another important piece of information to confirm the chemical structure is to measure the amount of lithium in the product. Indeed, ionic conductivity is associated with the lithium cation content. Ideally, the expected lithium content should be ~ 0.80 wt.% in A:D=2:1 ratio. The

EO:Li ratio should be around 15 when considering all the lithium atoms. However, the carboxylate lithium is less dissociative than TFSI-based ionic functions, thus the effective EO:Li ratio could be lower, which is ~44.

The lithium cation content was determined by two methods, which is atomic absorption spectroscopy (AAS) and NMR. With AAS, the device was calibrated with LiCl and NaCl standard solution. The sample of mPEGME-PTFSIVE was dissolved in DI water with a concentration of 158 mg L^{-1}. The lithium cation concentration is determined as 0.82 mg L^{-1}, which is 0.52 wt.% of the sample.

NMR spectroscopy was conducted with a small, sealed tube with lithium triflate ($LiSO_3CF_3$) in DMSO-d_6 as internal reference. The calibration was performed with three solutions of lithium triflate in acetone-d6 with known concentration, which has different chemical shift in ^{7}Li NMR spectrum, to avoid collapsing of the two Li^+ signal. Then the mPEGME-PTFSIVE in acetone-d6 sample was analyzed with the internal reference and the concentration of Li^+ can be calculated from the integration of the peaks. The lithium content yielded with this method is ~0.77 wt.%, which is aligned with the ME:VE=2:1 structure. The ^{7}Li NMR data are listed in Table 2.

Table 2. ^{7}Li NMR results.

Entry	Sample	concentration (g L^{-1})	Integration	Li concentration in solution (mol L^{-1})	Li (wt.%)
Sample1	PTFSIVE-mPEGME	4.50	0.73	0.0050	0.76
Sample2	PTFSIVE-mPEGME	8.00	1.26	0.0087	0.78

The integration was normalized by the internal reference of $LiSO_3CF_3$ in DMSO-d_6. All the samples were prepared in acetone-d_6.

All the analysis of this product (which was repeated many times) led to the unexpected

conclusion that the donor-acceptor polymerization of an ionic vinyl ether copolymerizes with PEG-based maleate specially yielded a copolymer with an A:D=2:1 ratio. However, the mechanism of the reaction remains unrevealed, which requires further investigation. Therefore, model molecules were designed with different vinyl ethers and maleates to help understanding this unique reaction.

3 Synthesis of model molecules to understand the polymerization mechanism

First, common aliphatic vinyl ether and maleate were chosen to confirm the normal donor-acceptor copolymerization. Butyl vinyl ether (BVE) and diethyl maleate (DEM) were polymerized with the same protocol described before. The product was purified by dissolution in ethanol and precipitation in water. After drying under vacuum, a white polymer was obtained. The reaction is shown in Figure 36.

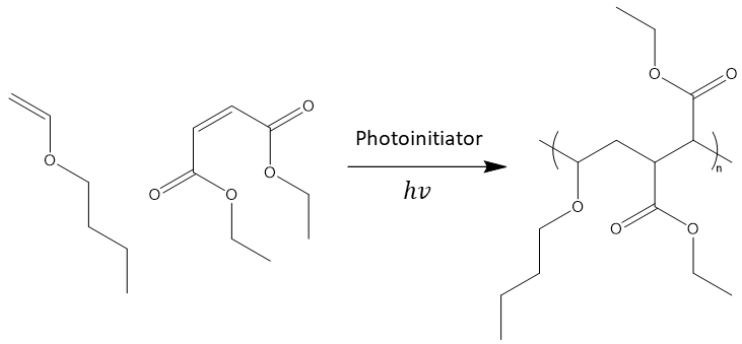

Figure 36. Synthesis of BVE-DEM copolymer

A ^{1}H NMR spectrum, shown in Figure 37, was taken to examine the A: D ratio of this BVE-DEM copolymer. By comparing the spectra of the monomers, although the broad peaks are overlapped and the integral are not easy to make, the specific peaks could be clearly assigned. The peak at the lower chemical shift of 0.89 ppm is the signal of CH_3 at the end of the BVE, which integrated as 3. Then the peak at the highest chemical shift of 4.10 ppm corresponds to the CH_2 close to carboxyl with an integration of 4.45. These two peaks are well separated from all the other broad peaks that are easy to recognize and integrate properly. Thus, the A: D ratio of the monomers can be determined as 1: 1.11, which is close to one and aligned with most of

the cases in donor-acceptor polymerization.

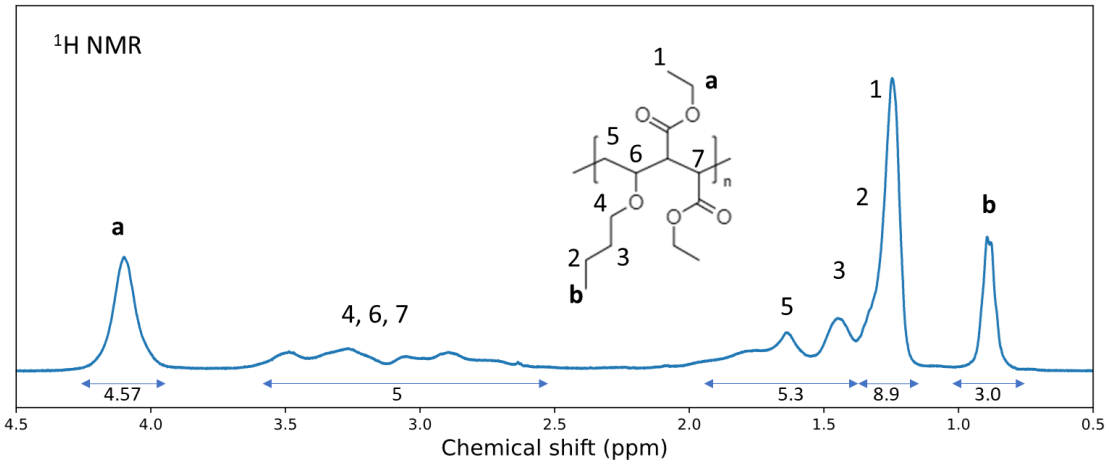

Figure 37. ^{1}H NMR of BVE-DEM copolymer in $CDCl_3$.

Second, ionic PTFSIVE was mixed with diethyl maleate and polymerized (Figure 38). The product was purified by dialysis. Similarly, the product showed an A:D ratio of 2, again regardless of the feeding ratio of the two monomers. As shown in ^{1}H NMR (Figure 39), in PTFSIVE-DEM copolymer, CH_3 from DEM (a) and the aromatic protons from PTFSIVE (b) integrated as 6 and 2.14, which could be converted to DEM:PTFSIVE with a ratio of x:y=2:1.07. The copolymer obtained by this polymerization confirms the formation of $(A\text{-}D\text{-}A)_n$ structure. Taking into account in both polymerizations involving the ionic monomer PTFSIVE lead to such structure it can be supposed that is linked to the presence of PTFSIVE monomer.

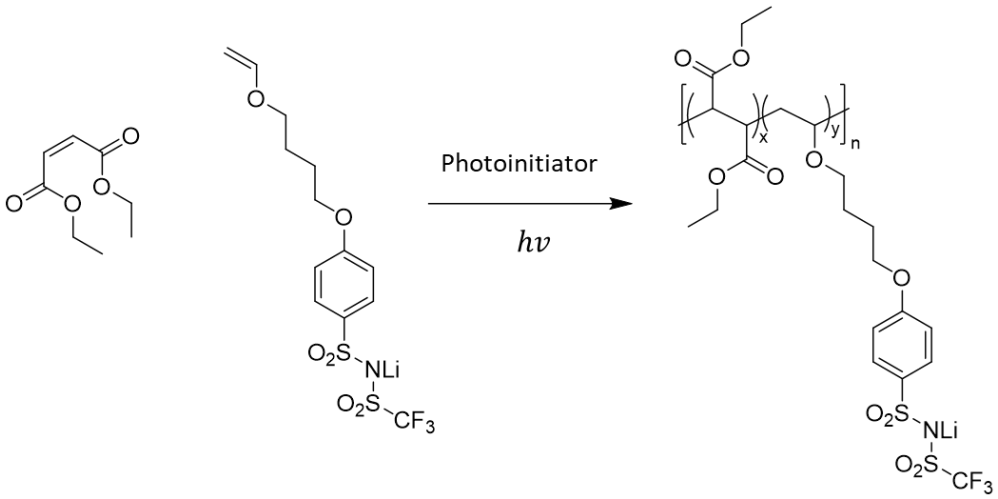

Figure 38. Synthesis of PTFSIVE-DEM copolymer.

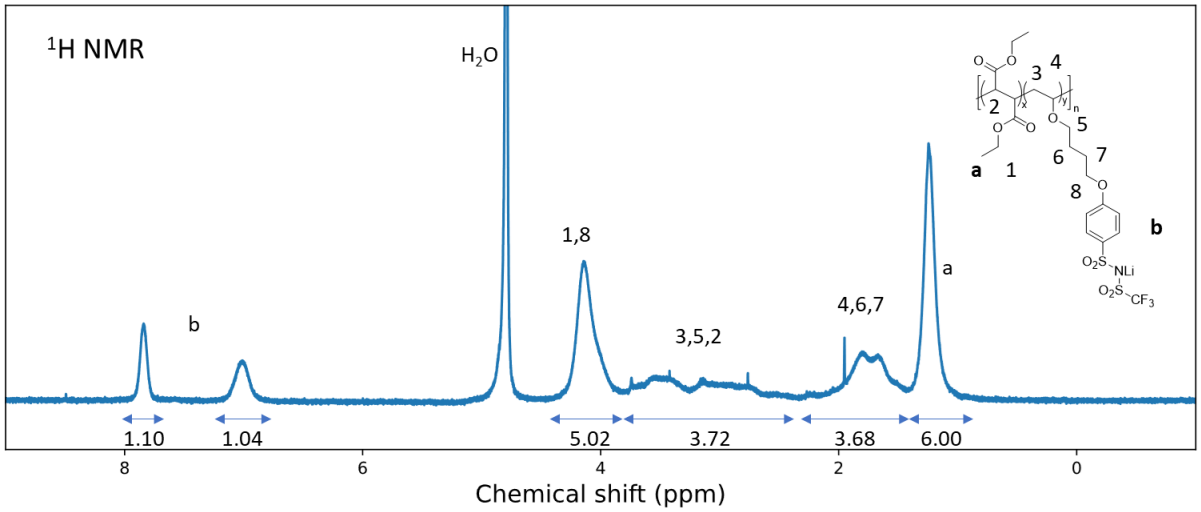

Figure 39. ^{1}H NMR of DEM-PTFSIVE copolymer in $CDCl_3$.

Following the discussion above, a different mechanism for this specific donor-acceptor polymerization with unique 2A-1D repeating units was proposed. Recent research[8–10] unveiled that vinyl ether could be homopolymerized in the presence of LiOH, which is due to the coordination of Li^+ with the vinyl ether double bond and reduced its donor number (electron richness). A similar effect could be related to the ionic vinyl ether in this case. The Li^+ could coordinate with the electron-rich double bond of the vinyl ether, and the $TFSI^-$ could coordinate with the acceptor (malate). Therefore, we assume that with the ionic vinyl ether monomer, the donor-acceptor effect was altered which allowed the monomers form donor-acceptor complex of [2A-1D] and then the complex go through radical polymerization. By altering the double bond donor or acceptor ability we suppose: i) an [A-D-A] complex is formed and then polymerized, ii) formation of some A-A segments (favorized by the complexation of malate double bonds with the TFSI anion) cannot be excluded even though we don't observe any radical homopolymerization of maleate monomer in the tests.

4 Characterizations of mPEGME-PTFSIVE and membrane with PVDF-HFP

The mPEGME-PTFSIVE are characterized with different methods in order to evaluate their properties as polymer electrolyte and separator. Due to the highly branched structure and not enough high molecular weight the mPEGME-PTFSIVE is not able to form a free-standing film

which can act as separator in a battery. Therefore, it was blended with a polymer with good mechanical properties, i.e., poly(vinylidene fluoride-co-hexafluoropropene) (PVDF-HFP) , and then cast as a membrane.

PVDF-HFP is a semi-crystalline copolymer that has lower crystallinity compared to PVDF due to the randomly inserted HFP sequence hindering the packing of the polymer chain and due to their highly fluorinated structure it exhibits a very good electrochemical stability, thus being well adapted for the applications in batteries. The formula of PVDF-HFP is shown in Figure 40.

Noticeably, PVDF-HFP is not miscible with the strongly hydrophilic polymer electrolyte. So, phase segregation is expected with an insulating and strong mechanically PVDF-HFP phase and a conductive one i.e., mPEGME-PTFSIVE. The ratio between PVDF-HFP and mPEGME-PTFSIVE has to be optimized in order to obtain a better compromise between conductivity and mechanical strengths.

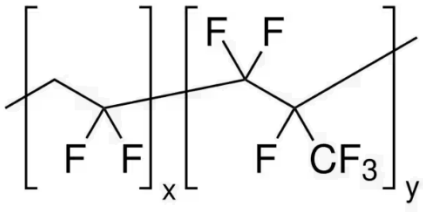

Figure 40. Structure of PVDF-HFP.

To cast the film, a mixture of the mPEGME-PTFSIVE copolymer and PVDF-HFP with a mass ratio of 55:45 and 70:30 was dissolved in a DMSO/acetone (1:1) solvent mixture. The polymers were dissolved under stirring to form a homogeneous solution and then cast in a glass petri dish. The solvent was first evaporated in an oven at 80 °C for 12 h and then further dried under vacuum for another 12 h.

4.1 Morphology and porosity

The image of the membrane is shown in Figure 41. The membrane was a yellowish, opaque thin film. The typical thickness of the membranes was between 70 and 90 μm.

Figure 41. SIPE membrane with mPEGME-PTFSIVE and PVDF-HFP with a ratio of 70:30.

The morphology of the membrane was investigated by scanning electron microscopy (SEM), which is shown in Figure 42.

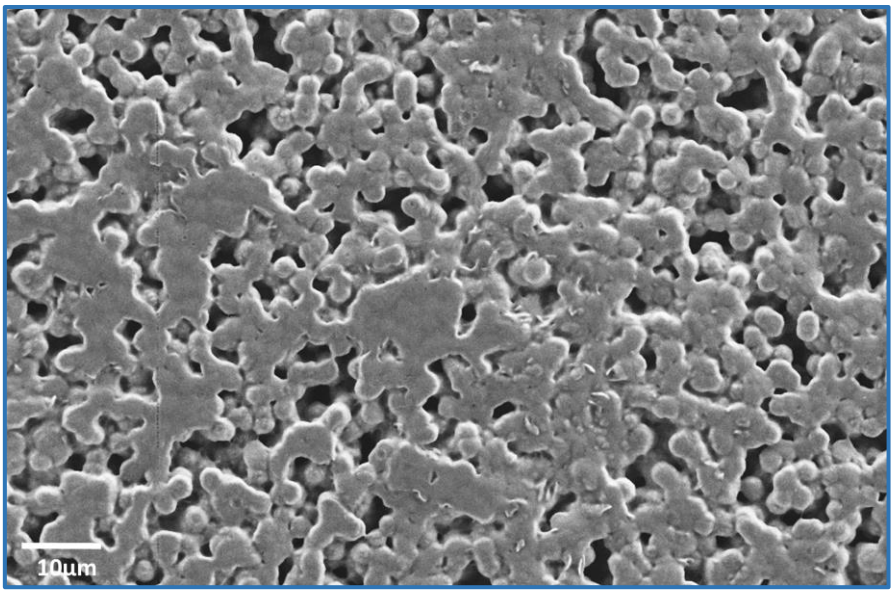

Figure 42. SEM image of the SIPE membrane, with an in-lens detector.

With the SEM image, although the phase segregation between the mPEGME-PTFSIVE copolymer and PVDF-HFP was not easily observed at small scale due to the limited stability under the beam, especially for the PEO based polymer. However, a porous surface was observed. The porosity can be calculated from the density of the membrane. The porosity can affect the membrane conductivity, as the porosity could hinder the ionic pathway (increasing tortuosity) and decrease the ionic conductivity. The density of the membrane was measured with a microbalance kit. The dimensions of a piece of SIPE70 with well-defined geometry were measured in an argon filled glove box to avoid absorbing humidity. The weight of this piece of membrane was measured in argon atmosphere as well after immersion in heptane, the last could fill the porosity but not swell the membrane. After removing the buoyancy of the heptane, the density of the membrane can be calculated with following equation:

$$\rho = \frac{A}{A - B}(\rho_0 - \rho_L) + \rho_L$$

where A is sample weight in air, B is the sample weight in heptane, ρ_0 and ρ_L are the densities of heptane and argon respectively. The density of the SIPE70 membrane determined with this

method was 1.50 g cm^{-3}, while the apparent density calculated with geometric dimensions was 1.22 g cm^{-3} . Considering the density of PVDF-HFP is around 1.8 g cm^{-3}, and PEO based polymer is around 1.2 g cm^{-3}. The density of SIPE70 membrane calculated was within the expectation. The porosity of the SIPE70 membrane could be determined by:

$$porosity = 1 - \frac{V_{real}}{V_{geometric}} = 1 - \frac{\rho_{geometric}}{\rho_{real}}$$

Thus, the porosity of the SIPE70 membrane was calculated to be 18.7%, which seems coherent with the SEM image.

4.2 Thermal characterizations

To understand the thermal stability of the SIPEs, thermogravimetric analysis (TGA) was conducted. Pure mPEGME-PTFSIVE copolymer (SIPE100), membrane with 30% and 45% PVDF-HFP (SIPE70 and SIPE55) were examined separately under nitrogen gas with a temperature ascension rate of 10 °C min^{-1} from 25 °C until complete thermal decomposition. The thermograms are presented in Figure 43. All the samples showed good thermal stability, with negligible mass loss before 320 °C. If we define the decomposition temperature (T_d) as the point with 1 wt.% loss, the SIPE100, SIPE70, SIPE55 samples exhibited similar T_d of 324, 320 and 334 °C, respectively, which corresponds to the thermal decomposition of the mPEGME-PTFSIVE copolymer. The SIPE70 and SIPE55 samples exhibited another plateau between 390-470 °C which suggests the complete degradation of mPEGME-PTFSIVE. The PVDF-HFP then decomposes beginning from ~470 °C. The mass loss of the PVDF-HFP part was coherent to the ratio in the mixture. Thus, the SIPEs exhibited great thermal stability with a T_d > 320 °C.

The polymer electrolytes apparently have a huge advantage in terms of thermal stability with no evaporation and high T_d to avoid thermal runaway.

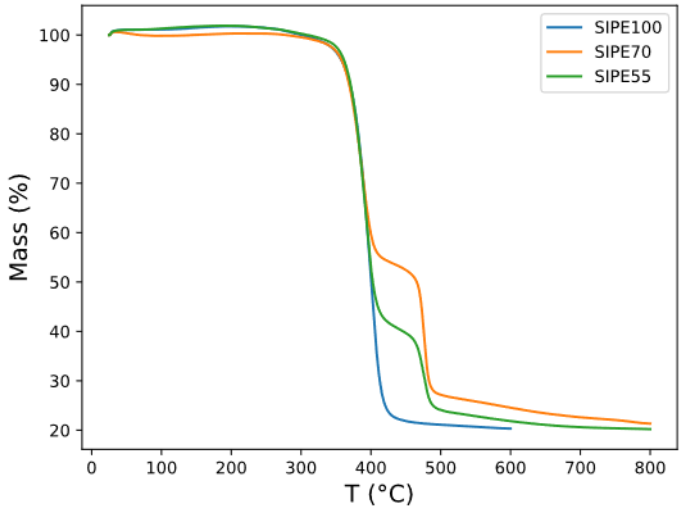

Figure 43. TGA Thermogram of the different SIPEs.

Differential scanning calorimetry (DSC) was applied to unveil the thermal responds of the electrolyte, especially glass and phase transitions. The DSC traces are shown in Figure 44. After blending with PVDF-HFP, the T_g of the mPEGME-PTFSIVE copolymer shifted from -55 (SIPE100) to -45 °C in both cases of SIPE70 and SIPE55. During all the tests (even the pure PVDF-HFP sample), the T_g of PVDF-HFP is missing (which is around -35 °C), which might require a quenching step. This increase suggests the blending with PVDF-HFP affects the chain mobility of the electrolyte. The melting point of the PVDF-HFP was found at ~140 °C which defined the higher temperature limit of the electrolyte membrane. By integrating the melting peak (PEG moiety in mPEGME-PTFSIVE copolymer) at 40 °C of the SIPE100, SIPE70 and SIPE55 samples, the area normalized by mass of SIPE is -9.9, -6.5, and -4.5 mW K mg^{-1}, which suggests that the blending with PVDF-HFP decreases the ability of PTFSIVE-mPEGME to crystalize. The observations on T_g and melting temperature suggest that the two polymers, although immiscible, have strong interactions. The microstructure can be further investigated by diffraction or scattering techniques such as X-ray diffraction (XRD) and small angle X-ray scattering (SAXS) in the future.

The melting temperature of PVDF-HFP is increasing from 121 to 125, 128 °C with 55, 70% SIPE, respectively. And the normalized (by mass of PVDF-HFP) melting area was -3.1, -4.2, -5.2 mW K mg^{-1} with PVDF-HFP, SIPE55,SIPE70, respectively. This means the presence of

SIPE favored the PVDF-HFP crystallization.

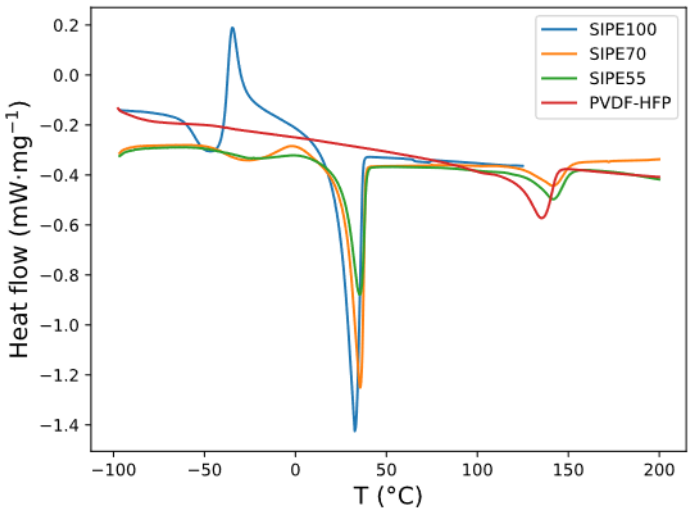

Figure 44. DSC traces of SIPEs and PVDF-HFP.

4.3 Ionic conductivity and transference number

Ionic conductivity measurements were carried out by EIS. For the pure mPEGME-PTFSIVE copolymer (SIPE100), a liquid cell with two parallel platinum plane electrodes was used. The liquid cell was calibrated with 0.01M KCl aqueous standard before use. For the polymer membranes (SIPE70 and SIPE55), a coin cell with SS|SIPE|SS configuration was used. The samples were kept in a Votsch VTM-4004 oven for temperature control. Between each measurement, a 1h interval time was taken to reach the isothermal state. The typical Nyquist plot obtained consists of one semicircle which corresponds to electrolyte resistance in parallel to its capacitance and followed by the line which is ascribed to the capacitance of the blocking electrodes. A typical Nyquist plot of conductivity cell is shown in Figure 45.

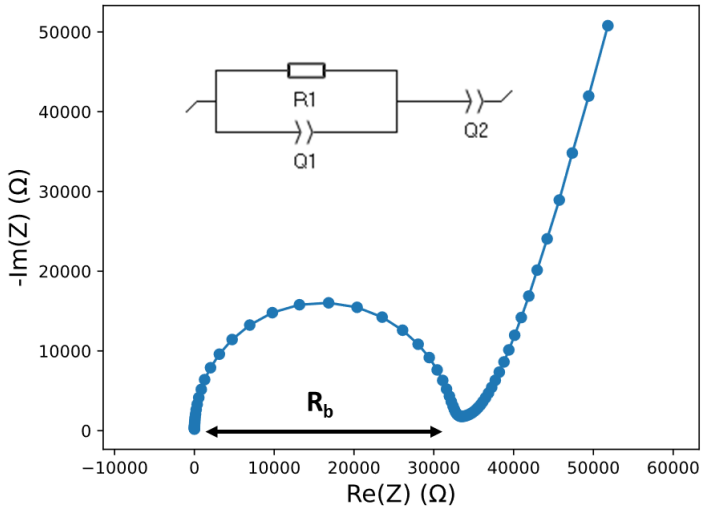

Figure 45. Nyquist plot of the SIPE100 at 90°C using blocking electrodes with its equivalent circuit. The resistance of the electrolyte can be determined by circuit fit of the semicircle.

The ionic conductivity was evaluated with the following equation:

$$\sigma = \frac{l}{R_B \cdot A}$$

where l is the thickness of the electrolyte, R_B is the bulk resistance and A is the area of the electrode. The pure mPEGME-PTFSIVE exhibited a high conductivity of 5×10^{-5} S cm^{-1} at 90 °C. After blending with non-conductive PVDF-HFP to form membrane, the conductivity was decreased to 3×10^{-5} S cm^{-1} and 8×10^{-6} S cm^{-1} for SIPE70 and SIPE55, respectively. The decrease in ionic conductivity could be explained by the increase of non-conductive PVDF-HFP phase, as well as increase of ionic tortuosity. In the case of SIPE70, the conductivity loss was almost proportional to the amount of PVDF-HFP. However, for SIPE55, the conductivity loss was more significant, suggesting both the percolation of the ionic pathway was poor and high tortuosity.

To better present the trend of the conductivity improvement with increasing temperature, the conductivity was plotted in semi-log graph in Figure 46. For polymer electrolytes the semi-log graph of the conductivities usually shows a nonlinear behavior which can be explained by the VTF model. For all the three SIPEs, VTF-type behavior was observed.

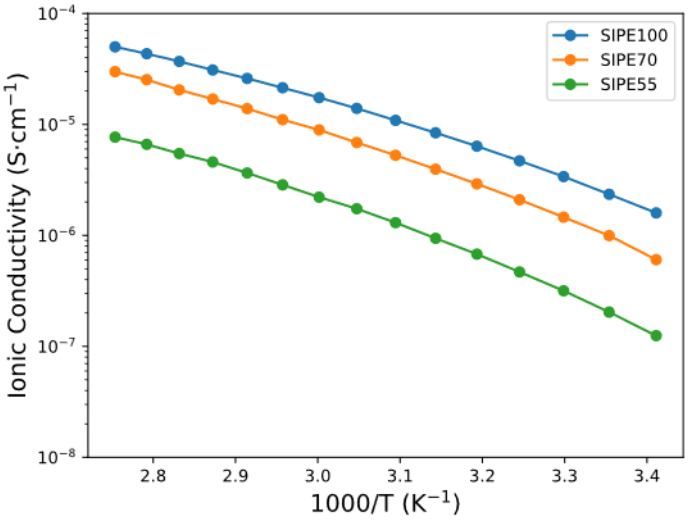

Figure 46. Conductivities of SIPEs versus temperature.

To further understand the VTF type of activation, the conductivity-temperature relation was fitted with the equation below.

$$\sigma = \sigma_0 \cdot T^{\frac{1}{2}} \cdot e^{-\frac{E_a}{K_b \cdot (T - T_0)}}$$

where, σ_0 is the pre-exponential factor which related to the number of charge carriers, T_0 is the polymer ideal transition temperature with zero configurational entropy, E_a is pseudo-activation energy and K_b is the Boltzmann constant. All the three curves were successfully fitted to the VTF model with R^2 >0.99, which suggest that the conductivity of the SIPE is strongly correlated with the polymer segmental motion. The VTF fitting parameters are listed in Table 3. Notably, the fitted σ_0 of SIPE55 is much smaller than the other two samples, which could explain the much lower ionic conductivity of the SIPE55. With 45 wt.% of non-conductive PVDF-HFP, the percolation of the ionic conductive phase might be much worse (high tortuosity) than the other two samples and reflected as a low concentration of effective charge carrier and low σ_0.

Table 3. VTF parameters obtained by fitting.

Electrolyte	σ_0 (S cm^{-1} K$^{-0.5}$)	T_0 (K)	E_a (kJ mol^{-1})	E_a (eV)
SIPE100	0.208	187	7.86	0.0810
SIPE70	0.273	184	9.22	0.0950
SIPE55	0.058	195	8.33	0.0858

The lithium-ion transference number was determined electrochemically with three methods: DC polarization, the Bruce-Vincent method, and the Watanabe method. The lithium-ion transference number can be determined by a chronoamperometry polarization with a small potential bias:

$$T_{Li}^{+} = \frac{I_{ss}}{I_0}$$

I_0, I_{ss} is the initial and steady-state current during the chronoamperometry polarization. This method also has been modified by considering interfacial resistance evolution during the polarization. It can be calculated by the equation:

$$T_{Li}^{+} = \frac{I_{ss}(V - I_0 R_0)}{I_0(V - I_{ss} R_{ss})}$$

where V is the bias potential. R_0, R_{ss} was the interfacial resistance of the initial and steady-state. In most cases, the determination of initial current I_{ss} depends on the respond of the device, thus it can be difficult to measure. The Watanabe method is using impedance information to estimate the initial current and thus avoid the error from the measurement. The T^+ can be calculated by the following equation:

$$T_{Li}^{+} = \frac{R_b}{\frac{V}{I_{ss}} - R_e}$$

where R_b is the bulk resistance and R_e is the charge transfer resistance or the interfacial resistance.

The chronoamperometry polarization and EIS spectra of Li|SIPE70|Li cell is shown in Figure 47 and Figure 48.

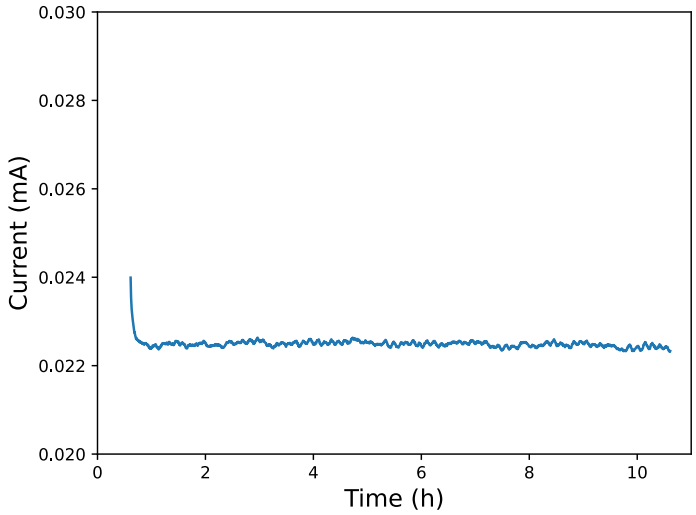

Figure 47. Chronoamperometry polarization of Li|SIPE70|Li cell with bias voltage of 20 mV.

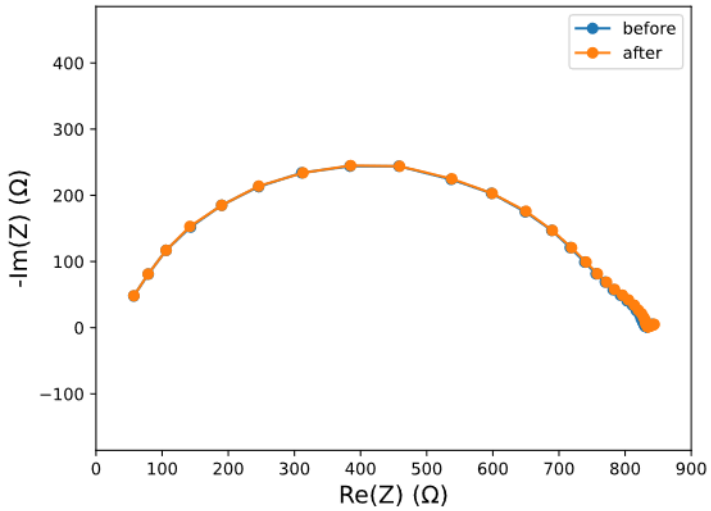

Figure 48. EIS spectra of Li|SIPE70|Li cell before and after the polarization, 7 MHz to 100 mHz.

The current went through a quick drop at the very beginning of polarization and then stabilized at a constant current. The EIS before and after 10 h of polarization gave nearly identical results, suggesting stable SIPE-lithium interface has been achieved. However, the bulk response and

SEI response overlapped. The electrolyte and interphase (SEI) contributions were determined with the help of an electric circuit model in Figure 49. In the circuit, R1, R2 and R3 represent the wire resistance, bulk resistance of the electrolyte and the SEI resistance, respectively. Q2 and Q3 are the constant phase elements of the electrolyte and interphase. The fitting results are given in Table 4.

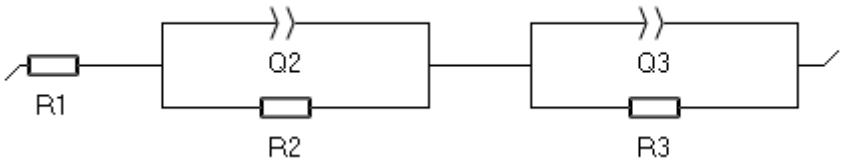

Figure 49. Equivalent circuit model for the Li|SIPE|Li cell system.

Table 4. EIS fitting results of Li|SIPE70|Li cell before and after the polarization.

	R1 (Ω)	R2 (Ω)	R3 (Ω)	Q2 (F $s^{-0.2}$)	Q3 (F $s^{-0.2}$)
Before	38	705	85	10.33×10^{-9}	1.392×10^{-6}
After	38	706	85	10.30×10^{-9}	1.361×10^{-6}

With all the three methods discussed before, the lithium transference number of SIPE70 was calculated as 0.93, 0.92 and 0.87, respectively. The single ion conducting nature of the linear SIPE was well addressed by this high lithium transference number.

4.4 Comparison with state-of-art solvent-free SIPEs

To evaluate this work, the comparison with the solvent-free SIPE reported in the literature is shown in Table 5. The comparison was consisted of three distinct aspects of properties, which are glass transition temperature, the conductivity (at a certain temperature), and the lithium transference number. These properties mainly represented the charge transport behavior of the SIPE. The PTFSIVE-mPEGME copolymer showed comparable ion transport behavior compared to state-of-art results.

Table 5. Comparison of the solvent-free SIPEs

Name of electrolyte	T_g (°C)	Conductivity (S cm^{-1})	Testing temperature (°C)	T_{Li^+}	Ref.
PEO-PSLiTFSI	160 (PSLiTFSI)	3.8×10^{-4}	90	0.95	[11]
PS-b-P(MALi-co-POEGMA)	-70	10^{-8}	20	~1	[12]
LiPSsTFSI / PEO	44.3	1.35×10^{-4}	90	0.91	[13]
LiBC-1	-61	2.3×10^{-6}	25	0.83	[14]
LiMTFSI-PEO-LiMTFSI	95 (LiMTFSI)	10^{-4}	70	0.91	[15]
P(STFSILi)-PEO-P(STFSILi)	-	1.3×10^{-5}	60	0.85	[16]
PEOMA-TFSI$^-$Li$^+$	-17	4.73×10^{-5}	90	0.99	[17]
LiPBPAB / PEO	-	1.7×10^{-4}	60	0.96	[18]
LiPCSI / PEO	-4.5	7.3×10^{-5}	60	0.84	[19]
poly[TMC_n-b-(LiM_m-r-$PEGM_k$)]	-49, -16	4×10^{-6}	70	0.91	[20]
PTFSIVE-mPEGME	-55	5.01×10^{-5}	90	0.9	This work

4.5 Electrochemical stability

The electrochemical stability of the electrolyte was studied by cyclic voltammetry with Li|SIPE70|stainless steel cells. The stainless-steel acts as the working electrode and lithium metal acts as both counter and reference electrodes. Firstly, the cell was examined from OCV to 4 V and scanned back to -0.5 V (*vs*. Li/Li^+) for three cycles with a sweep rate of 0.2 mV s^{-1}. The CV traces are displayed in Figure 49-51.

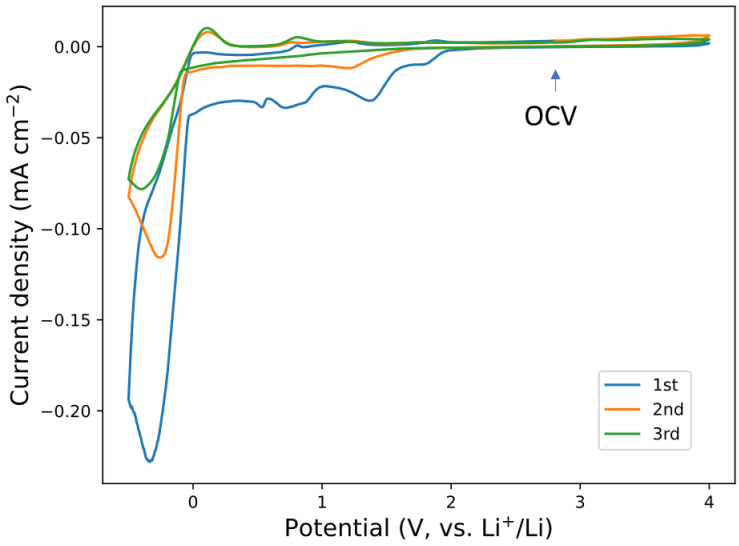

Figure 49. CV trances of the Li|SIPE70|SS cell, swept from -0.4 – 4.0 V.

The determination of the electrochemical stability consisted of two processes, i.e., a cathodic and an anodic scan in a first step conducted for the same cell. The OCV of the Li|SIPE70|SS was around 2.5-3 V and depends on the surface composition of the stainless steel. Starting from OCV, the cell was polarized up to 4.0 V with no obvious oxidation. Subsequently, the anodic scan was carried out, which exhibited irreversible reduction peaks at ~1.5 and 1.0 V. A strong reduction peak was observed between 0 to -0.5 V, which is ascribed to lithium plating on the stainless-steel surface. To our surprise, the stripping of lithium was very suppressed, which could suggest that the lithium metal plated on the stainless-steel electrode in the previous step reacted with the electrolyte. In the CV process, the amount of lithium plated on the working electrode is very small (0.11 mAh cm^{-2} for the 1st cycle, 0.03 for the 3rd cycle), which could be due to the mass transport limitation (because of low Li^+ content in SIPE). This small amount of lithium deposition could be largely consumed by the initial side reaction and reflected as low CE. Although the amount of lithium plated largely decreased upon cycling, the overall reversibility of the lithium stripping/plating process was improved.

To further investigate the electrochemical stability, cathodic and anodic scan was performed separately, which can avoid the influence of degradation of oxidation in the following reduction process, vice versa.

The anodic scan between OCV and 4.0V was performed on a pristine Li|SIPE70|SS cell with a

scan rate of 0.2 mV s-1 for 10 cycles. The first scan showed some minor current evolving between 3.4 and 4.0 V, indicating some side reaction upon oxidation part. The following cycles showed a much more stable behavior and the intensity of the current decreases with cycling, which indicates a stabilization of the interface with the electrode.

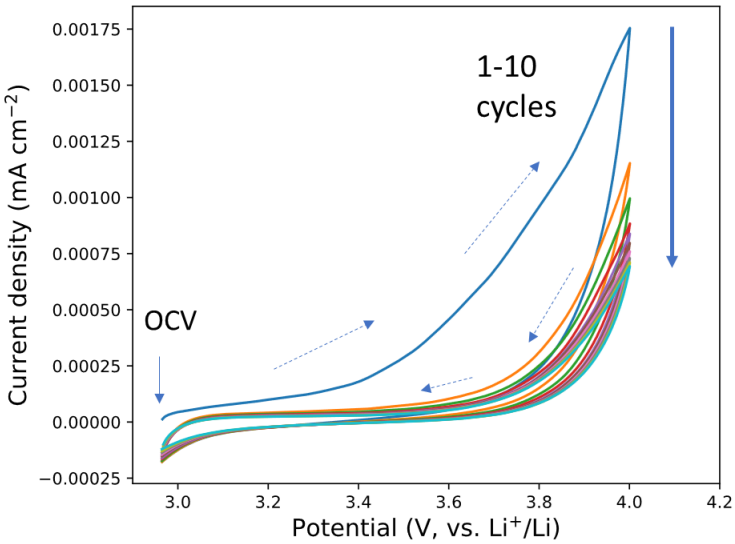

Figure 50. CV traces of the Li|SIPE70|SS cell form OCV to 4.0 V.

Similarly, cathodic scans were conducted on another cell between 0 V and OCV to avoid lithium plating/stripping and observe any potential side reaction(s) only. The first cycle showed a strong reaction between 0 -1.5 V which could be associated with the formation of a passivation layer, and then the intensity of the reaction decreased in the following cycles. Additionally, a pair of small peaks could be observed at 0.5 and 0.8V, which seem to be reversible. These tiny peaks could be associated with the presence of oxides on the surface of the working electrode.[21]

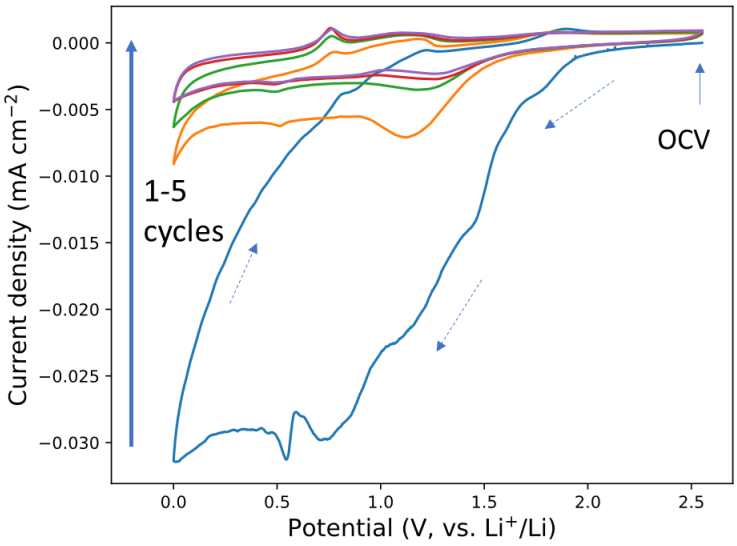

Figure 51. CV traces of Li|SIPE70|SS cell form 0 V to OCV.

The CV tests unraveled that the SIPE shows some irreversible side reaction between 0 and 1.5 V in the first cycle, while the interface stabilized in the following cycles. The lithium stripping/plating behavior in presence of the SIPE can also be investigated with symmetric Li||Li cells which is described in the following part.

5 Lithium stripping/plating tests

Lithium stripping/plating tests were conducted with symmetric Li|SIPE|Li cells, which are widely used to demonstrate the compatibility of the electrolyte with lithium metal electrodes. In this test, chronopotentiometric cycling was used to strip lithium from one electrode and plate it on the other one. The morphology of the lithium metal will be strongly altered due to this stripping/plating process, which could lead to an inhomogeneous SEI formation, the “dead lithium” and potential lithium dendrite growth. These instabilities could be reflected from the overpotential of the cell. EIS was conducted after each step to monitor the resistance evolution during the cycling. The profile of lithium stripping/plating is shown in Figure 52.

By increasing the current density stepwise from 10, 50, and 100, to 150 μA cm^{-2} (corresponding capacity: 0.04, 0.2, 0.4, 0.6 mAh cm^{-2}), the cell remains stable for more than 700 h at 80 °C without any sign of an instable interface or dendrite formation.

At 150μA cm^{-2}, the capacity of the lithium deposited and removed was 0.6 mAh cm^{-2},

corresponding to ~3 μm of lithium metal , which is one the best result with SIPEs compared to commonly reported values of ~0.1 mAh cm^{-2}.[22,23]

The evolution of the cell voltage during the lithium plating and stripping at 10 and 150 μA cm^{-2} is shown in Figures 52 B and C. The cell showed good stability during all the current densities, no short circuit was observed for more than 700 h. Even at high current densities, the potential remained constant and showed an almost perfect rectangular shape without any increase in potential or fluctuation, which indicates homogenous stripping and plating of lithium without concentration polarization, evolution of the SEI interphase and dendrite formation. This shape confirms the single-ion conductivity of the polymer electrolyte and the benefit of such electrolyte design. In addition, the EIS performed during the stripping/plating test (Figure 53) suggest that the solid electrolyte interface went through a stabilization at the beginning of each current density and then remained stable. Each time with the increase of the current density, the increase of the resistance is more related to the bulk resistance rather than SEI resistance, which may be due to the morphology change during the plating/stripping which leads to contact issues. Additionally, the interfacial resistance was small (~ 65 Ω) during the lithium plating/stripping, which reflected a conductive interphase between the Li electrode and the SIPE.

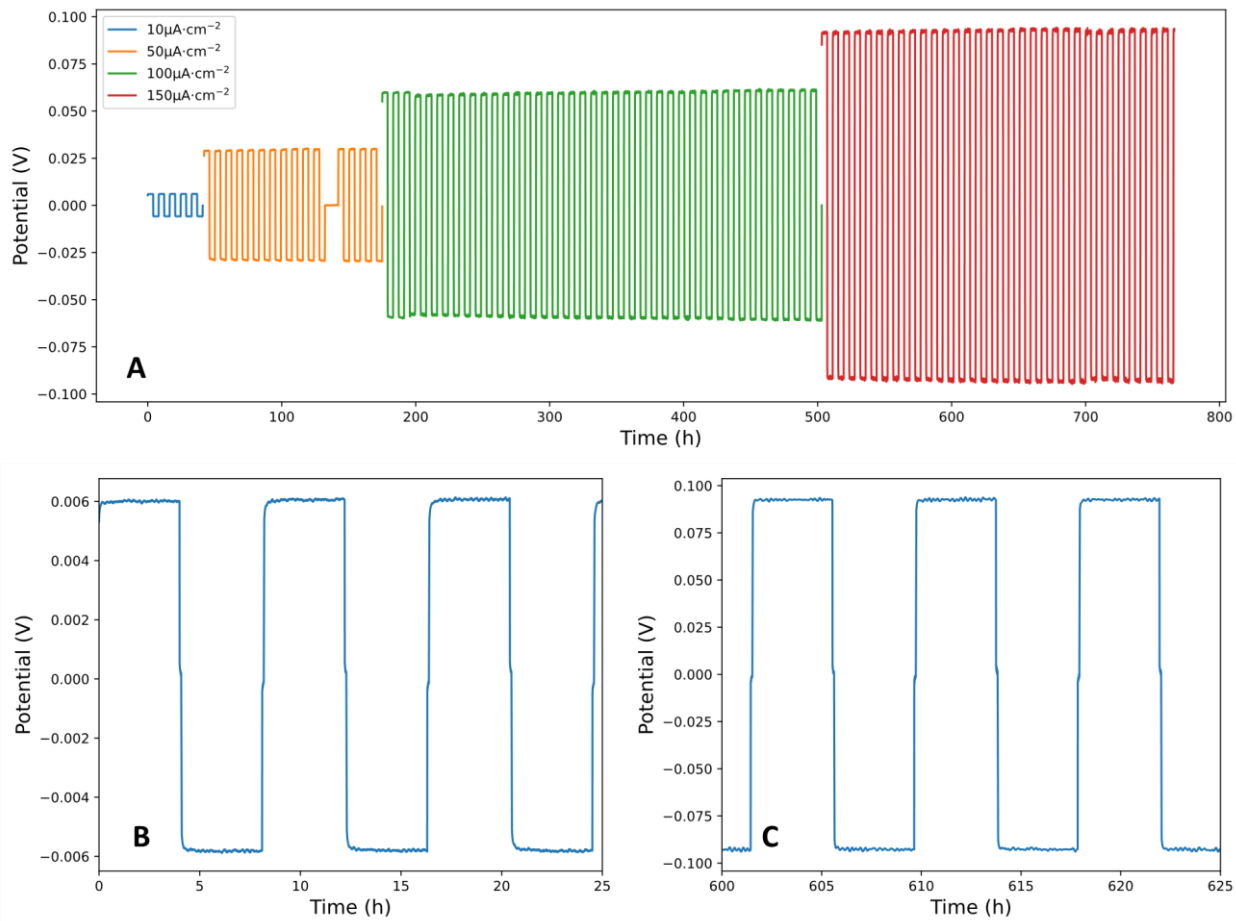

Figure 52. Lithium stripping/plating test symmetric of Li|SIPE70|Li cells at 80 °C. (A) Li plating/stripping test with varying current density; (B) magnified regions of the lithium stripping/plating test from 0-25 h, with a current density of 150 μA cm^{-2}; (C) magnified regions of the lithium stripping/plating test from 600-625 h, with a current density of 150 μA cm^{-2}.

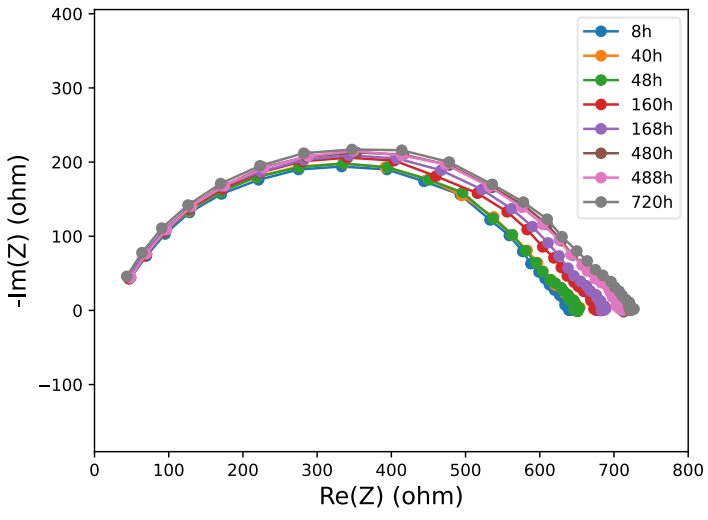

Figure 53. EIS spectra of the Li|SIPE70|Li cell recorded during the lithium stripping/plating test.

The determination of the critical current density was conducted with a plating/stripping test with step increase of current density from 10 to 500 μA cm^{-2}. The potential of each step was shown in Figure 55. By simple removal potential of the ohmic drop contribution (corresponding to 420 Ω of electrolyte bulk resistance, measured after the plating/stripping test), the overpotential that drives the lithium plating/stripping showed a severe increase starting from a current density of ~400 μA cm^{-2}. The increase in polarization greater than the ohmic drop indicates a sluggish charge transfer at the interface, potentially owing to the depletion of Li^+ in the interphase.[24] This phenomenon of Li^+ depletion can also be confirmed by the shape of the potential-time curve in Figure 54. The potential obtained before a current density of 400 μA cm^{-2} could stabilize rapidly and maintain its essentially rectangular shape. For current densities higher than 400 μA cm^{-2}, the overpotential increases during time and cannot stabilize during the 1h test, indicating an increase of the polarization during the test. More importantly, during all the tests, the cell did not show any sign of short circuit.

These excellent results proved that the electrolyte is compatible with lithium metal electrodes and allowed us to continue to examine the electrolyte in an LMB setup with positive electrode materials.

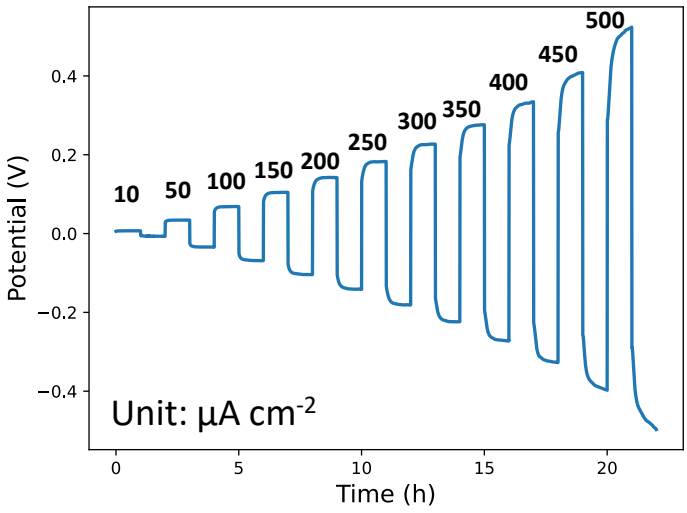

Figure 54. Lithium plating/stripping with an increasing current density.

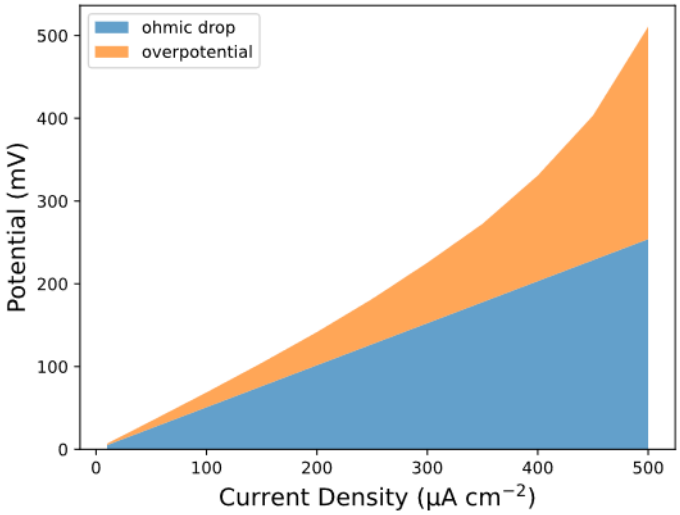

Figure 55. The overpotential during the Li plating/stripping tests with an increasing current density.

6 Evaluation in LMB

All the characterizations of the linear electrolytes have already proved that it seems to be possible to apply the SIPE70 in battery systems. Thus, LMBs with a LFP positive electrode were prepared and tested to examine the performance of such system with the SIPE electrolyte. The LMBs with LFP could be a good reference to evaluate the performance of SIPE since it is the most used positive electrode in the SIPE studies.

Other than LFP, organic perylene based polyimide PTCI has also been tested with this SIPE.

6.1 LFP Electrode Preparation

The electrode preparation is extremely important in solid-state batteries. Unlike liquid electrolytes, the polymer electrolyte cannot flow and infiltrate the electrode by just dropping it onto the electrode. To reach enough ionic conductivity inside the electrode, the linear mPEGME-PTFSIVE copolymer must be added directly during the elaboration of the electrode, which ensures the ionic transport from the active materials to the electrolyte and reversed.

Thus, the LFP active material, carbon black, PVDF and mPEGME-PTFSIVE copolymer were mixed with a mass ratio of 60:10:5:25. The mixture was dispersed in *N*-methyl-2-pyrrolidone

(NMP) by using mortar and pestle to form a homogeneous slurry. The slurry was cast on carbon coated aluminum foil serving as the current collector by doctor blade system and dried in an oven at 60 °C for 24 h. Then the electrode was cut into discs of 12 mm diameter and calendared to reduce porosity.

The average LFP mass loading was around 1.5 mg cm^{-2}.

6.2 LMB assembly

LMB cells comprising LFP positive electrodes were assembled with CR2032-type coin cells in an argon filled glovebox by sandwiching the SIPE70 membranes between the LFP-based positive electrode and lithium metal.

The coin cells were transferred to an isothermal chamber set to 80 °C and were allowed to rest for 6 h before the testing.

Firstly, the rate capability was investigated to evaluate the specific capacity at different current densities. Galvanostatic cycling was applied with current densities of 8.5, 17, 34, 85 and 170 mA g^{-1} , which corresponds to a C rate of C/20, C/10, C/5, C/2 and 1C (1C = 170 mA g^{-1}), respectively. Eventually, the current density was decreased again to 17 mA g^{-1} (C/10), and the battery was cycled for 10 additional cycles. The specific capacity and Coulombic efficiency (CE) are shown in Figure 56 and the corresponding charge/discharge profiles are presented in Figure 57.

The cells started with three slow cycles of C/20 with voltage limits of 2.5 and 3.7 V to form and stabilize the SEI layer at the lithium interface. The first charge exhibited a high specific capacity of 160 mAh g^{-1} which is very close to the theoretical capacity of LFP (~170 mAh g^{-1}). The first cycle CE was 97.2%. Here the CE is defined as charge capacity/discharge capacity.

After the three cycles at C/20, the cell was tested at C/10 for 10 cycles and exhibited a specific capacity of 159 mAh g^{-1}, close to the one obtained at C/20. The capacity decayed to 152.5 mAh g^{-1} after the 10^{th} cycle. Then the current density was increased to C/5, C/2, and C for 10 cycles each and the cell exhibited a specific capacity of 150, 144 and 136 mAh g^{-1}, respectively. The decline of the capacity is due to kinetic or mass transport limitation) and increased polarization from the increased current density which leads to an incomplete lithiation/delithiation of the

active material.

At last, the test was carried out at C/10 again to check if the capacity decline is reversible or not which yielded a capacity of 148 at the 44th cycle. The capacity of the 44th cycle can be considered as the result of a linear decay during the cycles 14-43 and is consistent with the previous C/10 cycle losses.

The cell demonstrated an overall average CE of 99.5% during the C rate test (including the first cycle). Noticeably, the cycles at higher current densities exhibited better CE than the cycles at C/20 and C/10. This is a common behavior in most battery tests and could be ascribed to the less degradation from high C rate due to the short time at elevated potentials, which lead to most of the degradation of the electrolyte.

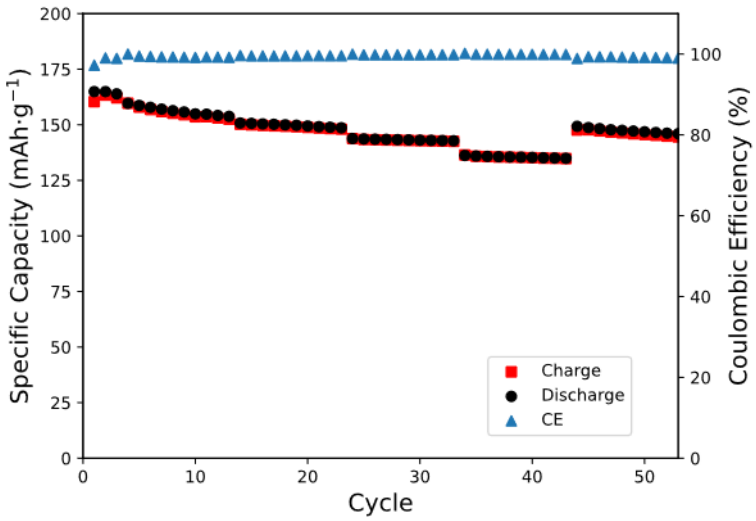

Figure 56. C rate test of Li|SIPE70|LFP cells at 80 °C.

The charge/discharge profiles showed a long flat characteristic plateau of the LFP material. At C/20 the end of the plateau showed a sharp end suggesting a complete reaction. However, at higher C rates, a slope was observed at the end of charge/discharge, which suggests that part of the lithium in the active material is less easily accessible and requires stronger driving force. The polarization of the cell can be estimated by the dis-/charge hysteresis, i.e., the voltage difference between charge discharge at the point of 50% capacity (midpoint of the plateau). The differences at C/20, C/10, C/5, C/2, and C were 37, 50, 76, 153 and 285 mV. These voltages

follow a perfect linear trend with corresponding current densities, which suggests the impedance of the cell at 50% of state of charge (SOC) was stable also at the increased current densities as shown in Figure 58. However, the capacity of the cell does not follow a linear relationship with polarization (associated with ohmic drop), especially in the low C rate region.

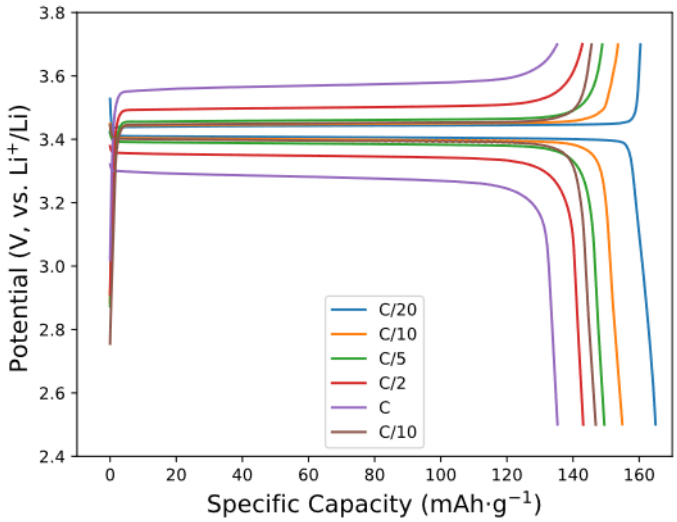

Figure 57. Charge/discharge profiles of Li|SIPE70|LFP cells subjected to a C rate test.

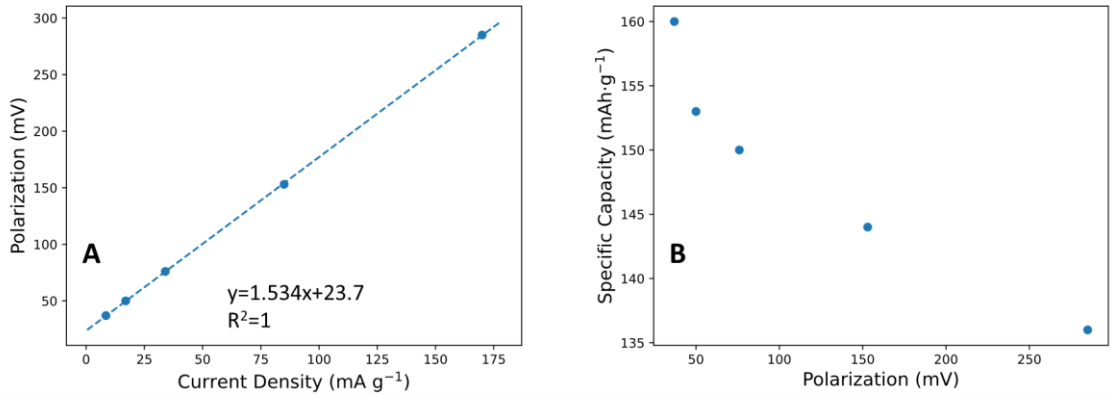

Figure 58. (A) Polarization *vs*. current density (B) Specific capacity *vs.* polarization of Li|SIPE|LFP cell subjected to a C rate test.

The C rate test has fully demonstrated that the Li|SIPE70|LFP cell has an excellent capacity retention at low current density and the capacity loss from increased C rate is moderate and reversible. These results reflect the good ionic conductivity of the electrolyte and fast ion

transport.

The durability of the cell was examined with a typical Li|SIPE70|LFP coin cell at 80 °C, which is shown in Figure 59 and 60. The cell was stabilized with 3 formation cycles at C/20 and then cycled at C/2 for more than 100 cycles. The specific capacity at C/20 was 158 mAh g^{-1} and at the beginning of C/2 was 155 mAh g^{-1}. Capacity retention after 100 cycles is 86% with an average CE of 99.7%. The capacity decay remains linear before 80 cycles, and then an acceleration of degradation occurred. The sudden degradation could be due to the accumulation of multiple factors including contact between LFP particles to the electrode, lithium-SIPE interphase degradation inducing side reactions at the negative electrode and so on, which finally reflects the increase of cell resistance and capacity decay.

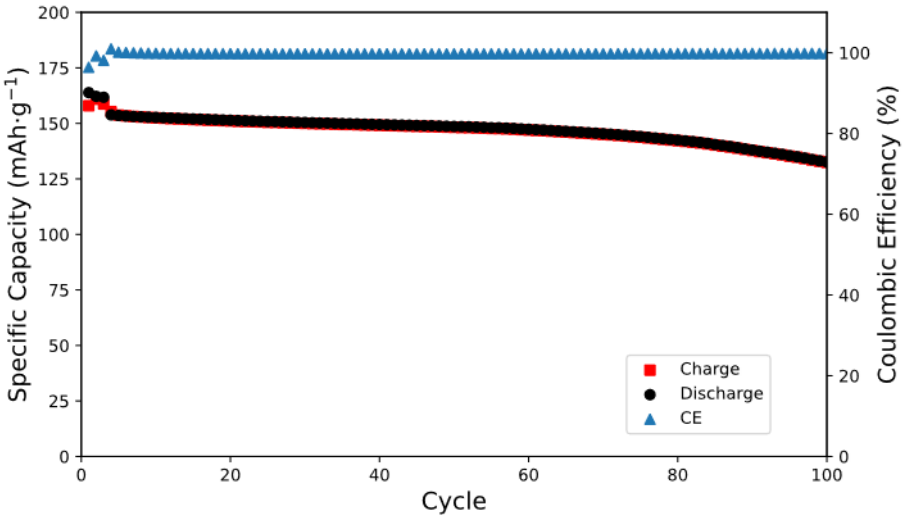

Figure 59. Cycling test of Li|SIPE70|LFP cell at 80 °C, 1-3 cycles at C/20, following cycles at C/2.

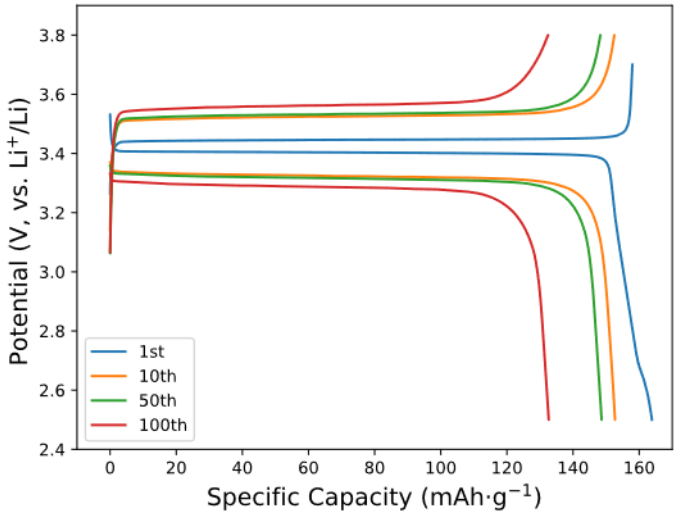

Figure 60. Charge/Discharge profile of Li|SIPE70|LFP cycling test.

Other than the cycling tests at 80 °C, the high ionic conductivity of SIPE70 allows us to perform cycling at 40 °C (Figure 61 and 62), which has never been reported with any solvent-free SIPE. A Li|SIPE70|LFP cell was cycled at C/20 for three formation cycles and then cycled at C/10 for more than 100 cycles. A significant overpotential was observed, due to the low ionic conductivity and Li^+ concentration. However, the battery showed a specific capacity of 145 mAh g^{-1} at C/20. At the beginning C/10, 129 mAh g^{-1} specific capacity was achieved and gradually improved to 151 mAh g^{-1} during 26 cycles, which is still competitive among state-of-art results. The increase of the capacity at the beginning could be attributed to improvement of contact between the electrolyte and the electrode during time. The cell at 40°C finally exhibited retention of 93% after 70 cycles with average CE of 98.7%. The cell showed a much higher polarization which is due to the lower conductivity of the SIPE at 40 °C.

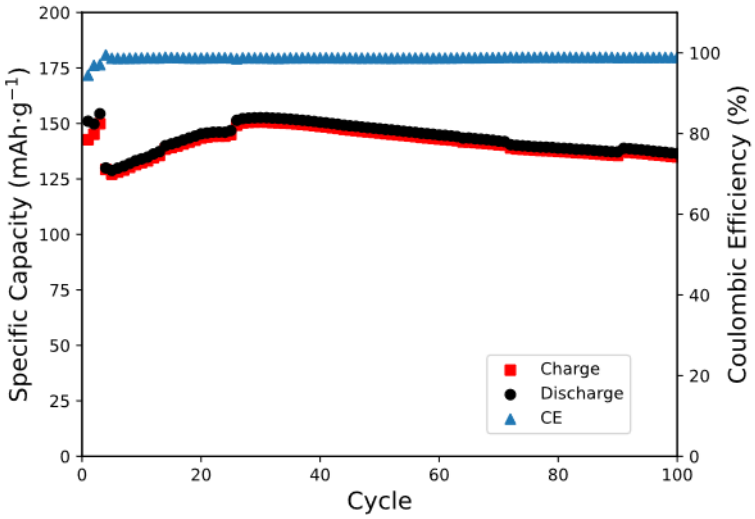

Figure 61. Cycling test of Li|SIPE70|LFP cells at 40°C, the first three cycles were conducted at C/20 and the following cycles at C/10.

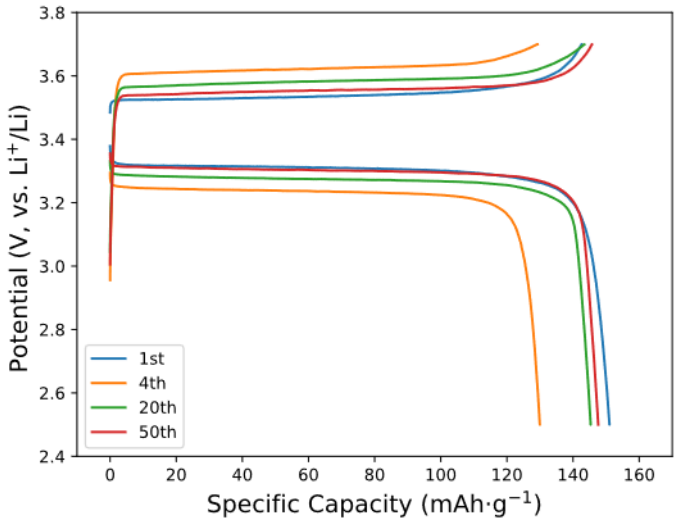

Figure 62. Charge/Discharge profiles of the Li|SIPE70|LFP cell at 40°C.

By comparison with six different results reported earlier, the PTFSIVE-mPEGME copolymer electrolyte showed the best capacity at higher temperatures together with the highest capacity retention after 100 cycles. Additionally, this is the only work that showed battery tests at 40 °C which also provided excellent battery performance even comparable to the other tests reported in previous studies and conducted at higher temperatures.

Table 6. Comparison performance of solid-state LFP battery

Name of electrolyte	T (°C)	Specific capacity (mAh g^{-1})	Cycle life (retention)	Ref.
PDMS−poly(STF−Li^+−r−PEGMA)$_{20}$	65	107 100th cycle at C/10	100 at C/10 (81.5)	[14]
LiBC-1	70	130 at C/15	100	[14]
poly[TMC$_n$-b-(LiM$_m$-r-PEGM$_k$)]	70	145 at C/20	>50 at C/20	[20]
LIPBPAB / PEO	80-50	147 1st cycle at C/25	>90	[18]
LiMTFSI-PEO- LiMTFSI	70	153 at C/10	300 at C/2 (77.8%)	[15]
LiPCSI/PEO	60	141 1st cycle at C/10	80 at C/10 (85.1%)	[19]
PTFSIVE-mEPGME	80	153 4th cycle at C/10	100(86%)	This work
	40	151 26th cycle at C/10	70(93%)	

6.3 Organic electrodes

As a new class of electrode materials, organic active materials such as quinone[25], have received

a lot of attention owing to its highly tunable properties and advantages concerning sustainability and accessibility, low cost, and toxicity.

However, they also suffer from several issues, including:

1) Solubility in organic solvent. The solubility of the active materials could lead to a loss of capacity.

2) Low electronic conductivity. Due to the nature of organic molecules, they are generally considered as insulators (except conjugated polymers).

3) Low density. Similar to electronic conductivity, the low-density issue is an intrinsic and universal issue of organic active materials, which limits its energy density.

The lack of electronic conductivity could block the electron transfer through the electrode to the current collector and eventually hinder the rate capability (due to the high resistance) and specific capacity (due to the accessibility of active material particles). Thus, in the preparation of organic electrodes, large amounts of conductive carbon filler are usually added, which leads to a low percentage of active material and low average density and capacity, which is unfavorable for the battery application.

Polyimide is a new class of carbonyl organic active materials.[26,27] Among them, poly(N-n-hexyl-3,4,9,10-perylene tetracarboxylic)imide (PTCI) has been proven to have both suitable electrochemical and thermal stability.[28–30] The perylene core could self-assemble into a layered structure due to the strong π-π stacking interaction between the aromatic rings and reduce the solubility of the product.

The redox reaction of PTCI material has been reported by Iordache et al., which is shown in Figure 63.

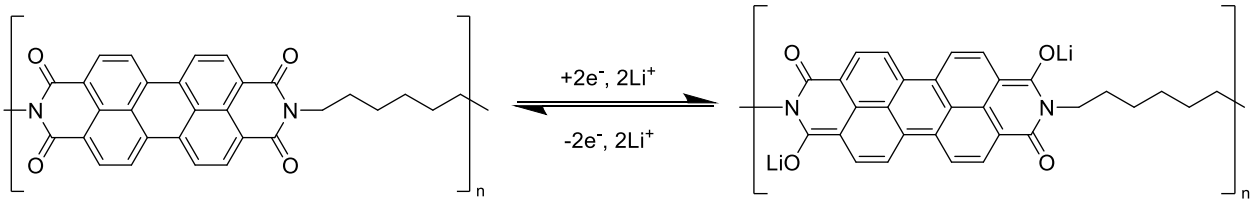

Figure 63. Lithiation/delihiation reaction of PTCI.

Theoretically, all the four carbonyl groups could be lithiated for the transformation into an enol, which provides high theoretical capacity. However, in reality only 2 of the 4 carbonyl groups are involved in the reaction, since the transition from di-lithiated PTCI to tetra-lithiated PTCI is rather irreversible.[31,32] Similar irreversibility has also been reported for other polyimide materials.

The theoretical specific capacity of the PTCI material can be calculated by Faraday's law:

$$\frac{Q}{m} = \frac{Fv}{M}$$

where m is the mass of the substance, M is its molar mass, Q is the charge, v is it the number of the electron and F is Faraday constant which is 26.801 Ah mol^{-1}. In this case, for 1 g of PTCI, the v is 1 for Li^+ and for the repeating unit of PTCI, M is 474 g mol^{-1}. Thus, for the 1 electron reaction, the specific capacity of PTCI is 57 mAh g^{-1}. If the reaction is as predicted, which consists of 2 electrons exchange, the theoretical specific capacity should be 113 mAh g^{-1}. However, in both the literature and our test with different electrolytes, PTCI did not reach the theoretical capacity. The typical capacity was between 60-90 mAh g^{-1},[28] which suggests that the second lithiation reaction remained incomplete.

The ratio of the active material, carbon black, PVDF and mPEGME-PTSIVE copolymer was 60:15:5:20. All the ingredients were mixed with mortar and pestle with NMP to form a homogeneous slurry and cast on carbon coated Al foil with a doctor blade. The electrodes were dried in an oven at 80 °C overnight. The electrodes were calendared before use to reduce the porosity. The typical active material mass loading was 1.4-1.7 mg cm^{-2}.

The electrodes were examined by SEM images (Figure 64). On the pristine electrode, a rough surface and cracks could be noticed. From the analysis of the cross section some delamination was observed due to the insufficient adhesion between the current collector and the electrode. The crack and delamination issues were improved by calendaring the electrodes. With magnified images, the microstructure in the composite electrode was shown in Figure 64 F. The PTCI particles with flake shape which aggregated into nacreous-like structure and the small particles were the carbon fillers. In Figure 64 E, which is the cracking part, filament structure

could be observed, which is ascribed to the polymer binders.

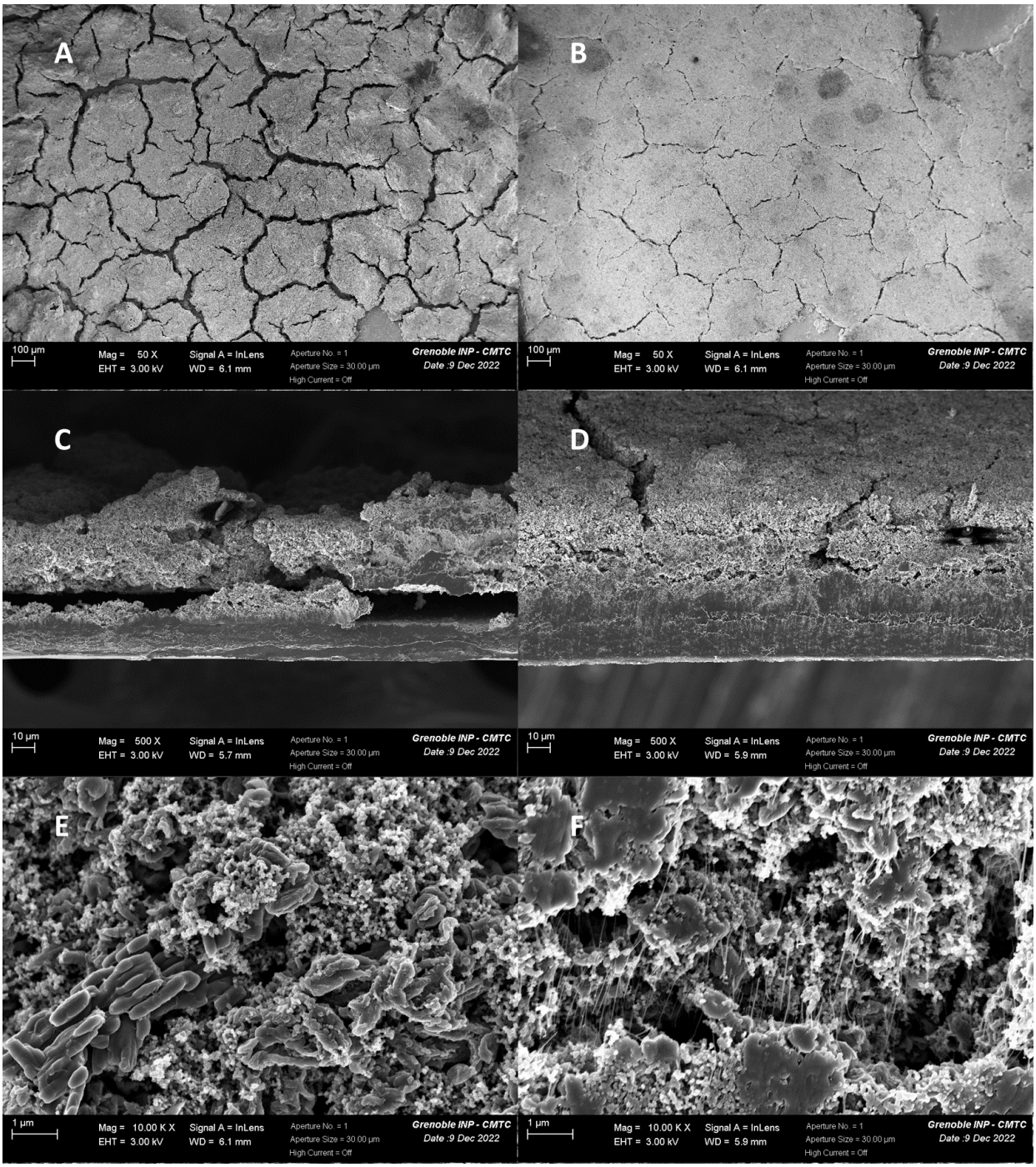

Figure 64. SEM images of the PTCI electrodes: (A-B) top view of the PTCI electrodes before and after calendaring; (C-D) cross section of the PTCI electrodes before and after calendaring; (E-F) magnified image of the active materials.

Although the quality of the pristine electrode is not ideal because of the high porosity and cracking, the electrode after calendaring could be used in the battery test as a prototype cell,

which is shown in Figure 65 and 66.

Organic lithium metal batteries were tested with PTCI electrode materials in coin cells. The rate capability was investigated by applying a varying specific current of 10, 20, 40, 60, 80 and 100 mA g^{-1}, each for 10 cycles. Specific charge capacities of 90, 87,82, 75, 69, and 61 mAh g^{-1} were observed, which is generally in good agreement with the previous studies using a liquid electrolyte.[28]

However, the Coulombic efficiency of the cell is not as good as expected. As the organic positive electrode material is not lithiated, the Coulombic efficiency could be defined as charge capacity divided by discharge capacity. Overall, average Coulombic efficiency calculated was 97.2%.

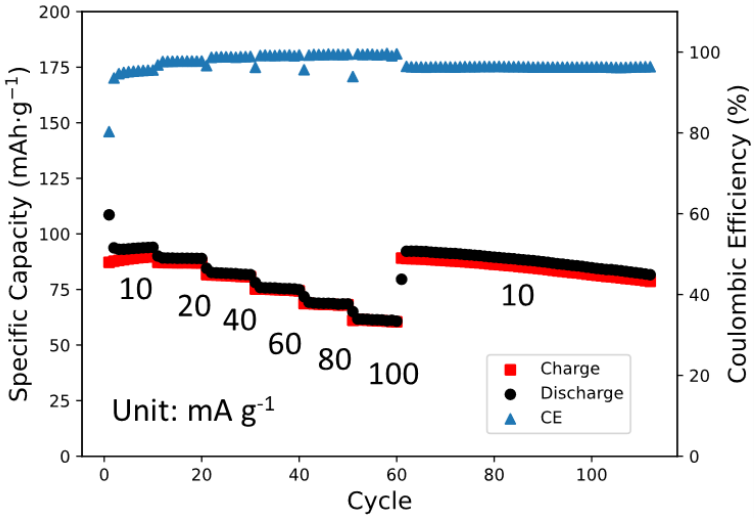

Figure 65. Rate capability test of Li|SIPE70|PTCI battery at 80 °C.

As shown in Figure 65, the polarization upon charge/discharge increases during the rate capability test, which leads to a decrease in capacity. The first cycle showed a different shape with significantly more discharge capacity than charge. This phenomenon has been observed in all the tests with PTCI electrodes suggesting the occurrence of irreversible side reactions during initial cycle. For different current densities, the capacity differences were due to the polarization (defined as voltage difference at 50% capacity) of the cell, which is confirmed in Figure 67, where the polarization was proportional to the current density and capacity decrease. With the

linear extrapolation, I can see the y-intercept of polarization was 155 mV (with 0 current density), which reflects the voltage difference between lithiation and delithiation.

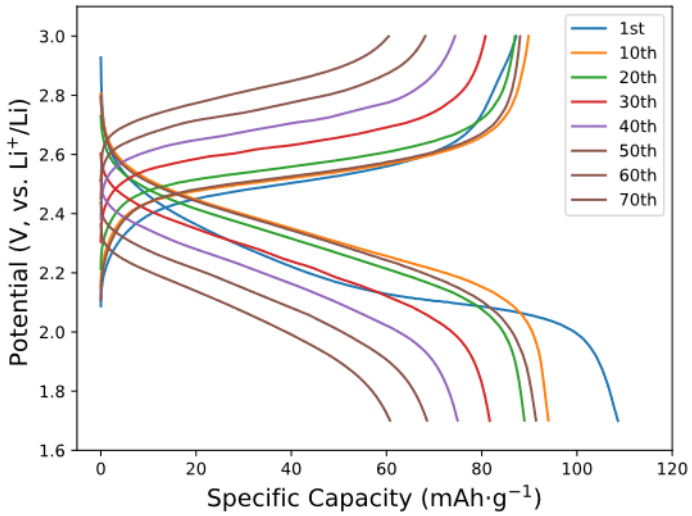

Figure 66. Charge/Discharge profile of Li|SIPE70|PTCI cell at 80°C at different C rate.

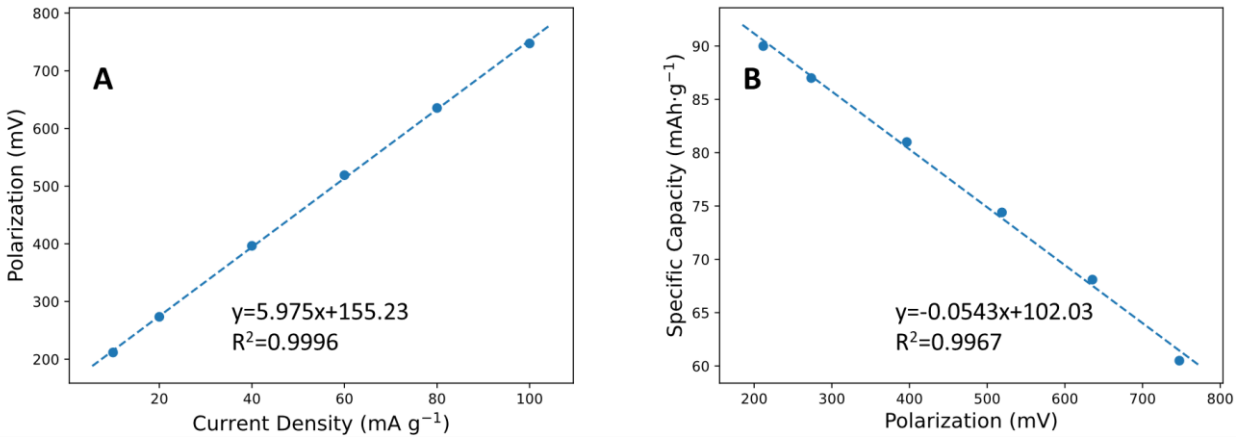

Figure 67. (A) Current density vs. polarization (B) polarization vs. specific capacity of Li|SIPE|PTCI cell in the C rate test.

CV was also conducted on a Li|SIPE|PTCI cell (Figure 68) to confirm the reversibility of the lithiation and delithiation processes. The reversing potential were set to 1.5 and 3.0 V with a scan rate of 0.04 mV s^{-1} for 10 cycles. The lithiation peak was first observed at 1.9 V and then shifted to 2.2V during the cycling, whereas the delithiation peak remained the same at 2.6 V.

The difference in potential and peak shape suggested an irreversible side reaction during the first discharge. The irreversibility disappeared in the following cycles, leading to a stable and reversible cycling of positive electrode.

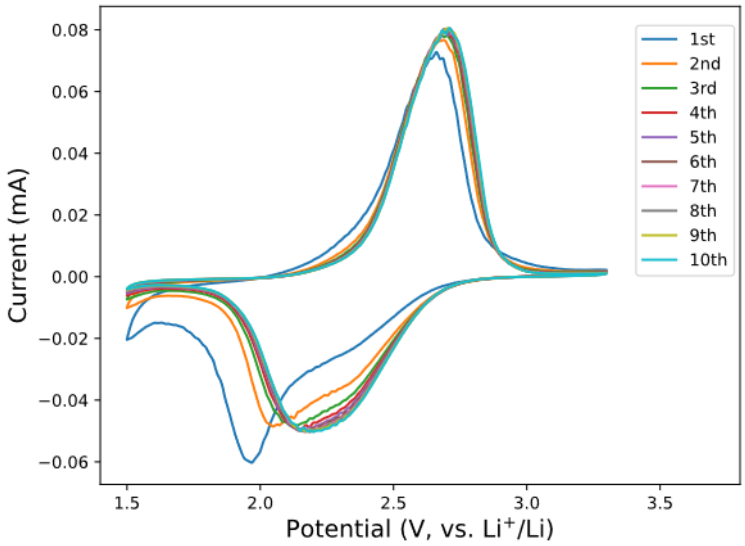

Figure 68. CV test of Li|SIPE70|PTCI cell at 80°C, with scan rate of 0.04 mV s^{-1}.

The specific capacity and Coulombic efficiency of the CV cell is plotted in Figure 69 by integrating the peaks. The cell showed a stable charge capacity during 10 cycles of ~95 mAh g^{-1}, which is higher than the value obtained from galvanostatic cycling. The first Coulombic efficiency was 78% and quickly increased to around 97% in the following cycles.

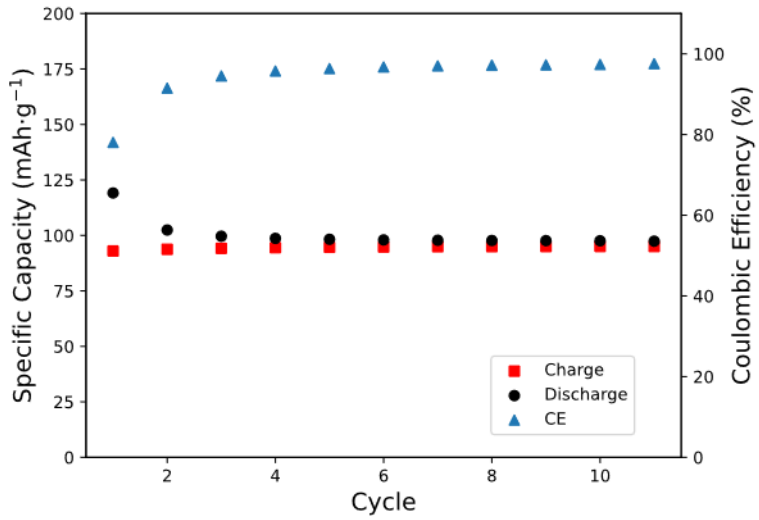

Figure 69. Specific capacity and Coulombic efficiency in the CV of Li|SIPE70|PTCI cell at

80°C.

Since it has been proved with LFP electrode that the electrolyte can exhibit enough ionic conductivity at 40°C for cycling the battery at low current density. Thus Li|SIPE|PTCI cell was also tested at 40 °C with current density of 10 mA g^{-1}. Due to the SIPE is less conductive at lower temperature, the polarization of the cell was more intense, thus I decreased the cut off voltage to1.5 V after the first cycle (due to the incomplete discharge to 1.7 V in the first cycle). The battery showed a stable specific capacity of ~56 mAh g^{-1} which is much lower than is at 80 °C. The average Coulombic efficiency was 97%. The shape of the charge/discharge profiles at 40°C showed exactly the same shape as the ones at 80 °C (except the more polarization), suggesting that temperature change does not alter the electrochemical behavior of the PTCI organic active material.

The battery cycled at 40 °C did not only show a good cycling stability, but also confirmed that the mPEGME-PTFSIVE copolymer could be used at 40 °C which is rare for solvent-free SIPEs.

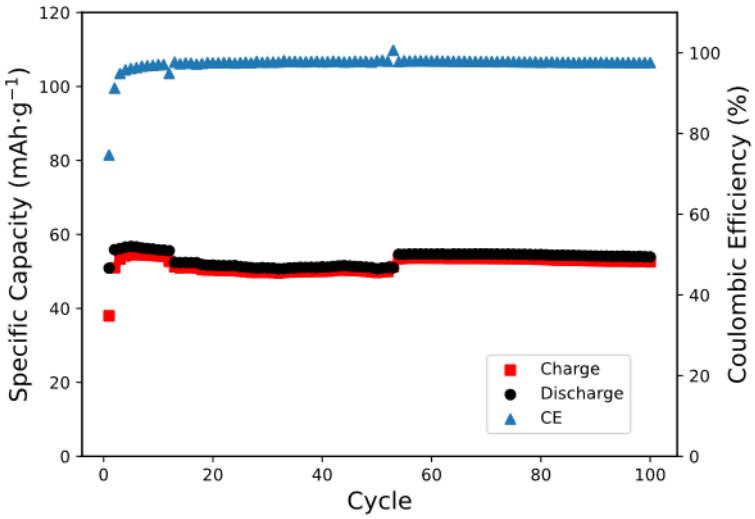

Figure 70. Specific capacity and CE of Li|SIPE70|PTCI cell at 40 °C.

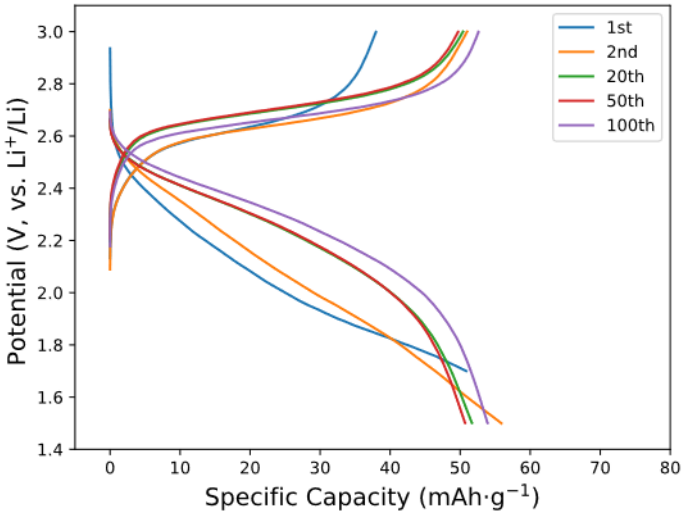

Figure 71. Charge/Discharge profile of Li|SIPE70|PTCI cell at 40 °C.

7 Conclusions

Three main aspects including electrolyte synthesis, electrolyte characterization and battery performance can be concluded:

(1) A novel single-ion polymer electrolyte was synthesized via donor-acceptor copolymerization of ionic vinyl ether and maleate monomers. The reaction yields a unique alternative copolymer with an A:D ratio of 2.

(2) By blending the copolymer with PVDF-HFP, self-standing, solvent-free polymer electrolyte membranes with high ionic conductivity and lithium transference number were achieved. These membranes exhibited excellent stability in contact with lithium metal electrodes in the lithium stripping /plating tests.

(3) LMB cells with LFP and PTCI positive electrodes have been cycled at 40 °C and 80 °C, showing a long-term stably cycling.

By comparing it to the state-of-arts results concerning solvent-free single-ion electrolytes, this material showed superior ionic conductivity and performance. These results revealed the potential of this well-designed single-ion polymer electrolyte for safe, stable, and sustainable LMB applications.

However, the insufficient mechanical strength of the mPEGME-PTFSIVE copolymer requires incorporating in polymer matrix such as PVDF-HFP affecting its conduction properties. In the

next Chapter, a self-standing PEO-based SIPE will be introduced to improve the concern.

Reference

1. Nishimori, K. & Ouchi, M. AB-alternating copolymers *via* chain-growth polymerization: synthesis, characterization, self-assembly, and functions. *Chem. Commun.* **56**, 3473–3483 (2020).
2. Motoyanagi, J., Oguri, A. & Minoda, M. Synthesis of Well-Defined Alternating Copolymer Composed of Ethylmaleimide and Hydroxy-Functionalized Vinyl Ether by RAFT Polymerization and Their Thermoresponsive Properties. *Polymers* **12**, 2255 (2020).
3. Fenimore, S. G., Abezgauz, L., Danino, D., Ho, C.-C. & Co, C. C. Spontaneous Alternating Copolymer Vesicles of Alkylmaleimides and Vinyl Gluconamide. *Macromolecules* **42**, 2702–2707 (2009).
4. Huang, Z. *et al.* Discrete and Stereospecific Oligomers Prepared by Sequential and Alternating Single Unit Monomer Insertion. *J. Am. Chem. Soc.* **140**, 13392–13406 (2018).
5. Yang, X. *et al.* Determining the limiting factor of the electrochemical stability window for PEO-based solid polymer electrolytes: main chain or terminal –OH group? *Energy Environ. Sci.* **13**, 1318–1325 (2020).
6. Narita, A., Shibayama, W. & Ohno, H. Structural factors to improve physico-chemical properties of zwitterions as ion conductive matrices. *J. Mater. Chem.* **16**, 1475 (2006).
7. Odian, G. *Principles of polymerization*. (Wiley-Interscience, 2004).
8. Sugihara, S., Yoshida, A., Fujita, S. & Maeda, Y. Design of Hydroxy-Functionalized Thermoresponsive Copolymers: Improved Direct Radical Polymerization of Hydroxy-Functional Vinyl Ethers. 11 (2017) doi:10/gcnt7j.

9. Sugihara, S., Sudo, M., Hirogaki, K., Irie, S. & Maeda, Y. Synthesis of Various Poly(2-hydroxyethyl vinyl ether)-Stabilized Latex Particles via Surfactant-Free Emulsion Polymerization in Water. 12 (2018) doi:10/gc7h9b.
10. Sugihara, S., Yoshida, A., Kono, T., Takayama, T. & Maeda, Y. Controlled Radical Homopolymerization of Representative Cationically Polymerizable Vinyl Ethers. *J. Am. Chem. Soc.* 8 (2019) doi:10/gjr6zv.
11. Inceoglu, S. *et al.* Morphology–Conductivity Relationship of Single-Ion-Conducting Block Copolymer Electrolytes for Lithium Batteries. *ACS Macro Lett.* **3**, 510–514 (2014).
12. Rolland, J., Poggi, E., Vlad, A. & Gohy, J.-F. Single-ion diblock copolymers for solid-state polymer electrolytes. *Polymer* **68**, 344–352 (2015).
13. Ma, Q. *et al.* Single Lithium-Ion Conducting Polymer Electrolytes Based on a Super-Delocalized Polyanion. *Angew. Chem. Int. Ed.* **55**, 2521–2525 (2016).
14. Porcarelli, L. *et al.* Single-Ion Block Copoly(ionic liquid)s as Electrolytes for All-Solid State Lithium Batteries. *ACS Appl. Mater. Interfaces* **8**, 10350–10359 (2016).
15. Porcarelli, L. *et al.* Single-ion triblock copolymer electrolytes based on poly(ethylene oxide) and methacrylic sulfonamide blocks for lithium metal batteries. *Journal of Power Sources* **364**, 191–199 (2017).
16. Bouchet, R. *et al.* Single-ion BAB triblock copolymers as highly efficient electrolytes for lithium-metal batteries. *Nature Mater* **12**, 452–457 (2013).
17. Li, S. *et al.* Single-Ion Homopolymer Electrolytes with High Transference Number Prepared by Click Chemistry and Photoinduced Metal-Free Atom-Transfer Radical Polymerization. *ACS Energy Lett.* **3**, 20–27 (2018).

18. Zhang, Y. *et al.* Toward ambient temperature operation with all-solid-state lithium metal batteries with a sp boron-based solid single ion conducting polymer electrolyte. *Journal of Power Sources* **306**, 152–161 (2016).
19. Yuan, H. *et al.* Single Lithium-Ion Conducting Solid Polymer Electrolyte with Superior Electrochemical Stability and Interfacial Compatibility for Solid-State Lithium Metal Batteries. *ACS Appl. Mater. Interfaces* **12**, 7249–7256 (2020).
20. Lingua, G. *et al.* Unique Carbonate-Based Single Ion Conducting Block Copolymers Enabling High-Voltage, All-Solid-State Lithium Metal Batteries. *Macromolecules* **54**, 6911–6924 (2021).
21. Wetjen, M., Kim, G.-T., Joost, M., Winter, M. & Passerini, S. Temperature dependence of electrochemical properties of cross-linked poly(ethylene oxide)–lithium bis(trifluoromethanesulfonyl)imide–N-butyl-N-methylpyrrolidinium bis(trifluoromethanesulfonyl)imide solid polymer electrolytes for lithium batteries. *Electrochimica Acta* **87**, 779–787 (2013).
22. Zeng, X. *et al.* Enhanced interfacial stability with a novel boron-centered crosslinked hybrid polymer gel electrolytes for lithium metal batteries. *Chemical Engineering Journal* **428**, 131100 (2022).
23. Borzutzki, K., Thienenkamp, J., Diehl, M., Winter, M. & Brunklaus, G. Fluorinated polysulfonamide based single ion conducting room temperature applicable gel-type polymer electrolytes for lithium ion batteries. *J. Mater. Chem. A* **7**, 188–201 (2019).
24. Borzutzki, K., Nair, J. R., Winter, M. & Brunklaus, G. Does Cell Polarization Matter in Single-Ion Conducting Electrolytes? *ACS Appl. Mater. Interfaces* **14**, 5211–5222 (2022).

25. Chen, H. *et al.* Lithium Salt of Tetrahydroxybenzoquinone: Toward the Development of a Sustainable Li-Ion Battery. *J. Am. Chem. Soc.* **131**, 8984–8988 (2009).
26. Hernández, G. *et al.* Redox-active polyimide–polyether block copolymers as electrode materials for lithium batteries. *RSC Adv.* **5**, 17096–17103 (2015).
27. Oyaizu, K., Hatemata, A., Choi, W. & Nishide, H. Redox-active polyimide/carbon nanocomposite electrodes for reversible charge storage at negative potentials: expanding the functional horizon of polyimides. *J. Mater. Chem.* **20**, 5404 (2010).
28. Iordache, A. *et al.* Perylene-Based All-Organic Redox Battery with Excellent Cycling Stability. *ACS Appl. Mater. Interfaces* **8**, 22762–22767 (2016).
29. Banda, H., Damien, D., Nagarajan, K., Hariharan, M. & Shaijumon, M. M. A polyimide based all-organic sodium ion battery. *J. Mater. Chem. A* **3**, 10453–10458 (2015).
30. Wu, D. *et al.* Perylene diimide-diamine/carbon black composites as high performance lithium/sodium ion battery cathodes. *J. Mater. Chem. A* **6**, 13613–13618 (2018).
31. Song, Z., Zhan, H. & Zhou, Y. Polyimides: Promising Energy-Storage Materials. *Angew. Chem. Int. Ed.* **49**, 8444–8448 (2010).
32. Leedy, D. W. & Muck, D. L. Cathodic reduction of phthalimide systems in nonaqueous solutions. *J. Am. Chem. Soc.* **93**, 4264–4270 (1971).

Chapter 3. A Highly Conductive, Self-standing SIPE for Organic Lithium Metal Batteries with 3D Carbon Current Collector

A SIPE (I_{1000}p-SO_3-cr), based on low crosslink degree polymer has been developed from the previous work in LEPMI.[1], with good ionic conductivity, transference number equals to 1 and stable with lithium metal, are studied in this chapter. The crosslinked nature provides extra benefit on the mechanical stability, specially forming solid-state membranes and ability to be manipulated without incorporation in another polymer matrix. Therefore, in parallel with the linear SIPE of mPEGEM-PTFSIVE, this polymer should be an excellent candidate to demonstrate the developing of solid-state organic lithium batteries, targeting better safety and stability.

The PTCI material used in chapter 2 showed good stability. Thus, further investigated to develop better composite electrode with organic materials with SIPE. One of the challenges is to obtain high mass loading electrodes. Therefore, in this study not only introduced a different SIPE but also a specific current collector. The PTCI electrode was first prepared on carbon coated Al foils as described in Chapter 2, and then with a novel 3D carbon nonwoven current collector, it could improve the quality of the organic electrode with a much higher active material mass loading by infiltrating the electrode with SIPE. With low electronic conductivity and low density, which is intrinsic to the organic active materials, it is difficult to achieve high mass loading of active material which is proportional to the area energy density of the electrode. Using carbon nonwoven as current collector with infiltration of SIPE, continuous contact between current collector, organic active material and SIPE could be achieved, allowing higher mass loading of organic active material. Additionally, substituting the metallic current corrector (Al and Cu foil) could improve the sustainability of the electrode, which is also the focus of applying organic active materials.

Here the chapter is organized with the following order:

(1) Preparation and characterization of I_{1000}p-SO_3-cr SIPE

(2) Lithium plating/stripping test with SIPE

(3) Organic lithium metal batteries with different structure of electrodes

1 Preparation of I_{1000}p-SO_3-cr electrolyte

The I_{1000}P-SO_3-db polymer was synthesized by a similar reaction as reported in a previous work[1]. The reaction was taken place in two steps. In the first step a SIPE with a molecular weight of 5000 g mol^{-1} were obtained by the polycondensation between PEG1000 and sodium 2-(2-(3,5-difluorophenyl)-1,1,2,2-tetrafluoroethoxy)-1,1,2,2-tetrafluoroethane-1-sulfonate in presence of NaH, in the second step the resulting SIPE ended in Na alcoholate was copolymerized with PEG1000 and 3-chloro-2-(chloromethyl)prop-1-ene. The product was then transferred into lithium form with an ion exchange resin. The linear polymer, I_{1000}p-SO3-db, with double bond was a yellowish wax, which is shown in Figure 74A. Here the term 1000 represents the molecular weight of the PEG macromonomer, used for the SIPE synthesis and represent the length of the chain between two ionic function functions. The SO_3 refers to the ionic function, which is perfluorosulfate, and the term "db" refers to the double bonds, which allows the polymer to further crosslink. After crosslinking the notation becomes I_{1000}p-SO_3-cr. With the chemical composition, it is easy to get the EO:Li ratio of both I_{1000}p-SO_3-db and I_{1000}p-SO_3-cr is around 23. The molecular weight of I_{1000}p-SO_3-db was determined by SEC-LS. The M_n and M_w was 18 and 44 kg mol^{-1} with a polyderpersity index of 2.4. The high molecular weight of I_{1000}p-SO_3-db indicates that the copolymer is a SIPE even without crosslink.

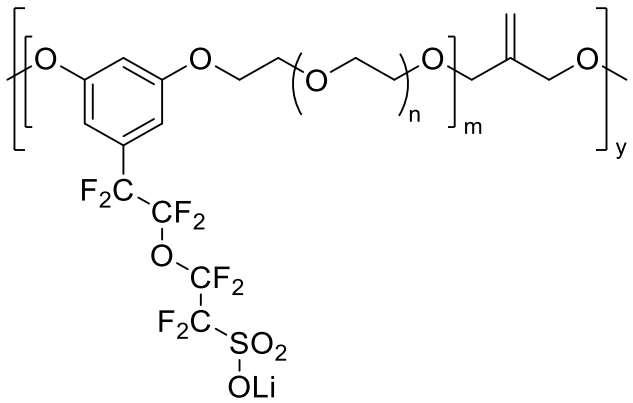

Figure 72. Chemical structure of I_{1000}p-SO3-db. The average n, m, and y was around 22, 4 and 3.5, respectively.

The chemical structure of the I_{1000}p-SO_3-db was confirmed with ^1H and ^{19}F NMR spectra. The peaks exhibit the correct integral, the spectra and peak assignments are shown in Figure 73.

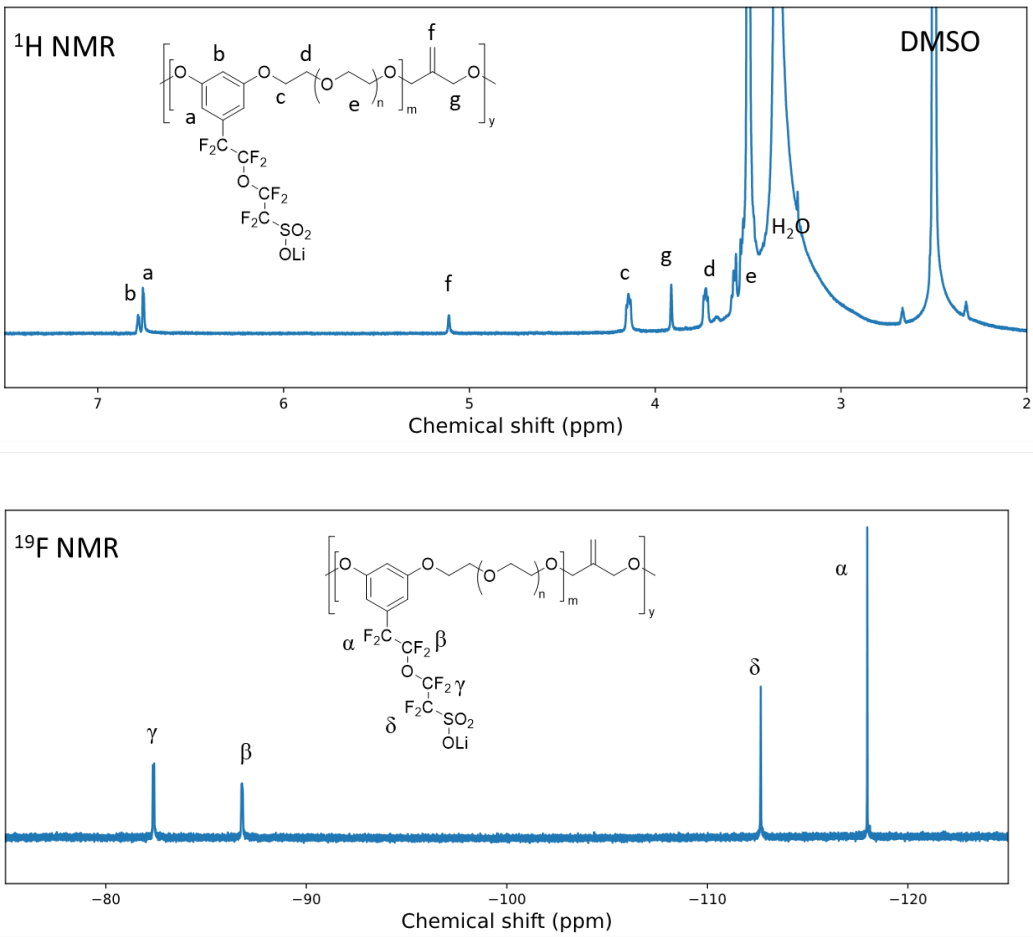

Figure 73. ^1H and ^{19}F NMR spectra of I_{1000}p-SO_3-db SIPE.

To fabricate an electrolyte membrane, the I_{1000}pSO_3-db polymer was mixed with 4 wt.% photoinitiator (Irgacure 2959, 2-hydroxy-4′-(2-hydroxyethoxy)-2-methylpropiophenone) and 6 wt.% of nanocrystalline cellulose (NCC). The NCC was added to reinforce the mechanical properties of the membrane. Then the mixture was laminated into thin films between two polyolefin films. The polymer was then crosslinked with UV irradiation to yield the self-standing, solid-state, and flexible SIPE membranes (image shown in Figure 74B), which has a typical thickness of ~70 μm.

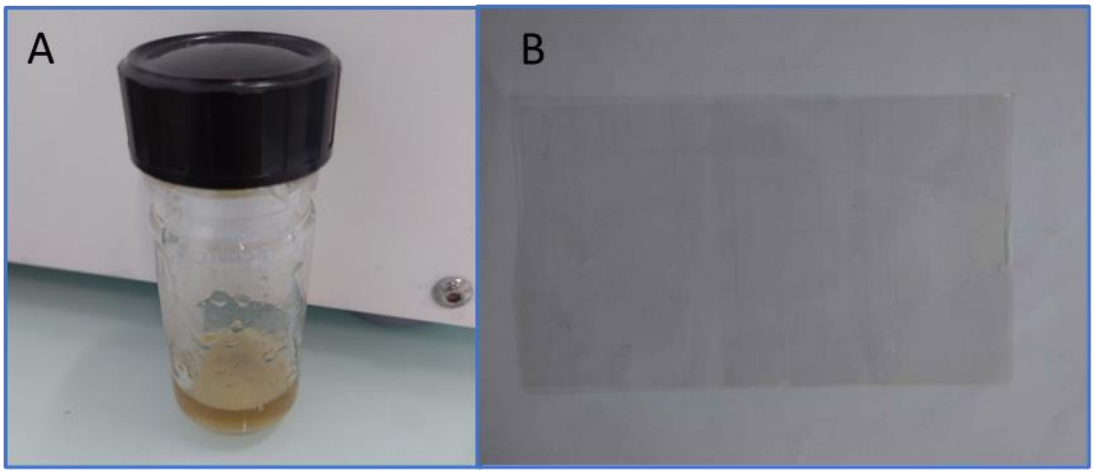

Figure 74. (A) Image of I_{1000}p-SO_3-db polymer; (B) I_{1000}-SO_3-db membrane.

2 Characterization of crosslinked I_{1000}p-SO_3-cr electrolyte

2.1 Thermal analysis

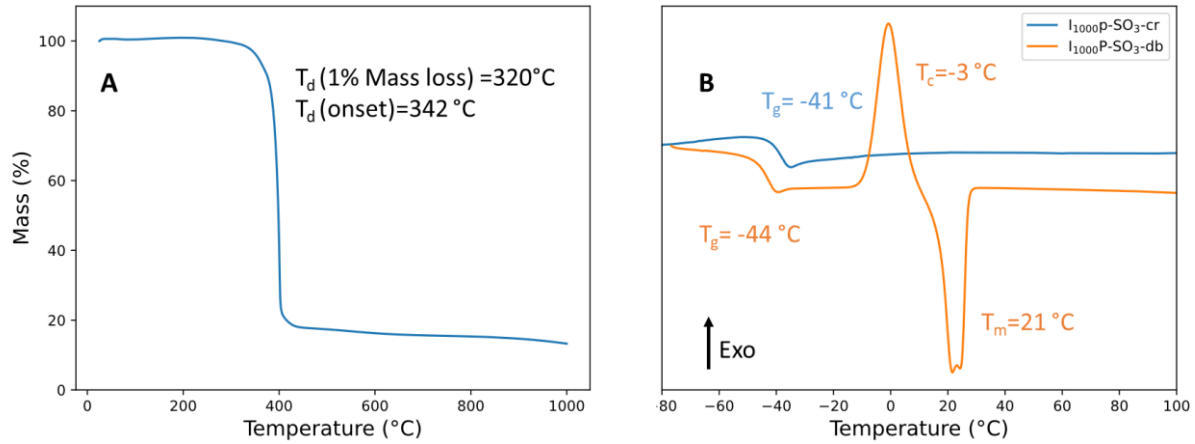

Figure 75. (A) TGA thermogram of the SIPE membrane. (B) DSC trace of the crosslinked SIPE membrane.

The thermal stability of the I_{1000}p-SO_3-cr SIPE was determined by thermogravimetric analysis (TGA) under nitrogen atmosphere, which is shown in Figure 75A. The SIPE exhibits excellent thermal stability with less than 1% mass loss at 320 °C. Thermal stability is mainly limited due to the decomposition of PEO backbones which leads to similar TGA results as compared to the linear SIPE in Chapter 2. The phase transition behavior of the SIPEs were determined with differential scanning calorimetry (DSC) and the results are shown in Figure 75B. For the non-

crosslinked I_{1000}p-SO_3-db, glass transition temperature was -44 °C and a pair of crystallization/melting peak could be found at -3 and 21 °C. The crystallization was due to the PEO chains in the backbone. As for the crosslinked I_{1000}p-SO_3-cr, only a glass transition temperature of -41 °C was observed. The T_g showed a minor shift of 3 °C compared to the non-crosslinked SIPE, because the crosslinking weakly hindered the chain segmental motion (due to the low crosslink density). The low concentration in double bonds, only one double bond/5000 g of polymer conduct, by crosslinking, to a 3D network with a good flexibility of the polymer chain. In addition, no crystallization and melting peaks were observed, which suggests the crosslinked SIPE achieved a fully amorphous structure. Both low T_g and amorphous structure are favorable to improve the ionic conductivity which is dominated by the polymer chain segmental motion in the amorphous phase.

2.2 Ionic Conductivity and lithium transference number

The ionic transport behavior was studied by ionic conductivity and lithium transference number measurements. The conductivity was measured by electrochemical impedance spectroscopy with SS|SIPE|SS blocking cells and calculated by the following equation:

$$\sigma = \frac{l}{R_b \cdot A}$$

where l and A are the thickness and area of the membrane, and R_b is bulk resistance. The temperature dependence of the ionic conductivity is plotted in Figure 76.

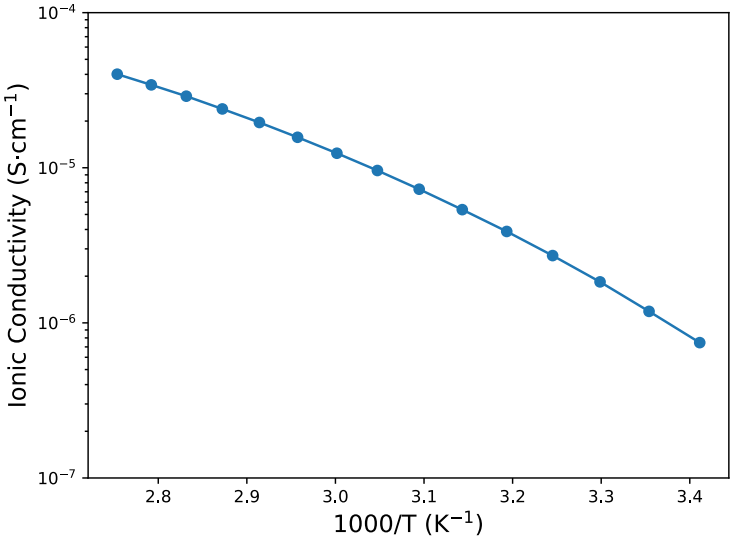

Figure 76. Ionic conductivity of I_{1000}p-SO_3-cr SIPE.

The SIPE exhibited good ionic conductivity of 1.2×10^{-6} S cm^{-1} at 30 °C and 4.0×10^{-5} S cm^{-1} at 90 °C, which is consistent to the state-of-arts solvent-free SIPEs which has ionic conductivity between 10^{-6} to 10^{-4} S cm^{-1} at 90 °C.[2]

The ionic conductivity showed a nonlinear behavior, which could be explained by VTF model, which is originally used to describe the molecular relaxation behaviors by means of temperature dependence such as viscosity. The VTF relationship is described in the following equation:

$$\sigma = \sigma_0 \cdot T^{\frac{1}{2}} \cdot e^{-\frac{E_a}{K_b \cdot (T - T_0)}}$$

σ_0 is the pre-exponential factor, E_a is pseudo-activation energy, T_0 is referred to as the Vogel temperature, i.e., polymer ideal transition temperature, and K_b is Boltzmann constant. σ_0 is related to the ion concentration of the electrolyte.

The VTF behavior of the SIPE was determined by Gaussian non-linear fitting with all the 3 parameters fitted. The fitting result were σ_0= 0.182 S cm^{-1}, T_0 =200 K (-73 °C) and pseudo activation energy E_a= 7.4 kJ mol^{-1}. In this case, T_0 is about 30 K below the T_g.

As the key factor to the single ion polymer electrolyte, high Li transference number is extremely important to address the single ion transport behavior. As predicted by Chazalviel[3] and Tikekar[4], high Li transference number could curb the lithium dendrite formation leading to a more stable

and safer battery.

As explained in Chapter 1, many electrochemical methods are applied to determine the Li transference number, namely Sørensen-Jacobsen (S-J),[5] Bruce-Vincent,[6] Watanabe,[7] Wiemhöfer[8], all these methods are based on the polarization behavior of the polymer electrolyte in symmetric Li||Li cells.

A Li|SIPE|Li cell was assembled moved in an isothermal chamber of 80 °C. The EIS and polarization tests (Figure 77) were performed instantly after sample temperature stabilized for 2 h. The polarization with 20 mV bias voltage was applied on the cell. The current response decreased from 0.036 mA to 0.030 mA during the 10 h of the experiment. At the same time, a significant increase in interfacial resistance was observed, which was the modification of passivation layer on the surface of Li electrode. The interfacial resistance evolution theoretically can be ruled out by Bruce-Vincent method.

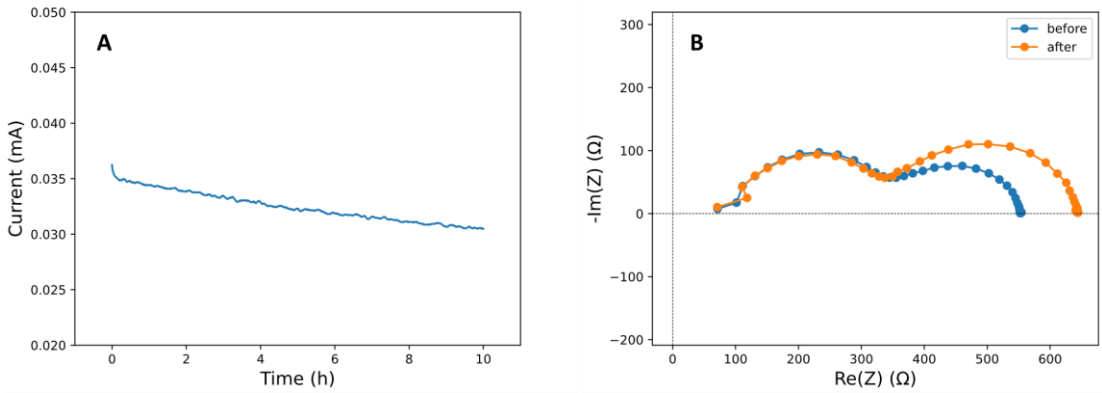

Figure 77. (A) Polarization of a pristine Li|SIPE|Li cell at 80 °C (B) EIS before and after polarization.

To repeat the determination of the Li^+ transference number for a stabilized cell, another symmetric Li|SIPE|Li cell was assembled and kept in an 80 °C isothermal chamber for 1 week to form a stable interface between the Li metal electrode and the SIPE. The EIS and polarization tests were conducted with the same method as the one used for pristine cells, which are shown in Figure 78. Less modification of the EIS spectra after 10 h of polarization was observed compared to the pristine cell.

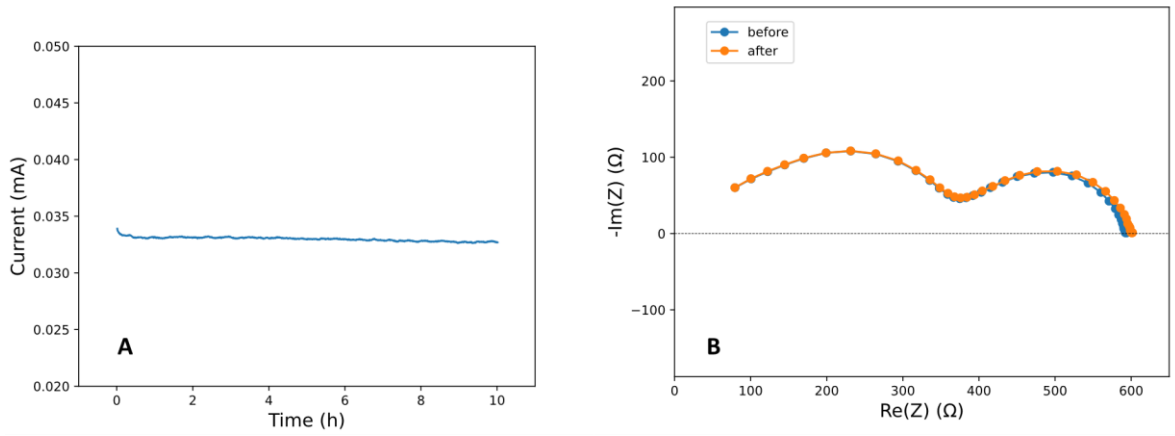

Figure 78. (A) Polarization of pristine Li|SIPE|Li cell at 80 °C (B) EIS before and after polarization.

By simple DC polarization, Bruce-Vincent, and Watanabe methods (for the methods, please refer to Chapter 1, 3.3.2), the Li transference number of the SIPE was determined and the results listed in Table 7.

Table 7. Li transference number of pristine SIPE and after aging with different methods.

	DC polarization	Bruce-Vincent	Watanabe	S-J	Wiemhöfer
Pristine SIPE	0.840	0.996	0.750	~1	11.5
Aged SIPE	0.965	0.962	0.896	~1	11.5

Neat DC polarization yielded a result of 0.84 for the pristine sample, which could be explained by the impedance evolution during the polarization leading to current drop. A higher value of 0.965 was determined after aging of the sample to yield a stable interphase. In the case of the Bruce-Vincent method, the pristine and aged sample showed more consistency, yielding 0.996 and 0.962, respectively. The Watanabe method provided lower transference numbers than the Bruce-Vincent method. Even after aging, the result was only ~0.9.

For the S-J method, the impedance of diffusion Z_d was close to 0 since the diffusion process in the low frequencies was absent in Figure 77B and 78B, and the data points almost overlapped. Thus, the Li^+ transference number was calculated as close to 1. At the same time, due to the overlap of the EIS data points at the low frequencies, using the S-J method was difficult to

precisely evaluate the SIPE with high transference number.

The Wiemhöfer method in both cases yielded results far beyond expectation, which means the method is not applicable in determining Li transference number of SIPEs. The Wiemhöfer method relays on the relaxation after the polarization to determine the bulk resistance of electrolyte, which is the first response after removing the bias voltage. In the case of the SIPE, lacking of charge charrier gradient a very fast relaxation of the electrolyte, which is not easy to observe. So, the linear regression of the OCV could not correctly reflect the gradient of the charge carriers and leading to a meaningless value in the calculation.

By combining the transference number of 0.97 determined by PFG-NMR reported in the previous work,[1] I could conclude that the Li^+ transference number of crosslinked I_{1000}p-SO_3-cr SIPE was ~0.96 which is very close to unity. Among the electrochemical methods, the most common Bruce-Vincent method was more creditable in the case of SIPE.

Compared to the linear SIPE (mPEGME-PTFSIVE copolymer) in Chapter 2, the crosslinked I_{1000}p-SO_3-cr electrolyte showed similar ionic conductivity at elevated temperatures. But at room temperature, the ionic conductivity is worse. This is mainly due to the difference in the polymer chain flexibility, which is limited by the crosslinked structure. On the contrary, the I1000p-SO3-cr show higher Li transference number, which is also due to the crosslinked structure which limits the anion (attached to the polymer backbone) motion.

2.3 Electrochemical stability

The electrochemical stability of the SIPE was examined by CV test with Li|SIPE|SS cells, as shown in Figure 79. With a slow scan rate of 0.2 mV s^{-1}, the cell cycled from open circuit voltage (OCV) to 4 V and then back to -0.5 V for three cycles. And in the following three cycles, the upper limit of the scan was increased to 4.5 V.

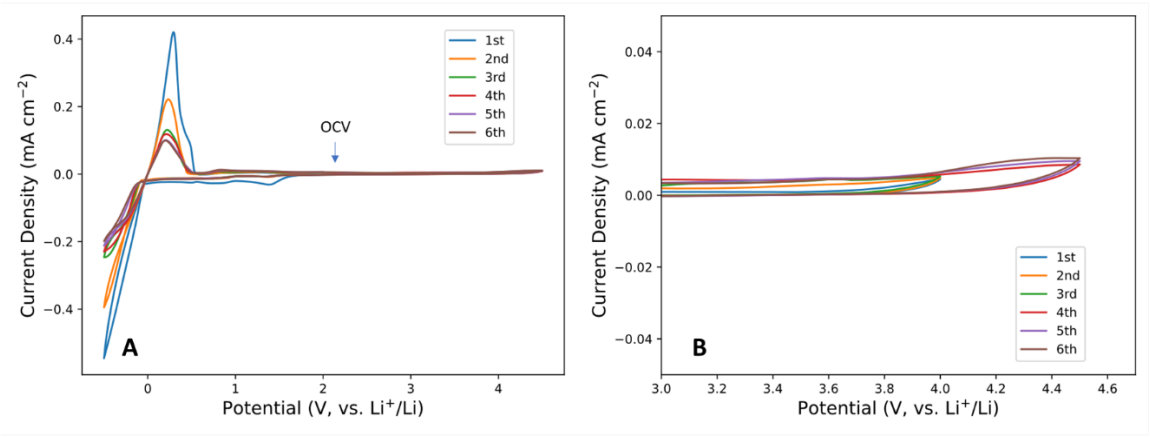

Figure 79. (A) Cyclic voltammetry of Li|SIPE|SS cell. (B) Magnification of the oxidation part.

In the anodic scan part, no obvious oxidation was observed, even for a high anodic reversing voltage of 4.5V, which exceeds the ESW of PEO. For the cathodic scan, an irreversible reduction reaction was observed at 1.4 V for the first cycle, which could be ascribed to the side reaction including SEI formation or reduction of surface oxide on the working electrode [9]. The lithium plating/stripping peaks were observed between -0.5 to 0.5 V. With cycling, the Li plating/stripping showed a decrease on the peak intensity which indicates the passivation of lithium surface.

The reversibility of lithium can be evaluated by the Coulombic efficiency (CE), which is calculated by integrating the area of lithium plating/stripping peaks. The CE was calculated as 38.7, 30.6, 26.5, 26.7 and 25.7 % for 1-6 cycles, which showed a decreasing at beginning and then stabilized at around 26 %, which is extremely low. The reactivity of lithium in CV tests was widely observed with PEO based electrolytes[10], which will be discussed in detail in the next chapter.

The SIPE was well-examined with many parameters ionic conductivity, transference number, electrochemical stability, which showed promising properties for use in battery systems. Thus, the SIPE was applied to the metallic lithium electrode to examine the compatibility of the electrolyte with the lithium metal.

3 Lithium plating/stripping test

The Lithium plating/stripping tests were conducted with symmetric Li|SIPE|Li cells at 80 °C.

Galvanostatic cycling was applied first with a small current density of 10 mA cm^{-2} for 80 h as the formation cycles (for each cycle, 4 h plating and 4 h stripping). Then the current density was increased to 200 mA cm^{-2}.

At low current density, the voltage profile (Figure 80) showed a stable rectangular shape with an overpotential of ~5 μV, indicating that there was no significant additional polarization in electrolyte due to concentration gradient upon plating/stripping. The essentially rectangular shape of the plating/stripping could be considered as proof of lithium transference number close to 1. After increasing the current density to 200 mA cm^{-2}, which is intense for the solvent-free SIPE, the overvoltage profile showed a non-symmetric shape and evolved for ~220 h and finally reached a stable rectangle shape again with a stable overvoltage of ~0.11 V. The asymmetric shape after increasing the current density suggests that the two lithium electrodes surfaces are not identical, and the difference was magnified by the large current density. For each cycle, the amount of lithium plated/striped was 0.8 mAh cm^{-2}, corresponding to 3.8 μm of lithium metal. During the more than 400 h at high current density, the symmetric cells showed no sign of short circuit or loss of contact with a stable overpotential, which successfully underlined the stability of this crosslink SIPE against lithium metal electrodes.

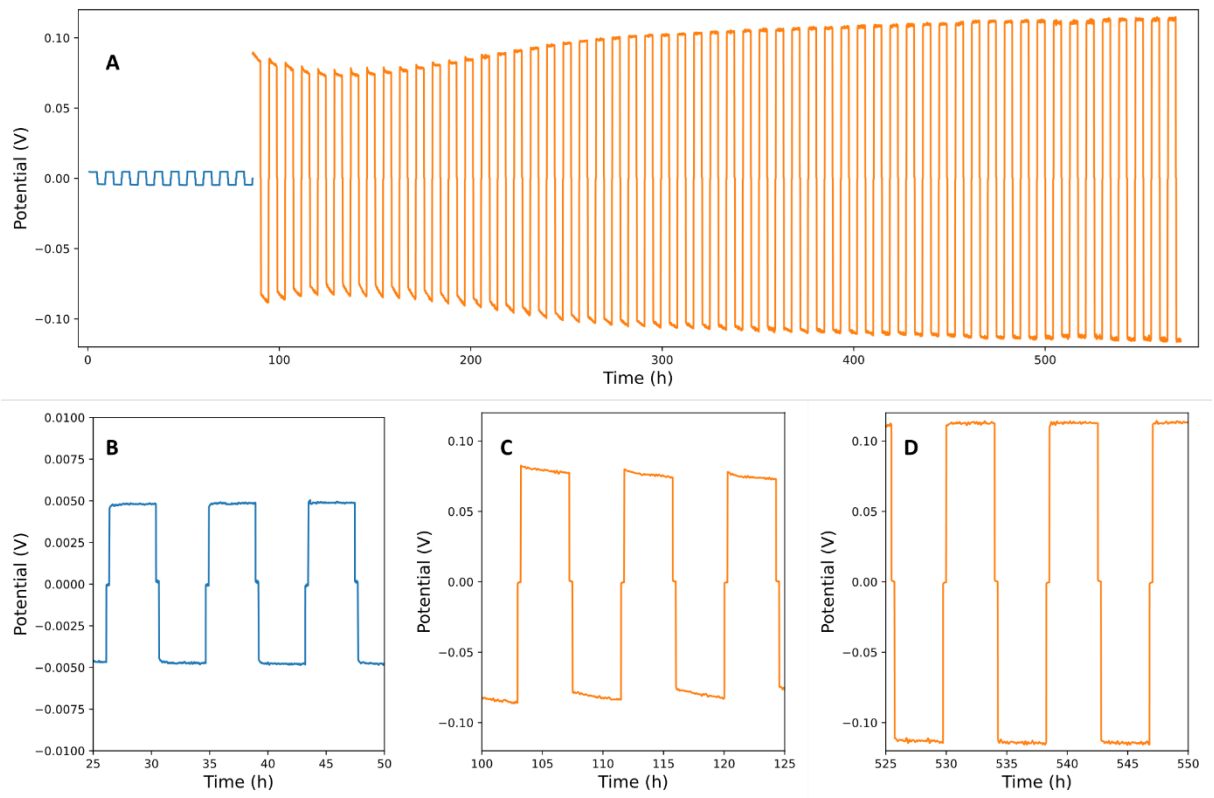

Figure 80. Lithium plating/stripping test with symmetric Li|SIPE|Li cells: 0-100 h is with current density of 10 mA cm-2 and after is 200 mA cm^{-2}: (A) Overall voltage profile; (B), (C), (D) magnified voltage profiles for 25-50, 100-125 and 525-550 h, respectively.

4. Lithium metal battery with an LFP positive electrode

Compared to the organic positive electrodes, which are not well-studied, LFP is known to be stable, which is perfect for a benchmark material to evaluate the SIPE and compare it with other state-of-arts electrolytes. Thus, before directly using organic electrode, LFP electrodes were prepared as tested with I_{1000}p-SO_3-cr SIPE.

LFP, carbon black, I_{1000}p-SO_3-db and PVDF were mixed in a mortar and added NMP as solvent to form a homogenous slurry. The LFP electrodes were prepared on carbon coated Al current collector by doctor blade casting and dried in an oven of 80 °C overnight. The electrode was composed of LFP: carbon black: I_{1000}p-SO_3-db:PVDF=60:10:25:5. The I_{1000}P-SO_3-db polymer to ensure the ionic conductivity inside the electrode.

To verify the effect on porosity of the electrode, pristine and calendared electrodes were used. Confirmed by SEM images (Figure 81), the surface of the electrodes was modified from rough

surface with particles to flat and homogenous surface by calendaring. More importantly, the porosity and the thickness were greatly reduced. The thickness of the pristine electrode was around 17 μm and decreased to 5 μm after calendaring. Additionally, with energy selective backscattered (ESB) detector, we could differentiate LFP from carbon black in the images and confirm a homogeneous dispersion of the LFP particles in the composite electrode. The porosity of the electrodes was estimated by combining the density of each component, for the non-calendared electrode the porosity was 63%. After calendaring, the porosity became negligible, which ensures the good percolation of the ionic and electronic pathways.

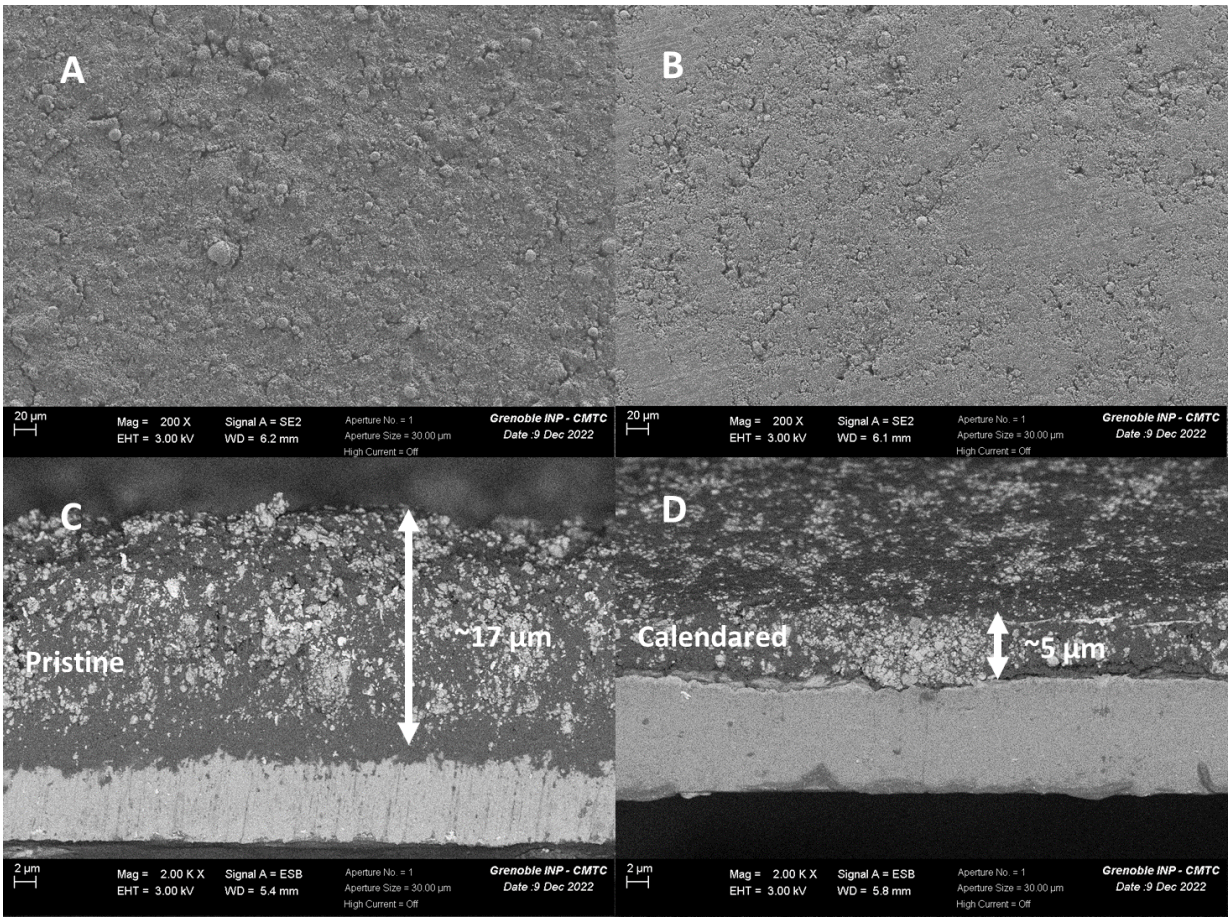

Figure 81. SEM images of LFP electrodes. (A, B) top view of pristine and calendared electrodes, respectively, with an SE2 detector; (C, D) cross section of pristine and calendared electrodes, with ESB detector.

Both pristine and calendared LFP electrodes (mass loading ~1.5 mg cm^{-2}) were first used in the LMBs cells to perform C rate tests (Figure 82). The first three cycles were performed at a slow

C rate of C/20 (C= 170 mA g^{-1}) and then stepwise increased to C/10, C/5, C/2, 1C for each 10 cycles and finally back to C/10 to examine the reversibility. For the electrode without calendaring, the discharge capacity was 153, 146, 136, 117, and 88 mAh g^{-1} for an increasing C rate. Significant capacity loss was observed when elevating the current density, which could be due to the large amount of porosity with a notable increase of tortuosity. The capacity was reversible, though, after reducing the C rate back to C/10 and got back to 141 mAh g^{-1}. After calendaring, the C rate capability of the cells was obviously improved, for a C rate of C/20, C/10, C/5, C/2 and 1C, a specific capacity of 162, 160, 156, 143, and 132 mAh g^{-1} was obtained, respectively. After the C rate test, in the following C/10 cycling, the calendared electrode showed a stable cycling with constant capacity loss. However, with non-calendared electrode, a fast fading between 60-80 cycles was observed.

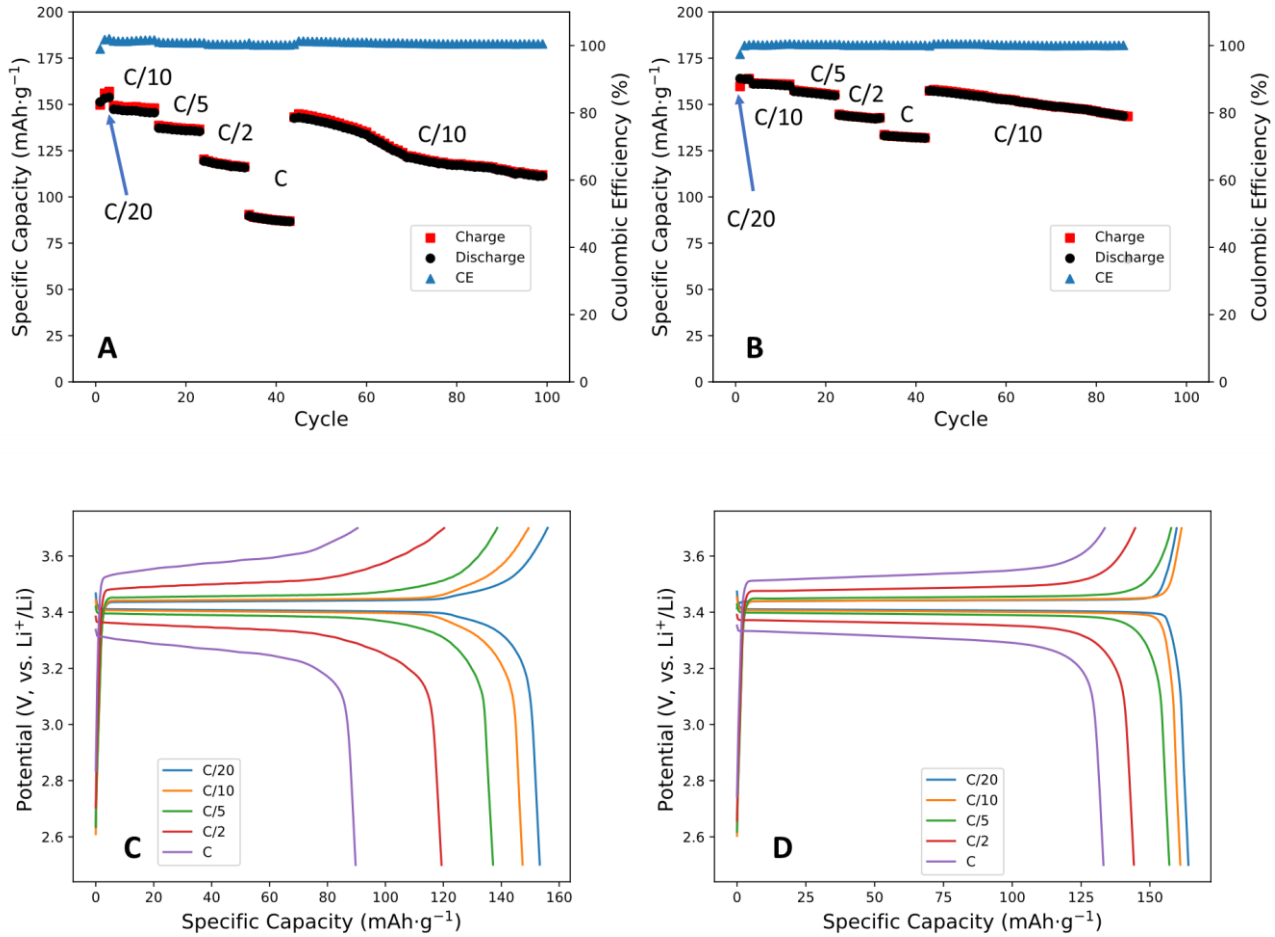

Figure 82. (A) Li|SIPE|LFP cells with non-calendared electrodes at 80 °C; (B) Li|SIPE|LFP cells with calendared electrodes at 80 °C; (C, D) corresponding charge/discharge profiles of cells with non-calendared and calendared electrodes.

The relationship between the current density and polarization was plotted in Figure 83. Both capacity and polarization (defined as the charge/discharge voltage difference at 50% capacity) follows a linear trend with the current density, which could be explained by the following equation:

$$polarization = E_{50\%\,charge} - E_{50\%\,discharge} = (E_{ocv} - E'_{ocv}) + 2IR$$

where E_{OCV} and E'_{OCV} are the open circuit voltage (OCV) of the cell for the charge and discharge process, which is associated to the charge/discharge thermodynamic process, I is the

current applied and R is the total resistance of the cell. With the equation, the total resistance of the two cells is 710 Ω and 1060 Ω, for the calendared and non-calendared electrode respectively. Here, the huge difference was assigned to the electrode morphology and porosity is crucial in utilizing polymer electrolytes owing to the required ionic pathway inside the electrode and seamless contact between electrode and electrolyte. Dense and smooth electrode is definitely favored in this situation. Notably, the Y-intercept of polarization, which is the difference between OCV in charge/discharge process, ideally should be 0 due to the same thermodynamic pathway in charge and discharge process. However, for all the three cells (including the LFP cell in Chapter 2, Figure 58), a tiny difference of ~20 mV could be observed.

Additionally, the relationship between specific capacity and polarization was plotted in Figure 83 B. For both electrodes, the capacity loss follows a less linear trend with the increase of the polarization, which showed the polarization is one of the dominant factors, but not only, factor for the capacity loss in the C rate test in these LFP cells. The slope of the capacity was higher in the case of the non-calendared electrode, reflecting more capacity loss with increasing polarization. The fact could be explained as the non-calendared electrode with higher porosity could limit both the ionic and electronic conduction, which are more detrimental as high current density.

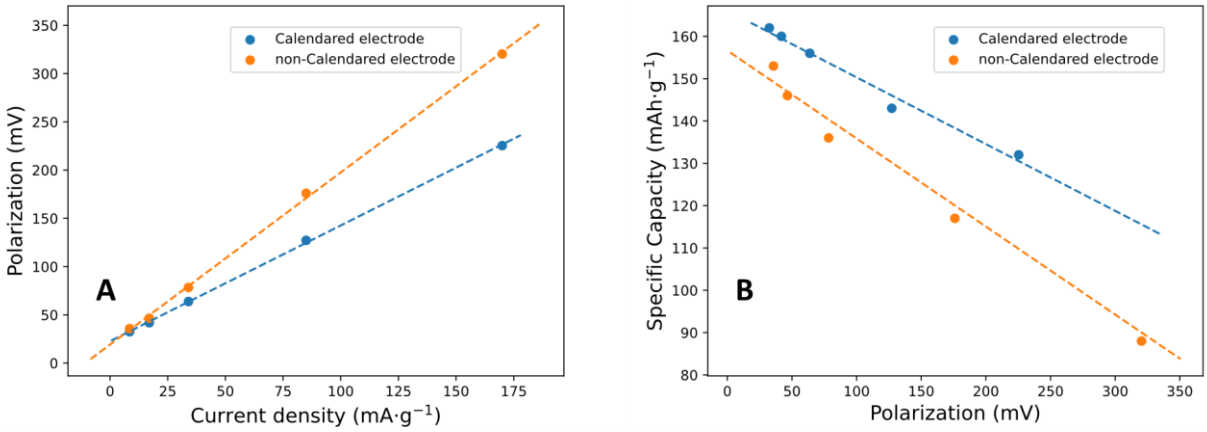

Figure 83. (A) Current density vs. polarization in Li|SIPE|LFP cells with calendared and non-calendared electrodes (B) Polarization vs. specific capacity for Li|SIPE|LFP cells with calendared and non-calendared electrodes.

The comparison between calendared and non-calendared electrode exhibited a huge difference in the capacity and rate capability of the cell, which underlined the importance of the electrode preparation in battery performance, especially when using solid electrolytes. Meantime, the good performance of the LFP cells could address the stability of the SIPEs.

5 Organic lithium metal batteries with PTCI electrode

The characterizations of the I_{1000}p-SO_3-cr polymer proved that the polymer is suitable for LMB applications, owing to its good conductivity, high transference number and stable against lithium metal. Thus, this part of thesis will focus on the fabrication of electrodes and battery elaboration, to adapt the SIPE to organic active materials.

The organic LMBs have been classified using different current collectors (aluminum and carbon nonwoven) which are important for the performance of the battery and overall energy density.

5.1 Electrode based on Al current collector and SIPE+PVDF as binder.

The electrode was first prepared with carbon coated Al foil as the current collector, as described in Chapter 2. The SIPE, I_{1000}p-SO_3-db, was used as electrolyte to provide ionic conductivity inside the electrode.

The composition of the electrode is especially important for organic active materials. Due to the low electronic conductivity of the active material, a higher amount of carbon black is needed (compared to the case of LFP). Similarly, SIPE is premixed to provide ionic conductive pathway inside the electrode. The inactive materials such as SIPE, binder, and carbon filler will reduce the total energy density of the electrode, so a complicated balance between active material, carbon black and SIPE is needed to boost the energy density as well as maintain the good performance. In this thesis, different combinations were used, with PTCI amount varied from 50-70%. But I have to admit that optimization of the electrode, especially adapted to SIPE with different mechanical properties, is extremely challenging and the electrode I used in the thesis still has a huge space for further improvement.

To assure a good electrode binding, 5% of PVDF was added. Carbon black (CB) Super C65 was used as conductive filler. The ratio of PTCI:(CB):PVDF:SIPE was 50:25:5:20. All the

ingredients were mixed in a mortar with the aid of *N*-methyl-2-pyrrolidone (NMP) to form a homogeneous slurry. The slurry was then cast on carbon-coated Al foil by doctor blade, and dried overnight in an oven at 80 °C.

Due to the low density of the organic material (which is intrinsic) and high amount of CB content, after drying, the cracking is inevitably observed and leading to an electrode with high porosity (Figure 84 A). Thus, before battery assembly, the electrode was calendared to reduce the porosity and dried under vacuum. After calendaring (Figure 84 B), the electrode showed a denser and smoother surface. With magnification figures of electrode on the cross sections (Figure 84 C and D), the particles of active materials could be recognized as stacks of ~1 μm flakes which form a nacreous-like structure. The active material was surrounded by conductive carbon particles which were smaller size (<200 nm), reflecting a good dispersion of PTCI and the carbon particles in the slurry.

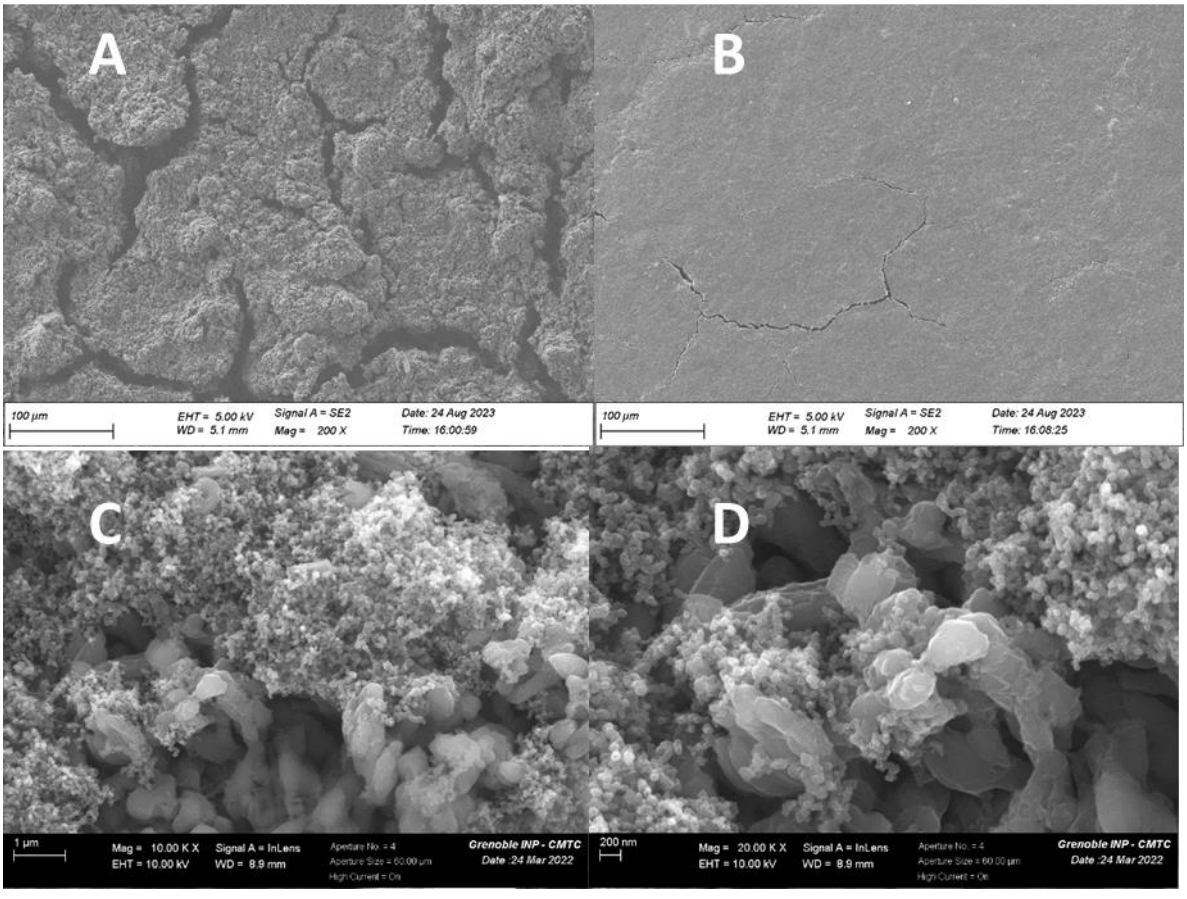

Figure 84. SEM images of the PTCI electrode on Al foil. (A) Pristine electrode (B) electrode after calendaring; (C) and (D) Magnification of the crack on the electrodes.

The cells were assembled in an Ar filled glove box as CR2032 type coin cell. SIPE membrane was sandwiched between PTCI based electrode and lithium metal. The cells were tested with galvanostatic charge/discharge cycling at 80 °C to ensure a good ionic conductivity of the SIPE. Specific capacity and Coulombic efficiency of a typical cell with mass loading of 0.67 mg cm^{-2} were shown in Figure 85. The 70 cycles at the beginning were performed with a rate capability test. The current density was increased after each 10 cycles. Here I did not use the term C rate because the practical capacity was commonly significantly lower than the theoretical value with about 70-100 mAh g^{-1}. Additionally, from the charge/discharge profiles (Figure 85B), it is obvious that the first discharge showed a quite different shape with extra capacity. After the initial cycles, the shape of the charge/discharge profile became symmetric.

The first cycle exhibited a discharge and charge capacities of 125 mAh g^{-1} and 84 mAh g^{-1} respectively with a low CE (defined as charge capacity divided by discharge capacity) of 69%. The insufficient CE could be ascribed to the unaccomplished lithiation and side reactions. The first discharge also showed a much different profile than the following cycles. A stabilization process of the organic electrode could be observed with decreasing discharge and increasing charge capacity during the following 10 cycles, and the CE reached 99.3% at 10^{th} cycle which indicates a good reversibility of the redox process. The specific capacity obtained at 10^{th} cycle was 90 mAh g^{-1}. This phenomenon of stabilization was also observed in the PTCI battery with linear SIPE in the previous chapter (Figure 65 and 70.).

With an increasing current density of 20, 40, 60, 80 and 100 μA cm^{-2} stable specific capacity of 81, 73, 69, 66 and 64 mAh g^{-1}, respectively, were obtained with an average CE higher than 99.5%. After high current density, the current density was then decreased to 10 μA cm^{-2} to check the reversibility of the process. A value of 84 mAh g^{-1} was obtained, a similar value as the one obtained before the C rate test, which proves that the redox process has good reversibility.

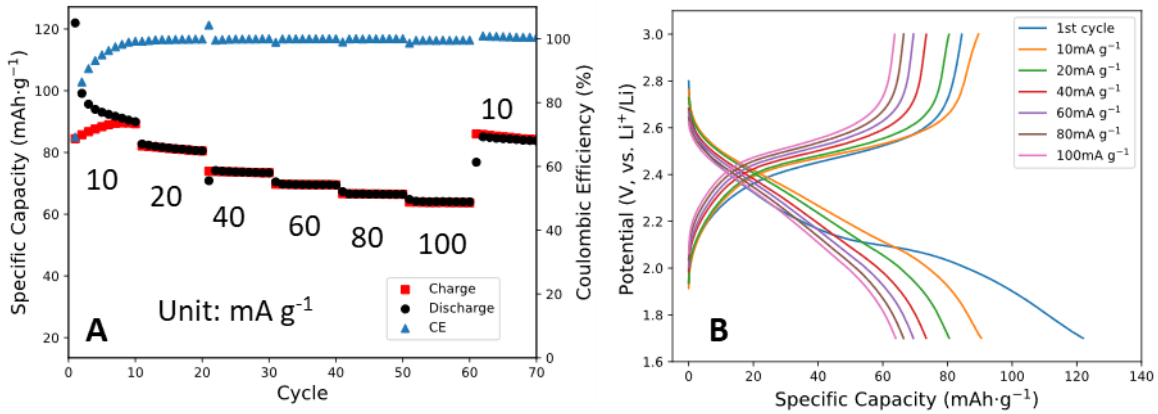

Figure 85. Rate capability test of Li|SIPE|PTCI cells using an Al current collector. (A) Capacity and Coulombic efficiency. (B) The corresponding charge/discharge profiles.

After 70 cycles of rate capability test, the cell was set to cycle with constant current of 40 mA g^{-1} and yield stable cycling for more than 150 cycles. A specific capacity of 71 mAh g^{-1} was obtained after 240 cycles, close to the one obtained at the beginning of the long-term cycling test (73 mAh g^{-1} at 71st cycle), which reflects a high capacity retention of 97%. In addition, an average CE of 99.9% was obtained during the 270 cycles indicating an excellent reversibility and stability of both organic electrode and electrolyte.

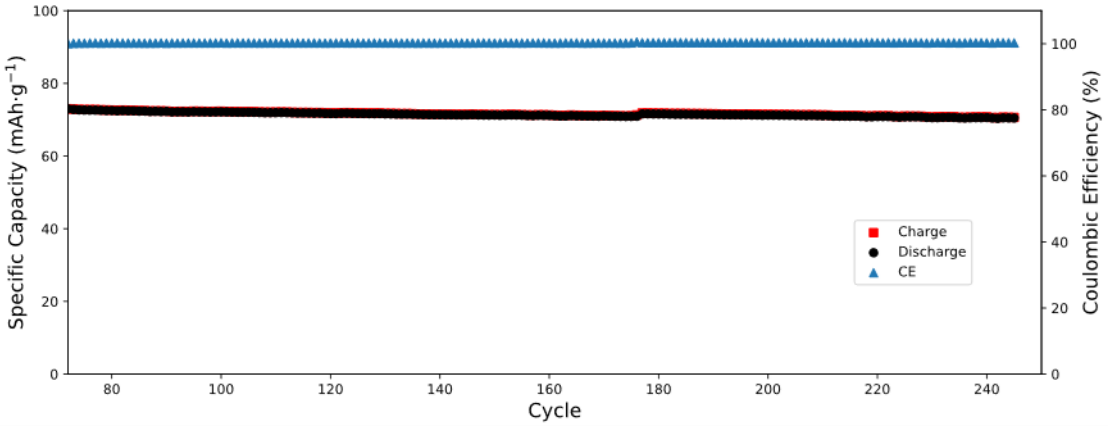

Figure 86. Long-term cycling of a Li|SIPE|PTCI cell with an Al current collector after the rate capability test.

The electrode with the Al current collector showed excellent performance in battery tests with SIPE. However, the mass loading of the electrode was low due to some limitations including: i) the low density of the active material PTCI; ii) high amount of carbon black/ polymer electrolyte needed in the electrode; iii) high porosity of the composite electrode leading to cracking and peeling-off from the current collector. With our best attempt, the mass loading could only achieve less than 2 mg cm^{-2} (e.g., in Chapter 2, Figure 64A, the mass loading is 1.7 mg cm^{-2}) which is insufficient for practical applications. Further increasing the thickness of electrode is challenging and faces risks such as cracking and peeling off. Thus, an improvement of the electrode fabrication is necessary to increase the mass loading and, hence, the energy density.

5.2 3D carbon current collector – Infiltration of the SIPE

As the Al current collector only provides a 2D surface to host the electrode material which provides neither enough surface area for binding nor space for accommodating large amount of the active material. Here, a 3D carbon fiber nonwoven was applied as a new type of current collector to improve both the electric conductivity and mass loading of the composite electrode. Compared to aluminum foil, which is the standard current collector for the positive electrode, the carbon nonwoven (Technical Fibre Products Inc., 8 g m^{-2}) exhibited lower areal density. Lower areal density could reduce the mass of inactive material in the electrode which improves total energy density. For example, in this thesis, the carbon-coated Al foil has an areal density of 4.16 mg cm^{-2}, whereas the carbon nonwoven has a density of only 0.78 mg cm^{-2}, which is 18.7% compared to the Al foil. However, there are also drawbacks for the carbon current collector, including the high porosity and thickness of this current collector.

The electrode was cast in a similar way by doctor blading the electrode material slurry (PTCI: CB: binder= 65:30:5, ~1 g active material in 1.5 mL NMP) on the surface of the carbon nonwoven. A slurry without SIPE was used, due to the SIPE being infiltrated in the next step. Although the slurry was partially gone through the porous carbon nonwoven. The electrode materials could be infiltrated into the carbon nonwoven and form a self-standing composite electrode. At the beginning, we chose a similar mass loading of ~ 1 mg cm^{-2}, as it was easier to compare the results eventually with the Al foil. The SEM images of the electrode are shown in

Figure 87.

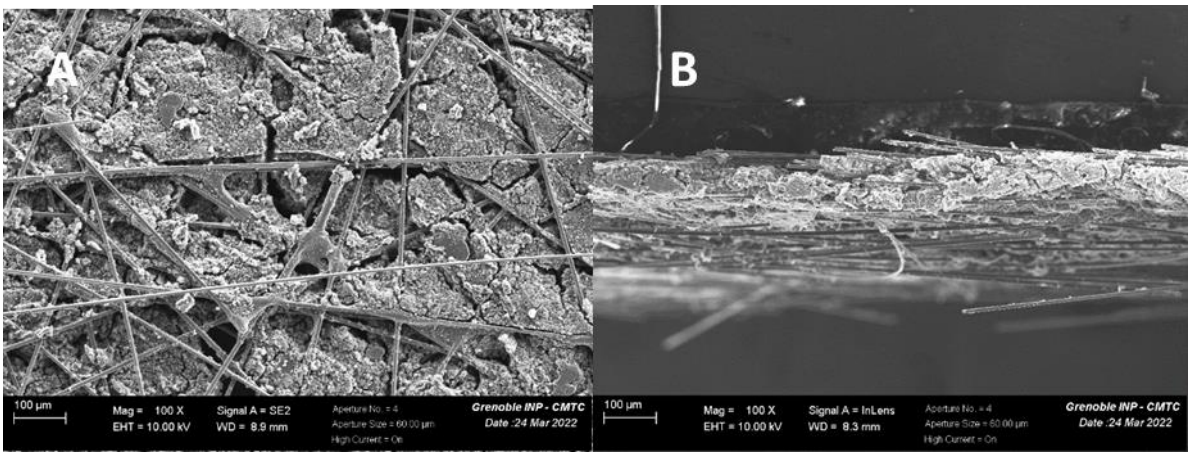

Figure 87. SEM images of the composite electrode comprising PTCI on the carbon nonwoven current collector. (A) Top view; (B) Cross section.

The composite electrode with the carbon current collector could not be directly used with a SIPE membrane due to its high porosity, coarse surface, and lack of ionic conductivity. Therefore, the electrode was infiltrated with a concentrated solution of I_{1000}p-SO_3-db polymer with a photoinitiator to fill the porosity and introduce ionic transport pathways. After UV curing and dying under vacuum, the electrodes were covered by crosslinked SIPE, as electrolyte, and tested in Li|SIPE|PTCI cells.

A typical cell of infiltrated electrode with carbon current collector is shown in Figure 88. With a low PTCI mass loading of 0.9 mg cm^{-2}, the cell reached a specific capacity of 64, 61, 56, 52, and 49 mAh g^{-1} at a specific current of 10, 20,40, 60 and 80 mAh g^{-1}, respectively. Although the capacity was lower than the cell with the Al current collector (which could be ascribed to the defects, the two-step infiltration process and porosity leading to an insufficient ionic percolation), the cycling of the cell was impressively stable. After 100 cycles at 10 mA cm^{-2} after the rate capability test, the cell exhibited a capacity retention of 97.3%. At the same time, an average CE during the whole test was more than 99.9%. These data indicate a very stable redox reaction without degradation of PTCI, the lithium electrodes or the infiltrated SIPE. The remarkable stability encouraged us to refine the process of the electrode preparation.

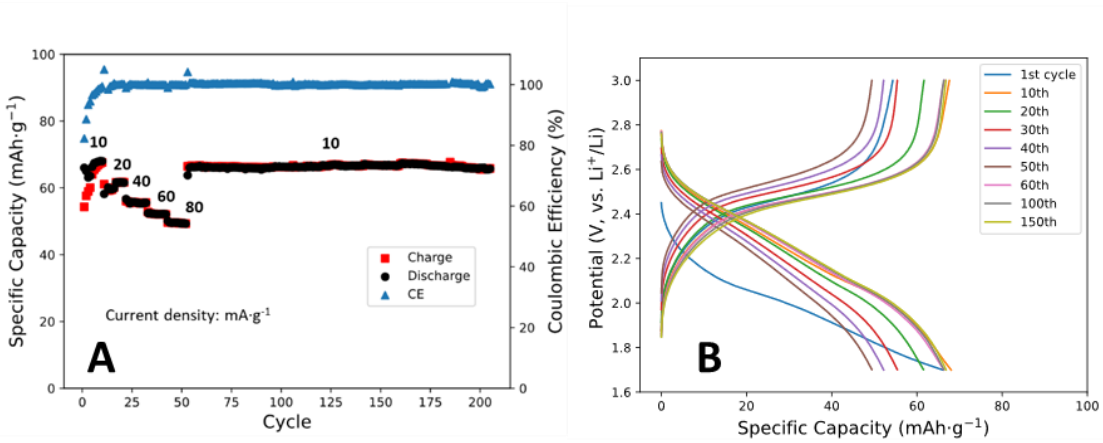

Figure 88. Rate capability and long-term cycling test of Li|SIPE|PTCI cells with a carbon current collector. (A) Capacity and Coulombic efficiency. (B) The corresponding charge/discharge profiles.

These results showed that the SIPE could be adapted to the organic electrode on carbon current collector. Thus, we further increased the thickness of the electrode to improve the PTCI mass loading. A viscous slurry (PTCI:CB: I_{1000}p-SO_3-db of 7:1:2,) was mixed with NMP and cast on carbon nonwoven to increase the mass loading. The electrode was then dried and infiltrated by I_{1000}p-SO_3-db polymer under vacuum at 60 °C. It should be noted that we could reduce the amount of carbon black to only 10 wt.% (thanks to the good electronic conductivity of the carbon nonwoven), which is the same value as in a typical LFP electrode at the lab scale (still much more than the commercial electrodes which is less than 5%) and remove all the PVDF as binder. The higher percentage of active material in the electrode could enable higher energy densities at the full-cell level. The filtrated electrode in a LMB cell is shown in Figure 89.

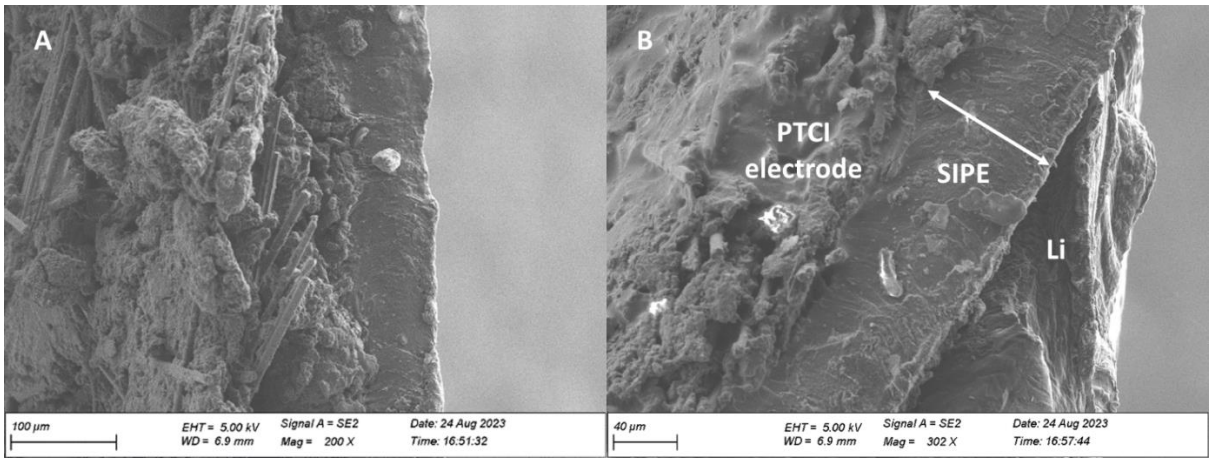

Figure 89. SEM images of the cross sections of (A) composite electrode with the SIPE membrane. (B) Cross section of PTCI|SIPE|Li organic LMB cells.

From the SEM images, the thickness of the SIPE layer and electrode was measured as 87±2 µm and the thickness of the electrode was 103±8 µm. The carbon fibers from the current collector could be easily distinguished, which are covered by the active materials. The SIPE infiltration was also confirmed on the cross section of the electrode. However, there was still some porosity. These issues could be solved by further optimization of the electrode preparation process.

As compared to well optimized commercial electrodes, which have a mass loading about 25 mg cm^{-2}, this PTCI composite electrode still showed a much lower mass loading. However, the ratio of the mass of active material and the current collector was higher than the one obtained with LFP on Al current collector, which is due to the low density of the carbon current collector. As an example, in a PTCI-based electrode with 4.5 mg cm^{-2} mass loading, the current collector was ~1.5 mg cm^{-2}, which equals to 20% of the whole electrode (including current collector). These values could reflect the advantage of the carbon current collector, not only in improving the mass loading of organic active material, but also reducing the mass of the current collector. The best result achieved with these electrodes is shown in Figure 90. The mass loading of the active material was 4.3 mg cm^{-2}. The cell was cycled at 80 °C with a constant current - constant voltage (CC-CV) procedure, which includes an additional of constant voltage (cut-off with 20% current or 1 h of time) after the galvanostatic cycling. The cycles 1-10 were conducted with a specific current of 10 mA g^{-1} and for the following cycles the specific current was 20 mA g^{-1}. The initial capacity was 70 and 67 mAh g^{-1} at 10 and 20 mA g^{-1}, respectively. The cell

successfully cycled more than 320 cycles with a capacity retention of 85.5% and an average CE of 99.9%, which demonstrates its excellent stability. Although a lower specific capacity was reached due to the increased electrode mass loading. Hypothetically, as compared to a typical electrode with 2 mg cm^{-2} mass loading (with specific capacity of 80 mAh g^{-1} at a specific current of 20 mA g^{-1}) using the same active materials on an Al current collector, this cell could deliver more than 1.8 times of energy density by area at the full-cell level, which effectively addresses the superiority of the carbon nonwoven current collector with organic active material.

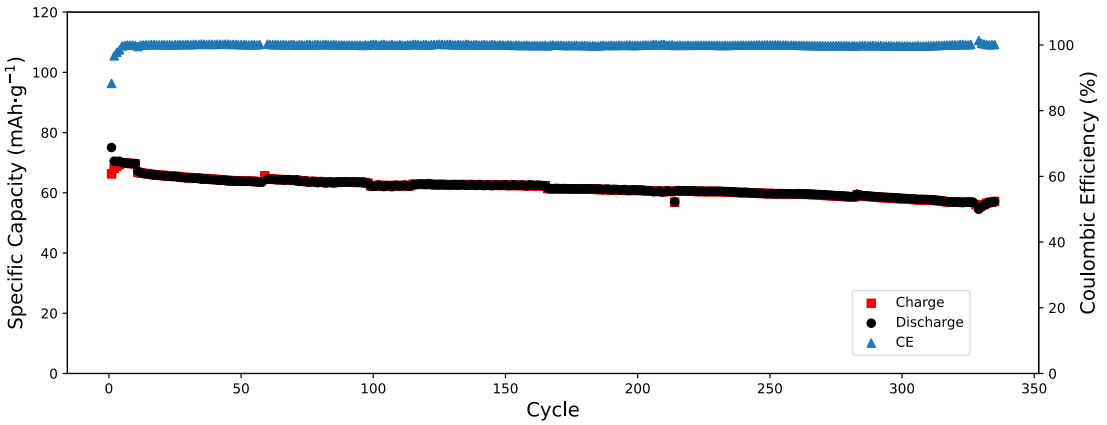

Figure 90. Long-term cycling test of a Li|SIPE|PTCI cell, with an active material mass loading of 4.3 mg cm^{-2} at 80 °C. 1-10 cycles: 10 mA g^{-1}, following cycles: 20 mA g^{-1}.

The charge/discharge profiles are shown in Figure 91. The first discharge (lithiation) showed a different shape than what has been observed earlier, and the shape became symmetrical in the following cycles. During all the cycles, the CV (constant voltage) step during the discharge contributes more capacity than upon charge. Before 200 cycles, the CV contribution upon charge was very small, and significantly increased together with an obvious polarization. From this cell, we could see the CV process could compensate for part of the capacity loss due to the polarization increase.

The ratio between the capacity of CV process and the complete capacity is shown in Figure 92. During all the cycles, the charge part showed less CV capacity than the discharge, which may be explained by two reasons: i) the cut-off voltage for the discharge step was not low enough

to complete the delithiation reaction; ii) the lithiation reaction (discharge) was more sluggish compared to the delithiation (charge). The capacity of the CV process was increasing during the cycling with three steps during charge and discharge. Before ~80 cycles, a minor increase of the CV capacity was observed and then stabilized until ~230 cycles and then significantly increased with a linear trend after 250 cycles. The three steps could also link to the polarization evolution of the cell, which suggests that the degradation of the cell goes through different stages.

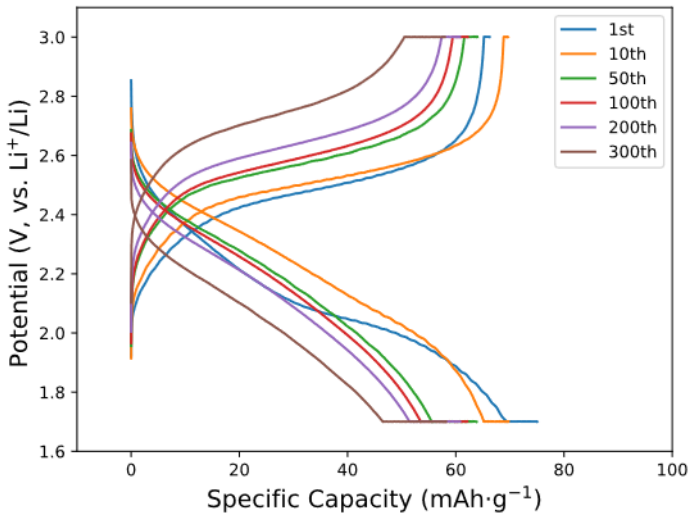

Figure 91. Charge/discharge profiles of the Li|SIPE|PTCI cell at 80 °C.

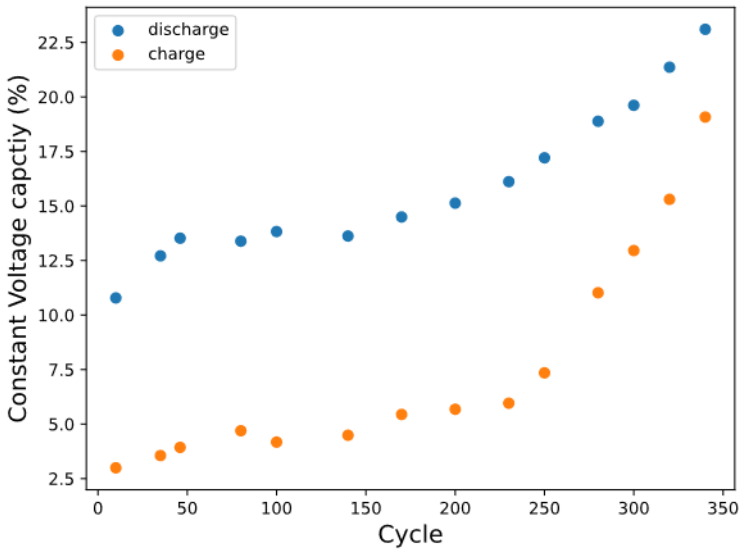

Figure 92. Capacity percentage associated with the constant voltage step during the long-term cycling test.

The polarization evolution could be further analyzed by the EIS, which is shown in Figure 93. EIS was measured for each cycle after charge (delithiation) from 7 MHz to 0.1 Hz. After the initial cycle, the EIS consists of two semicircles. The first one at high frequencies could be the response of the bulk electrolyte. The second one at lower frequencies could be a mixture of different responses including interfacial resistances (formation of SEI and CEI on both negative and positive electrode/electrolyte interface) and charge transfer resistance. Because of the complexity of the system, a quantitative analysis of the interfacial resistance is exceedingly difficult, but the trend of the interfacial resistance evolution is clear. The interfacial resistance increased slightly during the first 100 cycles; a significant increase was exceeded after ~150 cycles. A similar trend was observed for the polarization, which is strongly associated with EIS evolution due to the ohmic drop.

By plotting the specific capacity *vs.* the cell polarization (Figure 94), different from the linear relationship in LFP, a two-step capacity decay was recognized. Upon the ~150 cycles at the beginning, a fast capacity loss (~5mAh g^{-1}) was observed without significant polarization increase. A transition on the polarization increase was shown between 100-150 cycles and followed as linear relationship. This transition is well aligned with the EIS data, which confirmed that the interfacial resistance increase is the reason leading to the capacity decay.

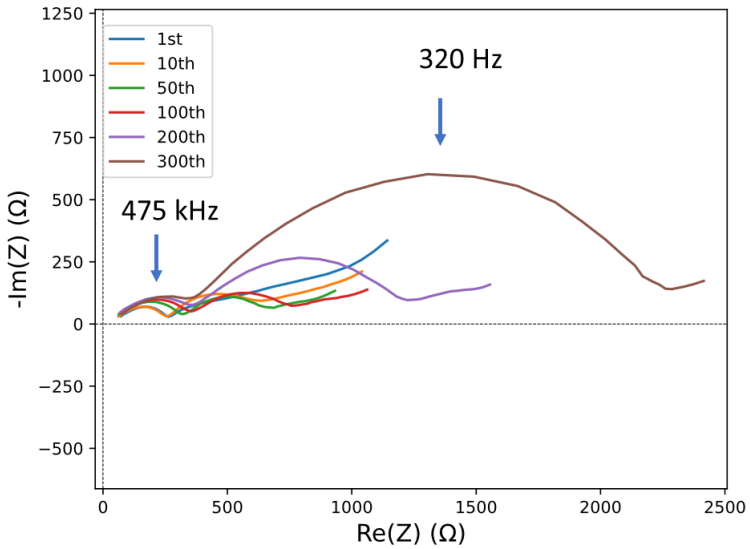

Figure 93. EIS data recorded for the Li|SIPE|PTCI cell at 80 °C.

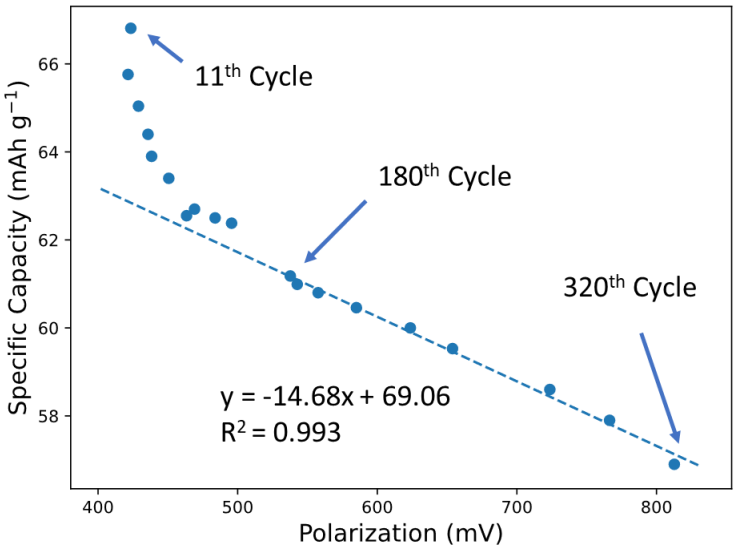

Figure 94. Polarization vs. specific capacity of the Li|SIPE|PTCI cell.

With the analysis of the CV capacity, EIS and polarization, which is consistent with the trend, a clear idea of the cell degradation could be concluded. We assume that the degradation occurred in two stages with different dominate mechanisms. At the beginning of the cycling (before ~150 cycles), the capacity loss with tiny increase on the polarization could be due to dissolution or contact loss of active material at the positive electrode. Indeed, soluble tests were performed (Annex 4), and some weak solubility in ether-based solvent was observed. And then after 150 cycles the capacity decay followed a linear trend with the increase of polarization which could be dominated by the interfacial degradation of the lithium electrode.

All these cycling tests with different electrodes showed similar high CE (>99.9%) and very good reversibility and stability of the PTCI organic material.

Compared to the linear mPEGME-PTFSIVE SIPE in Chapter 2, the crosslinked SIPE, I_{1000}p-SO_3-cr, showed better cycling stability and reversibility. The crosslinked network structure of the SIPE gives better mechanical strength of the crosslinked polymer and can contribute to the improvement of the cell performance.

6 Conclusion & Perspectives

In this chapter, I_{1000}p-SO_3-cr SIPE was prepared and characterized to showing a good ionic conductivity of 4×10^{-5} S cm^{-1} at 90 °C and high Li^+ transference number of 0.96. The SIPE was

also tested with cyclic voltammetry to confirm an electrochemical stability up to 4 V vs. Li^+/Li. Lithium plating/stripping tests showed no dendrite growth or short circuit with high current density and stable cycled for more than 500 h, addressing the reinforcement on the battery safety against the instable lithium metal electrode.

Finally, the organic Li|SIPE|PTCI cells were tested. With the PTCI embedded 3D carbon nonwoven and a mass loading of 4.3 mg cm^{-2}, the prototype cell could operate for more than 320 cycles with a high capacity retention of 85.5% and an average CE of more than 99.9% after several cycles of stabilization. The excellent stability underlined that both SIPE and organic active material have ideal stability, more importantly, their compatibility is also promising.

Notably, as a complex system, a battery consists of multiple components that are critical for the overall performance. A huge amount of work will be needed to adapt to a new material in the system, which is hardly done in a single thesis within the 3-year period. Thus, in this chapter, even with the best attempts of the author, the battery performance remained far from being optimized proved the concept of solid-state organic LMBs. Accordingly, it is easy to imagine that with further optimization the performance of this Li|SIPE|PTCI cell could be possible .The safe and sustainable organic LMB with the SIPE has the potential to deliver high performance to be a powerful candidate for further development.

Reference

1. Ngo, H. P. K. Development and characterization of safety and versatile electrolytes for lithium and post lithium batteries. (Université Grenoble Alpes, 2020).
2. Zhu, J. *et al.* Single-Ion Conducting Polymer Electrolytes for Solid-State Lithium–Metal Batteries: Design, Performance, and Challenges. *Adv. Energy Mater.* 2003836 (2021) doi:10/gjh7hk.
3. Chazalviel, J.-N. Electrochemical aspects of the generation of ramified metallic electrodeposits. *Phys. Rev. A* **42**, 7355–7367 (1990).
4. Tikekar, M. D., Archer, L. A. & Koch, D. L. Stability Analysis of Electrodeposition across a Structured Electrolyte with Immobilized Anions. *J. Electrochem. Soc.* **161**, A847–A855 (2014).
5. Ravn Sørensen, P. & Jacobsen, T. Conductivity, charge transfer and transport number—an ac-investigation of the polymer electrolyte LiSCN-poly(ethyleneoxide). *Electrochimica Acta* **27**, 1671–1675 (1982).
6. Evans, J., Vincent, C. A. & Bruce, P. G. Electrochemical measurement of transference numbers in polymer electrolytes. *Polymer* **28**, 2324–2328 (1987).
7. Watanabe, M., Nagano, S., Sanui, K. & Ogata, N. Estimation of Li+ transport number in polymer electrolytes by the combination of complex impedance and potentiostatic polarization measurements. *Solid State Ionics* **28–30**, 911–917 (1988).
8. Hiller, M. M., Joost, M., Gores, H. J., Passerini, S. & Wiemhöfer, H.-D. The influence of interface polarization on the determination of lithium transference numbers of salt in polyethylene oxide electrolytes. *Electrochimica Acta* **114**, 21–29 (2013).

9. Wetjen, M., Kim, G.-T., Joost, M., Winter, M. & Passerini, S. Temperature dependence of electrochemical properties of cross-linked poly(ethylene oxide)–lithium bis(trifluoromethanesulfonyl)imide–N-butyl-N-methylpyrrolidinium bis(trifluoromethanesulfonyl)imide solid polymer electrolytes for lithium batteries. *Electrochimica Acta* **87**, 779–787 (2013).
10. He, Y., Liu, N. & Kohl, P. A. Difunctional block copolymer with ion solvating and crosslinking sites as solid polymer electrolyte for lithium batteries. *Journal of Power Sources* **481**, 228832 (2021).

Chapter 4 Effect of $LiNO_3$ Doping in Single-Ion Polymer Electrolyte

In this chapter, the focus is on the lithium metal negative electrode. As described in Chapter 2 and Chapter 3, the SIPEs were proved compatible with lithium-metal electrodes via plating/stripping tests for hundreds of hours without short circuiting. However, when looking at the CV data and the deposition of lithium metal (Figure 49 and 79), a passivation behavior was usually observed in addition to low CE of lithium plating/stripping. This phenomenon suggests that SEI between the SIPE and lithium metal could play a significant role for the final performance of LMBs. However, little work has been done on this topic with SIPE. In liquid electrolytes, various additives were applied to improve the SEI and stabilize the interface with the lithium-metal electrode. Among them, lithium nitrate is a fluorine-free, low-cost choice which has been widely adopted in different battery systems.[1–3] The reduction of $LiNO_3$ leads to the formation of a stable passivation layer to mitigate the non-favorable side reactions at the lithium metal electrode. Thus, we chose to apply this additive and study, for the first time with SIPEs, its impact on the electrochemical behavior including SEI formation, lithium reversibility and battery performance.

This chapter is organized as follows:

(1) Introduction of the lithium electrode and the challenges
(2) Electrochemical characterization of $LiNO_3$-doped SIPEs: ionic conductivity, transference number, aging tests, CV, lithium plating/stripping.
(3) Investigation of the effect of $LiNO_3$ doping on the Li metal surface morphology with SEM microscopy and its surface chemistry with XPS.
(4) Investigation of $LiNO_3$-doped SIPEs on LI||LFP cells.

1 Introduction

In pursuing the higher energy density of Li and Post-Li batteries, lithium metal has been utilized since 1970s as the anode of primary Li batteries. Since then, numerous attempts have been made to adapt lithium to secondary Li batteries, i.e., LMBs. Due to its high specific capacity of 3860 mAh g^{-1} and low redox potential of -3.04 (V *vs.* SHE), lithium metal electrodes could maximize the cell voltage and boost the overall energy density.[4,5] However, after decades of studies, lithium-metal electrodes are still used only in very few commercial batteries. Li metal suffers a series of instability including dendrite formation,[6] inhomogeneous SEI formation, "dead" Li, and insufficient Coulombic efficiency,[7] which strongly undermined the safety and durability of the LMBs. Lithium dendrites could grow across the electrolyte and penetrate the separator to short-circuit the battery leading to a huge safety concern.

SIPEs are one of the potential solutions for dendrite-free lithium electrodes. Through immobilizing the anionic functional groups to the polymer chains by covalent bonds, the lithium cation becomes the only "free" ion in the electrolyte, which circumvents the concentration gradient in electrolyte and leads to a high lithium transference number (T_{Li^+}). As predicted by models of Chazalviel[8] and Tikekar[9], lithium can be homogeneously deposited when the anion is tethered on the polymer chain to avoid lithium dendrite formation, especially at higher current densities and/or low temperatures. This could be an efficient solution to improve the safety properties of LMBs.[10]

However, lithium metal still reacts with polymer electrolytes to form a SEI due to its ultra-low redox potential and high reactivity. The continuous reaction between electrolyte and lithium metal will form a thick and inhomogeneous SEI layer which significantly increase the interfacial resistance and reduces the CE of the lithium electrode (i.e., the reversibility of the lithium plating/stripping process). Furthermore, the SEI layer exhibited a different Li^+ diffusion behavior, which could lead to an extra polarization due to the depletion of Li^+ in the SEI especially at high current densities.[11]

The SEI control in the liquid electrolytes has drawn lot of attention, including strategies such as coating protective interlayer on the surface of lithium,[12] adding sacrificing agent,[13] and using lithium alloys.[14] Notably, using additives in the electrolyte could be the easiest way to tune the

SEI and improve the stability at low cost. Additives can be organic molecules such as vinylene carbonate (VC),[1,15] fluoroethylene carbonate (FEC),[16] or lithium salts such as $LiNO_3$,[17] lithium bis(oxalato)borate (LiBOB),[18,19] LiF[20,21] or even ammonium salts.[22] $LiNO_3$ has been applied widely in Li-S batteries as anti-shuttle agent[23] and Li-O_2 batteries.[24,25]

Although most of studies on SIPEs (or composites) claim a good stability against lithium dendrites,[26,27] few among them provide rigorous evidence on lithium reversibility. Indeed, for polymer electrolytes, there could be more difficulties on the surface monitoring and CE determination. The reason could be (1) the generally low conductivity of the SIPEs would not meet the requirements in battery tests (2) the solid-solid interface between Li metal and the polymer, and (3) uncompensated volume changes of lithium during plating/stripping.[28]

In this chapter, the interfacial reaction between a SIPE, with and without $LiNO_3$, and lithium metal was studied. The same SIPE used in Chapter 3, which has been proven to be compatible with lithium metal with dendrite-free plating/stripping was further investigated to understand the SEI formation and lithium reversibility.

2 Electrochemical characterizations of a $LiNO_3$-doped SIPE

As proven in the previous chapter, the I_{1000}p-SO_3-cr SIPE with high conductivity and transference number could be the best example to check the effect from the additive. The polymer electrolyte I_{1000}P-SO_3-db was synthesis following the previous work.[29] The prepolymer I_{1000}P-SO_3-db was dissolved in DI water at ambient temperatures and the photo-initiator and 0, 0.5, 1 wt.% of $LiNO_3$ were added to form a homogeneous solution. The solvent was evaporated, and the mixture was cast yielding thin films with ~60 μm thickness and crosslinked by UV irradiation.

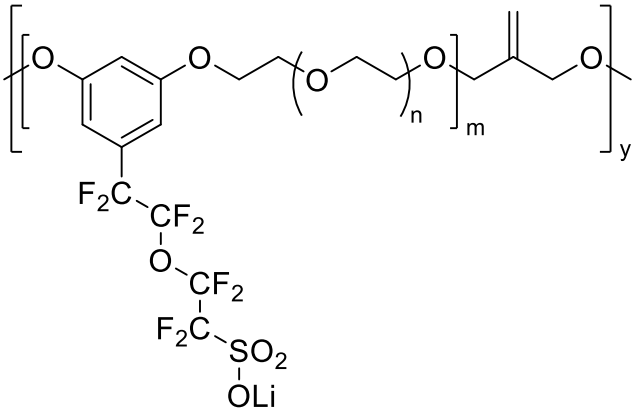

Figure 95. Structure of I_{1000}p-SO_3-db SIPE.

2.1 Ionic conductivity and Li^+ transference number

Thus, ionic conductivity and lithium transference number were measured in presence of $LiNO_3$ to compare with the SIPE without the additive in order to understand the impact of the addition of free ionic species.

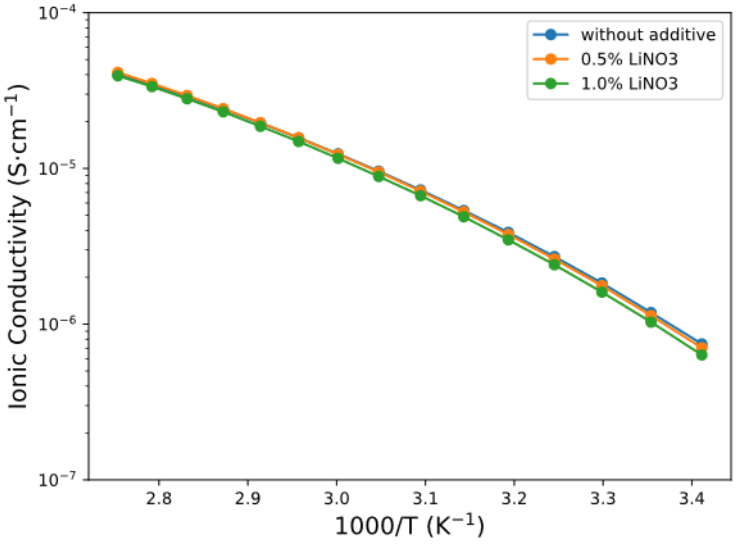

Figure 96. Ionic conductivities of 0, 0.5, and 1 % $LiNO_3$-doped SIPEs.

As shown in Figure 96, the ionic conductivity of the $LiNO_3$-doped SIPEs exhibited almost the same as the non-doped SIPE at higher temperature (≥ 60 °C). At lower temperatures, the doped SIPE showed a slightly lower ionic conductivity (7.5×10^{-7}, 7.0×10^{-7} and 6.3×10^{-7} S cm^{-1} for 0, 0.5, 1.0% $LiNO_3$-doped SIPEs at 20 °C, respectively.) than the non-doped SIPEs. All the

conductivity-temperature dependences follow a VTF-type behavior.

Via fitting, the three parameters of the VTF equation were determined, which are listed in the following table:

Table 8. VTF parameters of SIPE with 0, 0.5, 1% $LiNO_3$ doping, obtained by non-linear fitting.

Electrolyte	σ_0 (S cm^{-1} $K^{-0.5}$)	T_0 (K)	E_a (kJ mol^{-1})	E_a (eV)
SIPE 0 % $LiNO_3$	0.182	200	7.39	0.0766
SIPE 0.5% $LiNO_3$	0.238	198	7.82	0.0810
SIPE 1% $LiNO_3$	0.236	199	7.84	0.0812

Since the polymer matrix of the SIPEs was identical, the ideal transition temperature T_0 showed almost the same values of ~200 K. The pre-exponential factor and active energy increased with an increase of $LiNO_3$, which could explain the slight difference at low temperatures.

The doping of $LiNO_3$ can affect the lithium transference number due to the presence of free anionic species. Thus, the Li^+ transference number was evaluated electrochemically with the Bruce-Vincent method:

$$t_{Li}^{+} = \frac{I_{ss}(\Delta V - I_0 R_0)}{I_0(\Delta V - I_{ss} R_{ss})}$$

where I_0, I_{ss} and R_0, R_{ss} are the currents and interfacial resistances in the initial and steady-state, respectively. The ΔV is the voltage applied. As explained in the previous chapter, aging could affect the polarization process. To confirm this, and get an accurate lithium transference number, an aging process with 80 h of stripping/plating (5 cycles at 10 μA cm^{-2} and 5 cycles at 100 μA cm^{-2}) was applied. The measurement procedure is depicted in Figure 96.

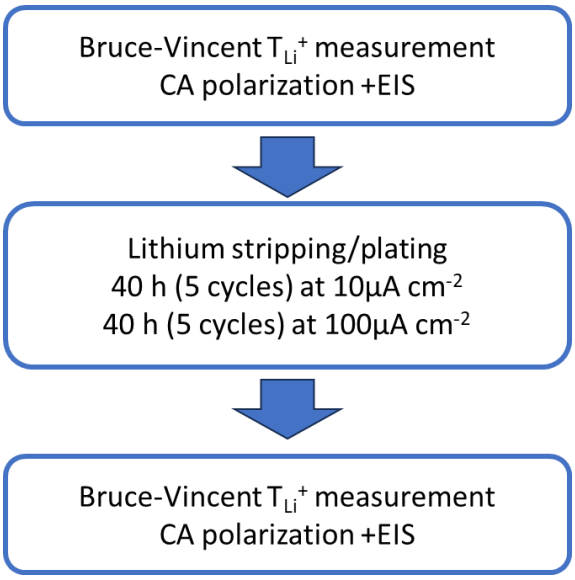

Figure 96. Illustration of the measurement of the Li^+ transference number.

The EIS spectra and polarization curve of pristine symmetric Li|SIPE|Li cells are shown in Figure 98. The pristine SIPE film without any doping showed an extremely high T_{Li}^+ of 0.996 by using the Bruce-Vincent method (from Chapter 3). Whereas the 0.5% $LiNO_3$-doped film exhibited a slightly lower value of 0.984. Due to the evolution of interfacial resistance, the current did not fully reach a steady-state after 10 h, which might undermine the accuracy of the result. Thus, the stabilization of the interfacial resistance was realized by a galvanostatic cycling (i.e., plating/stripping) of the same cell for 80 h. After stabilization, the transference number was measured again with the same Bruce-Vincent method, which is shown in Figure 98. A slightly lower T_{Li}^+ of 0.957 was obtained with the stabilized cell, which reached a steady-state current during the polarization. The EIS tests overlapped before and after polarization, suggesting a stable interface between the Li electrode and the electrolyte. The polarization and impedance values are listed in Table 9.

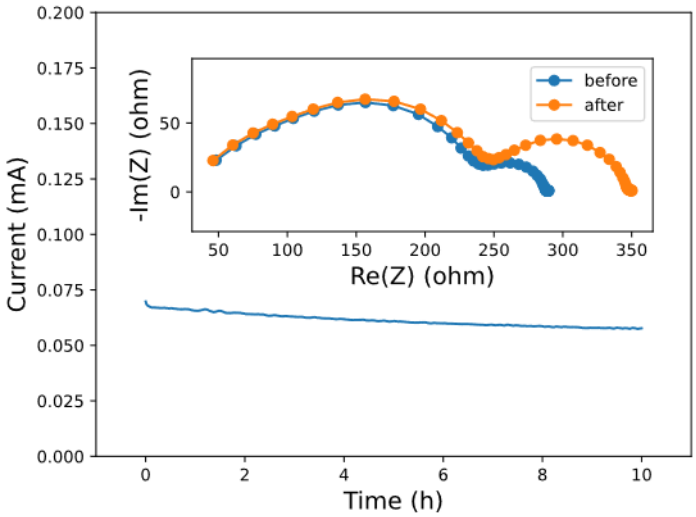

Figure 97. Lithium transference number determination, SIPE with 0.5% $LiNO_3$.

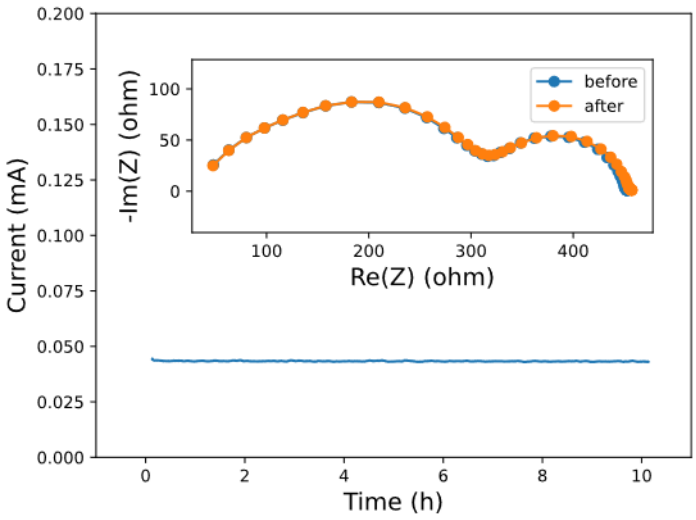

Figure 98. Determination of the lithium transference number for the SIPE comprising 0.5% $LiNO_3$ after 80 h cycling.

Table 9. The polarization and impedance values in the Li transference number measurements.

Sample	I_0 (mA)	I_{ss} (mA)	R_i (Ω)	R_i'(Ω)	T_{Li^+}
SIPE without additive	0.0362	0.0305	202	304	0.996
SIPE with 0.5% $LiNO_3$	0.0697	0.0577	50.6	106.5	0.984
SIPE with 0.5% $LiNO_3$ after 80h cycling	0.0445	0.0430	133.8	135.5	0.957

The repeating unit of I_{1000}p-SO_3-db has a molecular weight of 1377 g mol^{-1} and the molar mass of $LiNO_3$ is 69 g mol^{-1}. Thus, for the 0.5% $LiNO_3$-doped SIPE, the ratio between the immobilized anion (perfluorosulfate) and free anions (NO_3^-) corresponds to 10:1, which could yield a Li^+ transference number of 0.91 with a rough estimation, if we assume all the ionic species have a similar mobility and $LiNO_3$ has complete dissociation. The results from the electrochemical tests were higher than this prediction, which suggests that not all the $LiNO_3$ salt is dissociated and provided free nitrate anions in the PEO-type solvent. $LiNO_3$ has been proven to be less dissociated and forming ion clusters in blend-type polymer electrolytes, which is correlated with the phenomenon observed here.

To sum up, the 0.5% $LiNO_3$-doped SIPE did not greatly alter the ion transportation behavior including the ionic conductivity of 4×10^{-5} S cm^{-1} at 90 °C and lithium transference number of 0.96. This could be ascribed to not only the minor amount of additive used but also the lows dissociation of $LiNO_3$.

2.2 Aging test

As shown in the transference number determination process (Figure 77 and 78), the interfacial resistance of the cells was evolving during serval days suggesting a formation/modification of passivation layer. This SEI formation reaction is not only taking place when current passes through the cell, but also without any current, just by contact. Due to the low potential of Li metal (compared to most of organic compounds), the surface of the SIPEs can be reduced via a spontaneous reaction and the products form the SEI layer. Thus, an aging test was conducted by placing Li|SIPE|Li cells in isothermal chamber of 80 °C under open circuit condition.

The aging test was conducted with symmetric Li|SIPE|Li cells to record the evolution of the lithium|SIPE interphase. The cells with doped and non-doped SIPE were prepared using CR2032 type coin cells and placed inside an isothermal chamber of 80 °C. EIS spectra were collected each 4 h, with a 20 mV potential perturbation.

The EIS spectra of the cells comprising the SIPEs with and without $LiNO_3$ doping are shown in Figure 99 and 100.

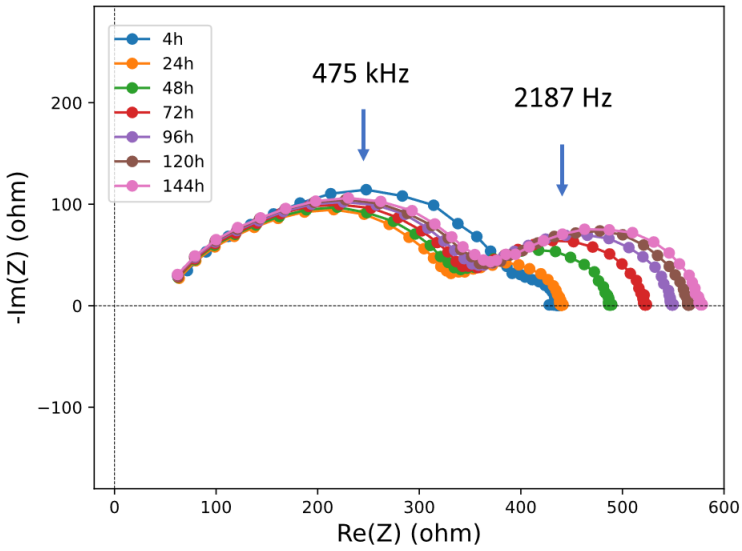

Figure 99. EIS spectra of the Li|SIPE|Li cell comprising the non-doped SIPE upon aging at 80 °C.

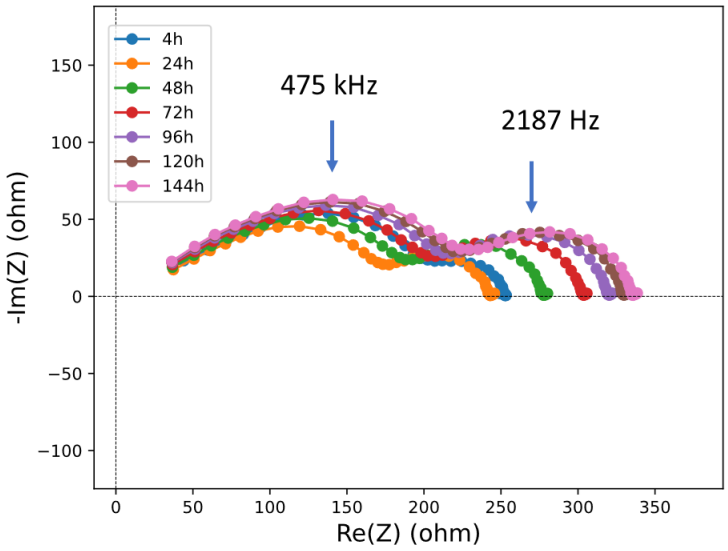

Figure 100. EIS spectra of the Li|SIPE|Li cell comprising the 0.5% $LiNO_3$-doped SIPE upon aging was performed at 80 °C.

The SIPE without additive showed two semi circles in the Nyquist plot, the one at higher frequencies (475 kHz) corresponds to the electrolyte response and that at lower frequencies (2.19 kHz) to the interface. Each electrochemical response may be represented as a parallel linked resistor and constant phase element (CPE). The equivalent circuit of the Li|SIPE|Li cell is shown in Figure 101, where R1, R2, R3 are the cable resistance, the bulk resistance of

electrolyte and the interfacial resistance, respectively. Q2 and Q3 are CPEs for the bulk and interface, respectively.

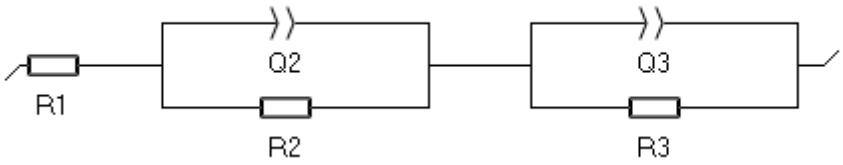

Figure 101. Equivalent circuit of the Li|SIPE|Li cell.

By fitting with the equivalent circuit, the interfacial resistance was plotted *vs*. the square root of time, in Figure 102. For both samples, linear trends in the plot could be associated to the SEI growing with a limitation of mass transport. The interfacial resistance of the $LiNO_3$-doped SIPE increases and then after ~64 h showed a stabilizing trend, which can be explained by the formation of a stable SEI. While the SIPE without additive showed similar trend, it could not reach the stable state within 144 h and exhibit a much larger interface resistance compared to the doped electrolyte. The interfacial resistance evolution proved that the reaction between the SIPE and the Li metal electrode was spontaneous even without a current passing through.

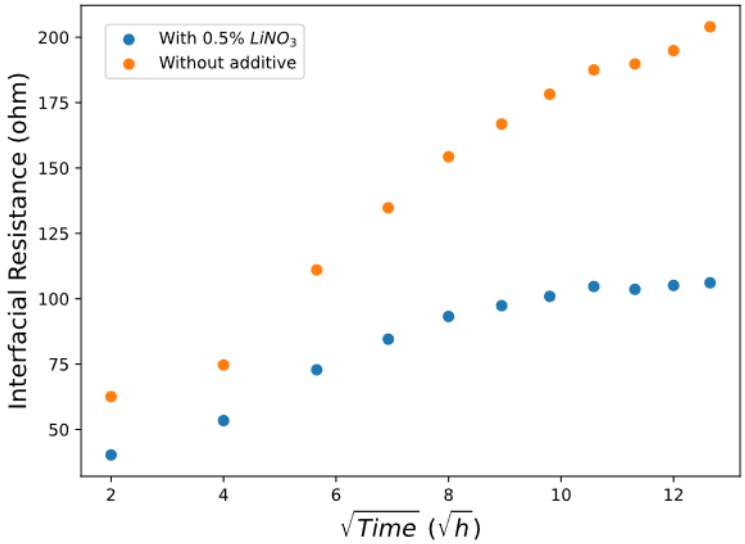

Figure 102. Interfacial resistance evolution of the Li|SIPE|Li cells *vs*. the squire root of time during 1 week.

The bulk resistance of both electrolytes also increased during the aging test, which was not

expected. Similar phenomena were also observed by aging tests[30] or during transference number measurement in the literature,[31–33] and the bulk resistance was increasing during the polarization process. Thus, we assume that the evolution of the bulk resistance is related to the contact between SIPE and Li metal which gets more resistive during the aging process due to the SEI formation.

2.3 Cyclic Voltammetry (CV)

The CV experiments with an inert working electrode, were conducted to examine the electrochemical stability, especially upon oxidation as well as the lithium plating/stripping efficiency.

The CV of the electrolyte was conducted with coin cell with Li|SIPE|SS configuration. The cells were cycled with a scan rate of 0.2 mV s^{-1} between 4.0 and -0.5 V (*vs*. Li^+/Li) for 8 cycles. The CVs start at OCV of the cell and scan towards oxidation up to 4.0 V and then reduced to -0.5 V.

As it shown in Figure 103 and 104, both electrolytes, with and without additive, no obvious oxidation before 4.0 V was observed during all 8 cycles, which corresponds to the flat line between 1-4 V. At lower potential region, lithium plating was observed between 0 and -0.5V, lithium stripping between 0 and 1 V. Contrary to the oxidation process, a continuous evolution of the intensity and the plating/stripping peaks were observed for both electrolytes. For the first cycle, both electrolytes showed a low amount of lithium plated in the experimental conditions used, potential > -0.5 V (*vs*. Li^+/Li) indicating a large polarization of the Li^+ reduction process. In addition, the CE was low, as shown in Figure 105. However, during cycling, the two electrolytes behaved differently. For the SIPE without $LiNO_3$ the amount of plated Li decreased after the third cycle and the plating/stripping CE stabilized at only 20%. The weak reduction process could be associated with the passivation of the working electrode inducing a strong polarization of the process. Regarding the poor CE, one explanation could be the spontaneous oxidation of the fresh lithium formed by plating with the formation of a passive layer which avoided its complete chemical oxidation. However, as the amount of deposit lithium was rather low, its consumption due to a chemical reaction had a significant impact on the lithium

plating/stripping CE.

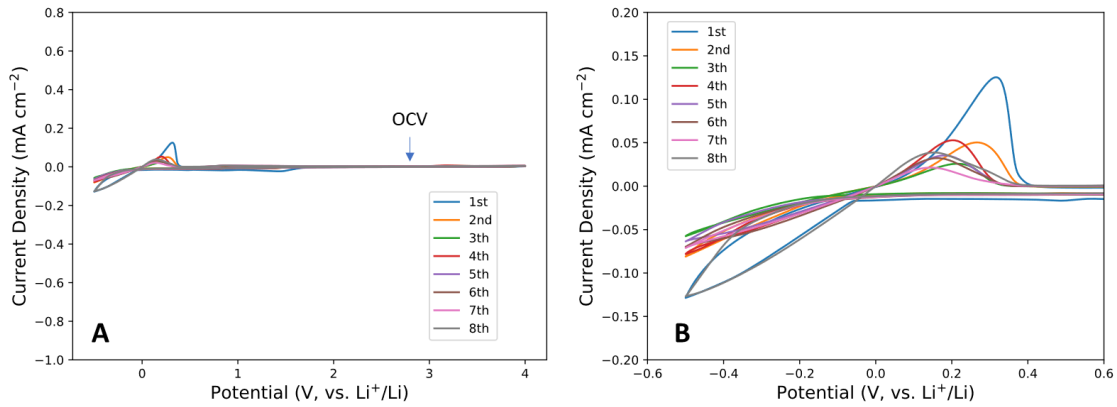

Figure 103. CV of Li|SIPE|SS cells with SIPEs without additive. (A) Scan between -0.5 to 4.0 V (B) Magnification on the lithium plating/stripping peaks.

Concerning the 0.5% $LiNO_3$-doped SIPE, similarly to the SIPE without $LiNO_3$ for the second cycle the amount of Li stripped decreased and the polarization of the oxidation process increased while for the third cycle both started to improve. The kinetics of the lithium deposition increased cycle by cycle up to some stabilization beginning from the 5th cycle.

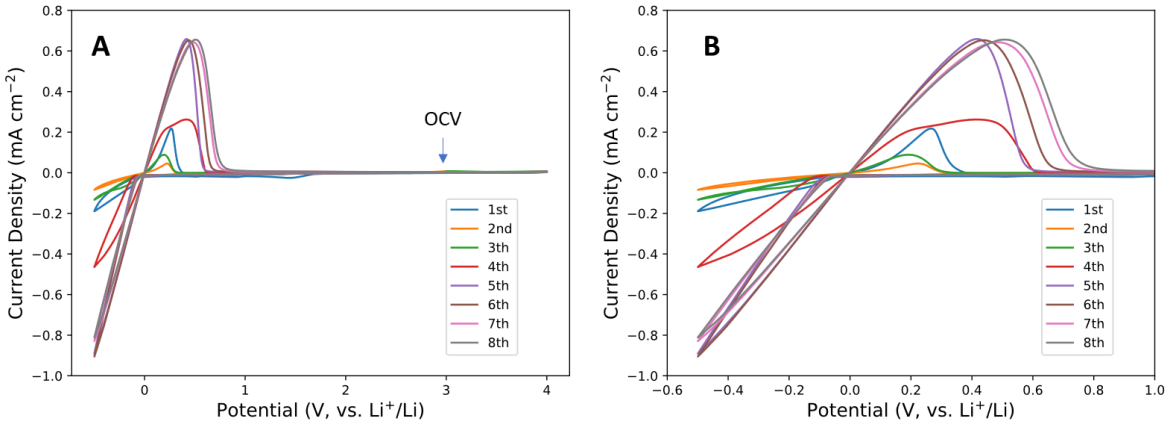

Figure 104. CV of Li|SIPE|SS cells with 0.5% $LiNO_3$-doped SIPE. (A) Scan between -0.5 to 4.0 V (B) Magnification on the lithium plating/stripping peaks.

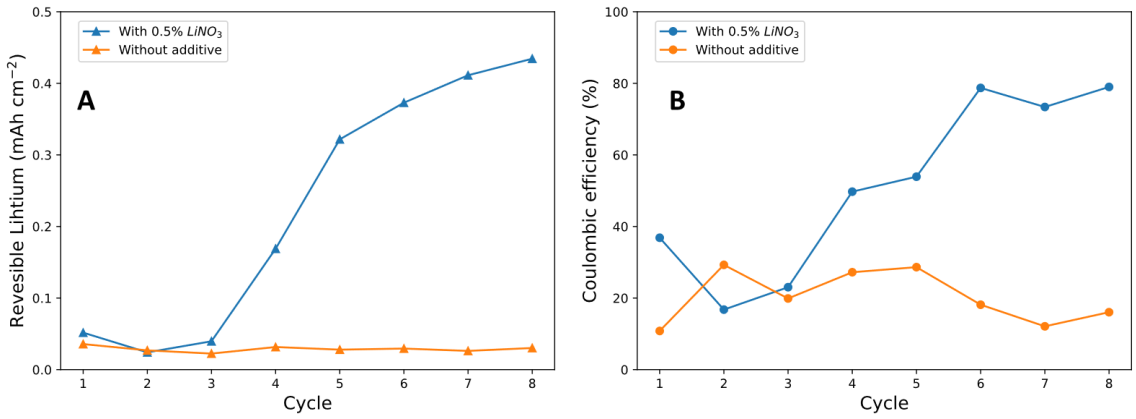

Figure 105. (A) Comparison of reversible lithium plating in CV tests of the 0.5% $LiNO_3$-doped SIPE and non-doped SIPE. (B) Comparison of the lithium plating CE in CV tests of the 0.5% $LiNO_3$-doped SIPE and non-doped SIPE.

Thus, we could confirm that the $LiNO_3$ doping of the SIPE has a strong effect on the surface of the Li metal electrode, indicating that $LiNO_3$ formed a stable passivation layer that mitigated further reaction between electrolyte and lithium metal, which increases the lithium reversibility. At the same time, the passivation layer with low resistance allowed lithium ion passing through, which improved the amount of lithium deposition.

To gain more insights and to better understand the impact of $LiNO_3$ on the plating/stripping behavior, the liquid electrolyte of 1 M $LiNO_3$ in tetraethylene glycol dimethyl ether (TEGDME) (with Celgard® 3401 as separator) was studied by CV in a Li||SS cells. The CV curves, the corresponding CE, and amount of lithium stripped were shown in Figure 105, A and B. The lithium plating/stripping in the first cycle was much better as compared to both SIPEs, with a CE of 93.4% and reversibly stripped lithium of 19.5 mAh cm^{-2}. The high amount of lithium plated can be explained by the high conductivity of the liquid electrolyte as compared to the cells comprising the SIPEs. However, the lithium plate decreases with the cycling from 19.5 to 14.3 mAh cm^{-2} from the first to the fourth cycles, indicating some polarization of the reduction process and the CE remained constant at a value of 0.91, which is very high. It can also be noticed, that the presence of two well distinguished peaks during the lithium stripping at 0.35 V and 0.69 V, possibly associated to the heterogeneity of the lithium passivation. Due to the N-rich SEI layer, from the reduction of $LiNO_3$, an additional polarization could be needed to finish

the lithium stripping beneath the SEI layer which led to the lithium stripping peak shifting to higher voltages. The liquid electrode showed a much larger amount of Li plating/stripping and much better CE than observed for the SIPEs, which is not only due to the higher ionic conductivity but also the excellent wettability of the liquid compared to crosslinked SIPEs.

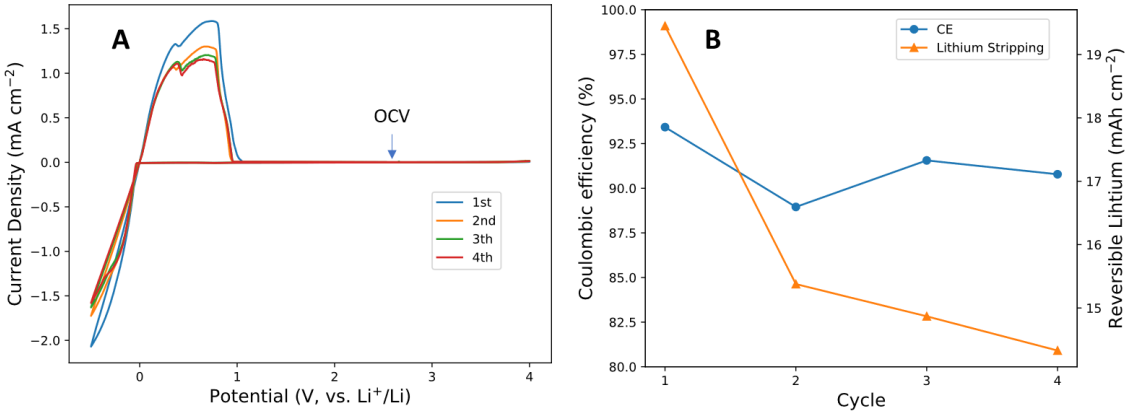

Figure 106. (A) CV of Li||SS cell with 1M $LiNO_3$ in TEGDME electrolyte (B) Lithium CE and lithium stripping from the CV of Li||SS cell with 1M $LiNO_3$ in TEGDME.

3. Lithium plating/stripping tests

The galvanostatic lithium plating/stripping allows to plate much larger amounts of Li and can give additional insights into the interfacial reactions, on the reactivity of lithium metal, as well as on the morphology of plated lithium. The evolution of the voltage profile upon cycling and the resistance against lithium dendrite growth are interesting parameters to study.

The lithium plating/stripping tests were conducted with two different types of cells i.e., symmetric Li|SIPE|Li cells and Li|SIPE|Cu cells for a deep analysis of the evaluation of resistance against lithium dendrite growth and the reversibility of lithium metal plating respectively.

3.1 Li|SIPE|Li cells

Symmetric Li|SIPE|Li cells are the typical cell configuration for lithium plating/stripping test. The plated/stripped was performed alternatively on both electrodes to dynamically keep the amount of lithium on the electrode constant. The amount of lithium plating/stripping was represented by the charge passing through the external circuit, which can be calculated by Faraday's laws of electrolysis:

$$m_{Li} = \frac{QM_{Li}}{Fn}$$

where Q is the charge passed through the external circuit, M_{Li} is the molar mass of lithium which is 6.94 g mol^{-1} , F is Faraday's constant (26.801Ah mol^{-1}) and n is the number of electrons transferred in the reaction (for Li, n = 1). With the density of Li metal (0.53 g cm^{-3}), m_{Li} can be converted into the thickness of lithium metal that is stripped/plated. The specific capacity of 1 g of lithium metal is 3860 mAh. For 1 mAh of charge, the lithium stripped/plated on the electrode is 0.26 mg cm^{-2} or 4.8 μm in thickness for the given area.

Each electrolyte was evaluated with a long-term plating/stripping test. For the non-doped electrolyte, the results shown in the previous chapter (Figure 80) has already proved that at high current density of 0.2 mA cm^{-2} and 0.8 mAh cm^{-2} (3.8 μm) of lithium, the cell could be cycled for more than 480 h, with no short circuit. This result has fully addressed the stability of the interface between the I_{1000}p-SO_3-cr electrolyte and the lithium-metal electrode and the mitigation of lithium dendrite formation, which could be the standing point of the following study.

Here, the target is to understand the effect of the $LiNO_3$ doping in SIPEs. To better compare the difference for the doped and non-doped SIPEs, plating/stripping tests were conducted with Li|SIPE|Li cells with the same parameters (0.1 mA cm^{-2}, 8 h per cycle). The voltage profiles of the SIPE without doping, and with 0, 0.5% and 1.0% $LiNO_3$ are shown in Figure 107 from top to bottom.

All the three SIPEs showed stable plating/stripping with low overvoltage and no sign of degradation, polarization or short circuit were observed. For the non-doped and 0.5% $LiNO_3$ SIPEs, both cells exceeded 700 h. 1% $LiNO_3$ SIPE achieved more than 400 h and is still cycling.

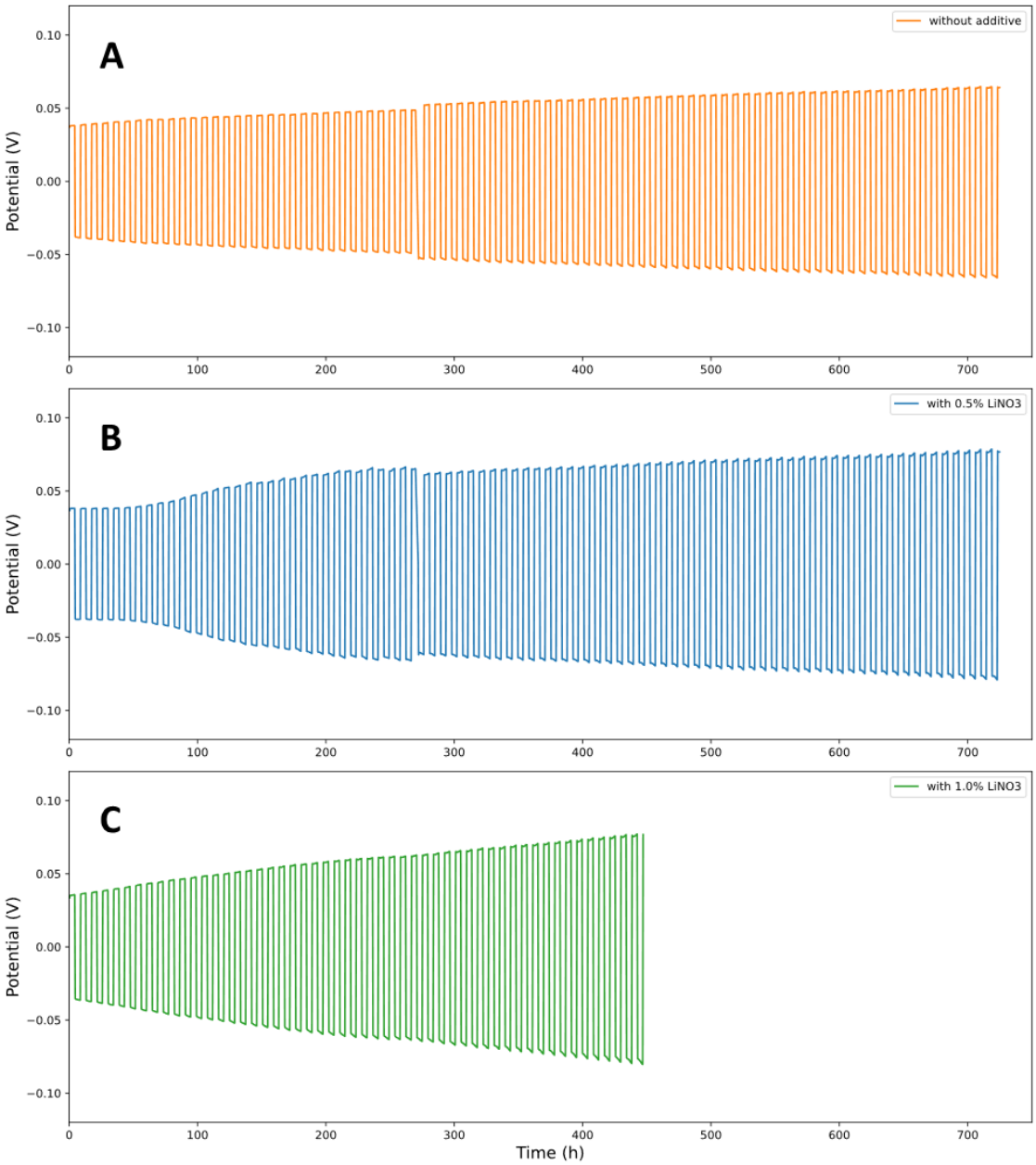

Figure 107. Lithium plating/stripping test Li|SIPE|Li cells: (A) non-doped SIPE (B) SIPE with 0.5% $LiNO_3$ (C) SIPE with 1.0% of $LiNO_3$.

By comparing the overvoltage of the three cells, a trend of non-doped SIPE< 0.5% $LiNO_3$ SIPE< 1% $LiNO_3$ SIPE was observed. The higher overpotential evolution was observed for $LiNO_3$ in addition with a non-flat shape curve is observed, which could be explained by the free NO_3^- anions, decreased the lithium transference number (although not observed with T^+ measurement), which led to extra concentration gradient and polarization. The modification of the overpotential for all the three samples in long-term was related to the accumulation of a

passive layer, which induced an increasing interfacial resistance. Anyhow, the overpotential for all the three cells was small and stable over the long-term tests. More importantly, no short circuit was observed, which indicated that all the three SIPEs suppressed dendrite formation and improved the safety of the LMB cells.

3.2 Coulombic efficiency determination

The plating/stripping was conducted with high excess of lithium in both electrodes, which cannot help to fully understand the reaction on the interface and particularly the reactivity of lithium. Therefore, we performed plating/stripping tests with limited lithium resources with the aim to have more information on the CE of the lithium plating/stripping process.

3.2.1 Depletive Li plating/stripping with Li|SIPE|Cu cells

In this test, Li|SIPE|Cu cells were used. First, a fixed amount of lithium was plated on the Cu electrode, which is represented by the charge passed in the external circuit Q_P. Since initially no lithium was on the Cu electrode, all the lithium plated formed a limited Li reservoir. Then a depletive stripping process followed to remove Li from the surface of Cu with a cut-off voltage of 1 V, which indicated that all the removable Li was stripped. The amount of lithium removed from the Cu surface was represented by the amount of charge passing through the external circuit Q_S. The scheme of the experiment is shown in Figure 108.

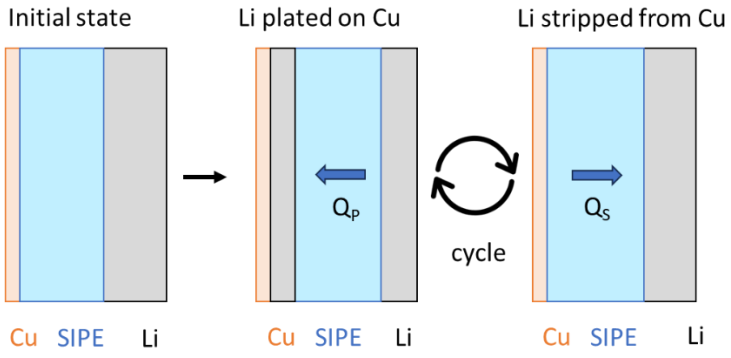

Figure 108. Li|SIPE|Cu striping/plating tests.

The CE of the lithium could be simply determined by the equation:

$$CE = \frac{Q_S}{Q_p} = \frac{t_s}{t_p}$$

where n is the number of cycles, t_S and t_P are the time of the stripping and plating process (as the current is constant), respectively. The average CE can be simply calculated by:

$$CE_{avg} = \frac{1}{n}\sum \frac{Q_s}{Q_p}$$

The plating/stripping tests were conducted with both 0.5% $LiNO_3$-doped and non-doped electrolytes for 20 cycles, which is shown in Figure 109. Each cycle consisted of 0.1 mA cm^{-2} plating for 4h, which equals to 0.4 mAh cm^{-2} or 1.9 μm lithium, and 0.1 mA cm^{-2} stripping until voltage exceeded 1.0 V to deplete lithium on Cu.

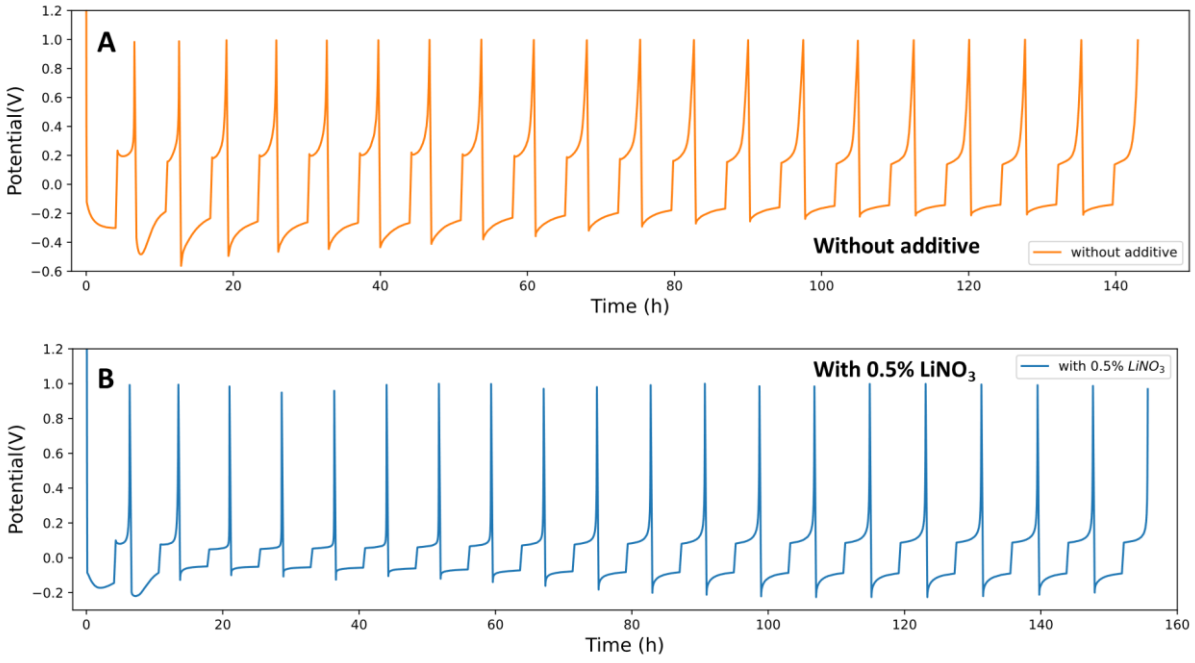

Figure 109. Lithium plating/stripping of Li|SIPE|Cu cells: (A) non-doped SIPE (B)SIPE with 0.5% $LiNO_3$.

For both electrolytes, the plating of lithium at the first cycles showed increasing and then decreasing of polarization during the plating, indicating the difficulty of the Li nucleation on the surface of Cu. Low CE was also observed for both SIPEs. This could be related to the different reaction at the surface of Cu including the SEI formation and reduction of surface oxides (e.g., $Cu_2O + 2Li^+ + 2e^- \rightarrow 2Cu + Li_2O$).

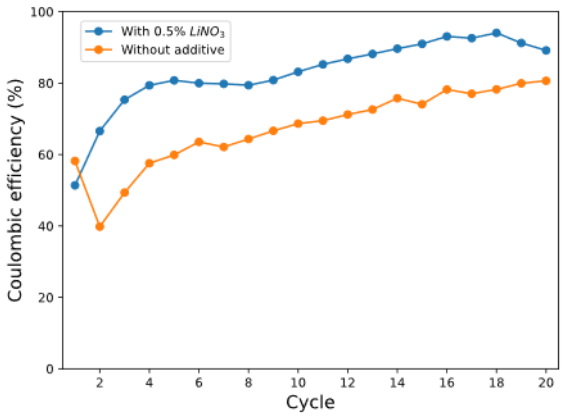

Figure 110. Coulombic efficiency of lithium plating/stripping with Li|SIPE|Cu cells.

For the SIPE doped with 0.5% $LiNO_3$, after the initial cycles that involved more side reactions, the following cycles showed a quick improvement of the CE from 51% to 79% (the 4th cycle) and finally reached a maximum of 94% in the 18th cycle. The SIPE without the additive showed a higher initial CE of 58% and a drop to 40% in the 2nd cycle, which gradually improved to 80% after 20 cycles. The CE evaluation of both cells is shown in Figure 110.

For the non-doped SIPE, the polarization decreased during cycling, while the 0.5% $LiNO_3$-doped SIPE showed an increasing trend. Although The polarization of the two samples showed different trend, the absolute value of the $LiNO_3$-doped SIPE is much lower than the non-doped SIPE throughout the tests.

The 5th cycle of the plating/stripping could be a good example to represent the difference between the $LiNO_3$-doped and non-doped electrolytes, as plotted in Figure 111. The Li plating process for the two SIPEs exhibited different shapes. For the SIPE without additive, the polarization decreased during the plating from an initial value of 0.46 V to the final value of 0.26 V. For the SIPE doped with 0.5% $LiNO_3$, a stable polarization was observed, which had

an initial value of 0.12 V and quickly dropped to 0.06 V. Compared to the SIPE without the additive, the $LiNO_3$-doped sample exhibited a much lower polarization, which is about one third of the voltage, suggesting an easier and more stable lithium plating on the Cu electrode. In the stripping part, the two SIPEs showed similar trends as the plating, i.e., less polarization was observed for the $LiNO_3$-doped electrolyte. More importantly, the CE of the two SIPEs were 81% *vs*. 60% for doped and non-doped SIPE, which means that the SIPE without additive is facing significantly more Li loss than the $LiNO_3$-doped SIPE.

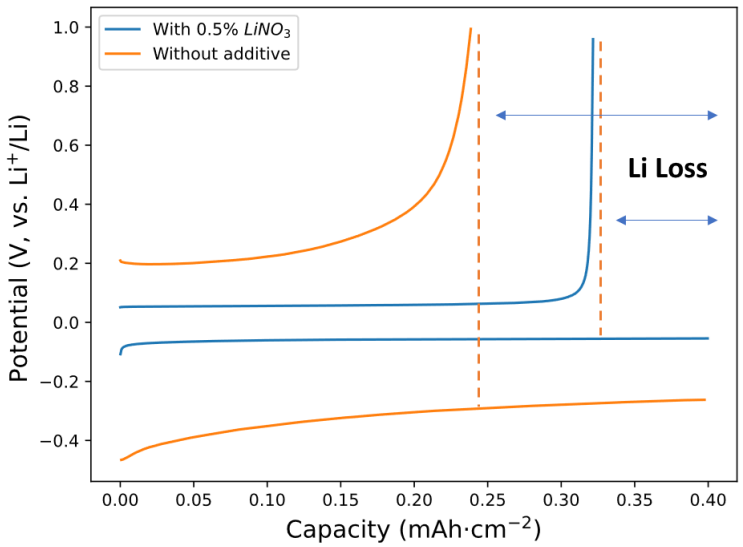

Figure 111. 5th cycle potential profile of the lithium plating/stripping test conducted in Li|SIPE|Cu cells.

3.2.2 Modified method for Li plating/stripping in Li|SIPE|Cu cells

To get rid of the side reactions between Li and Cu, which led to an initial Li loss, a modified method for the determination of the lithium CE was applied. With a pristine Li|SIPE|Cu cell, a long plating, and a depletive stripping of 2 mAh cm^{-2} (9.6 μm) Li was applied first to clean the surface of the Cu electrode and stabilize the interface. After this preconditioning process, another 2 mAh cm^{-2} of Li was plated on the Cu electrode as a limited reservoir (Q_R). Then, a plating/stripping of a small amount of lithium (Q_S and Q_P, 0.1 mAh cm^{-2}, 1/20 compared to the reservoir) was conducted between the lithium reservoir on the Cu and Li foil and cycles, until the Li reservoir was completely consumed, which indicated by the stripping voltage exceeding

its upper limit of 1.0 V. The experimental procedure depicted in Figure 112.

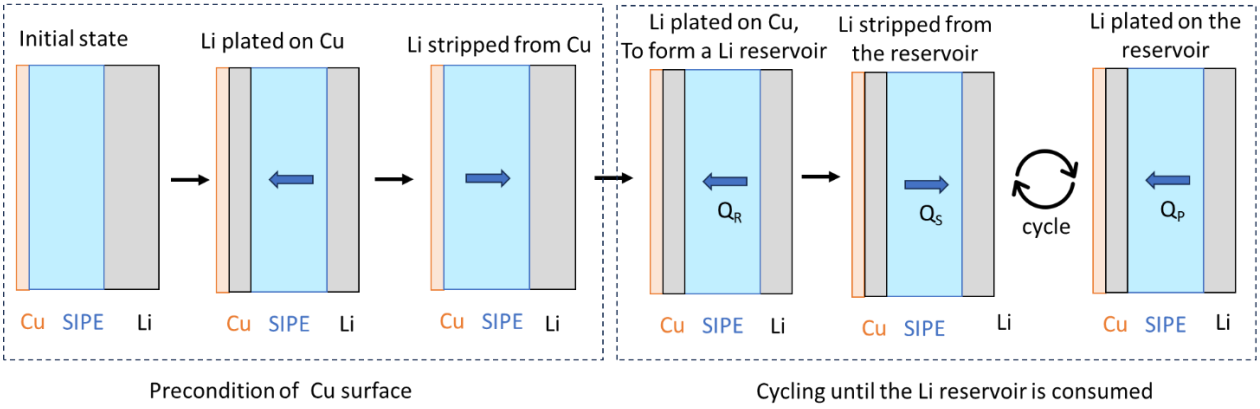

Figure 112. Schematic illustration the modified procedure for the determination of the CE.

The average CE can be determined by the following equation:

$$CE_{avg} = \frac{\sum Q_S}{\sum Q_P + Q_R}$$

Compared to the previous plating/stripping on the Cu electrode to determine the CE, this method could be more accurate due to the initial loss of Li, which is compensated by a precondition step.

Additionally, in this procedure, the cycling condition is closer to the cycling conditions of an LMB due to the fact that the plating is actually taking place on the lithium-metal rather than an "anode-free" LMB which the plating initially occurs on the surface of an inert working electrode (Cu).

For the non-doped SIPE, the preconditioning process showed an initial CE of 44.8%. The polarization of the cell showed a bump during the first 16 h during the Li plating, evidencing the difficulty of the first nucleation and the presence of side reactions. The minimum voltage is -0.42 V and finally reached -0.13 V.

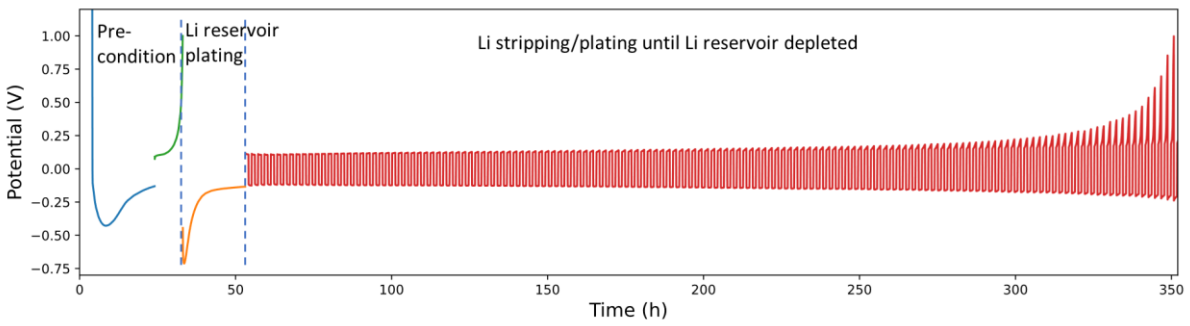

Figure 113. Modified CE determination with non-doped SIPE, in Li|SIPE|Cu cells.

The lithium plating/stripping of 0.1 mAh cm^{-2} was conducted for 146 cycles, until the stripping voltage exceeded 1.0 V, indicating that the Li reservoir was depleted. Thus, the total capacity of plating and stripping can be simply determined as the same $\Sigma Q_P = \Sigma Q_S$ = 14.6 mAh cm^{-2} and Q_r=2 mAh cm^{-2} and an average CE of 88.0%.

The EIS spectra recorded during the precondition process are shown in Figure 114. The Li|SIPE|Cu cell showed a blocking behavior in the first plating (precondition) due to lack of Li on the working electrode. SIPE bulk response of a semicircle (475 kHz) was observed and followed by capacitance behavior at low frequencies. After plating the first 2 mAh cm^{-2} of Li, a second semicircle response of SEI (4.7 kHz) appeared which was very tiny and noisy. The noise at very low frequencies (<200 Hz) indicates the fast evolution of the interface. After the first exhaustive stripping, all the removable Li was electrochemically oxidized. However, only 44% of plated lithium was removed, which indicates that the major part of the plated Li reacted with the electrolyte to form different products which can remain on the surface of Cu electrode. The EIS measurement exhibits an interfacial response with a large semi-circle (Z_{real}=8000 Ω) indicating the formation of a passivation layer on the surface of the Cu electrode, comprising also so-called “dead” lithium.

After the third plating of 2 mAh cm^{-2}, the EIS (Figure 114) showed a typical 2-semicircle shape in the frequency range used, which aligned with the Li|SIPE|Li cells. This confirmed the formation of a Li reservoir that could simulate symmetrical Li plating/stripping. The interfacial resistance of 1100 Ω was determined.

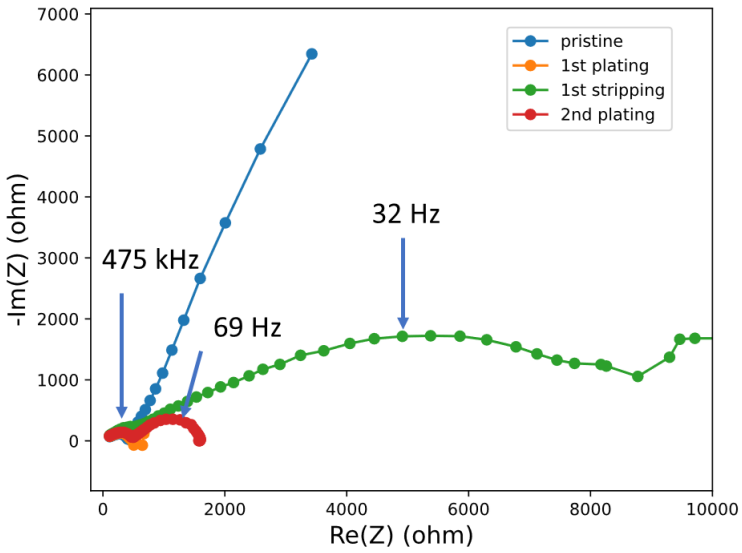

Figure 114. EIS spectra during the precondition of a Li|SIPE|Cu cell with the non-doped SIPE.

The following cycles of 0.1 mAh cm^{-2} plating/stripping showed similar EIS spectra (Figure 115.) as compared to the Li|SIPE|Li cell. The bulk and interfacial resistances obtained by fitting with the equivalent circuit, are shown in Figure 101. The interfacial resistance was 1100 Ω for the first cycle, which is aligned with the impedance after plating of Li reservoir (in Figure 114). The interfacial resistance decreased slightly during 50 cycles and reached a minimum of 850 Ω and then started to increase towards the 146^{th} cycle with an eventual interfacial resistance of 1740 Ω. The interfacial resistance of the Li|SIPE|Cu was always higher than in the corresponding symmetric Li|SIPE|Li cell (200-400 Ω), indicating that it is more difficult to plate Li on a Cu electrode than a Li metal electrode. Notably, the shape of the second semicircle was getting more depressed while the Li reservoir ass depleting. The depressed semicircle could be ascribed by the weakening symmetry of the two interfaces (Li-SIPE-Li and Cu-Li-SIPE -Li) or by the heterogeneity of the passive layers formed on both interfaces.

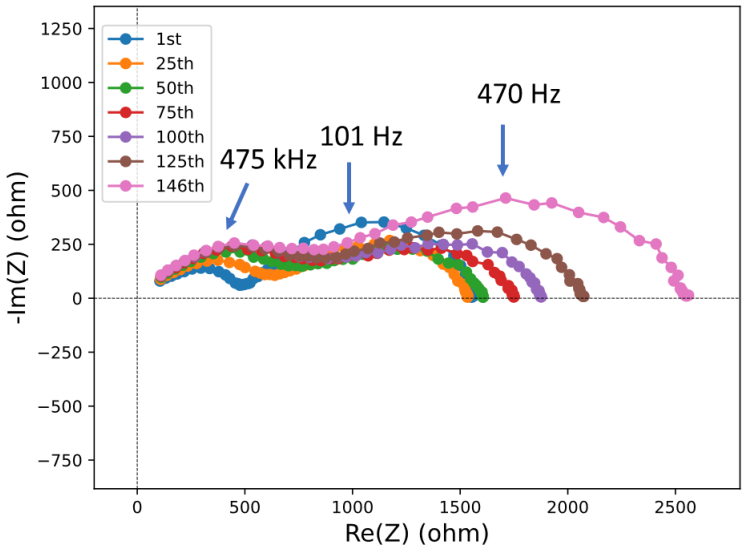

Figure 115. EIS spectra during the Li plating/stripping in Li|SIPE|Cu cells with the non-doped SIPE

The voltage profiles of the Li|SIPE|Cu cells comprising the $LiNO_3$-doped SIPEs are shown in Figure 116. For the 0.5% $LiNO_3$-doped electrolyte, the preconditioning of the Cu working electrode showed an initial CE of 44.9%, corresponding to a Li loss of 0.9 mAh cm^{-2}. In the test, excluding the formation cycle, all the Li stripped during the test yielded a capacity of 10.3 mAh cm^{-2}, and all the Li plated was 12.3 mAh cm^{-2}. With these numbers, the CE could be determined to 84% for the 0.5% $LiNO_3$-doped SIPE.

For 1% $LiNO_3$-doped SIPE, the preconditioning process showed an initial CE of 50% which was higher than the previous samples. After 134 cycles of plating/stripping, the 2 mAh cm^{-2} of the lithium reservoir was finally consumed, as indicated by the stripping voltage reaching 1.0 V. And the total CE was calculated as 87%.

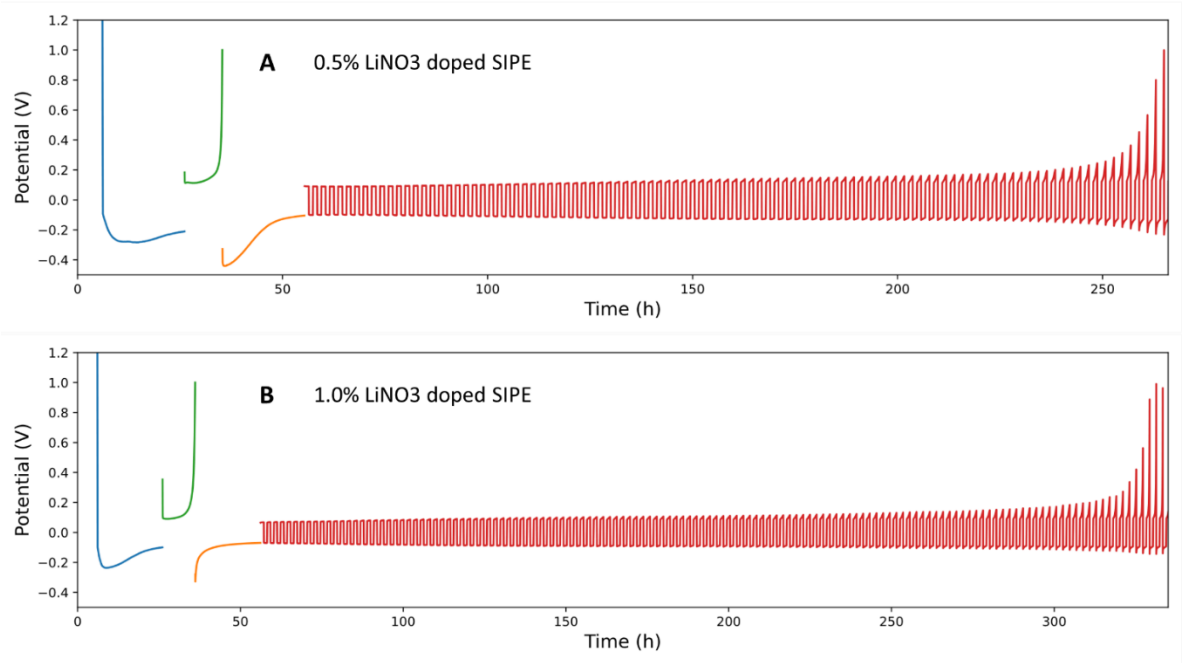

Figure 116. Coulombic efficiency determination for the 0.5 and 1.0% $LiNO_3$-doped SIPE in Li|SIPE|Cu cells.

EIS spectra of preconditioned and Li reservoir plating with $LiNO_3$-doped SIPE showed similar behavior as compared to the non-doped SIPE, as shown in Figure 117. With the in-situ plated Li reservoir, the EIS spectrum showed only a 2-semicircle response. The interfacial was 560 Ω, which was much less than the initial interfacial resistance of non-doped SIPE (1100 Ω). The EIS spectra of cell comprising the 0.5% $LiNO_3$ doped SIPE during the preconditioning steps showed a similar transition from a blocking electrode to a symmetric cell. After the 2nd plating, a well-defined 2-semi-circle shape of electrolyte bulk and interfacial was shown as well. The interfacial resistance with 1% $LiNO_3$ doping showed the smallest among the three samples, which was 210 Ω.

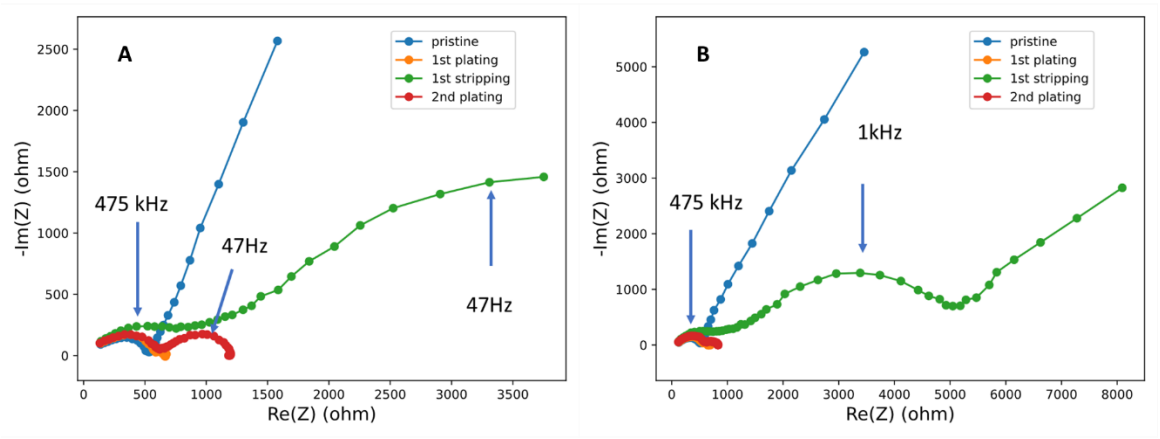

Figure 117. EIS spectra during the preconditioning of the Li|SIPE|Cu cells comprising the 0.5 and 1.0% $LiNO_3$-doped SIPEs.

The EIS spectra for the cells comprising the 0.5 and 1% $LiNO_3$-doped SIPE during the plating/stripping cycling exhibited a much more stable behavior than the non-doped SIPE. As shown in Figure 118, the total resistance almost remained stable from the 103 cycles which was between 1400-1600 Ω. Compared to the non-doped SIPE, whose total impedance was more than 2500 Ω, the much smaller resistance also led to a much lower polarization during the plating/stripping tests. The electrolyte bulk resistance showed an increasing trend as for all the samples tested before, whereas the interfacial resistance was more or less constant. I suppose that the bulk resistance increased due to the loss of contact between the SIPE and the electrode, which was caused by morphological changes of the lithium electrode during the plating/stripping test.

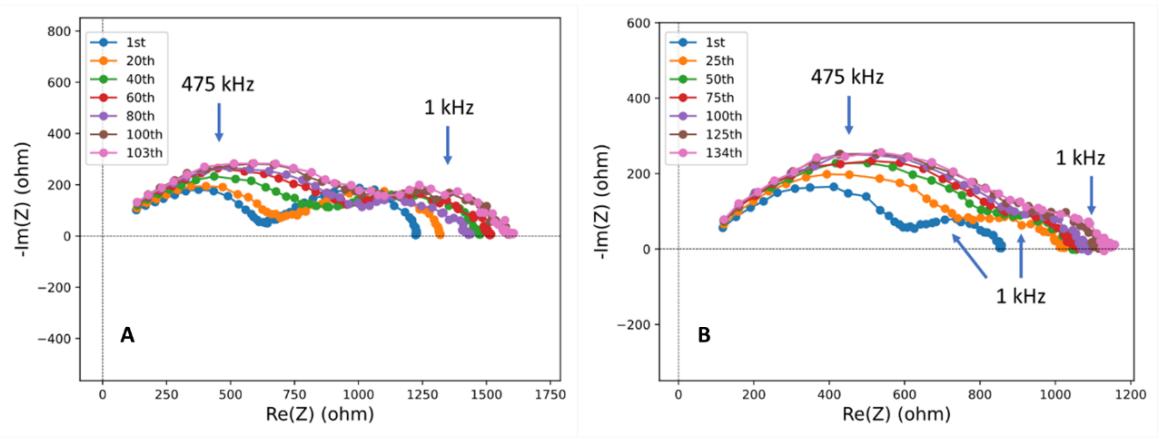

Figure 118. EIS spectra during Li plating/stripping of the Li|SIPE|Cu cell comprising the 0.5% and 1% $LiNO_3$-doped SIPE.

The comparison of the interfacial resistance of the three samples is shown in Figure 119. The SIPE without $LiNO_3$ doping has a more resistant interphase between the electrode and the SIPE. And more importantly, a significant increase could be observed after 110 cycles, demonstrating a deterioration of the interphase properties due to the depletion of Li on the Cu electrode, which was not observed for the $LiNO_3$-doped samples, indicating a more stable interphase formed in the presence of $LiNO_3$.

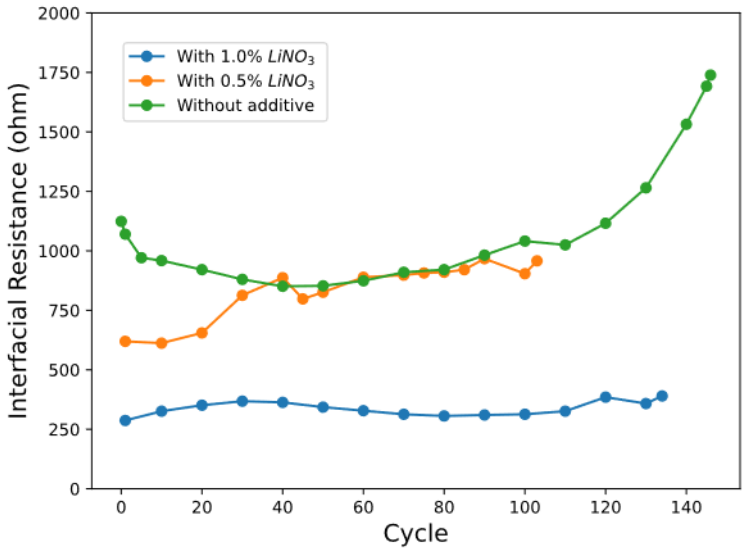

Figure 119. Comparison of the interfacial resistance of three Li|SIPE|Cu cells during the lithium plating/stripping tests.

The three samples showed a CE of 88, 84 and 87 % for the 0, 0.5 and 1.0 wt.% $LiNO_3$-doped SIPE. These results are also lower compared to the result reported with ether-based liquid electrolytes with high salt concentration (E.g., 4M LiTFSI in DME, CE=99.4%)[34], which suggests that the lithium loss was much severe with a solid polymer electrolyte compared to liquid electrolytes. We assume two possible reasons for these results: i) the long-term cycling has consumed all the $LiNO_3$ by reduction at the fresh lithium surface, which means the benefit of $LiNO_3$ doping could only be limited to the cycles in the beginning and we could not see the obvious difference in long-term test; ii) the Li loss upon long-term cycling was predominated by the "dead" lithium formation, which was due to passivation layer formation, but also related to contact loss at the solid-solid interface between the SIPE and the lithium metal.

Therefore, $LiNO_3$ could not improve the overall CE, even though it decreased the SEI layer resistance and increased its stability. In addition to the electrochemical tests, information about morphology is necessary to examine these two hypotheses. Thus, we performed SEM on the lithium-SIPE interface.

4 Morphology of plated Li electrode

After cycling, the different Li|SIPE|Cu cells were disassembled in a glove box. The images of the disassembled cells are shown in Figure 120 and Figure 121. The color of the SIPE membranes became brownish after long-term cycling. The lithium metal kept its sliver-white smooth surface with metallic luster. A thin layer of gray matter was observed. The gray matter could be mossy lithium generated during cycling.

Similarly, mossy lithium was found on the surface of the copper electrode, which is not homogenously distributed. When disassembling, the mossy lithium could be peeled off from copper easily with the SIPE membrane and led to a shining copper surface. Both the SIPE and the copper side were examined by SEM, confirming that the mossy lithium remained on the surface of SIPE rather than the copper electrode.

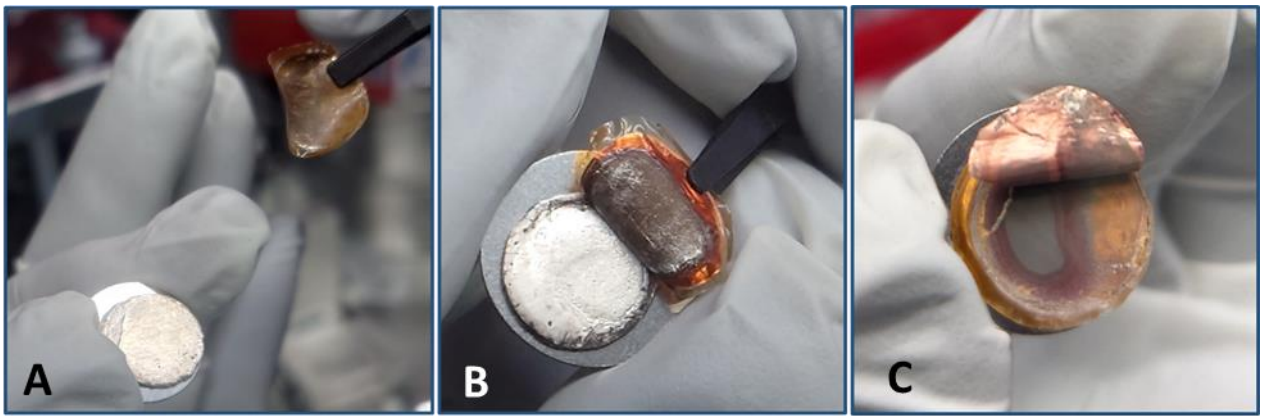

Figure 120. Images of the disassembled Li|SIPE|Cu cells. The diameter of the stainless steel discs was 16 mm. (A) Cell comprising the non-doped SIPE. (B) Cell comprising the 1% $LiNO_3$-doped SIPE (lithium electrode). (C) cell comprising the 1% $LiNO_3$-doped SIPE (copper electrode).

Mossy lithium on the SIPE membranes showed different morphologies and these could explain their different electrochemical behavior during the lithium plating/stripping tests. The edge of mossy lithium remaining on the SIPE is displayed in Figure 121. A clear boundary can be observed between the mossy lithium that completely covered the SIPE and the bare SIPE membrane.

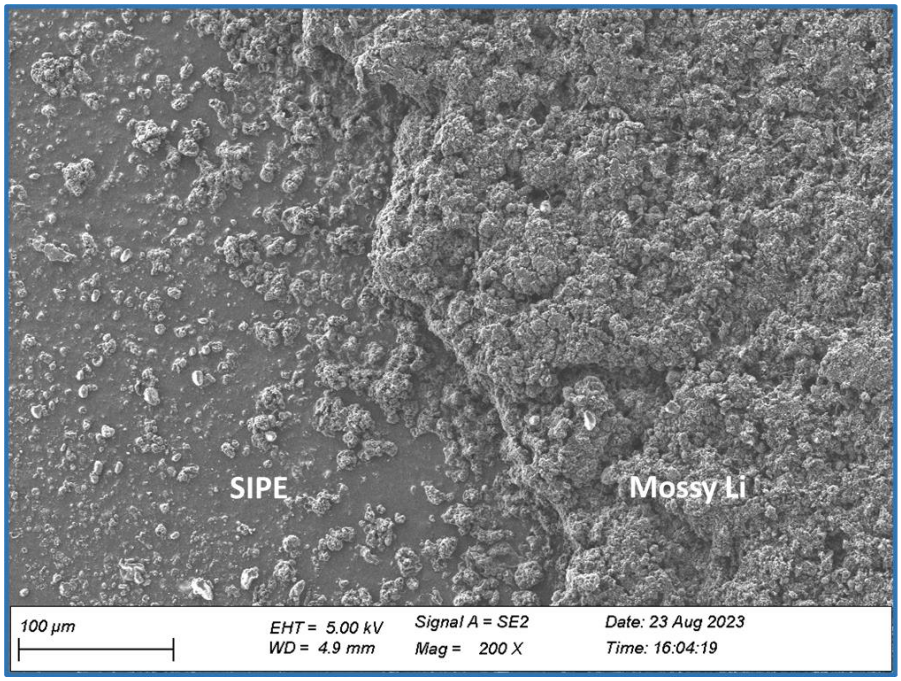

Figure 121. Edge of mossy lithium on the SIPE surface, the sample was recovered from a Li|SIPE|Cu cell comprising the non-doped SIPE after 350 h of cycling.

The deposition of the lithium led to a huge volume expansion and the contact between the SIPE and plated lithium could be lost, and the lithium became “dead lithium”. With the continuous plating/stripping, the contact between the lithium and the SIPE could be significantly escalated and induce a local current density increase, which could accelerate this process.

The mossy lithium on the SIPE without additive showed a rough surface with high porosity (Figure 122). For the $LiNO_3$-doped SIPEs, the surface was denser with a smooth surface. With the increasing content of $LiNO_3$, the trend was getting more obvious. The 1% $LiNO_3$-doped SIPE yielded the densest, and smoothest lithium layer on the SIPE among the three samples. The dense packing of the mossy lithium with the $LiNO_3$-doped SIPEs could lead to less volume expansion and better contact between the electrode and the electrolyte, which appears favorable for the interfacial stability.

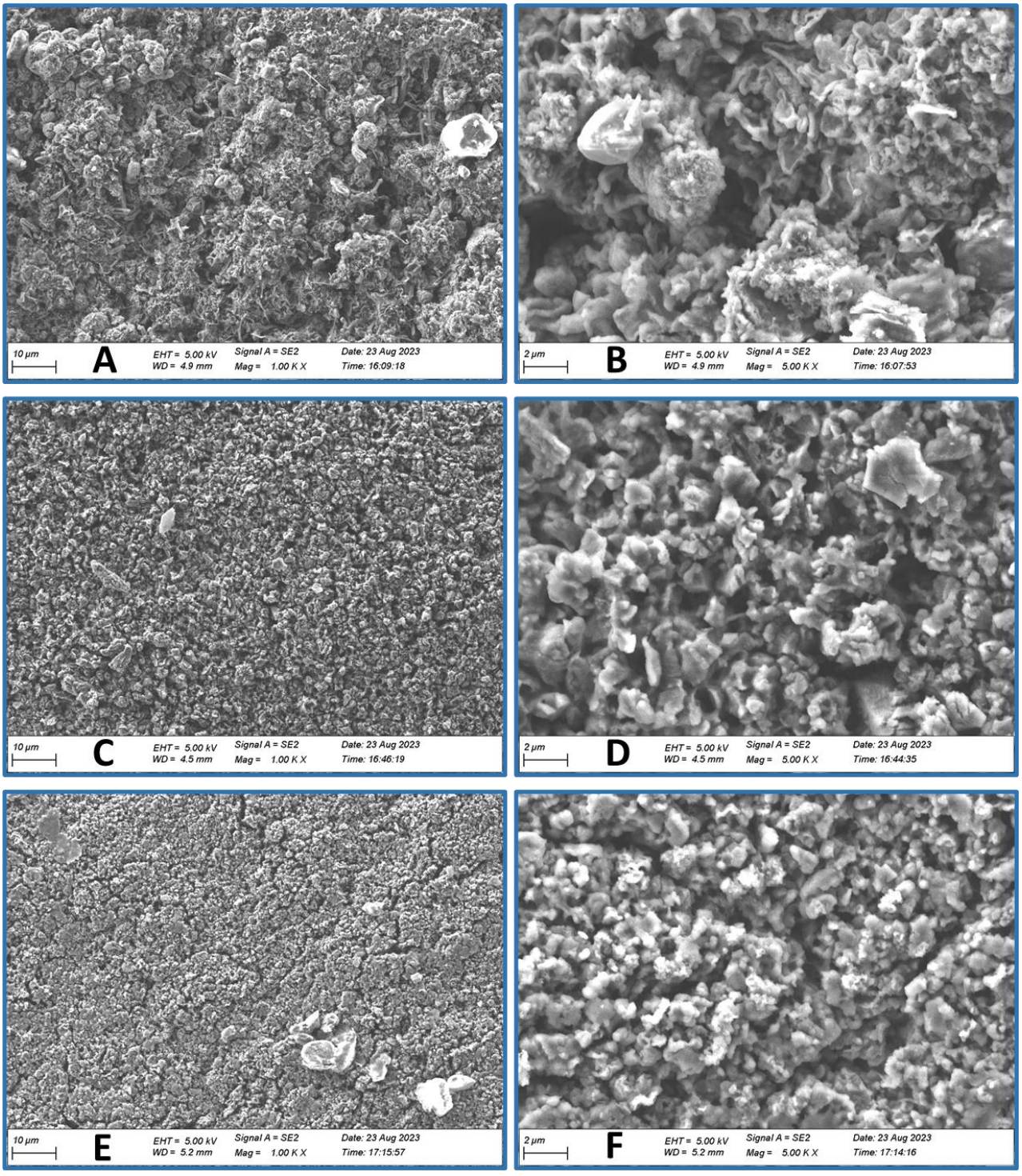

Figure 122. SEM images of the SIPE membranes recovered from the different Li|SIPE|Cu cells after the lithium plating/stripping test in Figure 113 and 116 (A, B) the SIPE without additive; (C, D) the SIPE with 0.5% $LiNO_3$, (E, F) SIPE with 1% $LiNO_3$.

The cross-sectional images of the Cu-SIPE recovered from the Li|SIPE|Cu cells after 350 h of

plating/stripping (Figure 123) showed the mossy lithium ("dead" lithium) between the Cu electrode and the SIPE membranes with a thickness of 7.0±1.2 μm. No dendritic lithium that intrudes in to the SIPE was observed, which agrees with the conclusion of the lithium plating/stripping test, i.e., no dendritic growth. Compared to the 9.6 μm of lithium deposited as reservoir, the thickness of "dead" lithium remaining on the Cu electrode was significant. With a rough estimation (assuming the "dead" lithium growth is homogeneous), the porosity of mossy lithium in the Figure 123 is ~50%. The loss of lithium due to the formation of "dead" lithium at the interface is significant.

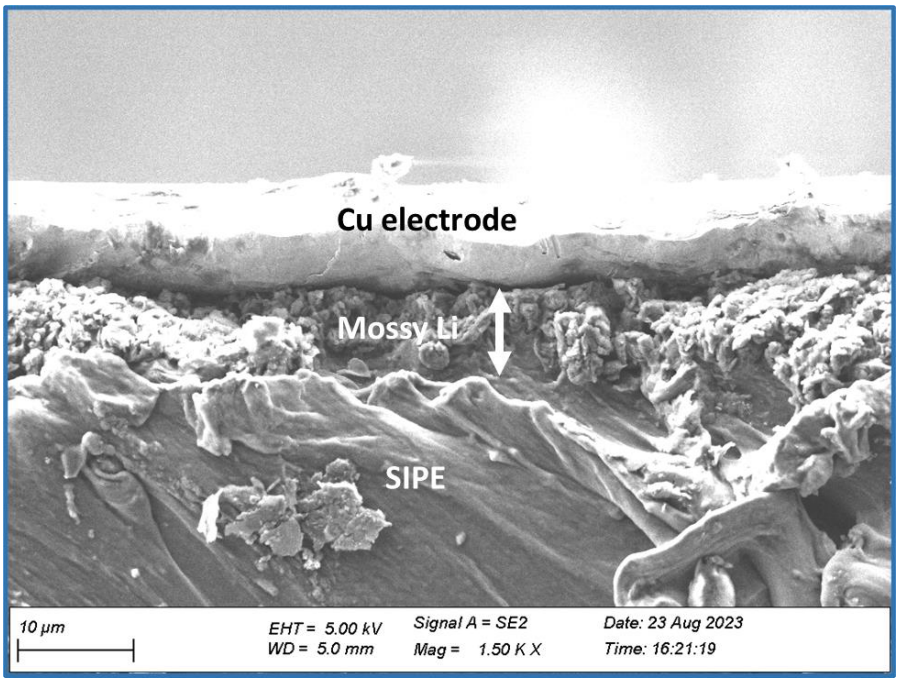

Figure 123. SEM image of the Cu-SIPE cross-section of the Li|SIPE|Cu cell after 350 h of plating/stripping with non-doped SIPE.

In summary, the determination of the lithium reversibility was performed by the plating/stripping test with Li|SIPE|Cu cells. An *in-situ* plated lithium reservoir on the Cu electrode was used as a limited lithium source to evaluate the consumption of lithium during the plating/stripping tests. Different from the depletive lithium plating/stripping test, the average CE of the cells with 0 as well as the 0.5% and 1% $LiNO_3$-doped SIPE were calculated as 88%, 84%, and 87%, respectively, which is lack of consistency with previous observations

(CV and depletive plating/stripping). The long-term average CE was similar (around 86%) in all the three samples. Compared to the cells with liquid electrolytes with better wettability, the solid-state cells suffered more from the volume expansion and contact issues. Combined with the mossy lithium morphology observed by SEM, a significant part of the lithium loss could be ascribed to the "dead" lithium formation during the plating/stripping, due to both contact issues and the isolating passivation layer formation.

In presence of $LiNO_3$, denser "dead" lithium was obtained which is due to the $LiNO_3$ doping in the SIPE. To investigate the chemical nature of the interface, XPS measurements of pristine and cycled lithium and SIPE were performed.

5 XPS characterization

To understand the degradation of the SIPE and the SEI formation, X-ray photoelectron spectroscopy (XPS) was used to analysis the SIPE and lithium surface after plating/stripping test. Two symmetric cells comprising the SIPEs with/without 0.5wt.% $LiNO_3$ were assembled and cycled for 48 h (current density: 0.1 mA cm^{-2}, 0.4 mAh cm^{-2} per half cycle) at 80 °C and then disassembled in an Ar-filled glove box.

Since the SEI formation was on the interface between the SIPE and the lithium metal electrode, the SEI compounds could exist on both the SIPE and the lithium surface. Thus, the XPS measurements were taken on both surfaces of the SIPE and the Li metal electrode. F1s, O1s, C1s, Li1s, S2p and N1s spectra were collected. The XPS spectra were calibrated by hydrocarbon response at 285.0 eV and fitted. In general, the O1s spectra in this work is difficult to fit, due to the strong overlapping of different species which lead to insufficient resolution.

For the pristine SIPEs, all the bonding from the I_{1000}p-SO_3-cr polymer could be observed. Hydrocarbon and ether responds were observed at 285.0 and 286.4 eV, respectively. The ether function could also be confirmed from O1s spectrum at 532.5 eV. The perfluorinated side chain was observed in F1s spectrum at 688.1 eV, corresponding to CF_2-O in O1s (536 eV) and C-F in C1s at 290.2 eV. The presence of LiF in the non-doped SIPE (not observed for the doped SIPEs) may be due to contamination or beam damage. The sulfonate moiety was confirmed by both the 168.2 eV signal in S2p spectrum and the peak at 534.3 eV in the O1s spectrum.

Additionally, an N-related signal, even though very weak, was observed only in the $LiNO_3$-doped SIPE. The weak response could be ascribed to two reasons: i) the N element usually shows low sensitivity in XPS, ii) the concentration of the $LiNO_3$ doping is generally very low. The spectra of SIPE after cycling were significantly different. For the SIPE without the additive, the changes after cycling were mainly observed in the F1s, O1s, C1s and S2p spectra. In the F1s and S2p spectra, the signals became very noisy which means that the amount of these elements decreased at the surface of the sample (XPS probes only about 5-10 nm). On the contrary, new signals were observed in O1s and C1s spectra. In the C1s spectrum, new peaks were observed at 288.6 and 289.8 eV. Correspondingly, a new peak could also be observed at 535.4 eV in the O1s spectrum, which are the signs of degradation products. Due to the position in O1s spectrum, the degradation products could not be assigned to Li_2CO_3, which has lower binding energy. As suggested by Aurbach et al.,[35] the cleavage of ether bonds could be the possible mechanism for the reduction of ether-based electrolytes generating alkoxides and radicals which led to a series of side reactions. Recent studies pointed out that more complicated organic molecules could be generated in the process, including ethylene, branched ethers, CH_3CHOLi, or vinyl ethers.[36,37] Based on literature data, we may assume that the new peaks were due to the cleavage of ether bonds, forming degradation products on the polymer surface, which contains multiple organic degradation products which could be lithium oligoethioxides, ethers, vinyl ether and carbonyl compounds (aldehydes, ketones and carboxylates).[38]

Notably, the weak signal in the F1s and S2p spectra suggests that the thickness of this layer of degradation products is thicker than 10 nm, because the XPS did not detect these two elements, although they are present in the bulk SIPE.

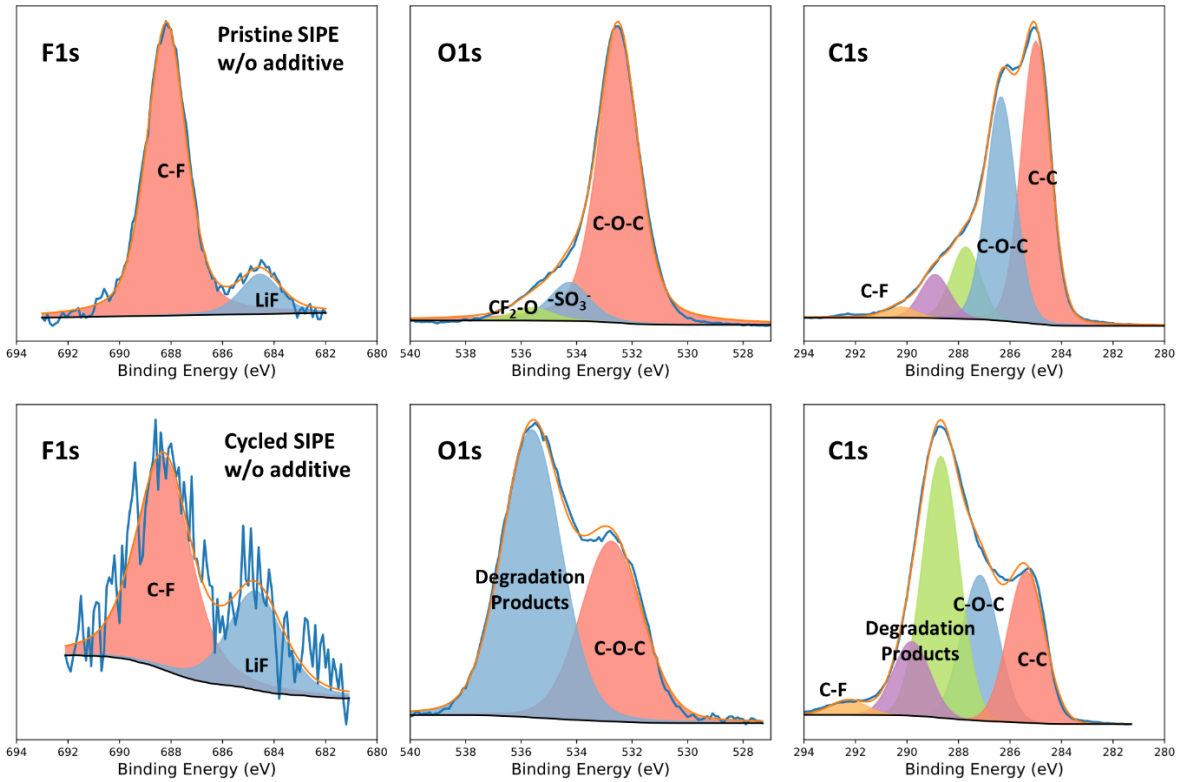

Figure 124. XPS spectra of pristine and cycled SIPEs without the additive.

For the SIPE with $LiNO_3$ doping, the pristine polymer showed a similar response as the non-doped one, except the missing LiF signal in the F1s spectrum and the shape of the features observed in the C1s spectrum is different, which may originate from some surface inhomogeneity. After cycling, new peaks at 535.7 eV in the O1s spectrum and at 288.6/287.6 eV in the C1s spectrum emerged, which are presumably related to the presence of degradation of polymer. The intensity of these two peaks was much less compared to the peaks obtained with the SIPE without $LiNO_3$, suggesting that less degradation of the ether bonds was taking place in presence of $LiNO_3$. The F1s and S2p spectra clearly showed peaks of CF_2 and SO_3^- moieties from bulk SIPE, suggesting that the SEI was thinner than 10 nm.

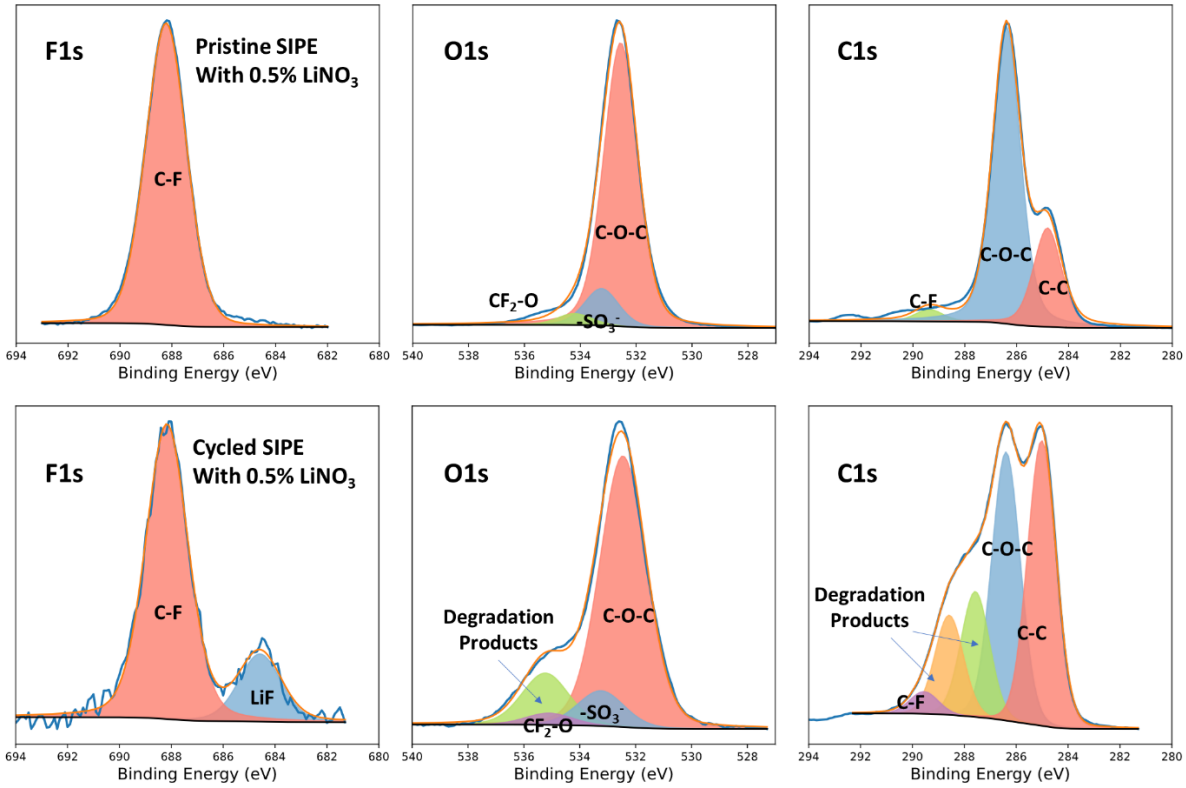

Figure 125. XPS spectra of pristine and cycled SIPEs with 0.5% $LiNO_3$.

The same investigation was performed on the fresh and cycled lithium surfaces.

Fresh Li was examined by XPS as a reference before we looked at the cycled lithium. In the F1s spectrum, peaks of fluorocarbons (such as PTFE or per/polyfluoroalkyl compounds, 687.1 and 688.3 eV) and LiF (685.0 eV) were observed. Correspondingly, the fluorocarbons (287.9 and 286.9 eV) could be observed in the C1s spectrum together with Li_2CO_3 (289.9 eV). Thus, we could assume a native passivation layer with LiF, Li_2CO_3 and Li_2O presence on the fresh lithium electrode. The Li_2CO_3 and Li_2O might be the result of the reaction with the atmosphere and F- containing compound could be due to the fluoropolymer used in lithium metal processing.

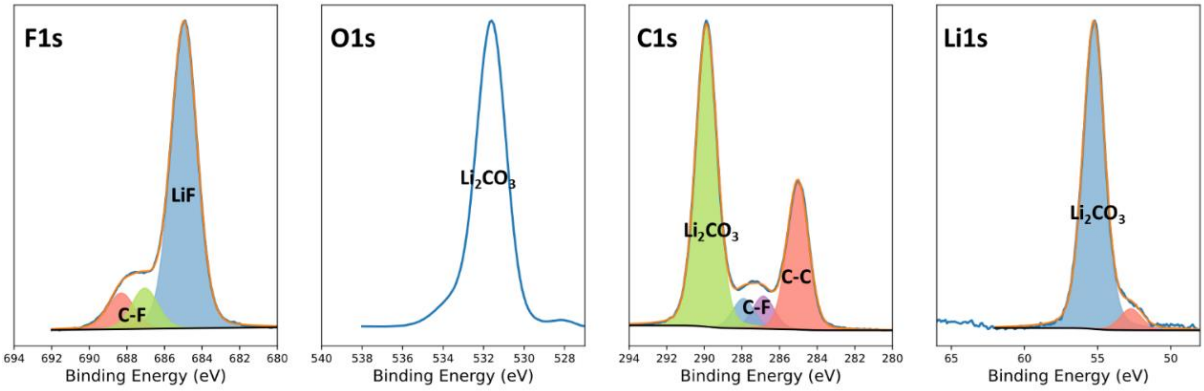

Figure 126. XPS spectra of Fresh Li.

The chemical information from the SEI close to the lithium surface was analyzed. For both SIPEs with/without additive, a clear LiF peak was observed together with a CF_2 peak on F1s spectrum, which could be related to the reduction of the SIPE or diffusion of degradation products. In the presence of $LiNO_3$, the LiF/CF_2 ratio was higher than the one without doping. In the C1s spectrum, the signal at 288.6 eV could be assigned to Li_2CO_3 (with corresponding signal in O1s spectrum). Some other degradation products were observed at 287.3 eV, which might be similar to the ones observed on SIPE, which can be products from ether bond cleavage. Admittedly, the deconvolution of the O1s spectra is difficult due to not only the complexity but also the shape of the peak allowing many possible combinations. Thus, it is necessary to refer to the atomic ratio information form C1s spectra to have some clue. By fixing the same amount of Li_2CO_3 in the C1s spectrum, the Li_2CO_3 signal in O1s spectrum was set to 531.2 eV . An additional peak which could be assigned to Li_2O, essentially overlapping with Li_2CO_3, had to be added. Ether moiety can be determined at 532.7 eV. We may assume -SO_3^- and -CF_2-O- moieties exist, due to their F1s and S2p signals, and fitted at higher binding energies of 533.8, 534.8 eV respectively. In the S2p spectrum, in addition to the -SO_3^- signal at 168.2 eV, a series of degradation products could be observed between 158-166 eV which could be assigned to polysulfides and Li_2S.[39]

For both samples, we could summarize that the SEI directly on the lithium surface is rich in Li_2CO_3, Li_2O, LiF and Li_2S as degradation products of the SIPE. Specifically, traces of Li_3N could be detected for the $LiNO_3$-doped SIPE. Notably, although chemical signals including LiF and Li_2CO_3 were observed in the native passivation layer, after cycling, the surface is greatly

changed, which means that the origin of these compound could be different from the native passivation layer on lithium metal.

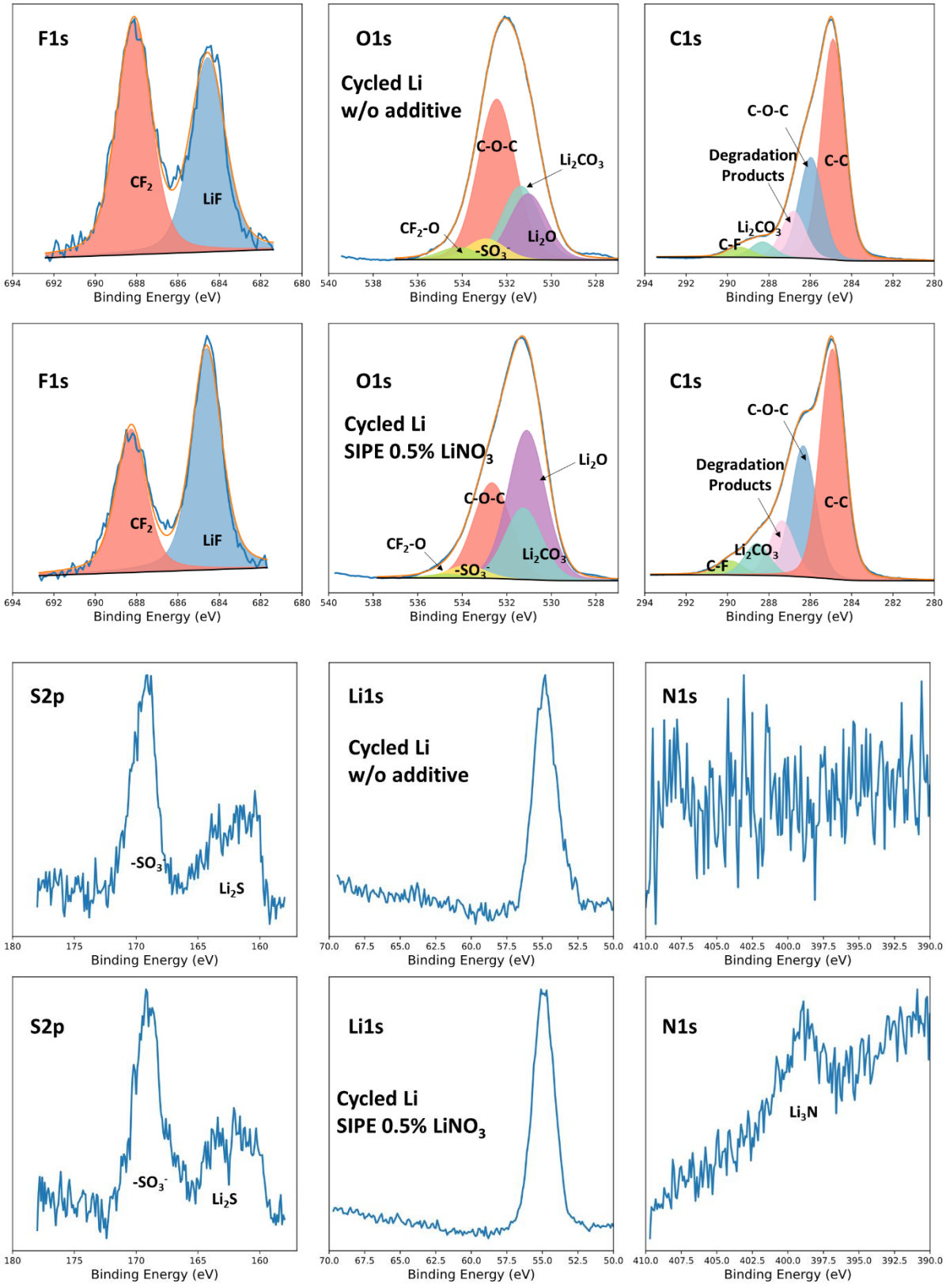

Figure 127. XPS spectra of Li from symmetric cells with SIPEs with and without $LiNO_3$.

Based on the XPS results, we might propose the degradation mechanism of the SIPE and the SEI formation. For SIPE without $LiNO_3$, a thick SEI layer with composition gradient was formed by SIPE degradation products. The SEI near the Li metal was rich in inorganic degradation products containing LiF, R-CF_2, Li_2S, Li_2CO_3 and Li_2O and resulting from the perfluorinated side chains. On the other side of the SEI, close to the electrolyte, an organic compound-rich layer was obtained, containing mainly carbonyl-based products, which could be due to the cleavage of ether bonds. The organic SEI on the SIPE surface was thicker than 10 nm, as there was no signal of the polymer electrolyte.

With $LiNO_3$ doping, the inorganic layer on the lithium metal surface was also rich in LiF, Li_2S, Li_2CO_3 and Li_2O. More specifically, Li_3N was only present as the $LiNO_3$ degradation product. Whereas on the SIPE side, a thinner organic SEI was found. The SEI chemistry compositions are illustrated in Figure 128.

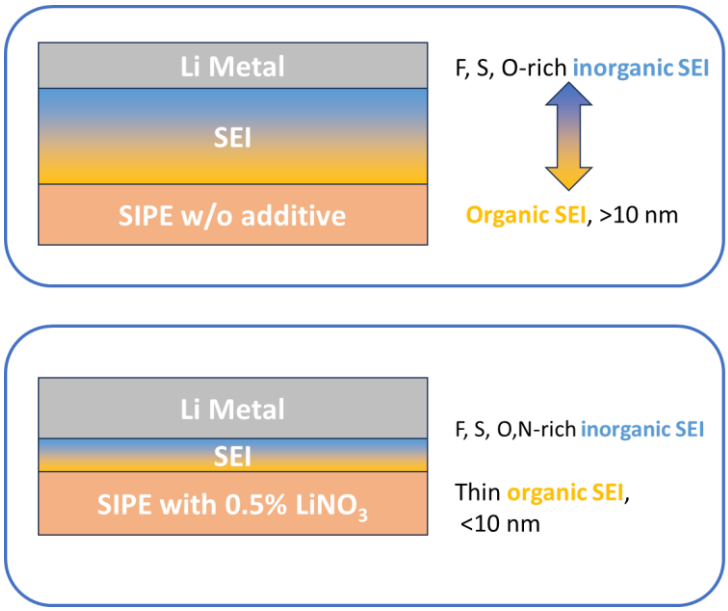

Figure 128. Illustration of the SEI composition between the SIPEs and lithium metal.

The differences of the SEI structure and composition could be explained as follows: When lithium got in contact with the SIPE the decomposition could lead to organic and inorganic compounds. Based on the XPS data, it seems that mostly an organic layer with degradation

product was formed on the surface of the SIPE and an inorganic layer with Li_2CO_3, Li_2O, Li_2S and LiF was formed on the lithium surface. The organic layer was thicker than 10 nm and lacks S and F elements. Whereas in the case of the $LiNO_3$-doped SIPEs, due to the formation of Li_3N passivation layer and competition between polymer and $LiNO_3$ reductions, the polymer was partially protected. Only a small amount of decomposition products could be found on the surface of doped SIPE, and the thickness of this organic layer is less than 10 nm. The inorganic layer on the Li was composed of Li_2CO_3, Li_2O, Li_2S, LiF and Li_3N. The similar layered structure SEI was also observed with ether-based SEI.[36]

The differences on composition and thickness of the SEI layers could be explained by the difference on the deposited lithium morphology and electrochemistry of the SIPEs with/without $LiNO_3$ doping. The thicker and more organic SEI in the case of the non-doped SIPE could be less dense compared to the thin and inorganic, Li_3N-rich SEI in the case of the $LiNO_3$-doped SIPE, which could be easier to break when lithium deposition. The difference on the SEI composition could induce different morphology in lithium deposition and finally impact the interfacial resistance, lithium reversibility, and contact between electrode and SIPE, which finally leading to the distinct behaviors in the CV and the Li plating/stripping tests, which did not involve the same amount of fresh lithium deposition.

6 LMB comprising the $LiNO_3$-doped SIPE

To confirm the stabilization effect of $LiNO_3$ doping, LMB cells were assembled with LFP positive electrodes.

LFP was proven as an electrode material with good stability, which is suitable for the evaluation of the stability of the Li-metal electrode. The LFP electrodes were prepared with a formulation of LFP:Super C65:PVDF:I_{1000}-SO_3-db= 65:10:5:20. All the ingredients were mixed with mortar and pestle with NMP to form a homogeneous slurry and cast on carbon coated Al foil. The electrode was dried at 80 °C overnight and cut into discs with a diameter of 12 mm. The electrodes were calendared to reduce the porosity and dried again under vacuum.

The battery cells were assembled in an argon filled glove box. The $LiNO_3$-doped and non-doped SIPEs were sandwiched between the Li foil and LFP electrode and sealed in CR2032-type coin

cells. The active material mass loading of the LFP|SPE|Li cells was about 1.9 – 2.0 mg cm^{-2}. The LFP|SPE|Li cells were examined with galvanostatic charge/discharge cycles in oven at 80 °C. The first three cycles were conducted at a rather low C rate of C/20 (1C = 170 mA g^{-1}) as formation cycles and following cycles were operated with C/2. The first cycles exhibited a similar specific capacity of 142 mAh g^{-1}, which provides a good basis to compare the performance of the two different cells.

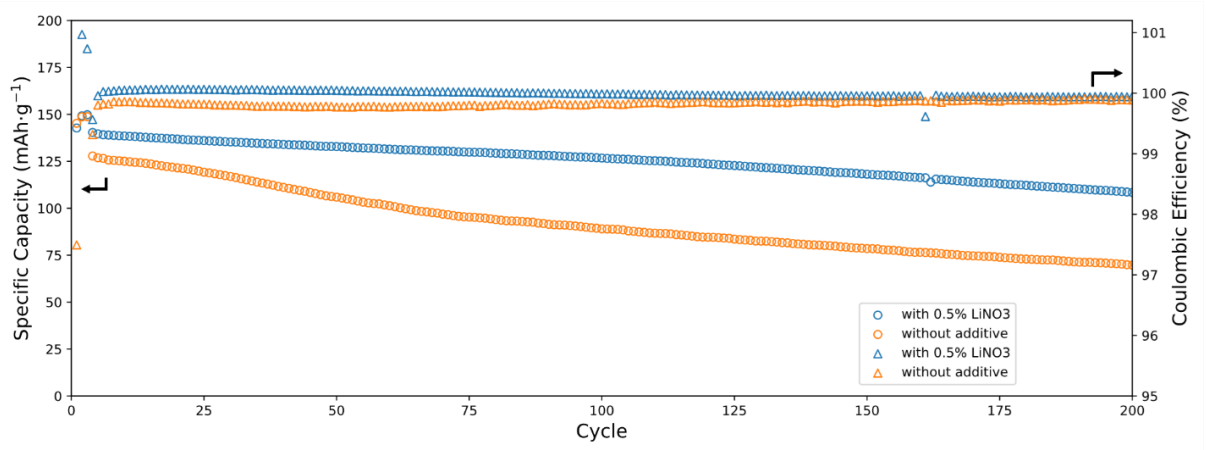

Figure 129. Charge capacity and CE of the Li|SIPE|LFP cells at 80 °C

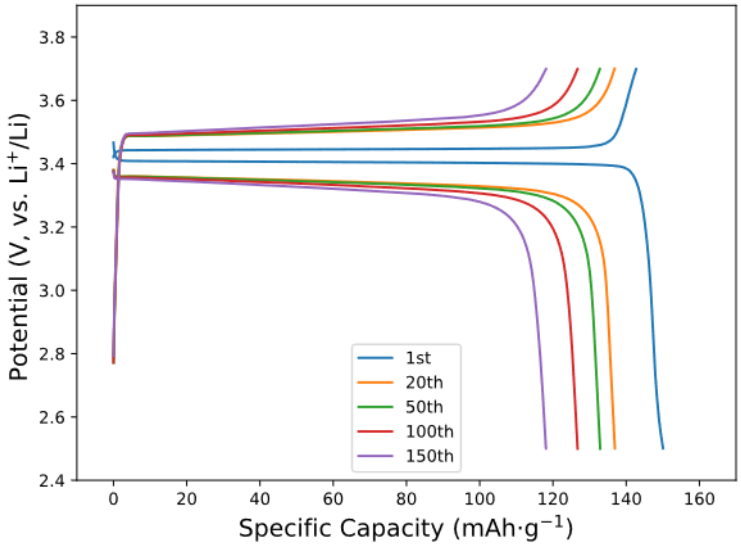

Figure 130. Charge/discharge profiles of the Li|SIPE|LFP cells comprising the 0.5% $LiNO_3$-doped SIPE.

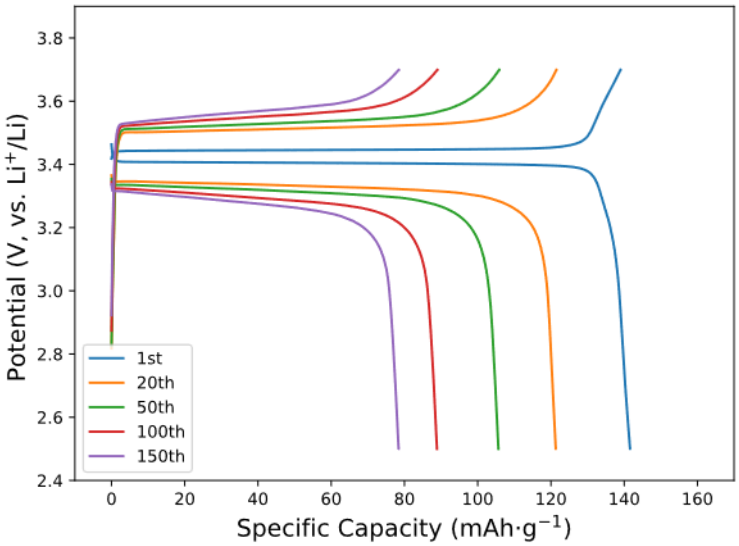

Figure 131. Charge/discharge profiles of the Li|SIPE|LFP cells comprising the non-doped SIPE.

The decay of specific capacity could be defined as follows:

$$Decay = \frac{Q_{N-1} - Q_N}{Q_N}$$

where Q_N and Q_{N-1} are the specific capacity of the N^{th} and $(N-1)^{th}$ cycle. In this chapter, charge capacity is used to calculate the rate of decay (which could be converted into the corresponding discharge capacity decay rate by multiplying with the CE), which is shown in Figure 132. The decay behavior showed a scattered distribution. The cells comprising the $LiNO_3$-doped SIPE exhibited a stable cycling and low decay after the initial two cycles. During the 160 cycles, the cell with $LiNO_3$-doped SIPE exhibited an average decay rate of 0.12% per cycle. This was much lower than the cell with non-doped SIPE, which showed an average capacity decay of 0.32% per cycle.

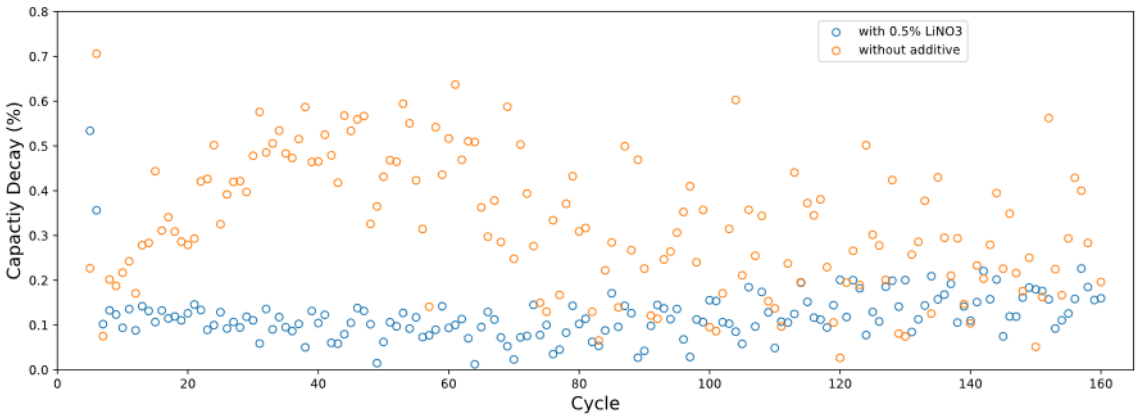

Figure 132. Decay rate of Li|SIPE|LFP cells, cycled at C/2.

To further understand the reason of capacity decay and the effect of the $LiNO_3$ doping, a closer look at the charge/discharge profile is necessary. By comparing the charge/discharge profiles of the two cells, an increased polarization was observed together with the capacity decay, especially in the case of the cell with non-doped SIPE. The polarization upon cycling was evaluated by the voltage difference between the charge and discharge plateau (defined as cell voltage at 50% charge/discharge capacity). The polarization of the cell comprising the $LiNO_3$-doped and non-doped SIPE was initially 156 mV and 170 mV (4^{th} cycle) and then increased to 209 mV and 285 mV (154^{th} cycle), respectively.

The relationship between capacity and polarization is visualized in Figure 133, which exhibited a strong linear trend. The linear regression was made with both cells and the results are listed in Table 10.

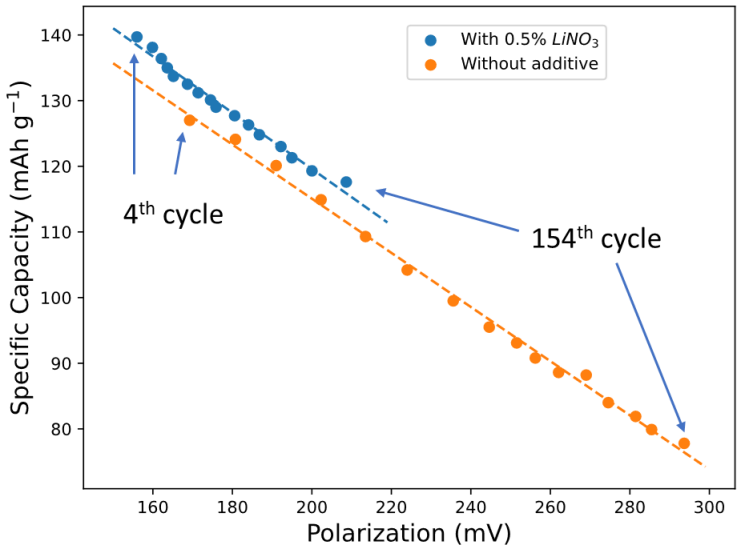

Figure 133. Evolution of the discharge capacity *vs.* the polarization in Li|SIPE|LFP cells.

Table 10. Linear regression of capacity-polarization relation

	Slope	Y-Intercept	R^2
SIPE with 0.5% $LiNO_3$	-0.429	205.3	0.984
SIPE without additive	-0.413	197.6	0.996

The two cells exhibited a similar slope of around -0.42, which can be explained as for every 1 mV increase, the capacity loss was 0.42 mAh g^{-1}. These results suggest that the increase of cell polarization is linked to the capacity loss. We assume that the degradation of cell capacity is due to the loss of active LFP particles.[40] Although the volume change of the LFP is only 6.77%,[41] the lithium-metal electrode side suffers much more volume changes that which might lead to an inhomogeneous mechanical stresses and induce the local degradation (loss of contact) of the LFP electrode. From the previous characterizations we could link the lithium morphology to the cell resistance which also could be reflected by the polarization.

The polarization can be simply explained as the following equation:

$$polarization = E_{50\%\,charge} - E_{50\%\,discharge} = (E_{ocv} - E'_{ocv}) + 2IR$$

where E_{OCV} and E'_{OCV} are the open circuit voltage of the cell for the charge and discharge

process, which is determined by LFP thermodynamics, I is the current applied and R is the total resistance of the cell. Since the current is constant in this case, the only plausible reason leading to the polarization increase was increased cell resistance. Unfortunately, EIS spectra were not collected during cycling of these cells thus no deconvolution of the processes (lithium interface, positive electrode response, charge transfer reaction), could be performed. But it is reasonable to assume, based on plating/stripping results, that the evolution of cell resistance was mainly due to the formation of mossy lithium leading to bad contact between electrolyte and Li electrode. Thus, the $LiNO_3$ doping would form a stable SEI layer on the lithium metal which induces a better morphology with less porous mossy lithium and interfacial resistance, finally improving the battery performance.

7 Conclusion

In this chapter, I_{1000}p-SO_3-cr SIPE was doped with 0.5 and 1.0 wt.% of $LiNO_3$. The electrochemical behaviors were compared for the doped and non-doped SIPE.

The SIPE doped with $LiNO_3$ salt showed a good ionic conductivity of $3x10^{-5}$ S cm^{-1} at 80 °C and lithium transference number of >0.95. The single-ion conducting behavior was not altered due to the low amount of free salt and less dissociation of the NO_3^- group. However, the electrochemical behavior of the cell and SEI composition was sharply affected by the doping.

The difference of the SEI layer could be reflected by many electrochemical tests. In the simple aging test conducted for the symmetric Li|SIPE|Li cells, the cell comprising $LiNO_3$ showed faster stabilization of the interfacial resistance than non-doped SIPE. CV tests revealed a different lithium plating/stripping behavior with $LiNO_3$ doping which greatly improved the lithium reversibility.

No dendrite formation was observed with all the SIPEs during a long-term lithium plating/stripping test. However, the reversibility of the lithium and interfacial resistance are much different after $LiNO_3$ doping. The reversibility of Li metal cycling was improved by the $LiNO_3$ doping during the short-term cycling which is ascribed to a better SEI formation and lithium surface morphology.

Finally, the comparison of doped and non-doped electrolyte in LFP-based LMB cells, the 0.5%

$LiNO_3$ additive efficiently improved the cycling stability with a low average capacity decay of 0.12% compared to 0.32% for the non-doped SIPE. These results demonstrate the effect of $LiNO_3$ additive in SIPEs and systemically discussed the relationship between the SEI composition and the interfacial morphology of lithium metal electrode.

Thus, the conclusions of this chapter could be drawn as follows:

(1) The $LiNO_3$-doped SIPE showed advantages for the interfacial resistance and Li reversibility in aging and CV tests, compared to the SIPE without the additive. Long-term Li plating/stripping proved that both SIPEs could avoid the lithium dendrite formation. Lithium reversibility was determined with Li|SIPE|Cu cells. In a short period, the $LiNO_3$ doping could improve the CE of lithium. However, in long-term conditions, the reversibility was not altered with doping. The lithium loss could be attributed to the formation of "dead" lithium.

(2) The morphology of the cycled lithium showed a typical mossy morphology. And with the $LiNO_3$ doping, the cycled lithium became dense, and smooth, which could be explained by the different SEI composition.

(3) LMBs with LFP positive electrodes were cycled with both the $LiNO_3$-doped and the non-doped SIPE. The cells comprising the $LiNO_3$-doped SIPE showed a better cycle life and less polarization.

However, there are still too many details that remain unclear in the lithium deposition behaviors in the case of SIPE or other solid-state electrolytes. Especially the influence of the large volume expansion, between the solid-solid interface is not well understood yet. Other than electrochemical methods, advanced techniques such as in-situ/operando X-ray and neutron scattering for the evolution of chemical composition in SEI, tomography to understand morphologies with both electrode and electrolyte. Molecular dynamic and Density-functional theory (MD/DFT) simulations to predict the possible reaction on the surface of lithium metal. Quartz crystal microbalance (QCM) to directly monitor the amount of Li deposition and SEI formation. These experiments could be helpful to add more information on the formation and effect of the SEI formation and lithium plating/stripping process.

References

1. Guo, J., Wen, Z., Wu, M., Jin, J. & Liu, Y. Vinylene carbonate–LiNO3: A hybrid additive in carbonic ester electrolytes for SEI modification on Li metal anode. *Electrochemistry Communications* **51**, 59–63 (2015).
2. Li, L., Deng, Y., Duan, H., Qian, Y. & Chen, G. LiF and LiNO3 as synergistic additives for PEO-PVDF/LLZTO-based composite electrolyte towards high-voltage lithium batteries with dual-interfaces stability. *Journal of Energy Chemistry* **65**, 319–328 (2022).
3. Rosy, Akabayov, S., Leskes, M. & Noked, M. Bifunctional Role of $LiNO_3$ in $Li–O_2$ Batteries: Deconvoluting Surface and Catalytic Effects. *ACS Appl. Mater. Interfaces* **10**, 29622–29629 (2018).
4. Varzi, A., Raccichini, R., Passerini, S. & Scrosati, B. Challenges and prospects of the role of solid electrolytes in the revitalization of lithium metal batteries. *J. Mater. Chem. A* **4**, 17251–17259 (2016).
5. Lin, D., Liu, Y. & Cui, Y. Reviving the lithium metal anode for high-energy batteries. *Nature Nanotech* **12**, 194–206 (2017).
6. Harry, K. J., Hallinan, D. T., Parkinson, D. Y., MacDowell, A. A. & Balsara, N. P. Detection of subsurface structures underneath dendrites formed on cycled lithium metal electrodes. *Nature Mater* **13**, 69–73 (2014).
7. Ota, H., Sakata, Y., Wang, X., Sasahara, J. & Yasukawa, E. Characterization of Lithium Electrode in Lithium Imides/Ethylene Carbonate and Cyclic Ether Electrolytes. *Journal of The Electrochemical Society*.

8. Chazalviel, J.-N. Electrochemical aspects of the generation of ramified metallic electrodeposits. *Phys. Rev. A* **42**, 7355–7367 (1990).
9. Tikekar, M. D., Archer, L. A. & Koch, D. L. Stability Analysis of Electrodeposition across a Structured Electrolyte with Immobilized Anions. *J. Electrochem. Soc.* **161**, A847–A855 (2014).
10. Diederichsen, K. M., McShane, E. J. & McCloskey, B. D. Promising Routes to a High Li^+ Transference Number Electrolyte for Lithium Ion Batteries. *ACS Energy Lett.* **2**, 2563–2575 (2017).
11. Borzutzki, K., Nair, J. R., Winter, M. & Brunklaus, G. Does Cell Polarization Matter in Single-Ion Conducting Electrolytes? *ACS Appl. Mater. Interfaces* **14**, 5211–5222 (2022).
12. Zheng, G. *et al.* Interconnected hollow carbon nanospheres for stable lithium metal anodes. *Nature Nanotech* **9**, 618–623 (2014).
13. Qiao, Y. *et al.* A high-energy-density and long-life initial-anode-free lithium battery enabled by a Li2O sacrificial agent. *Nat Energy* **6**, 653–662 (2021).
14. Park, C.-M., Kim, J.-H., Kim, H. & Sohn, H.-J. Li-alloy based anode materials for Li secondary batteries. *Chem. Soc. Rev.* **39**, 3115 (2010).
15. Xu, Y. *et al.* Atomic to Nanoscale Origin of Vinylene Carbonate Enhanced Cycling Stability of Lithium Metal Anode Revealed by Cryo-Transmission Electron Microscopy. *Nano Lett.* **20**, 418–425 (2020).
16. Zhang, X.-Q., Cheng, X.-B., Chen, X., Yan, C. & Zhang, Q. Fluoroethylene Carbonate Additives to Render Uniform Li Deposits in Lithium Metal Batteries. *Adv. Funct. Mater.* **27**, 1605989 (2017).

17. Phiri, I. *et al.* Synergistic Effect of a Dual-Salt Liquid Electrolyte with a $LiNO_3$ Functional Additive toward Stabilizing Thin-Film Li Metal Electrodes for Li Secondary Batteries. *ACS Appl. Mater. Interfaces* **13**, 31605–31613 (2021).
18. Li, S. *et al.* A Superionic Conductive, Electrochemically Stable Dual-Salt Polymer Electrolyte. *Joule* **2**, 1838–1856 (2018).
19. Liang, W., Shao, Y., Chen, Y.-M. & Zhu, Y. A 4 V Cathode Compatible, Superionic Conductive Solid Polymer Electrolyte for Solid Lithium Metal Batteries with Long Cycle Life. *ACS Appl. Energy Mater.* **1**, 6064–6071 (2018).
20. Lu, Y., Tu, Z. & Archer, L. A. Stable lithium electrodeposition in liquid and nanoporous solid electrolytes. *Nature Mater* **13**, 961–969 (2014).
21. Ko, J. & Yoon, Y. S. Recent progress in LiF materials for safe lithium metal anode of rechargeable batteries: Is LiF the key to commercializing Li metal batteries? *Ceramics International* **45**, 30–49 (2019).
22. Di Cillo, D., Bargnesi, L., Lacarbonara, G. & Arbizzani, C. Ammonium and Tetraalkylammonium Salts as Additives for Li Metal Electrodes. *Batteries* **9**, 142 (2023).
23. Rosenman, A. *et al.* The Effect of Interactions and Reduction Products of $LiNO_3$, the Anti-Shuttle Agent, in Li-S Battery Systems. *J. Electrochem. Soc.* **162**, A470–A473 (2015).
24. Hayashi, Y. *et al.* Synergy between $LiNO_3$ and Tetraglyme-Sulfone Dual-Solvent Electrolyte Solutions in Li-O_2 Batteries. *J. Electrochem. Soc.* **167**, 160531 (2020).
25. Iliksu, M. *et al.* Elucidation and Comparison of the Effect of LiTFSI and $LiNO_3$ Salts on Discharge Chemistry in Nonaqueous Li–O_2 Batteries. *ACS Appl. Mater. Interfaces* **9**, 19319–19325 (2017).

26. Zhou, W. *et al.* Plating a Dendrite-Free Lithium Anode with a Polymer/Ceramic/ Polymer Sandwich Electrolyte. *J. Am. Chem. Soc.* 4 (2016).
27. Nguyen, H.-D. *et al.* Nanostructured multi-block copolymer single-ion conductors for safer high-performance lithium batteries. *Energy Environ. Sci.* **11**, 3298–3309 (2018).
28. Zor, C., Turrell, S. J., Uyanik, M. S. & Afyon, S. Lithium Plating and Stripping: Toward Anode-Free Solid-State Batteries. *Adv Energy and Sustain Res* 2300001 (2023) doi:10.1002/aesr.202300001.
29. Ngo, H. P. K. Development and characterization of safety and versatile electrolytes for lithium and post lithium batteries. (Université Grenoble Alpes, 2020).
30. Wang, X. *et al.* Exploring polymeric lithium tartaric acid borate for thermally resistant polymer electrolyte of lithium batteries. *Electrochimica Acta* **92**, 132–138 (2013).
31. Krause, C. H. *et al.* Quasi-solid single ion conducting polymer electrolyte membrane containing novel fluorinated poly(arylene ether sulfonimide) for lithium metal batteries. *Journal of Power Sources* **484**, 229267 (2021).
32. Li, C., Chen, Y., Zhang, Y. & Bao, H. A gel porous single-ion conducting polyelectrolyte with double anionic functional group for enhancing lithium ion battery performance. *Materials Letters* **288**, 129309 (2021).
33. Chen, L. *et al.* A Single-Ion Polymer Composite Electrolyte Via In Situ Polymerization of Electrolyte Monomers into a Porous MOF-Based Fibrous Membrane for Lithium Metal Batteries. *ACS Appl. Energy Mater.* **5**, 3800–3809 (2022).

34. Adams, B. D., Zheng, J., Ren, X., Xu, W. & Zhang, J. Accurate Determination of Coulombic Efficiency for Lithium Metal Anodes and Lithium Metal Batteries. *Adv. Energy Mater.* **8**, 1702097 (2018).

35. Aurbach, D. *et al.* Recent studies on the correlation between surface chemistry, morphology, three-dimensional structures and performance of Li and Li-C intercalation anodes in several important electrolyte systems. *Journal of Power Sources* **68**, 91–98 (1997).

36. Liu, Q. *et al.* Insight on lithium metal anode interphasial chemistry: Reduction mechanism of cyclic ether solvent and SEI film formation. *Energy Storage Materials* **17**, 366–373 (2019).

37. Ushakova, E. E. *et al.* Solid electrolyte interface formation between lithium and PEO-based electrolyte. *Applied Surface Science* **589**, 153014 (2022).

38. Siggel, M. R. F. & Thomas, T. D. Linear correlation of oxygen core-ionization energies of alcohols and acids with those of the corresponding methyl and ethyl ethers and esters. *Journal of Electron Spectroscopy and Related Phenomena* **48**, 101–116 (1989).

39. Xu, C. *et al.* Interface layer formation in solid polymer electrolyte lithium batteries: an XPS study. *J. Mater. Chem. A* **2**, 7256–7264 (2014).

40. Wang, L. *et al.* Insights for understanding multiscale degradation of LiFePO4 cathodes. *eScience* **2**, 125–137 (2022).

41. Zhang, W.-J. Structure and performance of LiFePO4 cathode materials: A review. *Journal of Power Sources* **196**, 2962–2970 (2011).

Conclusions and Perspectives

Conclusions

In this thesis, I systematically studied organic LMBs with SIPEs as a sustainable and safe energy storage system. In the research background part (Chapter 1), I generally analyzed the gap between the fast-growing demand of battery and the insufficient sustainability, safety, and cost in the current systems. By reviewing the current materials for batteries, I noticed that the superiority of organic active materials could be one of the solutions to improve the sustainability of batteries. Organic active materials are composed of earth abundant elements (C, H, N, O and S) with a lower environmental footprint and toxicity. And the production of organic active materials could be independent from the price and geopolitical limits of critical elements such as Co and Ni, making them greener and more sustainable candidates for battery applications. However, the drawbacks including solubility in organic solvents, low electronic conductivity, and low density are impeding the application of organic active materials.

To better understand and demonstrate the idea of this sustainable and safe organic LMB, a prototype cell configuration of Li|SIPE|PTCI was studied. In Chapter 2, I focused on developing novel SIPEs with linear/branched structures. The mPEGME-PTFSIVE copolymer is synthesized and characterized to have good ionic conductivity of 5×10^{-5} S cm^{-5}, high lithium transference number of 0.9 and low T_g of -55 °C. After blending with PVDF-HFP to cast a thin film, the SIPE was tested via CV and lithium plating/stripping tests to demonstrate the electrochemical stability. Finally, Li|SIPE|LFP and Li|SIPE|PTCI cells was fabricated and

cycled at 80 and 40 °C. High capacity retention and Coulombic efficiency were achieved, demonstrating excellent stability of the SIPE.

In Chapter 3, I_{1000}p-SO_3-cr SIPE, which possesses a crosslinked structure, is also characterized with high ionic conductivity, lithium transference number close to 1 and good mechanical strength. To adapt the SIPE to organic active material PTCI, electrodes with different structures are designed. With carbon nonwoven current collector, 3D composite electrode of PTCI can be infiltrated with SIPE to ensure both ionic and electronic conductivity in the electrode. The prototype organic LMB with active materials mass loading of 4.3 mg cm^{-2} successfully cycled more than 320 cycles at 80 °C with a capacity retention rate of 85.5% and average Coulombic efficiency of 99.9% which fully demonstrates its excellent stability.

Other than positive electrodes, the lithium metal as negative electrode, is still facing a lot of concerns, including dendrite growth, low Coulombic efficiency, inhomogeneous SEI formation, "dead" lithium etc. To understand the interaction between the SIPE and lithium metal electrode, a series of experiments were performed in Chapter 4. We compared I_{1000}p-SO_3-cr SIPE with and without $LiNO_3$ doping. For the ionic conductivity and transference number, the doping effect is negligible. The $LiNO_3$-doped SIPE showed advantage in interfacial resistance and Li reversibility throughout the CV, aging, and Li plating/stripping tests. The $LiNO_3$-doped SIPE, which altered the composition of SEI layer, enabled plating a dense and smooth lithium film rather than mossy lithium in the absence of $LiNO_3$.

The overall conclusions from this thesis are:

(1) By rational molecular design, SIPEs with good ionic conductivity with transference number close to 1 could be realized, which is favorable for the safe and stable battery application, especially with Li metal electrodes.

(2) The SEI between Li and SIPE plays an important role for the battery performance. By doping the SIPE with small amount of lithium nitrate, an advantageous SEI composition and lithium morphology was obtained, resulting in an improved reversibility and stability of lithium electrode.

(3) Organic active materials showed unique advantages of low-cost, sustainability and flexibility. By improving the design of the organic electrodes to incorporate the SIPE, organic LMBs could be developed with long-term cycling stability achieved. The safe and sustainable organic LMB could be a promising candidate for future energy storage devices.

Perspectives

In Chapter 2, the linear alternative copolymer of mPEGME-PTFSIVE showed unique donor-acceptor reaction with an A:D ratio of 2. The reaction mechanism still needs to be further investigated. Other model molecules, kinetic analysis ,electron spin resonance (ESR) and DFT simulation could be helpful to unveil the reaction intermediate and understand the polymerization mechanism. Ionic conductivity of the mPEGME-PTFSIVE copolymer can be further improved by reducing the EO:Li ratio by using mPEGME monomer with smaller molecular weight.

On the SIPE design, fluorine containing ionic function are used due to their benefit on dissociation to deliver good performance. In facing the environmental challenges, fluorine-free SIPE can be developed by substituting TFSI, FSI, perfluorosulfonate moieties with borate or other ionic functions. The development of these fluorine-free SIPE will be a challenging topic. $LiNO_3$ was used in Chapter 4 as an additive due to low-cost and availability. With the similar idea of doping SIPE, different additives including lithium borate, nitriles, and ionic liquids (and their combinations) could also be tested with SIPE to examine their effect on the SEI formation, in order to further improve stability of Li metal electrode.

In the thesis, only PTCI material was used as organic positive electrode material. Other types of organic active materials such as quinone-derivatives and ferrocene-derivatives could also be ideal choices to use with SIPEs. With organic active material with different voltage ranges, organic LMB or full organic lithium ion battery could be developed. Moreover, substituting the charge carrier from to sodium ion or even organic cations could be another potential solution to further improve sustainability of the organic batteries by substituting lithium content.

Annex

1. Synthesis

1.1 Materials

Poly(ethylene glycol) monomethyl ether (mPEG, Mw=1000) was purchased from TCI. Maleic anhydride (MA), 4-fluorobenzenesulfonyl chloride, sodium hydride, lithium hydride and 4-hydroxyl butyl vinyl ether were purchased from Sigma-Aldrich. Lithium nitrate was purchased from Alfa Aesar. Trifluoromethanesulfonamide was purchased from Fluorochem. Photoinitiator Irgacure 2959 was from Ciba and lucirin lr 8893 was from BASF. All the chemicals were used without purification.

Carbon coated Al foil was purchased form MSE supplies, thickness of 16 μm (with 1 μm of caron coating). Carbon nonwoven was purchased from Technical Fibre Products Inc, with grammage of 8g m^{-2}. LFP powder was purchased from MTI corp. Binder PVDF (Solef® 6020) was form Solavy S.A. Conductive carbon black powder (Super C 65) was from TIMCAL.

1.2 Synthesis of lithium ((trifluoromethyl)sulfonyl) ((4-(4-(vinyloxy) butoxy) phenyl) sulfonyl) amide (PTFSIVE)

5 g 4-fluorobenzenesulfonyl chloride, 4.22 g trifluoromethanesulfonamide and 20mL anhydrous dichloromethane were added to a three-neck flask under argon gas protection and ice bath. 5.72 g triethylamine was introduced via a dropping funnel. The reaction was then kept at room temperature for 10 h to yield a yellowish solution. After reaction, the solution was washed with DI water to remove excess of trifluoromethanesulfonamide. Then dichloromethane was removed by rotary evaporation. The product was dissolved again in 15 mL anhydrous THF and 1.5 g NaOH powder was added and stirred at ambient temperature overnight. Then excess of NaOH was removed by filtration and THF was evaporated to yield intermediate product sodium ((4-fluorophenyl)sulfonyl)((trifluoromethyl)sulfonyl)amide. The conversion of 4-fluorobenzenesulfonyl chloride was close to 100% determined by ^{19}F-NMR, the yield was >95%.

To yield the final product, 1.5 g of 4-hydroxybutyl vinyl ether was dissolved in 10 mL dry diglyme under argon protection. 328 mg NaH powder was introduced at 60 °C and stirred for

30 min to be fully dispersed. Then 3 g of intermediate product was added and the temperature was elevated to 120 °C. The reaction was monitored by ^{19}F NMR, until the aromatic fluorine peak at ~-109 ppm completely disappeared (conversion of sodium ((4-fluorophenyl)sulfonyl)((trifluoromethyl)sulfonyl)amide was close to 100%). After the reaction, the diglyme was evaporated and the solid was dispersed in acetonitrile and filtrated to remove the insoluble part. The solution was then mixed with 50% (v/v) DI water and passed through an amberlite IR120 lithium form ion exchange column. The acetonitrile was removed by evaporation and DI water was removed by freeze drying to yield PTFSIVE. The yield of PTFSIVE >80%.

1.3 Synthesis of poly(ethylene glycol) methyl ether maleate (mPEGME)

10 g mPEG was dissolved in 20 mL of anhydrous THF and then mixed with 0.98g maleic anhydride and stirred for 15 min at 40 °C. Then 79.5 mg LiH was added. After reacting for overnight, the mixture was filtrated though paper filter. Then THF was removed by rotary evaporation. Conversion of mPEG was >60%. The product was used without purification.

1.4 Synthesis of mPEGME-PTFSIVE copolymer

In a Schlenk flask, 0.93g PTFSIVE, 5 g mPEGME and 60 mg of photo initiator lucirin lr 8893 was dissolved in 5 mL anhydrous THF. The mixture was degassed with three cycles of freeze-pump-thaw. Then the flask was placed under UV irradiation (mercury lamp, 365 nm, 6.8 W) with magnetic stirring for 3 h, The product was purified by dialysis with a regenerated cellulous tubing against DI water for two days. The water was then removed by freeze drying. The yield of the polymer was ~ 30%

2. Membrane casting

In a typical process for 70% of SIPE, 210 mg of mPEGME-PTFSIVE copolymer was mixed with 90 mg of PVDF-HFP and dissolved in 5 mL DMSO and acetone mixture (50:50) and cast in a small Petri dish. The solvent was dried in an oven at 80 °C for 12 h and then under vacuum for 12 h.

3. Methods

3.1 NMR spectroscopy

^{1}H, ^{19}F, ^{7}Li NMR spectra were taken by a Bruker Avance III HD 400MHz NMR spectrometer and processed with Bruker topspin software. The samples were prepared in DMSO-d_6 or D_2O solvents for obtaining the spectra.

^{7}Li NMR was taken with an internal reference of $LiSO_3CF_3$ in DMSO-d_6 to determine the lithium content. The insertion tube was calibrated with three solutions of $LiSO_3CF_3$ in acetone-d_6 with different concentrations by integrating the Li signals. The SIPE sample was dissolved in $LiSO_3CF_3$ and inserted with the same internal reference to take ^{7}NMR spectra. Li concentration was determined by linear extrapolation of the calibration data.

3.2 SEC

SEC was measured on Waters 515 HPLC pump and 2414 RI detector with Styragel HR GPC column in THF. The SEC was calibrated with standard polystyrene samples before use.

To evaluate the molecular weights and distribution, the sample was dissolved in the HPLC grade THF with a concentration of 4 mg mL-1 and filtered with a 0.45 μm PTFE filter.

SEL-LS was conducted with Agilent PLgel-Mixed-LS columns. The SEC-LS sample was prepared with HPLC grade DMAc with 0.5 g mol-1 LiCl. The concentration of sample is ~1 mg mL^{-1}.

3.3 AAS

Atomic absorption spectroscopy (AAS) was conducted on a PerkinElmer PinAAcle 900 atomic absorption spectrometer. The device was calibrated with LiCl standards before use. The SIPE sample was prepared with an aqueous solution with Li concentration ~1 mg L^{-1}.

3.4 SEM

SEM images of polymer membrane, PTCI and LFP electrodes were collected with a ZEISS Ultra 55 SEM equipped with SE2, backscattered electron detector and Inlens detector. The

sample was coated with graphite to improve the conductivity.

SEM images of mossy lithium in chapter 4 were collected with a ZEISS Gemini SEM. The samples are prepared in Ar-filled glove box and transfer into SEM with airlock protection.

SEM images was processed by ImageJ software.[2]

3.5 Thermal analysis

Differential scanning calorimetry (DSC) was conducted using a Mettler Toledo DSC1 STAR system, by decreasing the temperature from RT to 125 °C then decreasing it to -100 °C and increasing to 125 °C with rate of 10 °C min^{-1} under nitrogen flow.

Thermogravimetric analysis (TGA) was conducted with a Mettler Toledo TGA1 STAR system, by increasing temperature from RT to 500 °C with a rate of 10 °C min^{-1} under nitrogen flow.

3.6 Electrochemical methods

All the electrochemical tests were conducted using a Biologic VMP-300 potentiostat/galvanostat, and the data were processed using the Biologic EC-lab software.

Electrochemical impedance spectroscopy (EIS) was conducted in a frequency range from 7 MHz to 0.1 Hz. For each frequency, three measurements were performed, and the final spectra represents the average.

3.7 Cell assembly

All the cells with SIPE in the thesis, including CV cells, symmetrical Li||Li cells, Li|SIPE|Cu cells, and LMBs were assembled in CR2023-type coin cells. The parts of a coin cell are shown Figure 134. The cells were assembled in an Ar-filled glove box.

Figure 134. (A) Parts of CR2032 type coin cell. From left to right, the parts are bottom shell, spacer of 1mm , spacer of 0.5 mm, spring, top shell with sealing ring, respectively. (B) A CR2032 type coin cell after assembly.

3.8 Ionic conductivity

Ionic conductivity is the most important property to evaluate an electrolyte. To achieve an ideal functional battery, high conductivity 10^{-3} S cm^{-1} is preferred. The method to measure ionic conductivity is electrochemical impedance spectroscopy (EIS) with a blocking cell with two parallel inert electrodes and the electrolyte is sandwiched in between. In the EIS Nyquist plot, a semicircle at high-frequency region and straight line at low frequency can be observed. The semicircle is determined by the bulk resistance (R_b) of the electrolyte and double layer capacitance, therefore R_b can be obtained by fitting the diameter of the semicircle. The ionic conductivity is calculated with the following equation:

$$\sigma = \frac{l}{R_b \cdot A}$$

Where l is the distance between two electrodes, and A is the contact area of electrolyte with electrode, R_b is the bulk resistance of the electrolyte. For the SIPE membranes, which was cut into disc with a known diameter was assembled into a CR2032 type coin cell with two stainless-steel electrodes. To confirm the geometric parameters of the membranes, the samples was disassembled after all the EIS tests and the surface area and thickness was measured again.

The liquid electrolyte conductivity is usually measured with glass cells with platinum electrodes. The cell needs to be calibrated with 0.01 mol L^{-1} KCl standard solution to obtain the cell constant K_{cell}. Where K_{cell} can be calculated as follows:

$$K_{cell} = \frac{l}{A} = 1412\mu S \cdot cm^{-1} \times R_{KCl}$$

where R_{KCl} is the bulk resistance of standard solution at 25°C.

3.9 XPS

XPS data was fitted with XPSPEAK4.1 software (written by Raymund W.M. Kwok, The Chinese University of Hong Kong). All the XPS data was calibrated by the hydrocarbon peak at 285 eV before fitting. The photoelectron energy referenced the NIST X-ray Photoelectron Spectroscopy Database (https://srdata.nist.gov/xps/).

3.10 Data processing

The data was processed with Microsoft Office suite and open-source python package pandas (https://pandas.pydata.org/). All the data was plotted with matplotlib, which is an open-source 2D graphics package used in python for data visualization.[1]

4. Solubility test of PTCI

Since their solubility is one of the major issues for organic active materials leading to capacity fading. To reduce the solubility of the organic active materials, different strategies including polymerization to increase the molecular weight and functionalization with polar group (such as -SO_3Na).

It is necessary to examine the solubility of the PTCI material in different solvents. The solubility test could provide information for choosing solvent for electrode preparation and electrolyte for cycling.

To examine the solubility of the PTCI material,10 mg of PTCI was added to 1 mL of different solvents in a small vial, including water, ethanol (EtOH), acetonitrile (ACN), diethyl carbonate (DEC), diglyme (DEGME), dimethyl sulfoxide (DMSO), and N-Methyl-2-pyrrolidone (NMP). The solvent was chosen to represent typical solvents for electrode processing (water, NMP) and electrolytes including nitrile (ACN), carbonate (DEC) and ether (DEGME).

After mixing and setting still for overnight, for all the solvents, most of PTCI material did not

dissolve and stayed at bottom as sediment and the solution showed completely different colors. For water, ethanol and acetonitrile, the solution remained colorless, suggesting non-soluble behavior. For DEC, DEGME, DMSO and NMP, yellow-orange color was observed, which indicates PTCI is partially soluble in these solvents. And the solubility follows the order of DEC<DEGME<DMSO<NMP. The image of the solubility test was displayed in Figure 135.

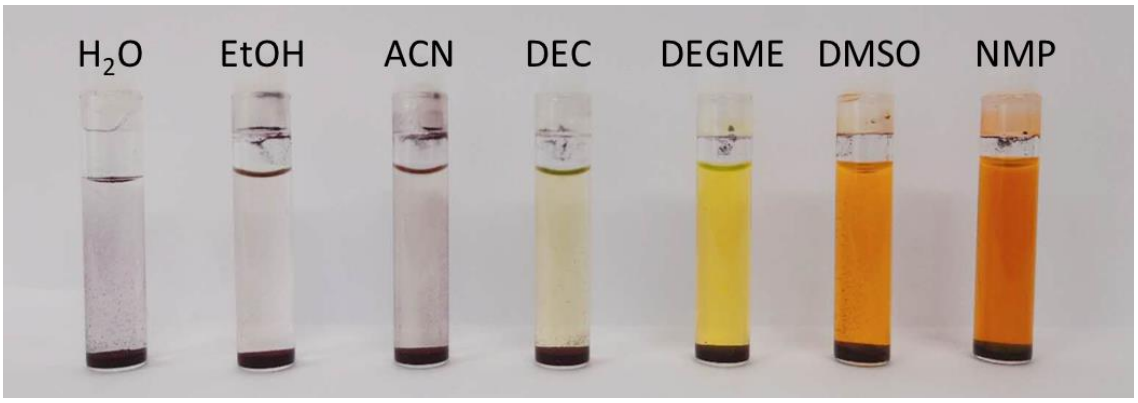

Figure 135. Solubility test of PTCI material in different solvents.

These tests proved that PTCI has low solubility in most solvents which are used in electrolyte and electrode processing, which is favored in battery applications. The low solubility of PTCI is also related with the polymer structure that was used to reduce the solubility.

5. Additional cycling tests

Additional cycling tests are presented to support the conclusions in the thesis.

LFP|SIPE70|Li cells were prepared with the same method as in Chapter 2, Figure 56-61 and cycled at 40 °C, with CC-CV charge/discharge at C/10 for 50 cycles. The LFP mass loading of the cell was ~1.94 mg cm^{-2}. The cell showed a good average capacity of 160 mAh g^{-1} and average Coulombic efficiency more than 99.9%, which exhibited the satisfying stability of the SIPE70 electrolyte at 40 °C. The capacity, Coulombic efficiency and charge/discharge profiles are shown in Figure 136.

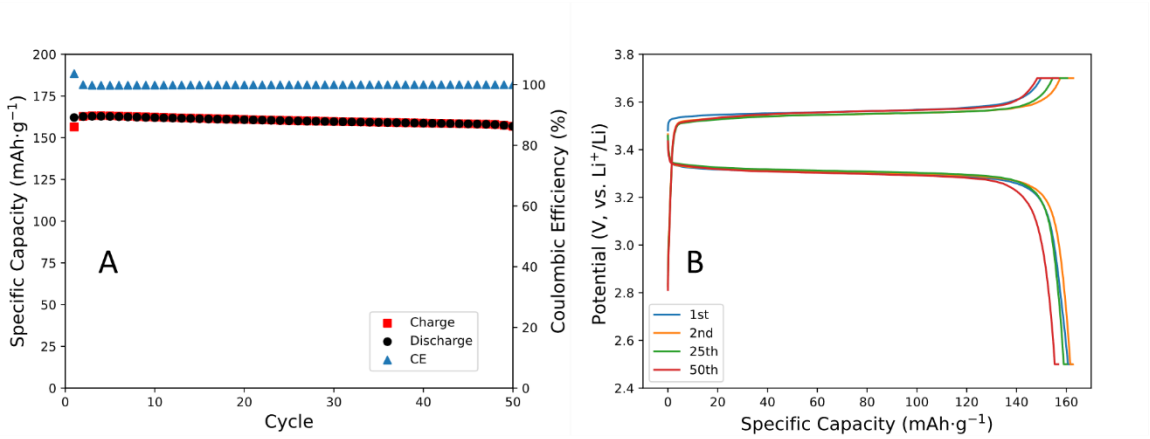

Figure 136. Li|SIPE70|LFP cells with mPEGME-PTFSIVE electrolyte at 40 °C: (A) capacity and Coulombic efficiency; (B) charge/discharge profiles.

Li|SIPE70|PTCI cells were prepared with similar method of Chapter 2, Figure 65-66. The mass loading of PTCI electrode was ~1.08 mg cm^{-2}. The cells were cycled at 80 °C with different current densities of 10, 20, 40, 60, 80 and 100 mA g^{-1}. The average charge capacity at each current density was 85, 82, 75, 68, 63 and 54 mAh g^{-1}, respectively. The Coulombic efficiency of the cell showed an increase trend with increasing current density from 94.6% at 10 mA g^{-1} to 99.4% at 100 mA g^{-1} and the average Coulombic efficiency for 100 cycles was 98.4%. The capacity, Coulombic efficiency and charge/discharge profiles are shown in Figure 137.

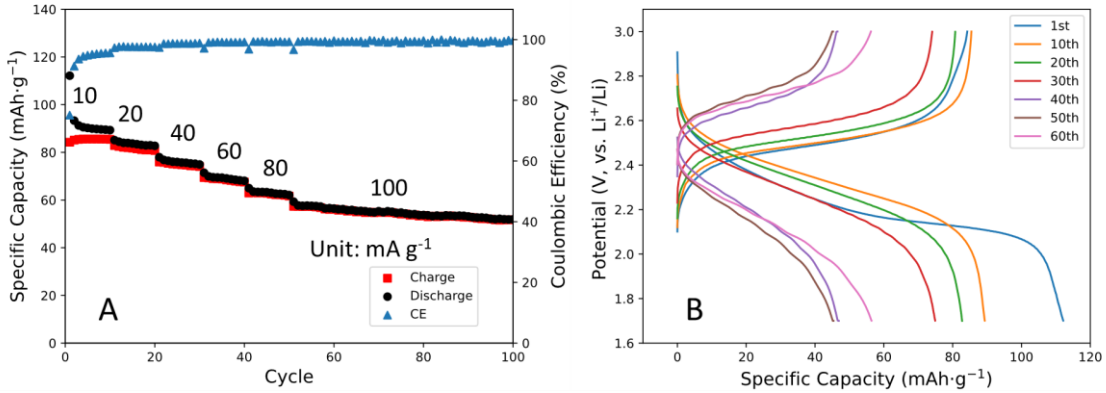

Figure 137. Li|SIPE70|PTCI cells with mPEGME-PTFSIVE electrolyte at 80 °C: (A) capacity and Coulombic efficiency; (B) charge/discharge profiles.

Li|SIPE|PTCI cells was prepared by the same method in Chapter 3, Figure 90. The electrode

was cast on 2 layer of carbon nonwoven fabric and infiltrated by I_{1000}p-SO_3-db polymer and then crosslinked to reach higher mass loading of PTCI organic active material. The mass loading of the cell was 2.9 mg cm^{-2}. The cell was cycled with galvanostatic charge/discharge at 80 °C with a current density of 10 mA g^{-1} for 10 cycles. The cell showed a stable cycling with an average capacity of 63 mAh g^{-1} and an average Coulombic efficiency of 96.4%.

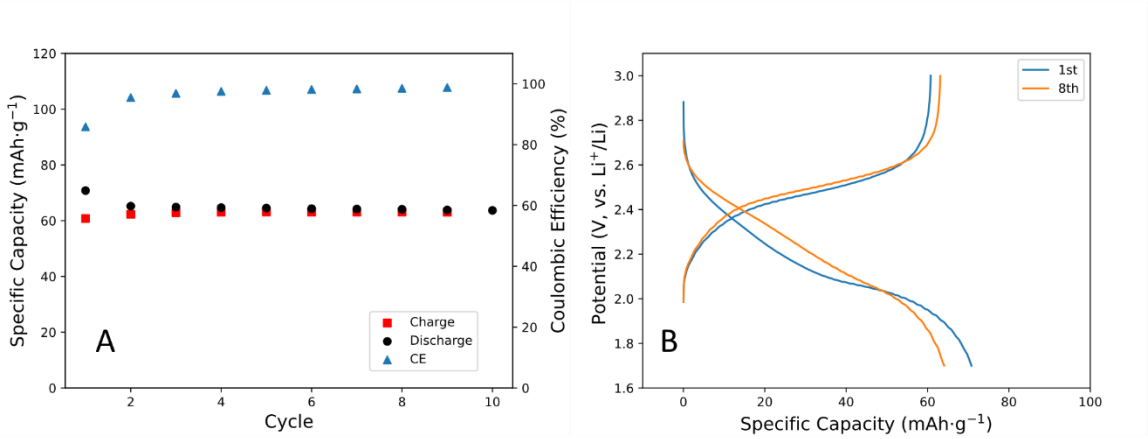

Figure 138. Li|SIPE70|LFP cells with carbon current collector infiltrated in I_{1000}p-SO_3-cr SIPE at 80 °C: (A) capacity and Coulombic efficiency; (B) charge/discharge profiles.

Li|SIPE|LFP cells with 0.5% $LiNO_3$ doped I_{1000}p-SO_3-cr electrolyte were prepared with the same method in Chapter 4, Figure 129. The LFP electrode was cast on carbon coated Al foil with a mass loading of 1.82 mg cm^{-2}. The cell was cycled with galvanostatic charge/discharge at 80 °C. The 3 cycles at the beginning were at current density of C/20 and the following cycles were at C/2 (C = 170 mA g^{-1}). The specific capacity was 147 mAh g^{-1} at C/20 and 126 mAh g^{-1} at C/2. Nearly no capacity decay was overserved over 70 cycles with an average Coulombic efficiency of 99.2%, which indicated the good stability of the cell and $LiNO_3$ doped SIPE. The cycling data was shown in Figure 139. The EIS data during the cycling was recorded after each cycle, where the cell was fully discharged. In the impedance, a semicircle at high frequencies and a tail at lower frequencies could be noticed. After 4^{th} cycle, the EIS spectra showed almost overlapped, which suggests the good stability of the cell. The EIS spectra were shown in Figure 140.

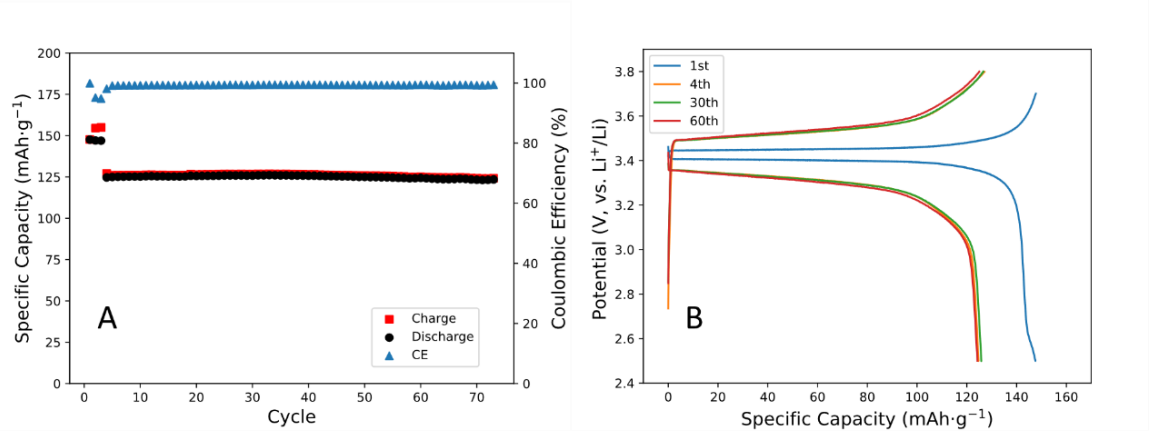

Figure 139. Li|SIPE|LFP cells with 0.5% $LiNO_3$ doped I_{1000}p-SO_3-cr electrolyte at 80 °C: (A) capacity and Coulombic efficiency; (B) charge/discharge profiles.

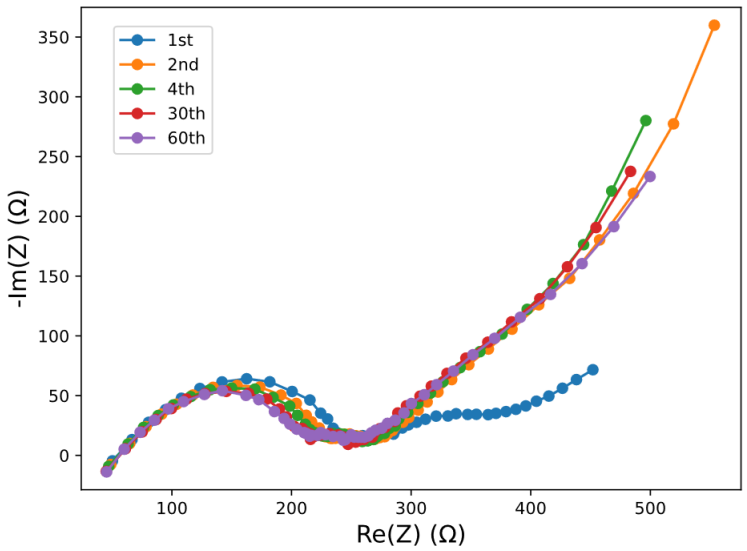

Figure 140. EIS spectra of with 0.5% $LiNO_3$ doped I_{1000}p-SO_3-cr electrolyte at 80 °C cells after discharge.

References

1. Hunter, J. D. Matplotlib: A 2D Graphics Environment. *Comput. Sci. Eng.* **9**, 90–95 (2007).
2. Schneider, C. A., Rasband, W. S. & Eliceiri, K. W. NIH Image to ImageJ: 25 years of image analysis. *Nat Methods* **9**, 671–675 (2012).